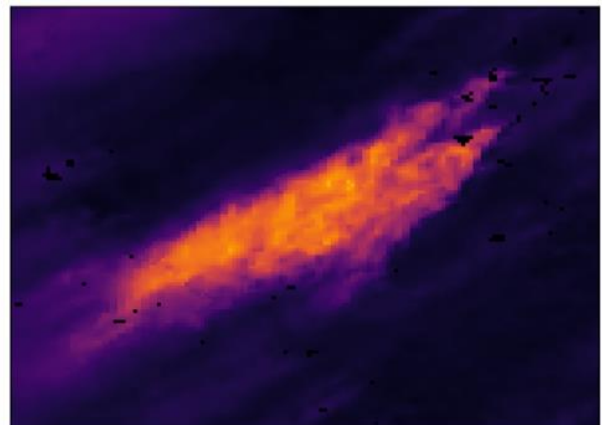


# Smoke Emissions from African Landscape Fires Characterised via Satellite Remote Sensing and Atmospheric Modelling



Hannah Mai Linh Nguyen

A thesis submitted for the degree of Doctor of Philosophy (PhD)

Department of Geography, King's College London

11<sup>th</sup> June 2021

# Abstract

Landscape fire is an essential part of the Earth-Atmosphere system, and quantitative assessment of the emissions from biomass burning is of vital importance in a number of research fields, from long term climate modelling to public health. Over the satellite era, the study of landscape fire emissions at scales up to the continental and global and down to the level of individual fires has been made possible. However, significant sources of uncertainty remain in fire emissions estimation methodologies, as well as large discrepancies between the emissions reported in the resulting fire emission inventories. This thesis exploits satellite remote sensing observations and atmospheric modelling to develop and evaluate a new high spatio-temporal resolution fire emission inventory for Africa. It focuses on a method that can supply emissions estimates in near-real time that can, in future, support applications like air quality forecasting and near-real time atmospheric composition monitoring.

The primary data used are satellite active fire (AF) detections and assessments of their fire radiative power (FRP) coming from the SEVIRI sensors aboard the Meteosat geostationary satellites. Simultaneous Meteosat-11 and Meteosat-8 data are investigated for the first time and compared to matching AF observations from MODIS to determine the impact of sensor view zenith angle (VZA) on the quantification of African fire with these geostationary AF datasets. Results show that the differing orbital positions of the Met-8 and Met-11 geostationary platforms, located over East and West Africa respectively, cause the FRP data from the former to be on average 20% higher than the latter in terms of matched daily fires in Africa. This effect is a result of the lower VZA data offered by the Met-8 sensor over areas of Africa showing the highest amounts of fire activity - meaning that in these areas pixels are smaller in Met-8 than Met-11 and thus more low FRP fires can be detected. Results also show that AF detections in biomes characterized by higher amounts of tree canopy cover are more dependent on these sensor VZA effects, and that the newly operational Meteosat-8 FRP product currently features a significant number of false AF detections at  $VZA > 40^\circ$ .

To estimate fire emissions from these geostationary FRP data sources, a number of improvements to the FREM “top-down” fire emission inventory of Mota and Wooster (2018) were devised, applied and tested. A set of new (FREMv2) biome-specific smoke emission

coefficients,  $C_{biome}$  (g MJ<sup>-1</sup>), linking FRP observations to total particulate matter (TPM) emissions were generated. This was done by combining the FRP record stored within the Met-11 SEVIRI FRP-PIXEL product with data from the MODIS MAIAC aerosol optical depth (AOD) product - which is shown to be far more appropriate for this application than the standard 10 km MODIS AOD product used in the original FREM approach. These new  $C_{biome}$  values directly link measured FRP with emission rates of total particulate matter (TPM), and are used with the long-term SEVIRI FRP-PIXEL dataset to produce a six-year (2013 to 2018) fire emission inventory for Africa covering TPM, CO<sub>2</sub>, CO and CH<sub>4</sub>. This inventory was compared with other state-of-the-art emission inventories (GFAS, GFED and FEER) and the FREMv2 emissions are shown to agree with those of FEER to within 7%, but to also be 80% higher and 43% higher than those of GFAS and GFED respectively. The FREMv2 estimates of CO<sub>2</sub>, CO and CH<sub>4</sub> were used to estimate total carbon emissions, and these were used in combination with the Sentinel-2 FireCCISFD11 20 m burned area product to produce one of the first satellite data driven mappings of fuel consumption per unit area,  $F_c$  (kg m<sup>-2</sup>), for Africa.

The FREMv2-derived fire emissions were evaluated for their absolute accuracy through atmospheric modelling. The emissions were used within the WRF-CMAQ model and the resulting simulations made across southern Africa at a 9 km grid cell resolution were compared to independent observations coming from the Sentinel-5P TROPOMI CO product, the AERONET AOD network and the MODIS MAIAC AOD product. These comparisons indicate that the CMAQ-driven FREMv2 emissions showed very good agreement with satellite-derived CO measures – CMAQ-modelled total column CO values were within 13% of those of the Sentinel-5P CO product over the whole model domain. Results from these CO inter-comparisons show that the CMAQ model parameterized with FREMv2 emissions shows better agreement with observations than has any other model-based validation study which uses alternative emission inventories. However, AOD fields from the same simulations did not show as good agreement between model and observation as those based on CO, partly due to inaccuracy in the TPM emissions estimates but most probably more due to model error related to the evolution and treatment of aerosols in the CMAQ model configuration used.

Overall, the methods developed and tested in this PhD thesis, as well as the other investigations carried out using the various input and output datasets, have improved understanding of sensor-specific factors impacting the quantification of African fire activity using geostationary satellites. Crucially, it has also significantly enhanced the approach used for delivering top-down FRP-based fire emissions from geostationary data and has demonstrated the efficacy of this approach using atmospheric modelling and comparisons of model outputs to independent measures. Based on these findings the work includes some suggestions for future advancements in the remote determination of fire emissions. These include the development of a top-down approach similar to FREMv2, but instead exploiting satellite-determined CO measures to obtain  $C_{biome}^{CO}$  emission coefficients, and an expansion of the current FREMv2 fire matchup dataset used to derive  $C_{biome}$  values to (i) more accurately quantify emissions from fires in closed canopy forests biomes and ii) account for the effect of sensor VZA on the geostationary satellite determination of AFs.

# Acknowledgements

I would first like to thank my supervisor Prof. Martin Wooster for all his input and guidance over the last 4 years. His advice and encouragement have helped me developed as a scientist and enabled me to pursue the amazing opportunities I have had during my time at King's. He is a brilliant scientist and his passion for research and ever warm and open attitude have made it a real pleasure to be part of the King's NCEO/Wildfire Research group. My thanks go also to my second supervisor Dr Alessia Annibale for her support and for always making the time to help me, especially in the early stages of my PhD.

My thanks go to the Engineering and Physical Sciences Research Council's (EPSRC) Centre for Doctoral Training in Cross-Disciplinary Approaches to Non-Equilibrium Systems (CANES) for funding this PhD award (EP/L015854/1). I also would like to also acknowledge Sumit Sharma, Nimish Singh and the CMAS Forum Team who provided helpful input during the setup of the WRF-CMAQ model.

Many thanks to my colleagues Jiangping, Danial and Weidong for their advice, coding fixes and IT input over the last few years. I am also deeply grateful to Tom, Tianran and Mark for all our discussions over cups of tea and the shared code snippets, invaluable comments and feedback and help staying on track during write up.

As the daughter of a refugee who came to the UK with nothing, I feel humbled and privileged to have had the opportunity to undertake this PhD and the completion of this thesis is marked by the love and support of all those dear to me.

My PhD experience at King's would not have been the same without the amazing friends that I have made along the way and I would like to thank Tom, Mary, Big T, Mark, Anna, Rory, Renee and the rest of the gang for being such great humans. Their moral support, constant encouragement and silly dance moves have helped me through what could have been a very tough and isolated year of write up. I'd like to thank my best friend Finja who, even after twenty years of friendship, is still always there for me with a pep talk and tasty baked goods. A big thank you also to my other great friends who have supported me through all the ups and downs of PhD life, Jen, Ellie, Benj and Sheevs. I am very grateful to Bà for accommodating me the last few years and to my Grandma and the Nguyen clan for always cheering me on.

I would like to thank my boyfriend Saad for being by my side through it all. From helping me with my CANES maths problems to sorting out my lockdown office to just patiently listening to my PhD life rants. For sharing in all the big and small successes and always being there to push me on when I felt close to giving up, I am so very grateful.

Lastly, I would like to express my profound gratitude to my incredible family for all they have given me, both before and during this PhD. To Tom for his ever-sincere concern and interest, even when he has no idea what I'm talking about and for his sense of humor when the numbers just don't add up. To Tam who is always close behind with reassuring words of encouragement. To Nat for putting up with my endless nonsense for the last 10 months and for our long evening walks pondering the questions of life. Finally and most importantly, to my wonderful parents for a lifetime of wisdom, guidance and unfailing love. Without you both I would not have been able to do this, thank you.

*To Ông - Trải qua nhiều hy sinh, mong Ông diu dàm nhìn xuống với ánh mắt tự hào*

*To Grandma – for your steadfast love and ever faithful prayers*

# Table of Contents

<b>ABSTRACT .....</b>	<b>2</b>
<b>ACKNOWLEDGEMENTS .....</b>	<b>5</b>
<b>TABLE OF CONTENTS .....</b>	<b>8</b>
<b>LIST OF FIGURES.....</b>	<b>12</b>
<b>LIST OF TABLES.....</b>	<b>22</b>
<b>LIST OF ABBREVIATIONS .....</b>	<b>24</b>
<b>CHAPTER 1 INTRODUCTION.....</b>	<b>25</b>
<b>CHAPTER 2 BACKGROUND AND SPECIFIC OBJECTIVES .....</b>	<b>28</b>
<b>2.1 INTRODUCTION .....</b>	<b>28</b>
<b>2.2 SATELLITE REMOTE SENSING OF FIRE – ALGORITHMS .....</b>	<b>28</b>
<b>2.2.1 Burned Area Methods .....</b>	<b>29</b>
<b>2.2.2 Active Fire Detection and Fire Radiative Power.....</b>	<b>31</b>
<b>2.2.3 Remote Sensing of Other Fire Related Variables .....</b>	<b>35</b>
<b>2.2.3.1 Aerosol Optical Depth .....</b>	<b>36</b>
<b>2.2.3.2 Total Column Trace Gases.....</b>	<b>38</b>
<b>2.3 SATELLITE REMOTE SENSING OF FIRE – INSTRUMENTS .....</b>	<b>38</b>
<b>2.3.1 Polar Orbiting Satellites .....</b>	<b>39</b>
<b>2.3.2 Geostationary Satellites.....</b>	<b>42</b>
<b>2.3.3 Integrated Fire Products.....</b>	<b>43</b>
<b>2.4 FIRE EMISSION INVENTORIES.....</b>	<b>46</b>
<b>2.4.1 Bottom-up Fire Emission Inventories.....</b>	<b>47</b>
<b>2.4.1.1 The Global Fire Emissions Database - GFED .....</b>	<b>49</b>
<b>2.4.1.2 The Global Fire Assimilation System - GFAS .....</b>	<b>52</b>
<b>2.4.1.3 The Fire Inventory from NCAR – FINN.....</b>	<b>53</b>
<b>2.4.2 Top-down Approaches.....</b>	<b>54</b>
<b>2.4.2.1 The Fire Energetics and Emissions Research <math>C_e</math> product - FEER .....</b>	<b>55</b>
<b>2.4.2.2 The Fire Radiative Energy Emissions - FREM .....</b>	<b>57</b>
<b>2.5 VALIDATION AND ASSESSMENT OF FIRE EMISSIONS ESTIMATES .....</b>	<b>60</b>
<b>2.5.1 An Overview of Atmospheric Modelling .....</b>	<b>61</b>
<b>2.5.1.1 NWP Model and CTM Model Selection .....</b>	<b>62</b>

2.5.1.2 Model Configuration and Domain Set-up.....	64
2.5.1.3 Initial and Boundary Conditions .....	64
2.5.1.4 Non-fire Emission Inventories.....	65
2.5.2 CTMs for Fire Emissions Evaluations .....	65
2.6 SUMMARY AND RESEARCH OBJECTIVES.....	69

## **CHAPTER 3 ASSESSING THE VIEW ZENITH ANGLE (VZA) AND VEGETATION**

### **DEPENDENCIES OF METEOSAT SEVIRI FRP RETRIEVALS.....71**

3.1 INTRODUCTION.....	71
3.2 METHODOLOGY.....	75
3.2.1 Datasets .....	75
3.2.2 Study Region and Biome Classification.....	76
3.2.3 M8 and M11 Validation with MODIS .....	78
3.2.3.1 Active Fire Detection performance .....	78
3.2.3.2 FRP Measurement Analysis .....	81
3.2.4 M8 and M11 Comparison .....	82
3.2.5 VZA and Biome Effect on FRP .....	82
3.3 RESULTS.....	84
3.3.1 M8 and M11 Validation using MODIS FRP .....	84
3.3.1.1 FRP Characterisation Analysis .....	86
3.3.1.2 Errors of Omission and Commission.....	94
3.3.2 M8 and M11 SEVIRI Inter-comparison.....	96
3.3.3 FRP Sensitivity to Observation VZA.....	101
3.3.4 M8 SEVIRI False AF Detections .....	106
3.3.5 Biome Effect on FRP and Interaction with VZA .....	109
3.4 DISCUSSION.....	115
3.4.1 M8 Measurements of FRP .....	115
3.4.2 Vegetation Type and VZA Effect on FRP .....	116
3.5 SUMMARY AND CONCLUSIONS .....	118

## **CHAPTER 4 ADVANCES IN THE ESTIMATION OF HIGH SPATIO-TEMPORAL RESOLUTION PAN-AFRICAN TOP-DOWN BIOMASS BURNING EMISSIONS MADE USING GEOSTATIONARY FIRE RADIATIVE POWER (FRP) AND MAIAC AEROSOL OPTICAL DEPTH (AOD) DATA .....**122

4.1 INTRODUCTION.....	122
4.2 LIMITATIONS IN CURRENT TOP-DOWN METHODOLOGIES.....	124

4.2.1 MODIS AOD Observations .....	124
4.2.2 Other Limitations .....	128
4.3 DEVELOPMENTS TO THE FREM APPROACH.....	128
4.4 SMOKE EMISSION COEFFICIENTS, $C_{biome}$ , DERIVATION.....	131
4.4.1 Geographic Area and Biome Classification.....	131
4.4.2 FRP and AOD 2015 Datasets and Fire Matchups .....	135
4.4.3 Derivation of Smoke Emission Coefficients ( $C_{biome}$ ) .....	138
4.5 FREMV2 EMISSIONS INVENTORY DEVELOPMENT.....	143
4.5.1 Total Particulate Matter (TPM) Emissions.....	143
4.5.2 Trace Gas and Total Carbon Emissions .....	150
4.5.3 Fuel Consumption per Unit Area $F_c$ from Burnt Area Observations.....	154
4.6 SUMMARY AND CONCLUSIONS .....	156

## **CHAPTER 5 VALIDATION OF A THE FREMV2 FIRE EMISSION INVENTORY USING WRF-CMAQ, AERONET AND MAIAC OBSERVATIONS OF AOD AND SENTINEL-5P**

MEASUREMENTS OF CO .....	160
5.1 INTRODUCTION .....	160
5.2 METHODS .....	161
5.2.1 Model Description and Setup.....	161
5.2.2 Emissions.....	166
5.2.2.1 Anthropogenic emissions .....	166
5.2.2.2 Fire emissions.....	167
5.2.3 Validation Datasets.....	168
5.2.3.1 Sentinel-5P TROPOMI CO .....	169
5.2.3.2 AERONET AOD .....	170
5.2.3.3 MAIAC MODIS AOD .....	171
5.3 RESULTS.....	172
5.3.1 WRF Metrological Fields Compared to ERA-Interim .....	172
5.3.2 CMAQ Column CO Comparisons with Sentinel-5P CO .....	174
5.3.2.1 Full Domain and ROIs .....	174
5.3.2.2 Individual CO Plumes .....	179
5.3.3 CMAQ AOD Comparisons to AERONET .....	182
5.3.4 CMAQ AOD Comparisons with MAIAC.....	190
5.3.4.1 Full Domain and ROIs .....	190
5.3.4.2 Individual Smoke Plumes .....	195
5.3.5 Biome Specific Assessment of Emissions.....	197

5.4 DISCUSSION.....	204
5.4.1 Model Error in CMAQ .....	204
5.4.2 FREMv2 Emissions Overestimation.....	210
5.4.2.1 High-woodland Savanna and Closed Canopy Forest $C_{biome}$ values .....	210
5.4.2.2 Intrinsic ‘Small fire’ Correction.....	213
5.5 CONCLUSIONS AND FURTHER WORK .....	214
<b>CHAPTER 6 SUMMARY OF FINDINGS, CONCLUSIONS AND FUTURE WORK .....</b>	<b>218</b>
6.1 SUMMARY OF FINDINGS IN RELATION TO SPECIFIC RESEARCH OBJECTIVES .....	218
6.2 OVERALL CONCLUSIONS AND IMPLICATIONS .....	223
6.3 RECOMMENDATIONS FOR FUTURE WORK .....	224
<b>REFERENCES.....</b>	<b>228</b>
<b>APPENDIX A.....</b>	<b>249</b>
<b>APPENDIX B .....</b>	<b>250</b>
<b>APPENDIX C .....</b>	<b>251</b>

# List of Figures

<b>Figure 2.1</b> Reflectance change detection using two MODIS channels (diamonds and crosses) used to determine the presence of a fire burn scar occurring on day 240 (Giglio et al., 2009) .....	30
<b>Figure 2.2</b> Planck's Law showing the behaviour of black body radiance at different temperatures from Calle and Casanova (2008). .....	32
<b>Figure 2.3</b> True colour RGB image from MODIS aboard Terra and VIIRS aboard Suomi NPP showing global coverage on single day (May 29 <sup>th</sup> 2013). Taken from Levy et al. (2015). ....	40
<b>Figure 2.4</b> Variations in minimum, maximum and mean FRP per pixel in the (a) MODIS and (b) VIIRS FRP products, plotted as a function of sensor View Zenith Angle (VZA). Taken from (Li et al., 2020). .....	41
<b>Figure 2.5</b> The field of view of sensors aboard several geostationary satellite platform which are currently operational. ....	43
<b>Figure 2.6</b> A comparison of the native SEVIRI FRP and MODIS FRP products with the virtual FRP generated by the empirical f-D distribution database of Freeborn et al. (2009).....	45
<b>Figure 2.7</b> Mean burned area fraction, fuel consumption and total carbon emissions per unit area between 1997 and 2014, as determined by GFEDv4s (Van Der Werf et al., 2017) .....	51
<b>Figure 2.8</b> The relationship between the emission rate of TPM in a smoke plume and the FRP of the fire associated with that plume, for all fires in a single 1.0° grid cell (Ichoku and Ellison, 2014). .....	56
<b>Figure 2.9</b> The FEER global TPM smoke emission coefficient product with a spatial resolution of 1.0° with which $C_e$ values (in $\text{kg s}^{-1} \text{MW}^{-1}$ ) can be used to directly generate emission of TPM from FRP data (Ichoku and Ellison, 2014). .....	56
<b>Figure 2.10</b> The relationship between FRE and TPM from fire-plume matchups observed in each of the five biomes defined with the GLOBCOVER 2009 landcover map. The slope of these gives the $C_{biome}$ value for a) closed canopy forest b) open canopy forest/woody savanna c) shrublands d) grasslands and e) managed land. ....	59
<b>Figure 2.11</b> Schematic describing the different approaches to NWP and CTM coupling in on-line and off-line modelling systems (Kukkonen et al., 2012).....	63
<b>Figure 2.12</b> GFASv1.0, GFASv1.1, SEVIRI FRP-PIXEL based and SEVIRI WF_ABBA based fire emissions used as input in CMAQ compared with MODIS true colour imagery and MODIS AOD observations of smoke resulting from a fire near Antalya on 1 <sup>st</sup> August 2008 at 14:30 UTC. ....	66

<b>Figure 2.13</b> Comparisons between FLAMBE, FINNv1.0, GFEDv3.1, FEER-SEVIRIv1.0, GFASv1.0, GBBEP-Geo and QFEDv2.4 for (a1–a7) monthly total smoke OC+BC emissions (unit: g m <sup>-2</sup> ) during February 2010; (b1–b7) the ratio of individual smoke emissions to their means among different inventories; (c1–c7) February mean column total PM2.5 (unit: mg m <sup>-2</sup> ); (d1–d7) the ratio of PM2.5 from different emission inventories to their means simulated by WRF-Chem. (e and f) MODIS AOD (from Terra and Aqua) at 550 nm as plotted within the NASA Giovanni. Taken from (Zhang et al., 2014) .....	68
<b>Figure 3.1</b> True colour image taken by the SEVIRI sensors operating aboard Meteosat-11 (Left) and Meteosat-8 (right) - showing the full disk imagery collected from their respective positions centred over 0° N, 0° E and 0° N, 41.5° E. (Images adapted from EUMETSAT: <a href="https://www.eumetsat.int/website/home/">https://www.eumetsat.int/website/home/</a> ) .....	73
<b>Figure 3.2</b> Growth in SEVIRI pixel footprint area as a function of VZA as assumed in the FRP-PIXEL product algorithm detailed in Wooster et al. (2015) which is used to generate the Met-8 and Met-11 FRP-PIXEL products analysed herein. The data for this plot were derived from the AF pixels in the Met-11 SEVIRI FRP-PIXEL products collected between 1 <sup>st</sup> January and 31 <sup>st</sup> December 2018.....	74
<b>Figure 3.3</b> (a) Region of interest (outlined in red) within which MODIS and SEVIRI observations were limited to in this study. Also shown are the nadir positions of the SEVIRI sensor operating aboard Meteosat-8 and Meteosat-11, and the spatial distribution of VZA for each. (b) 0.5° × 0.5° gridded vegetation map derived from CCI Landcover (from 300m PROBA-V measures) and 30 m Landsat VCF percentage tree cover above 5 m as detailed in <b>Section 3.2.2</b> .....	77
<b>Figure 3.4</b> Mean latitude and longitude of nadir pixels in the M8 SEVIRI FRP product during 2018, calculated from close-to-nadir AF pixels (VZA < 0.5°). These data show a significant latitudinal shift of the satellite view occurs over the year, resulting in the nadir position varying by up to 10°.....	79
<b>Figure 3.5</b> Schematic showing the three potential AF pixel classifications in the detection performance analysis conducted herein, and how they were classified. A) errors of omission – no SEVIRI AF pixels were detected within a 3×3 pixel window surrounding a MODIS AF pixel B) correct detections – a SEVIRI AF pixel is detected at or within the 3×3 pixel window surrounding a MODIS AF pixel and C) errors of commission – no MODIS AF pixels were detected within 3×3 pixels of a SEVIRI AF pixel. The axes in this diagram represent the image line and columns of the SEVIRI full disk image.....	80
<b>Figure 3.6</b> Total FRP (GW) measured in each 0.5° × 0.5° grid cell by MODIS and by SEVIRI, as calculated from all the SEVIRI FRP-PIXEL product AF pixels available within ±5 minutes of a	

MODIS overpass and which were within the spatial extent of the MODIS AF observations made between VZA of  $\pm 18.3^\circ$  and between 1<sup>st</sup> January and 31<sup>st</sup> December 2018. .... 88

**Figure 3.7** Relationship between SEVIRI and MODIS FRP derived from spatially and temporally matched AF pixels identified over Africa in 2018. Three different comparison methods described in **Section 3.2.3.2** are used, total areal, per-area and per-fire. (a) M8 SEVIRI in relation to MODIS (b) M11 SEVIRI in relation to MODIS. In each comparison plot, the least-squares linear best fit is shown (blue) along with the 1:1 line (black solid), 50% line and 20% line (black dashed). The density of points in each case is represented by the colour bar for ease of visualisation. The results of the above least-square fits are summarised in **Table 3.3**. 90

**Figure 3.8** Relationship between M8 and M11 FRP and FRP from the matching MODIS observation for the same per-area and per-fire data as shown in **Figure 3.7**, averaged to daily comparisons. (a) M8 SEVIRI relation to MODIS b) M11 SEVIRI relation to MODIS. In each comparison plot the least- squares line-of-best-fit is shown (blue) along with the 1:1 line (black solid), 50% line and 20% line (black dashed). The results of the least-square fits for per fire comparisons are summarised in **Table 3.4** along with the results of previous studies..... 93

**Figure 3.9** Errors of omission and commission for the M8 and M11 SEVIRI FRP-PIXEL products in relation to MODIS, calculated at different SEVIRI VZA ranges. .... 96

**Figure 3.10** Total summed FRP (in GW) measured in each  $0.5^\circ \times 0.5^\circ$  grid cell in the per-area comparisons made using both SEVIRI products over Africa between 1<sup>st</sup> January and 31<sup>st</sup> December 2018. The region outlined in red indicates an area where many false AF detections occur in M8 (see **Section 3.3.4**). The regions outlined in yellow are areas encompassing some of the highest fire activity over the year where the impact of SEVIRI VZA is most obvious (see **Section 3.3.3**). .... 97

**Figure 3.11** Comparison of M8 and M11 FRP data. a) Relationship between M8- and M11-derived FRP from 1<sup>st</sup> January to 31<sup>st</sup> December 2018 as compared using three different methods – total areal, per-area and per-fire. In each comparison plot the least-squares line of best fit is shown (blue) along with the 1:1 line (black solid), 50% line and 20% line (black dashed) and the density of points in each case is represented by the colour bar for ease of visualisation. b) 3-day total FRP measured in the total-areal comparisons, plotted over the year for each SEVIRI product..... 99

**Figure 3.12** Daily averaged (median) FRP for the per-area and per-fire dataset shown in **Figure 3.11a**. The least-squares line of best fit is shown (blue) along with the 1:1 line (black solid), 50% line and 20% line (black dashed) and regression statistics are reported in **Table 3.7** ..... 100

<b>Figure 3.13</b> Distributions of FRP (left) and VZA (right) of grid cells used in the per-area comparisons made with M8 and M11 active fire datasets. The FRP of a single grid cell at any given observation time is calculated from the sum of all the FRP pixels falling within that cell, whilst the cell's VZA is the mean VZA of any SEVIRI pixel having a centre point in that grid cell.....	102
<b>Figure 3.14</b> Distributions of $FRP_{DIFF}$ (left) and $VZA_{DIFF}$ (right) in grid cells (per-area) and individual fires (per-fire). Frequency is presented on a log scale in the $FRP_{DIFF}$ distributions while $VZA_{DIFF}$ frequency is shown in thousands.....	103
<b>Figure 3.15</b> . Spatial distribution of $FRP_{DIFF}$ (a) calculated as the difference between M8 and M11 median FRP values over the year for each grid cell and $VZA_{DIFF}$ (b) calculated as the difference between M8 and M11 mean VZA for each grid cell.....	104
<b>Figure 3.16</b> Relationship between M8 and M11 total grid cell FRP calculated as the summed FRP of each $0.5^\circ \times 0.5^\circ$ grid cell between 1 <sup>st</sup> January and 31 <sup>st</sup> December 2018 in per-area comparisons and in per-fire comparisons. The $VZA_{DIFF}$ of each grid cell is represented in the colour scale.....	105
<b>Figure 3.17</b> Least-squares linear best fit of $FRP_{DIFF}$ and $VZA_{DIFF}$ calculated from median FRP values in each grid cell from the per-area and per-fire datasets. ....	106
<b>Figure 3.18</b> Matching Meteosat-8 and Meteosat-11 SEVIRI FRP-PIXEL Quality products from 6 <sup>th</sup> September 2018 19:45 UTC – shown over a region covering Sierra Leone and Guinea ( $10.6^\circ$ N, $11.3^\circ$ W). Shown alongside is the key each quality mark value. Groups of SEVIRI pixels classed as active fires (Quality mark = 1) are circled in red. Full details of the quality mark values are available in (Wooster et al., 2015).....	108
<b>Figure 3.19</b> Per-area grid cells as shown in <b>Figure 3.10</b> , categorised by the mean month of 2018 in which M8-detected fires in each grid cell were observed.....	109
<b>Figure 3.20</b> Per-area grid cell comparisons, separated by biome between (top row) M8-MODIS, (middle row) M11-MODIS and (bottom row) M8-M11. ....	112
<b>Figure 3.21</b> Least-squares linear best fits between data of grid cell $FRP_{DIFF}$ and $VZA_{DIFF}$ , split by the majority vegetation coverage in each grid cell using the biome map in <b>Figure 3.3b</b> . ....	114
<b>Figure 3.22</b> Schematic showing the interception of the FRP signal from a surface fire measured by satellite in an area of significant tree canopy, and the potential impact of sensor VZA in amplifying this effect (adapted from Wang et al., 2009) .....	117
<b>Figure 4.1</b> Example plume from a fire burning north of the Save River (Mozambique), imaged on 8 <sup>th</sup> October 2015 at 11:15 UTC via (Aqua) MODIS sensor (at a VZA $40.6^\circ$ ). (a) 10 km MxD04_DB AOD product; (b) MxD04_DB field showing the number of 1 km reflectance pixels (out of	

100) used to retrieve each 10 km AOD pixel value; (c) 500 m MODIS Corrected Reflectance (True Colour) image; and (d) 1 km MCD19 MAIAC AOD product derived from the same MODIS imagery shown in (c). The colour scale shown in (d) is also relevant for (a). The plume is far more easily distinguished in the 1 km than the 10 km AOD product and better matched to the smoke spatial distribution shown in the MODIS true colour image of (c). Unlike the 1 km AOD product of (d), the 10 km MxD04\_DB AOD data of (a) rather poorly defines the plume bounds and some pixels in this product are heavily impacted by the cloud mask which removes AOD pixels over the thickest smoke (b). Some erroneous masking does occur in the 1 km product of (d), shown as the black pixels, but this is minimal and addressed via the interpolation described in **Section 4.3** ..... 126

**Figure 4.2** (a) Estimated fire emitted Total Particulate Matter (TPM) in 635 individual smoke plumes, as derived from the 10 km MxD04\_DB AOD product (orange) and the 1 km MAIAC AOD product (blue), shown as a function of sensor view zenith angle (VZA). (b) Direct comparison of the matching MxD04\_DB and MAIAC-derived TPM values for each plume in (a), restricted to those observed at  $VZA \leq 20^\circ$  ..... 130

**Figure 4.3** (a) Mapped percentage tree cover above 5 metres, as determined from the 30 m spatial resolution Landsat Vegetation Continuous fields (VCF) product for 2015. (b) FREMv2 biome map for Africa derived from the 2015 ESA CCI Landcover map (itself derived from 300 m PROBA-V imagery) and the Landsat VCF product. Biomes were aggregated from the 36 land cover types defined in the original CCI map, with the two woodland savanna biomes separated using (a) (see **Table 4.1**) ..... 133

**Figure 4.4** Mean percentage contribution of different biomes to the fire radiative energy (FRE) released by fires between 2013 and 2018. FRE measures are derived from the SEVIRI FRP-PIXEL product. On average woodland savanna fires contribute the greatest total FRE throughout the year, except for in November, and this means their determination is especially important for overall smoke emission estimate accuracy. The importance and abundance of fires in this biome is reflected in the high numbers of fire-plume matchups identified for both the low- and high- woodland savanna biomes (see **Section 4.4.3**) ..... 134

**Figure 4.5** Example region of interest (ROI) containing the fire shown in **Figure 4.1** along with matchup active fire pixels (white triangles) from the SEVIRI FRP-PIXEL product detected between 00:00 local time and the MODIS overpass time. (a) MAIAC 1km AOD and SEVIRI active fire (AF) pixels; (b) histogram thresholding to discriminate the plume from the surrounding ‘ambient’ background. (c) SEVIRI AF pixels detected within the convex hull of the plume are considered to come from the same ‘fire’ that produced the smoke plume. The

fire radiative energy (FRE) of the causal fire is then calculated from these observations and used to match to the AOD-derived total particulate matter (TPM) (see **Figure 4.7**).....136

**Figure 4.6** Sensitivity analysis of the RBF interpolation procedure applied to plumes to account for the, up to 5% , missing MAIAC AOD pixels in fire-plume matchups.....137

**Figure 4.7** Smoke emission coefficients ( $C_{biome}$ ; in g.MJ<sup>-1</sup>) for the six African fire-affected biomes defined in **Section 4.4.1**, each derived from the slope of an ordinary least-squares (OLS) regression between data of fire-emitted total particulate matter (TPM) and matching fire radiative energy (FRE). The grey shaded area defines the 95% probability prediction interval of the OLS-derived slope. Each scatterplot is accompanied by an illustrative insert that depicts the typical landcover for the biome as seen in Google Earth (example locations are Closed Canopy Forest 10.359° S, 19.086° E; Grassland 21.180° S, 19.560° E; Managed Land 10.495° N, 7.586° E; Low-Woodland Savanna 7.085° N, 27.095° E, High-Woodland Savanna 12.523° S, 23.323° E and Shrubland 23.055° N, 22.242° E).....139

**Figure 4.8** (a) FREMv2 smoke emission coefficient ( $C_e$ ) mapped at 0.05°; (b) the matching 1° FEER  $C_e$  product; and (c) the difference between (a) and (b). In (c), FEER grid cells whose value was derived from gap-filling or which were calculated from less than 15 samples were removed (see Ichoku and Ellison (2014) for full details). (d) Shows the spatial distribution of the fire matchups used to derive the FREMv2  $C_{biome}$  values of **Figure 4.7** .....143

**Figure 4.9** Monthly total particulate matter (TPM) emissions from landscape fires for 2013 to 2018, as derived using the FREMv2 methodology (blue) applied to the Meteosat FRP-PIXEL product of Wooster et al. (2015). Corresponding monthly TPM emissions are shown from GFEDv4.1s (green), GFASv1.2 (purple), and the FEERv1.0 coefficients applied to the GFASv1.2 FRP (red) and SEVIRI FRE data (yellow).....145

**Figure 4.10** Total particulate matter (TPM) emission density (g.m<sup>-2</sup>) across Africa for 2016 as determined by GFEDv4.1s (0.25° grid cells), GFASv1.2 (0.1° grid cells), FEERv1.0-GFASv1.2 (0.1° grid cells), FEERv1.0-SEVIRI (0.05° grid cells), and FREMv2 inventory derived herein (0.05° grid cells). The red 20° × 20° region outlined in the top left GFED plot is shown magnified for each inventory in the right-hand column. .....148

**Figure 4.11** Mean monthly contribution (%) of fires to total particulate matter (TPM) emissions in each of the six FREMv2 biomes from 2013 to 2018 in (a) Northern Hemisphere Africa and (b) Southern Hemisphere Africa. .....150

**Figure 4.12** Monthly total emissions (Tg) of (a) CO2; (b) CO; and (c) CH4 for African landscape fires as estimated by FREMv2 (blue) between 2013 and 2018. Corresponding values from

GFEDv4.1s (green), GFASv1.2 (purple), FEERv1.0-GFASv1.2 (red) and FEERv1.0-SEVIRI (yellow) are shown for comparison ..... 152

**Figure 4.13** Fuel consumption per unit area ( $F_c$ , kg.m $^{-2}$ ) mapped at 0.25° from (a) 2016 FREMv2 dry matter consumed (DMC) totals and the FireCCISFD11-estimated burned area, and (b) GFEDv4.1s. (c) difference in fuel consumption per unit area ( $F_c$ , kg.m $^{-2}$ ) calculated from a and b). Note that  $F_c$  values in (a) apply only to the burned area patch inside a given pixel, and not the 0.25° pixel as a whole. ..... 155

**Figure 4.14** Per-biome FREMv2  $F_c$  frequency distributions and derived means, medians and standard deviations calculated from the fuel consumption per unit area map of **Figure 4.13a** and the biome map of **Figure 4.3b** using pixels with more than an 80% fractional coverage of a single biome and more than 5% pixel burned area according to the FireCCISFD11 product. ..... 156

**Figure 5.1** The WRF-CMAQ model domain covering southern hemisphere Africa, along with the locations of the AERONET sites used for comparison to the model output. The coloured boxes indicate smaller regions of interest (ROIs) which were used in comparisons of model output to satellite observations (S5P CO and MODIS MAIAC AOD). ..... 163

**Figure 5.2** Flowchart depicting the input datasets, pre-processing stages and model components of the WRF-CMAQ setup used in this validation study. ..... 165

**Figure 5.3** FREMv2 summed Total carbon emissions (Gg) in each month of the simulation period between 15<sup>th</sup> June and 29<sup>th</sup> August 2019 calculated from the summed carbon content of CO, CO<sub>2</sub> and CH<sub>4</sub> emissions. The location of the six AERONET sites are also shown. ..... 168

**Figure 5.4** Selected metrological variables comparing monthly means for June, July and August over the simulation period. Comparison of WRF-CMAQ with ERA-Interim in terms of 2 metre temperature (°C) and 10 metre wind speed (m s $^{-1}$ ) and direction. ..... 173

**Figure 5.5** Mapped mean monthly total CO from a) S5P and b) CMAQ during the simulation period from 15<sup>th</sup> June to 29<sup>th</sup> August 2019. c) shows the percentage difference between S5P and CMAQ AOD. ..... 175

**Figure 5.6** Daily total CO averaged over the full domain extent and the ROIs shown in **Figure 5.1** as determined by CMAQ and observed in the S5P product. The difference between modelled and observed total CO is plotted by a solid grey line and a vertical dotted line on 29<sup>th</sup> July indicates the start of the seconds simulation ..... 177

**Figure 5.7** The relationship between daily CMAQ total column CO and S5P total column CO in the full domain extent and the four ROIS shown in **Figure 5.1**. The Pearson's correlation and NMBF of each dataset is shown and dotted lines show the 1:1, 20% and 50% lines. Results of these plots are summarised in **Table 5.2**. **Table 5.2** Monthly means of daily CMAQ and S5P

total column CO, in the full extent of the domain and the ROIs shown in <b>Figure 5.1</b> , the NMBF of daily CMAQ CO with respect to observations and the temporal Pearson's correlation coefficient of daily CO over each month and the whole modelled period (15th June to 29th August 2019) .....	178
<b>Figure 5.8</b> The mean location (left) of CO plumes identified in the S5P product between 15 <sup>th</sup> June and 29 <sup>th</sup> August 2019 and the bounding polygons used to define the area over these plumes (right). .....	180
<b>Figure 5.9</b> Daily total mean CO observed in each plume as determined by CMAQ and the S5P product. The difference between modelled and observed total in-plume CO is plotted by a solid grey line and a vertical dotted line on 29 <sup>th</sup> July indicates the start of the seconds simulation.....	181
<b>Figure 5.10</b> The relationship between fire emitted CMAQ total CO and fire emitted S5P measured total CO for individual smoke plumes identified in the S5P CO product. The Pearson's correlation and NMBF of the dataset is shown along with dotted lines indicating the 1:1, 20% and 50% lines. .....	181
<b>Figure 5.11</b> a) Hourly and b) daily AOD averaged over all six AERONET sites, both from the CMAQ simulations and AERONET observations. In daily mean AOD (b) the difference between model and observation is plotted by a solid grey line and a vertical dotted line on 29 <sup>th</sup> July indicates the start of the seconds simulation. ....	182
<b>Figure 5.12</b> Hourly AOD at each of the six AERONET sites as determined by CMAQ and observed by AERONET. A vertical dotted line on 29 <sup>th</sup> July indicates the start of the seconds simulation. The Misamfu and Welgagund sites did not have Level 2 AERONET data for the full simulation period, and AOD data from these sites were available from 15 <sup>th</sup> June until 27 <sup>th</sup> July and 13 <sup>th</sup> August respectively.....	184
<b>Figure 5.13</b> Daily AOD averaged over at each of the six AERONET sites as determined by CMAQ and observed by AERONET. The difference between modelled and observed AOD is plotted by a solid grey line and a vertical dotted line on 29 <sup>th</sup> July indicates the start of the seconds simulation. The Misamfu and Welgagund sites did not have Level 2 AERONET data for the full simulation period, and AOD data from these sites were available from 15 <sup>th</sup> June until 27 <sup>th</sup> July and 13 <sup>th</sup> August respectively.....	185
<b>Figure 5.14</b> The relationship between hourly CMAQ AOD at 381 nm AERONET measured AOD at 380 nm at each AERONET site. The Pearson's correlation and NMBF of each dataset is shown in figure and dotted lines show the 1:1, 20% and 50% lines. ....	187

<b>Figure 5.15</b> ‘Bias corrected’ daily AOD averaged over at each of the six AERONET sites as determined by CMAQ and observed by AERONET. The difference between modelled and observed AOD is plotted by a solid grey line and a vertical dotted line on 29 <sup>th</sup> July indicates the start of the second simulation. The Misamfu and Welgagund sites did not have Level 2 AERONET data for the full simulation period, and AOD data from these sites were available from 15 <sup>th</sup> June until 27 <sup>th</sup> July and 13 <sup>th</sup> August respectively.....	189
<b>Figure 5.16</b> Mapped mean monthly AOD at 550 nm from a) MAIAC and b) CMAQ (note - colour scale differences between a) and b)) during the simulation period from 15 <sup>th</sup> June to 29 <sup>th</sup> August 2019. c) shows the percentage difference between MAIAC and CMAQ AOD.....	191
<b>Figure 5.17</b> Daily AOD averaged over the full domain extent and the ROIs shown in <b>Figure 5.1</b> as determined by CMAQ and observed in MAIAC. The difference between modelled and observed AOD is plotted by a solid grey line and a vertical dotted line on 29 <sup>th</sup> July indicates the start of the second simulation. ....	194
<b>Figure 5.18</b> The mean location (left) of smoke plumes identified in the MAIAC 1 km AOD product between 15 <sup>th</sup> June and 29 <sup>th</sup> August 2019 and the bounding polygons used to define the area over these plumes (right).....	195
<b>Figure 5.19</b> The relationship between fire emitted CMAQ AOD and fire emitted MAIAC measured AOD for individual smoke plumes identified in the MAIAC AOD product. The Pearson’s correlation and NMBF of the dataset is shown along with dotted lines indicating the 1:1, 20% and 50% lines. ....	197
<b>Figure 5.20</b> The six biomes defined in <b>Chapter 4</b> over the CMAQ model domain, with the addition of bare area.....	198
<b>Figure 5.21</b> CO observed in each individual plume as determined by CMAQ and the S5P product as a function of time for each of the six biomes. The difference between modelled and observed total in-plume CO is plotted by grey squares and a vertical dotted line on 29 <sup>th</sup> July indicates the start of the second simulation. ....	199
<b>Figure 5.22</b> The relationship between fire emitted CMAQ total CO and fire emitted S5P measured total CO for individual smoke plumes identified in the S5P CO product separated by biome. The Pearson’s correlation and NMBF of the dataset is shown along with dotted lines indicating the 1:1, 20% and 50% lines. ....	201
<b>Figure 5.23</b> The relationship between fire emitted CMAQ AOD and fire emitted MAIAC measured AOD for individual smoke plumes identified in the MAIAC AOD product separated by biome. The Pearson’s correlation and NMBF of the dataset is shown along with dotted lines indicating the 1:1, 20% and 50% lines. ....	203

**Figure 5.24** Mean hourly AOD for each of the six AERONET sites as modelled by CMAQ and observed by AERONET.....209

**Figure 5.25** Distribution of % tree cover according to the Landsat 30 m VCF tree cover product in SEVIRI FRP pixels in Africa that are classified as either high or low woodland savanna. The black dotted line denotes the TC threshold used to distinguish these biomes.....212

# List of Tables

<b>Table 2.1</b> Summary of sensors used in measuring fire related variables and their uncertainties, categorised by their spatial resolution. Taken from (Ichoku et al., 2016) .....	37
<b>Table 2.2</b> Summary of several bottom-up and top-down fire emissions inventories which are regularly used in biomass burning research.....	47
<b>Table 3.1</b> Summary of previous MODIS-based SEVIRI-FRP Pixel product evaluation studies, including their spatio-temporal extent and other characteristics of importance .....	85
<b>Table 3.2</b> Summary of concurrent and co-located SEVIRI and MODIS AF pixel detections made in the region of interest bounded in red in <b>Figure 3.3a</b> between January 1st and December 31st 2018. ....	86
<b>Table 3.3</b> Summary of the OLS linear best fit parameters and statistics derived when comparing M8 and M11 SEVIRI FRP retrievals against those made from MODIS via three methods – total areal, per-area and per fire.....	91
<b>Table 3.4</b> Summary of the results from previous works which have compared SEVIRI and MODIS FRP. Also shown are results obtained from this study for the daily averaged per-fire comparisons shown in <b>Figure 3.8</b> . .....	94
<b>Table 3.5</b> Summary of the AF errors of omission and commission obtained in previous validation studies, along with those from this study comparing M8 and M11 AF detections against those of MODIS in 2018. ....	95
<b>Table 3.6</b> Summary of SEVIRI AF pixels detected by M8 and M11 in the region of interest bounded in red in <b>Figure 3.3</b> between January 1st and December 31st, 2018.....	98
<b>Table 3.7</b> Summary of the linear-best-fit plots between M8 and M11 measurements of FRP over Africa made between Jan 1st 2018 to 31st Dec 2018 ( <b>Figure 3.11a</b> and <b>Figure 3.12</b> ). ....	101
<b>Table 3.8</b> Results from a Kruskal-Wallis H test of grid cell FRP measurements from per-area comparisons where grid cells are categorised by their majority vegetation cover. This test was applied to M8, M11 and MODIS AF products separately. A <i>p</i> -value between groups of less than 0.05 indicates that two groups are statistically distinct, whereas groups whose <i>p</i> -values are greater than 0.05 are highlighted in orange.....	111
<b>Table 4.1</b> CCI landcover classes assigned to the FREMv2 biomes in this study and the Landsat VCF tree cover threshold used to separate the woodland savanna class. CCI class codes are detailed in <b>Appendix A</b> .....	133
<b>Table 4.2</b> Biome-dependent smoke emission coefficients ( <i>Cbiome</i> ) and accompanying uncertainties for the African fire-affected biomes mapped in <b>Figure 4.3b</b> and calculated from FREMv2 and	

from FREMv1 (reported in Mota and Wooster, 2018). Matching FEER-equivalent coefficients are also shown, based on the geographical location of fire matchups and the FEER $C_e$ ( $1^\circ \times 1^\circ$ ) product of Ichoku and Ellison (2014).....	140
<b>Table 4.3</b> Mean annual total carbon and trace gas emissions for 2013 to 2018, along with dry matter consumed (DMC) totals (Tg.yr $^{-1}$ ), for Northern and Southern Hemisphere Africa (NHAF and SHAF) as estimated by the different fire emissions inventories compared herein including FREMv2 .....	153
<b>Table 5.1</b> Summary of WRF-CMAQ model configuration .....	164
<b>Figure 5.7</b> The relationship between daily CMAQ total column CO and S5P total column CO in the full domain extent and the four ROIS shown in <b>Figure 5.1</b> . The Pearson's correlation and NMBF of each dataset is shown and dotted lines show the 1:1, 20% and 50% lines. Results of these plots are summarised in <b>Table 5.2</b> . <b>Table 5.2</b> Monthly means of daily CMAQ and S5P total column CO, in the full extent of the domain and the ROIs shown in <b>Figure 5.1</b> , the NMBF of daily CMAQ CO with respect to observations and the temporal Pearson's correlation coefficient of daily CO over each month and the whole modelled period (15th June to 29th August 2019). .....	178
<b>Table 5.3</b> Monthly mean of hourly CMAQ and AERONET AOD, the NMBF of hourly CMAQ AOD with respect to observations and the temporal Pearson's correlation coefficient of hourly AOD over each month and the whole modelled period (15th June to 29th August 2019). .....	188
<b>Table 5.4</b> Monthly means of daily CMAQ and MAIAC AOD, in the full extent of the domain and the ROIs shown in <b>Figure 5.1</b> , the NMBF of daily CMAQ AOD with respect to observations and the temporal Pearson's correlation coefficient of daily AOD over each month and the whole modelled period (15th June to 29th August 2019). .....	193
<b>Table 5.5</b> Mean total CO of plumes in each biome as defined by CMAQ and S5P, and the NMBF of CMAQ plume CO with respect to S5P observations and the Pearson's correlation coefficient of between plume CO values of each. Red highlighted rows indicate biomes which do not give statistically significant measures ( $p > 0.1$ ).....	201
<b>Table 5.6</b> Mean AOD of plumes in each biome as defined by CMAQ and MAIAC, and the NMBF of CMAQ plume AOD with respect to MAIAC observations and the Pearson's correlation coefficient of between plume AOD values of each. Red highlighted rows indicate biomes which do not give statistically significant measures ( $p < 0.1$ ). .....	203

# List of Abbreviations

AF	Active Fire
AOD	Aerosol Optical Depth
AQ	Air Quality
BA	Burned Area
BC	Boundary Condition
CAMS	Copernicus Atmospheric Monitoring Service
CC	Combustion Completeness
CMAQ	Community Multiscale Air Quality
CTM	Chemical Transport Model
DMC	Dry Matter Consumed
ECMWF	European Centre for Medium-Range Weather Forecasts
EF	Emission Factor
EO	Earth Observation
EUMETSAT	European Organisation for the Exploitation of Meteorological Satellites
FEER	Fire Energetics and Emissions Research
FINN	Fire Inventory from NCAR
FL	Fuel Load
FRE	Fire Radiative Energy
FREM	Fire Radiative Energy Emissions
FRP	Fire Radiative Power
GFAS	Global Fire Assimilation System
GFED	Global Fire Emissions Database
GOES	Geostationary Operational Environmental Satellites
IC	Initial Conditions
IR	Infrared
LSA SAF	Land Surface Analysis Satellite Applications Facility
LWIR	Long-wave infrared
MIR	Mid infrared
MODIS	Moderate resolution Imaging Spectroradiometer
NHAF	Northern Hemisphere Africa
NWP	Numerical Weather Prediction
OLS	Ordinary Least-squares
PM	Particulate Matter
SEVIRI	Spinning Enhanced Visible and InfraRed Imager
SHAF	Southern Hemisphere Africa
SPP	Sub-Satellite Position
SWIR	Short-wave infrared
TC	Tree Cover
TPM	Total Particulate Matter
VIIRS	Visible Infrared Imaging Radiometer Suite
VZA	View Zenith Angle
WACCM	Whole Atmosphere Community Climate Model
WRF	Weather Research and Forecasting

# Chapter 1 Introduction

This research focuses on landscape fire at spatial scales observable via Earth observation – this can range from 10s of m<sup>2</sup> to 100s of km<sup>2</sup> and involves the combustion of living and dead vegetation and organic surface matter. Fire has been part of the Earth system for millions of years (Scott and Glasspool, 2006) and has affected a larger area, in a wider range of biomes than any other natural disturbance regime (Lavorel et al., 2007). Fire occurs naturally in the form of wildland fires but is also driven by anthropogenic factors for example, landcover change and agricultural practices (Bowman et al., 2009).

Biomass burning is recognised as a one of the most significant sources of aerosol and trace gas emissions into the atmosphere (Andreae and Merlet, 2001; Koppmann et al., 2005; Bowman et al., 2009). Perturbations to local and global atmospheric composition occur from emissions of CO<sub>2</sub>, CH<sub>4</sub>, CO and other trace gases from biomass burning and aerosols such as black carbon (BC) and organic carbon (OC) which are also emitted in abundance. Open biomass burning is estimated to contribute up to 40% of the global loadings of total BC (Forster et al., 2007). Fire emissions impact regional and global weather, climate and air quality (Kaufman et al., 1989; Crutzen and Andreae, 1990; Bowman et al., 2009; Tosca et al., 2013) and fire activity is in turn influenced by climate (Westerling et al., 2006; IPCC, 2013; Archibald et al., 2018). Fire-emitted aerosols are involved in cloud micro-physical processes and directly alter the radiation budget through their optical properties (Penner et al., 1992; Reid et al., 2005a), while greenhouse gases such as CO<sub>2</sub> and CH<sub>4</sub> have a well-known impact on climate and play a role in the global carbon cycle (Randerson et al., 2006; Bowman et al., 2009).

Regional air quality is regularly driven by human and natural biomass burning (e.g. Phuleria, 2005; Hu et al., 2008; Yang et al., 2011; Huang et al., 2013; Baldassarre et al., 2015; Cusworth et al., 2018; Larsen et al., 2018; Sembhi et al., 2020) through fire emissions of particulate matter (PM) and gases such as CO, NO<sub>x</sub> and SO<sub>2</sub>. With acute and chronic mortality from poor air quality estimated at around 7 million annually (WHO, 2012), and the known contribution of

biomass burning to poor air quality and excess deaths (e.g. Koplitz et al., 2016; Roberts and Wooster, 2021), the impact of biomass burning on public health is significant. Indeed, the unprecedented large-scale fire events of recent years, for example, those in the Arctic Circle, California, the Amazon and Indonesia highlight, more than ever, the importance of robust and accurate estimates of emissions from landscape fires.

Fire emission inventories supply emissions estimates and are used as input in regional and global atmospheric models to forecast and understand the impact of fire emissions on climate, weather and air quality. However, current fire emission inventories are recognised to still have large uncertainties and limitations. The amounts of aerosol and gas generated in an open-air fire are dependent on many factors at surface level. This includes, for example, the type of vegetation burned (Andreae and Merlet, 2001; Akagi et al., 2011), its moisture content (Nelson, 2001; Smith et al., 2013), and its burning regime - smouldering or flaming (Wooster et al., 2011). Biomass burning emissions are fundamentally difficult to quantify due to the highly dynamic nature of fire, both temporally and spatially. Fires often occur in remote or inaccessible areas where direct *in-situ* measurements are not possible, and even in instances where a fire is accessible, measuring its behaviour and the chemical species it emits is still very challenging and prone to much uncertainty. For example, whilst point-based samples can be collected, these do not represent the total amount of material emitted and so can only be used to assess the chemical composition of a fire-generated smoke plume, at that moment in time. Earth observation platforms offer the only appropriate tool to estimate fire emissions at the regional to global scale. The key challenge in the use of remote sensing data to estimate biomass burning is the characterisation of the previously mentioned close-to-surface variables, which control fire behaviour and influence the amounts of aerosol and trace gas emitted. It is the estimation of these parameters, as well as limitations in the spatio-temporal resolution of satellite sensors, that contribute to the uncertainty in current biomass burning emission inventories.

This research focuses on the use of high-temporal resolution geostationary satellite observations of fire to estimate emissions from biomass burning. The broad aims of this thesis are (i) to investigate the performance of SEVIRI FRP-PIXEL geostationary satellite products to detect and characterise fire in Africa, (ii) to develop and apply updates to a current top-down

fire emission inventory that uses this SEVIRI product in an aim to address key uncertainties in the current approach and (iii) to evaluate the performance of this updated fire emission inventory through the use of atmospheric modelling and ground-based and satellite-based observations of aerosol and trace gas concentrations. The structure of this thesis and details of each chapter are as follows:

- **Chapter 2** provides an overview of the theoretical basis for the remote sensing based measurement of landscape scale fire and details specific satellite platforms used and their respective limitations. The chapter also discusses the current state-of-the-art in global fire emissions inventories and techniques used in their evaluation. The chapter concludes with the specific research objectives of this thesis.
- **Chapter 3** investigates the SEVIRI FRP-PIXEL product of two near-identical geostationary satellite sensors, stationed over different locations with a view of Africa. It provides a validation of both products against the MODIS active fire product, and specifically explores the impact of sensor view zenith angle and vegetation type on the measurements of active fire coming from these geostationary satellite datasets.
- **Chapter 4** develops and applies methodological improvements to the FREM ‘top-down’ fire emissions inventory (Mota and Wooster, 2018) for Africa using satellite-based observations of fire radiative power (FRP) and aerosol optical depth (AOD). Work from this chapter culminated in a peer reviewed publication (Nguyen and Wooster, 2020), but is presented in this thesis in chapter form in order to include updates which were incorporated after the publication of this paper.
- **Chapter 5** presents a validation study of the top-down emission inventory developed in Chapter 4. Evaluations are carried out through the exploitation of an atmospheric chemical transport model, and observations of AOD and carbon monoxide from ground-based and satellite-based observations.
- **Chapter 6** summarises the findings in each of the research chapters of this thesis and presents overall conclusions and recommendations for future work.

# Chapter 2 Background and Specific Objectives

## 2.1 Introduction

This chapter provides an overview of research topics relevant to this thesis and presents a critical assessment of the state-of-the-art in fire emissions estimation via Earth observation. It concludes with a description of the specific research objectives of this work.

The first two sections of this chapter provide an overview of past and current techniques used in the satellite-based monitoring of fires (**Section 2.2**), followed by a discussion of specific platforms and instruments that provide these measurements of fire, and their relative limitations and advantages (**Section 2.3**). **Section 2.4** details key methods and features of specific fire emissions inventories that are widely used in the research community and provides further detail on the uncertainties and limitations of these methodologies. Approaches used in the validation and assessment of fire emissions inventories are described in **Section 2.5**, with a particular focus on the use of atmospheric modelling as a means of evaluation. Finally, a summary of this chapter is presented in **Section 2.6** along with the specific objectives for the remaining chapters of this thesis.

## 2.2 Satellite Remote Sensing of Fire – Algorithms

This section describes the practical application of remote sensing data in the measurement of landscape fires. It details the two main methods used in the remote detection of fires – the Burned Area (BA) method and Active Fire (AF) based methods, with a primary focus on AF methods since they are the ones most relevant to this thesis. This section also discusses other features related to active fires and fire emissions that can be observed and characterised through satellite remote sensing.

Open landscape fire is a highly complex phenomenon that is extremely variable in terms of its spatial and temporal extent. This makes it challenging to characterise and quantify and satellite remote sensing offers the only suitable and robust means of monitoring landscape fire at the regional to global scale. Biomass burning produces three signals that can be observed via remote sensing. These are: heat and smoke, which are released simultaneously at the time of combustion, and burn scar and/or char which are observed post combustion. The methods used to quantify fire activity can generally be separated into two types - BA methods which aim to remotely map the burn scars created by fires (e.g. Pereira et al., 1999; Roy et al., 2008; Roteta et al., 2019) and AF methods which aim to identify the thermal emission signal of an actively burning fire (e.g. Flannigan and Vonder Haar, 1986; Wooster et al., 2003; Schroeder et al., 2014). Measurements of the aerosols and trace gases released by a fire can also be acquired from satellite data (e.g. Jackson et al., 2013; Remer et al., 2013; Lyapustin and Wang, 2018) and are discussed in **Section 2.2.3**.

### 2.2.1 Burned Area Methods

BA methods rely on the change in surface reflectance that occurs when vegetation or surface matter is burned in a fire. The combustion of plant matter and soil and deposition of ash and charcoal in an area recently burned by a fire alters the surface spectral characteristics of that area in the visible and near infrared (NIR) wavelengths of the electromagnetic spectrum (Roy et al., 1999). BA methods exploit this characteristic by detecting these changes in surface reflectance. Simplistically, surface reflectance is observed via satellite sensors in the visible and NIR channels and these values are collected over a fixed temporal window; this time series is then used to predict the surface reflectance of the following day. Statistical measures are then used to determine if there is a significant difference between the predicted and observed surface reflectance (**Figure 2.1**) – also accounting for the variability in surface reflectance from other sources such as the directional effect (Roy et al., 2002). The resultant satellite products return a measure of fire activity in terms of pixels being classified as burned or unburned and an estimated day-of-burn is associated with the day which the surface reflectance change is detected.

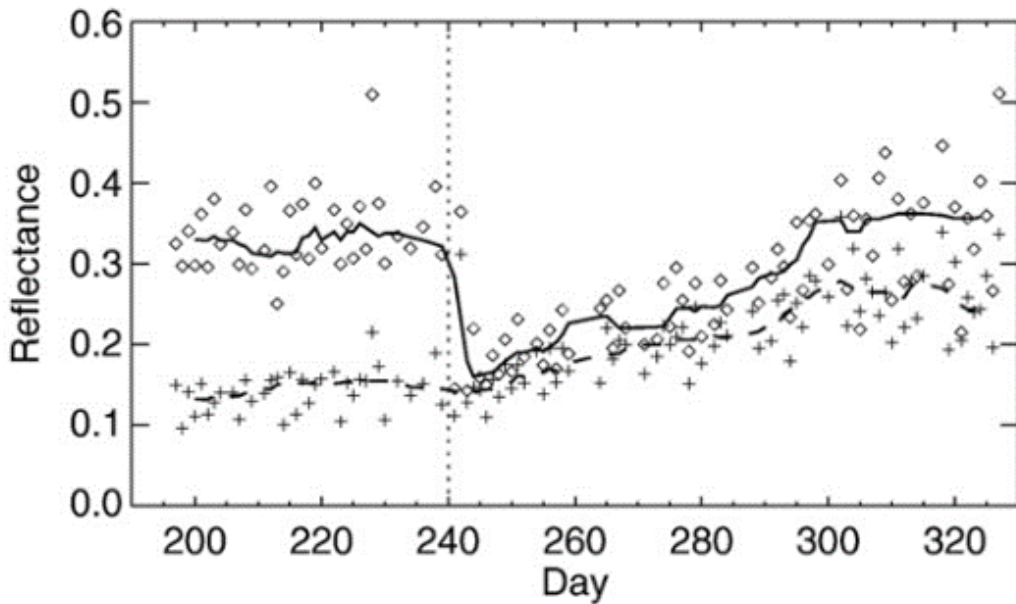


**Figure 2.1** Reflectance change detection using two MODIS channels (diamonds and crosses) used to determine the presence of a fire burn scar occurring on day 240 (Giglio et al., 2009)

The reliance of the BA method on fire scars - which are only observable post-combustion - limits the use of BA satellite products in real-time applications, such as air quality forecasting (e.g. Kaiser et al., 2012) or fire danger alert systems (e.g. San-Miguel-Ayanz et al., 2005). However, through the same feature, BA products benefit from the fact that burn scars can often be detected for some time after the fire event meaning that the simultaneous occurrence of an active fire and an overpass of the remote sensing instrument are not a requirement for detection.

There are currently a number of operational BA products that use data from various different satellite sensors (e.g. Plummer et al., 2006; Tansey et al., 2008; Chuvieco et al., 2016), however one of the most widely used and well validated (Giglio et al., 2009; Loboda et al., 2012; Tsela et al., 2014) datasets is the MCD64A1 BA product which uses MODIS 500 m resolution data (Giglio et al., 2018). A key limitation in many BA products is the minimum detectable fire size and in the MCD64A1 (Collection 5) product, burn scars covering less than 100 ha are often not mapped (Giglio et al., 2009). Randerson et al. (2012) estimated that inclusion of these small fires led to a 24% to 54% increase in global burned area. Though the most recent release of the product shows an improvement in the detection of small burns (Giglio et al., 2018), the BA

method fundamentally relies on a less easily obtained signal over noise relationship than AF methods do.

Measures of burned area from these satellite products can be used to estimate fire emissions by first converting BA to total fuel consumption,  $FC_T$  (in kg). This is done through the multiplication of  $BA$  ( $\text{m}^2$ ) by fuel load ( $\text{kg m}^{-2}$ ) and combustion completeness (unitless) (Seiler and Crutzen, 1980) as is discussed further in **Section 2.4**.

## 2.2.2 Active Fire Detection and Fire Radiative Power

An alternate approach to quantifying fire activity focuses on measuring the radiative heat signal produced by the combustion process. This method relies on the thermal emission signal of fires at short-wave infrared (SWIR: 1.6–3  $\mu\text{m}$ ), mid-infrared (MIR: 3–5  $\mu\text{m}$ ) and/or longwave infrared (LWIR: 8–14  $\mu\text{m}$ ) wavelengths. The method was first proposed by Dozier (1981) to detect sub-pixel high temperature phenomena - such as gas flares. According to Plank's Radiation Law, thermal emissions in the SWIR and MIR increase much more rapidly with increasing temperature than at LWIR wavelengths (**Figure 2.2**). Planck's Radiation Law governing the relationship between emitted spectral radiance and emitter temperature is given by:

$$B_\lambda(T) = \frac{2hc^2}{\lambda^5} \frac{1}{e^{hc/(\lambda kT)} - 1} \quad [2.1]$$

where  $B$  is spectral radiance ( $\text{W m}^{-2} \text{sr}^{-1} \mu\text{m}^{-1}$ ),  $\lambda$  is wavelength ( $\mu\text{m}$ ),  $T$  is temperature (K),  $h$  is the Planck constant ( $6.63 \times 10^{-34} \text{ J s}$ ),  $c$  is the speed of light ( $3.00 \times 10^8 \text{ m s}^{-1}$ ), and  $k$  is the Boltzmann constant ( $1.38 \times 10^{-23} \text{ J K}^{-1}$ ). Based on this relation, even a small fire within a satellite pixel will cause a significant increase in the pixel integrated SWIR and MIR signal but a far smaller (perhaps minimal) increase in the LWIR signal. SWIR signals are not commonly used however, because during the day when fires are most active this waveband is dominantly sensing solar reflected radiation, rather than thermally emitted radiation. So, the approach most commonly used exploits the MIR and LWIR signals. Their distinct signal response to sub-pixel hot objects allows satellite pixels containing even quite small actively burning fires to be distinguished from ambient non-fire background pixels. Hence, due to the extremely strong thermal signal produced by fires above the background, AF detection methods are able

to detect far smaller fires, relative to pixel area, than BA methods - fires covering as little as  $10^{-4}$  of a pixel can be detected (Roberts et al., 2005) by AF methods, whereas in BA approaches typically  $> 20\%$  of a pixel must be burned to cause a detection (Giglio et al., 2006).

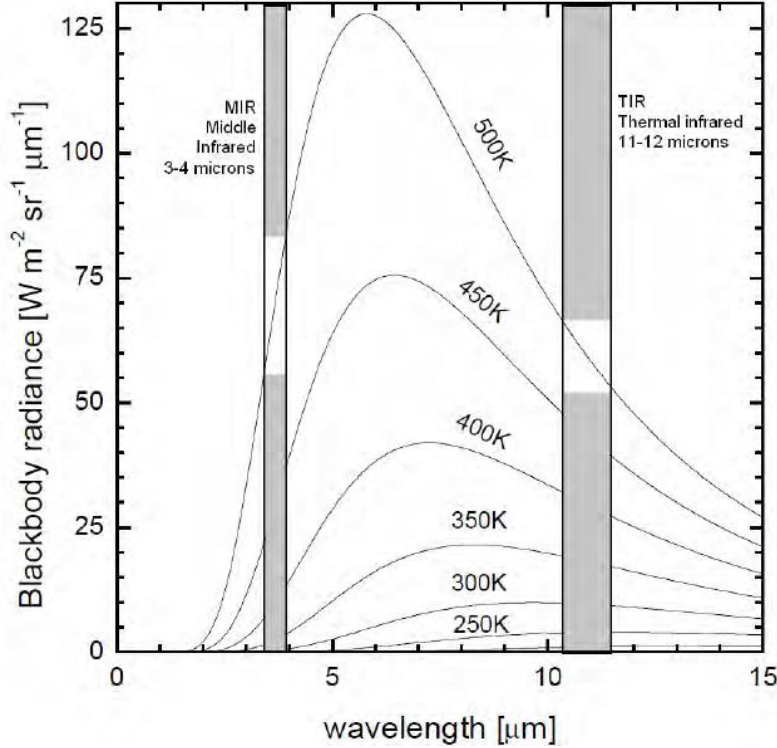


**Figure 2.2** Planck's Law showing the behaviour of black body radiance at different temperatures from Calle and Casanova (2008).

Active fire detections alone do not translate directly into aerosol and gas emissions, however. To estimate these another variable can be derived from the spectral signal of an actively burning fire - the fire radiative power (FRP) (Wooster et al. 2005). FRP (W) is the rate of radiant energy released by a fire - and when integrated over time gives the fire radiative energy (FRE in Joules). FRE can then be converted to total fuel consumption (e.g. Kaiser et al., 2012) and subsequently to emissions of aerosols and gases via use of emissions factors (see **Section 2.4**). The FRP of a fire can be estimated via several different approaches, which all rely in some way on the Stefan-Boltzmann Law:

$$FRP = \varepsilon_f \sigma T^4 \quad [2.2]$$

where  $\varepsilon_f$  is the fire grey body emissivity,  $\sigma$  is the Stefan-Boltzmann constant ( $5.67 \times 10^{-8} \text{ W m}^{-2} \text{ K}^{-4}$ ) and T is the kinetic temperature of the fire (K).

The first approach is based on the procedure proposed by Dozier (1981) and is known as the bi-spectral method. It utilises the difference in observed signal in two spectral channels, most often the MIR and LWIR channels, to first detect and then estimate the fire fractional area and temperature. These latter two estimates are then used with the Stefan-Boltzmann Law to estimate FRP. This bi-spectral method can be subject to large errors arising from inter-channel co-registration which affects the accuracy of fire characterization (Zhukov et al., 2005), and is generally better suited to high spatial resolution observations where the fires form larger fractions of the pixel area (Giglio and Kendall, 2001).

An alternative single channel method uses the empirical relationship between the brightness temperature in the MIR of fire pixels and non-fire background pixels of the MODIS instrument (Kaufman et al., 1996, 1998). This approach was used in the earlier iterations of the MODIS Active Fire Products (Giglio et al., 2003).

A third method known as the 'MIR radiance' method was proposed by Wooster et al. (2003) and also uses a single channel measurement in the MIR channel to estimate FRP, as with the (Kaufman et al., 1996, 1998) approach. However, it is based on the radiances rather than the brightness temperatures and is applicable to all sensors rather than being MODIS specific. It is now used with the latest generation MODIS Active Fire Products (Giglio et al., 2016) and also within the LSA SAF Meteosat FRP-PIXEL products which the research within this thesis rely on extensively.

As Wooster et al., (2005) detail in their explanation of the MIR radiance method, when a satellite observed pixel within which there is an actively burning fire is detected, it is unlikely that the thermal emission across the pixel will be homogeneous. Instead the pixel can be considered to be comprised of  $n$  thermal components which have different temperatures and different subpixel areas. For example, there may be both flaming and smouldering processes taking place within the same pixel. The total FRP for all components of the pixel can be expressed as:

$$FRP_{True} = A\epsilon\sigma \sum_{i=1}^n A_n T_n^4 \quad [2.3]$$

where  $A$  is the ground sampling area ( $\text{m}^2$ ),  $\epsilon$  is the emissivity of the pixel (dependant on the ratio of smouldering to flaming inside the pixel),  $\sigma$  is the Stefan-Boltzmann constant,  $A_n$  is the fractional area of the  $n^{th}$  thermal component in that pixel and  $T_n$  is the temperature (K) of the  $n^{th}$  thermal component. The FRP extends over a continuum of wavelengths in the thermal IR region and is emitted at all angles, however satellite sensors only measure the spectral radiance at discrete wavelength bands and at viewing angles determined by the sensor's location. It is therefore necessary to infer the energy emitted over all wavelengths at all angles from the spectral measurements at individual wavebands and in a single direction. The spectral radiance,  $L$  ( $\text{W m}^{-2} \text{ sr}^{-1} \text{ m}^{-1}$ ), at wavelength  $\lambda$  (m) and temperature  $T$  (K) is given by the Planck function:

$$L(\lambda, T) = \frac{C_1}{\lambda^5 \left( \exp\left(\frac{C_2}{\lambda T}\right) - 1 \right)} \quad [2.4]$$

where  $C_1$  and  $C_2$  are constants. It was shown that when the spectral radiance is approximated by the power law fit:

$$L(\lambda) = aT^b \quad [2.5]$$

(where  $a$  and  $b$  are empirically derived constants), the relation between spectral radiance and emitting temperature approaches that of the Stefan-Boltzmann Law for MIR wavelengths. Effectively,  $L^{MIR} \propto T^4$ , and at temperatures where this is true ( $> 600$  K) the ratio between the total power emitted over all wavelengths ( $FRP_{True}$ ) and the power emitted at the MIR ( $L_{MIR}$ ) is roughly constant. Above this temperature threshold the spectral radiance of MIR in a fire hotspot pixel with  $n$  subpixel thermal components becomes:

$$L_{MIR,h} = a\epsilon_{MIR} \sum_{i=1}^n A_n T_n^4 \quad [2.6]$$

where  $\epsilon_{MIR}$  is the surface emissivity in the appropriate MIR wavelength band and  $a$  is an empirically derived sensor- and channel-specific constant. The FRP in the MIR is then computed by combining **Equation 2.3** and **Equation 2.6** and subtracting the background MIR spectral radiance. Since the vast majority of active combustion in vegetation fires is occurring at temperatures in excess of 600 K this relation generally holds and can be used to characterise the FRP at the time a fire is observed.

The main limitation of active fire detection and characterisation of fires through FRP compared to BA approaches is associated with the dependence on observing the fire while it is burning. Fire hotspots are not detected if the active fire is not burning at the satellite observation time or if fires are obscured from the sensors view by clouds. Furthermore, clouds can in fact cause sun-glints at MIR wavelengths during the day, and these may be falsely classified as fires if appropriate steps are not taken within processing algorithms (Wooster et al., 2013). When fire-containing pixels have brightness temperatures in the MIR that are not sufficiently above the background pixels' brightness temperature they fall below the minimum FRP detection threshold. These fires are generally small, but low FRP 'small' fires are very common so their non-detection can cause an underestimation in regional-scale FRP measures. This underestimation is amplified as a function of increasing pixel size because the fire's subpixel thermal signature is diluted within a larger pixel area (Wooster et al., 2005). In this way, the spatial resolution of the satellite sensor used to retrieve FRP by the MIR method - and indeed by all FRP methods - has a significant impact on the minimum size of fire that is detectable.

### 2.2.3 Remote Sensing of Other Fire Related Variables

Further to observations of the heat emitted by a fire and the char and scar left behind after a burn, other physical signals produced by a fire can be measured remotely. **Table 2.1** is taken from the study of Ichoku et al. (2016) and aptly summarises the various attributes associated with fire that are of scientific interest and can be elucidated through remote sensing. In addition to the already discussed variables of BA and FRP, measurement of other fire characteristics such as flaming ratio and plume injection height are of significant scientific interest and work has been carried out on their quantification (Sofiev et al., 2012; Paugam et al., 2016; Martin et al., 2018; Fisher et al., 2020). Also of importance with respect to fire emissions are observations of the smoke and/or components of smoke that are generated in the combustion process - such as changes in aerosol optical depth (AOD) and observations of total column trace gases amounts, for example, NH<sub>3</sub>, CO and CH<sub>4</sub>. Due to the other potential emissions sources contributing to high AOD or high atmospheric trace gas concentrations. In the context of fire emissions these datasets are often used in tandem with BA or FRP fire

products, rather than on their own so that signals in AOD or trace gas concentrations are appropriately assigned to biomass burning.

### 2.2.3.1Aerosol Optical Depth

Aerosols can generally be defined as particles in the liquid or solid phase that are suspended in air. AOD is a lumped measurement of the optical impact of these aerosols in a column of air from all sources – both natural and anthropogenic, for example urban haze, sea salt, smoke particles and dust. Effectively, AOD is the extent to which the transmission of light from the Earth’s surface to the top of the atmosphere is prevented by the light scattering and light absorbing properties of aerosols. AOD is a basic optical property and information on it is generated using data from many different Earth observation instruments (e.g. MODIS, VIIRS, AVHRR, MIRS etc.). However, large discrepancies exist between AOD measures and these differences arise from algorithm differences in cloud masking, assumptions about aerosol microphysical processes, treatment of boundary surface conditions and instrument calibration (Li et al., 2009). Irrespective of these variations, satellite AOD products still offer an additional means to study not only the immediate emissions of aerosols generated by fires (Ichoku and Kaufman, 2005; Ichoku and Ellison, 2014; Mota and Wooster, 2018; Nguyen and Wooster, 2020), but also, the evolution of these aerosols after emission and the physical and chemical processes that drive their evolution (Konovalov et al., 2017, 2019; Noyes et al., 2020). AOD can be derived in wavebands across the UV to NIR spectral range. Different approaches exist, and many AOD algorithms use measurements in the blue visible range ( $\approx 0.4$  to  $0.5 \mu\text{m}$ ) to retrieve AOD in approaches that in some senses are similar to those of BA detection – by detecting changes in apparent surface reflectance which correspond to the presence or absence of aerosols (Levy et al., 2013, 2015; Remer et al., 2013; Lyapustin and Wang, 2018); though many other channels in the visible range are used prior to AOD retrieval for various types of filtering and masking. This thesis focuses on use of the AOD products generated from the MODIS sensors observations and these products are discussed in much greater detail in **Section 4.2.1** and **Section 4.3**

**Table 2.1** Summary of sensors used in measuring fire related variables and their uncertainties, categorised by their spatial resolution. Taken from (Ichoku et al., 2016).

Item no.	Essential questions	Satellite retrieved variable	Symbol	Spatial resolution Satellite sensors**	Uncertainty levels*				
					Very high (0.001–0.01 km)	High (0.01–0.1 km)	Medium (0.1–1 km)	Coarse (1–10 km)	Very coarse (10–100 km)
1	Fire location	Fire location	FL <sup>b</sup>	Landsat, ASTER, SPOT, (Lidar/SAR) <sup>f</sup>	~0.15 km	~0.75 km	~5 km		
2	Fuel load and conditions	Biomass	BM <sup>c</sup>	QuickBird, Ikonos	±50%	±50%			
3	Fire size/intensity	Fire Area	FA <sup>d</sup>			65–250%	±50%		
		Fire Temp	FT <sup>e</sup>			±30%	±100 K		
		Fire Radiative Power	FRP <sup>f</sup>			±30%	±50%		
4	Fire characteristics (flaming/smoldering)	Flaming ratio	FSR <sup>g</sup>			40%–140%			
5	Fire duration	N/A							
6	Burned area	Burned area	BA <sup>h</sup>		±10%	±20%	±30%		
		Burn Severity	BS <sup>i</sup>		±70%				
7	Smoke emission rate	N/A							
8	Plume injection height	Plume top height	PTH <sup>j</sup>				±0.5 km		
		Plume vertical profile	PVP <sup>k</sup>			±7%			
9	Major smoke constituents	Aerosol Optical Depth	AOD <sup>l</sup>				±0.15		
		Carbon Monoxide	CO <sup>m</sup>				±50%		
		Carbon Dioxide	CO <sub>2</sub> <sup>n</sup>				97%–102%		
		Methane	CH <sub>4</sub> <sup>o</sup>				96%–102%		
10	Smoke transformation	N/A							
11	Fire behavior	N/A							
12	Fire diurnal/seasonal cycles	N/A							

### 2.2.3.2 Total Column Trace Gases

Much like AOD, total column amounts of trace gasses observed close to fires can be used to probe aspects of the emissions from biomass burning. Most remote sensing products that include measures of pollutant gases such as CO, CH<sub>4</sub>, N<sub>2</sub>O and O<sub>3</sub> are based on fine spectral resolution measurements in the UV to IR spectral range, deploying radiative transfer model techniques and optimal estimation to estimate the composition and amounts of these gases between the surface and top of atmosphere (Edwards et al., 1999; Hurtmans et al., 2012; Landgraf et al., 2016; Deeter et al., 2017). Remotely sensed CO datasets are especially relevant to the study of biomass burning emissions and are also used within this thesis (see **Section 5.2.3.1**). Satellite observed CO measures have been widely used in studying emissions from specific fire events (Lamarque et al., 2003; Liu et al., 2005; Pfister et al., 2005; van der Velde et al., 2020), validation of BA or FRP derived fire emissions estimates (Baldassarre et al., 2015; Reddington et al., 2016) and even to back-calculate fuel consumption estimates from biomass burning (Wooster et al., 2018).

## 2.3 Satellite Remote Sensing of Fire – Instruments

As was discussed in **Section 2.2.1** and **Section 2.2.2**, the spatial resolution of remote sensing data is a crucial determinant in the minimum size of the active fire or burn scar that can be detected. The use of FRP products to determine total fire emissions generally relies on its temporal integration to FRE (see **Section 2.4**) and therefore the temporal resolution of FRP data is also of crucial importance. This is compounded by the fact that fires have a strong diurnal behaviour (Giglio, 2007; Roberts et al., 2009; Andela et al., 2015), and sometimes also are ignited and burn for relatively small amounts of time. In general, fire activity is relatively less intense at night and increases over the morning - peaking in the early to late afternoon. The BA approach is less sensitive to the temporal resolution of the measurements since burn scars can often be seen for many days, weeks and even years after a fire, depending on the affected vegetation type and biome. However as already discussed in **Section 2.2.1**, BA methods have other limitations in terms of the minimum detectable burn scar, unsuitability to real-time applications (since the BA can generally only be detected after the fire event), and

other uncertainties when used in fire emissions estimation (see **Section 4.3**). In the scope of FRP data for biomass burning emissions, the dual dependence of FRE characterisation on both the spatial and temporal resolution of observations often results in a single remote sensing platform being unable to capture the full extent of fire activity.

The next section thus provides an overview of the different remote sensing platforms used in the measurement of fire and the impact that features of these platforms have on fire characterisation. Satellite sensors used to retrieve FRP measures, and indeed satellite platforms in general, can be categorised as two main types and the data from each has specific advantages and limitations. Satellite sensors can be classified as either polar-orbiting or geostationary.

### 2.3.1 Polar Orbiting Satellites

Polar orbiting satellites orbit the globe longitudinally passing through the Earth's axis of rotation and over the poles. With the Earth rotating below, each of the satellite's orbits allows the sensor onboard to image a different section of the Earth's surface. These satellites orbit at relatively low altitudes of some hundreds of km and are often Sun-synchronous, causing the overpass time at each location on the surface to occur at roughly the same local time each day.

Several polar-orbit based sensors used in both FRP and BA quantification are detailed in **Table 2.1** (Ichoku et al., 2016). However, the most widely used, and most well validated FRP product, is that generated from the Moderate Resolution Imaging Spectroradiometer (MODIS) instrument aboard NASA's Terra and Aqua satellites. These have two daily equatorial overpasses each, at about 10:30 and 22:30 (Terra) and 01:30 and 13:30 (Aqua) local time. The daily coverage of the Terra MODIS instrument is shown in the true colour image in **Figure 2.3a.**

The MODIS sensor's MIR and LWIR waveband channels have a spatial resolution of 1000 m at nadir, and its visible to SWIR bands have a 500 m spatial resolution at nadir. The former are used to produce the Collection 6 Level 2 MOD14/MYD14 Active Fire and Thermal Anomalies Product (Giglio et al., 2016) which applies the FRP methodology of Wooster et al. (2003)

described in **Section 2.2.2** and the latter are used in generation of the Collection 6 Level 2 MCD64A1 and MCD45A1 Burned Area Product (Giglio et al., 2018) (discussed in **Section 2.2.1**). Both products have been extensively validated (Morisette et al., 2005; Csiszar et al., 2006; Schroeder et al., 2008; Chang and Song, 2009; Randerson et al., 2012; Giglio et al., 2013; Tsela et al., 2014; Boschetti et al., 2019). One feature of the MODIS sensor that effects retrievals of BA, FRP and indeed other quantities such as AOD (Sayer et al., 2015) is what is known as the 'bow-tie' effect. This arises from MODIS's design and scanning geometry and the curvature of the Earth which results in (i) raw Level 1B pixels growing significantly in terms of their footprint areas (by up to 8 times) at wide view zenith angles (VZA) and (ii) the overlap of successive scans at the edge of swath (by up to 50%) meaning features are duplicated in adjacent pixels in these areas (Masuoka et al., 1998; Wolfe et al., 1998, 2002). In terms of the MODIS FRP product the larger pixel footprint area towards the swath edge causes a reduction in the number of AF detections (Freeborn et al., 2011; Kumar et al., 2011) but higher overall per-pixel FRP. It has also been shown that the MODIS BA product tends to not detect small burn scars (Tsela et al., 2014; Hawbaker et al., 2017; Roteta et al., 2019).

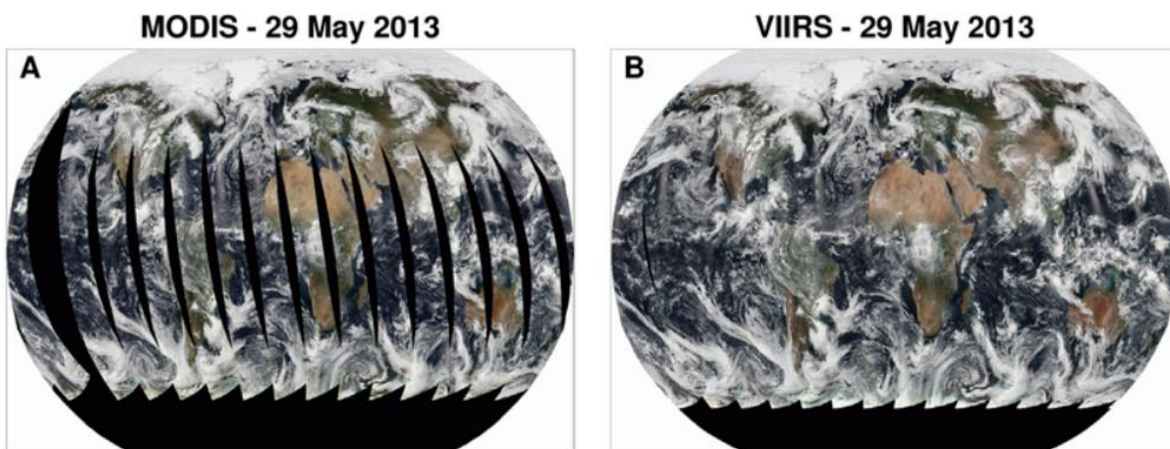


**Figure 2.3** True colour RGB image from MODIS aboard Terra and VIIRS aboard Suomi NPP showing global coverage on single day (May 29<sup>th</sup> 2013). Taken from Levy et al. (2015).

The Visible Infrared Imaging Radiometer Suite (VIIRS) aboard NASA's Suomi NPP satellite is another polar-orbiting sensor that provides AF detection and FRP measurements globally. This instrument has a wider swath and a finer spatial resolution than MODIS - 750 m at nadir and for some channels also 375 m at nadir. Daily coverage from the VIIRS visible channels is

shown in **Figure 2.3b** and the impact of VIIRS's wider swath can be seen in comparison to MODIS. Many of the algorithms used to generate VIIRS products are heritage algorithms of the MODIS sensor and this is true for the VIIRS AF product (Schroeder et al., 2014; Schroeder and Giglio, 2017). The higher spatial resolution of the VIIRS sensor and the pixel averaging procedure applied at VZA > 35° to keep the pixels from growing too large (Cao et al., 2017) significantly improves the AF detection performance of the VIIRS sensor compared to the MODIS AF product (Schroeder et al., 2014; Li et al., 2020). **Figure 2.4** shows how the pixel averaging procedure in VIIRS reduces the impact of the bow-tie effect compared to MODIS - more stable per-pixel FRP values are retrieved across different sensor VZA. It also shows how the higher spatial resolution of the VIIRS sensor results in a lower minimum (and maximum and mean) per-pixel FRP. The lower FRP detection threshold means that VIIRS is able to detect many more small fires than MODIS.

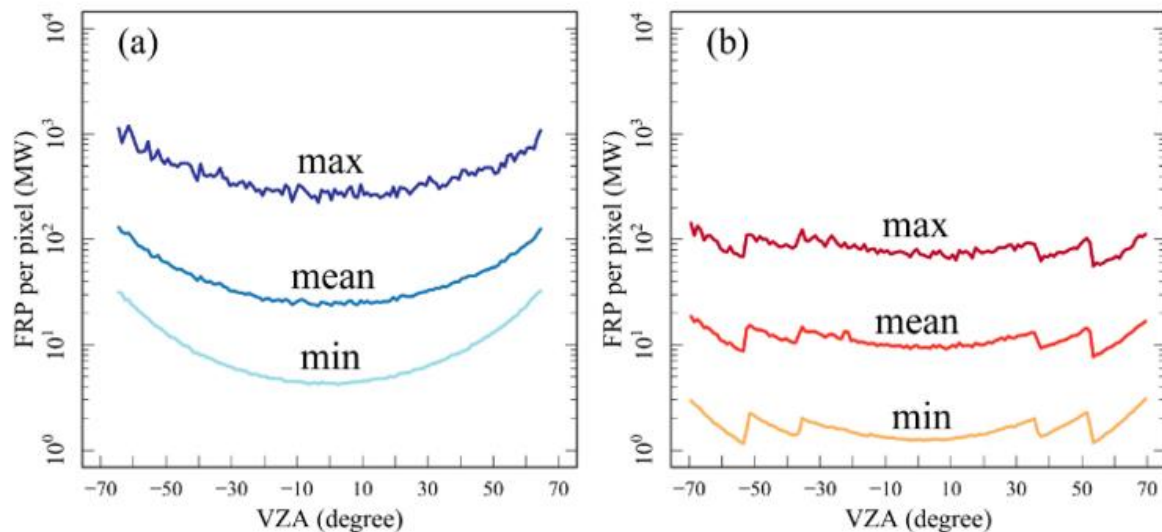


**Figure 2.4** Variations in minimum, maximum and mean FRP per pixel in the (a) MODIS and (b) VIIRS FRP products, plotted as a function of sensor View Zenith Angle (VZA). Taken from (Li et al., 2020).

Although the MODIS and VIIRS AF products are able to detect and quantify the FRP of many relatively small fires, both products have a limited temporal resolution. In a single location the MODIS AF product typically has 4 daily observations (2 at night) while the VIIRS AF

product has only 2 daily observations (1 at night). These polar-orbiting products therefore may often miss the peak of daily fire activity and fail to capture fully the diurnal variations in fire intensity. Further to this, if a fire is burning earlier or later in the day than the satellite overpass, the fire will be missed completely. These limitations are especially impactful when estimating emissions from these FRP datasets which require the temporal integration of FRP to obtain FRE - which is then used to estimate the total fuel consumption of a fire (see **Section 2.4**). In order to convert one or two daily FRP observations to daily FRE measures some form of interpolation must be applied to FRP data and the approaches used for this are discussed further in **Section 2.3.3**.

As previously mentioned, BA products from polar-orbiting sensors are less impacted by their limited temporal resolution because burn scars are visible for some time after a fire has burned, however, emissions derived from BA data alone have other disadvantages which are discussed in **Section 2.4**.

### 2.3.2 Geostationary Satellites

Geostationary satellites operate at far higher altitudes than polar-orbiting satellites - around 35,000 km - in a geosynchronous orbit that provides a view over a fixed position on the surface. Due to this, sensors onboard geostationary platforms are able to make near continuous measurements of the same location. However, because of this stationary orbit, global products cannot be generated from a single sensor, rather a suit of sensors over different areas provide this information. **Figure 2.5** shows the regions of the globe observed by several state-of-the-art geostationary sensors.

The Geostationary Operational Environmental Satellites (GOES) operate over North and South America and the Pacific, retrieving observations at 10-minute intervals with a 2 km spatial resolution at nadir, and the Himawari-8 AHI sensor provides the same spatio-temporal resolution over East Asia and Australia. The Spinning Enhanced Visible and Infrared Imager (SEVIRI) aboard the Meteosat-11 and Meteosat-8 satellites (MSG and MSD-IODC respectively in **Figure 2.5**) provide images of Europe, Africa, the Middle East and India at 15-minute intervals with a 3 km resolution at nadir.

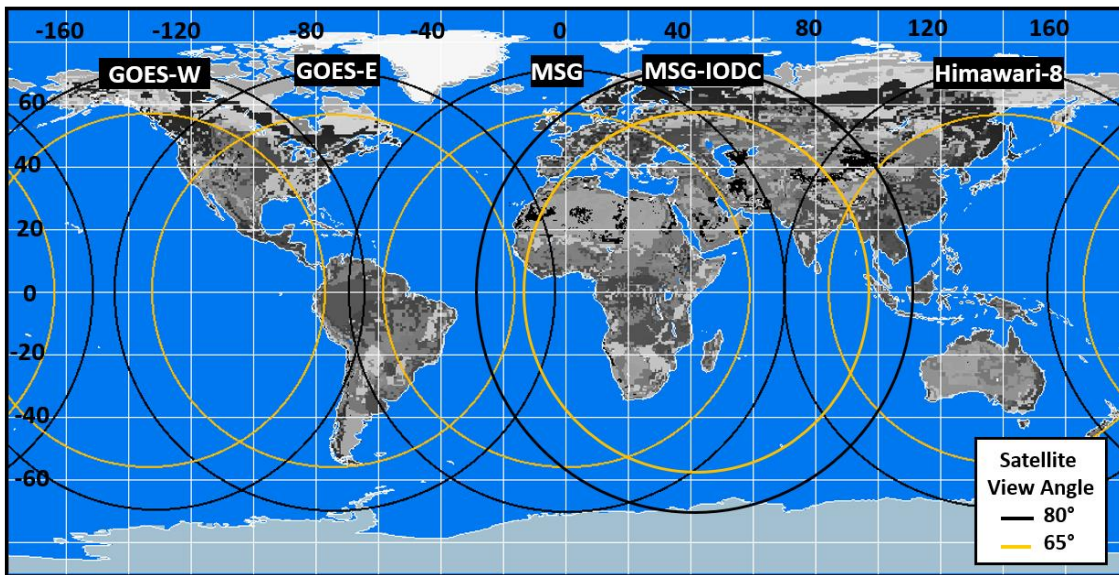


**Figure 2.5** The field of view of sensors aboard several geostationary satellite platform which are currently operational.

Geostationary instruments have a lower spatial resolution than polar-orbiting sensors due to their far greater distance above the surface, and similar to with MODIS a decreased spatial resolution is found towards the disk edges due to the curvature of the Earth and the high VZAs at such locations. In terms of FRP measurements, these characteristics mean that although fires can be well characterised at pixels with a strong fire signal, fewer small fires are detected and measured than by MODIS or VIIRS (Roberts and Wooster, 2008; Freeborn et al., 2014; Roberts et al., 2015; Hall et al., 2019), and the FRP detection limit increases even further at increased VZA towards the edges of the Earth disk.

### 2.3.3 Integrated Fire Products

Given the above described limitations and uncertainties, there has been significant research effort focused on combining polar-orbiting and geostationary based FRP and/or BA datasets to maximise the benefits of each data type (Boschetti and Roy, 2009; Ellicott et al., 2009; Freeborn et al., 2009; Vermote et al., 2009; Andela et al., 2015).

Boschetti and Roy (2009) merged the MODIS FRP and MODIS BA products by temporally interpolating FRP data linearly between observations and spatially extrapolating the resultant FRE over the extent of the MODIS burned area. They show MODIS FRP to be under sampled both spatially and temporally, with only a subset of AF pixels being detected when compared to the full extent of burned area - largely due to the limited temporal resolution of the MODIS FRP product.

Freeborn et al. (2009) developed a virtual fire product from the SEVIRI FRP-PIXEL and MODIS FRP products over Africa for 2004. They propose that the frequency density distributions (f-D) of FRP can serve as a unique thermal signature that summarises a collection of FRP pixels from a fire event. The SEVIRI and MODIS FRP pixel datasets are subset into near-simultaneous observations that occur in the same locale and f-D distributions were derived for various spatial and temporal aggregations of this dataset. An empirical database was constructed by matching SEVIRI and MODIS f-D distributions that were concurrent and collocated and the database generated contained more than 680,000 paired SEVIRI and MODIS f-D distributions. The virtual FRP product was produced by matching new SEVIRI FRP data with this empirical database of f-D distributions to generate a matching MODIS f-D distribution - the summed synthetic FRP was estimated from these matches on a  $5.0^\circ \times 0.5^\circ$  grid. This synthetic high-temporal resolution 'MODIS FRP product' is shown in **Figure 2.1** and appears to map well both the temporal patterns of SEVIRI FRP data and the magnitude of MODIS FRP data. Drawbacks to their approach include the requirement for large amounts of data to obtain reasonable statistics on predicted FRP values, the likely poor representation of inter-annual variability and other factors such as vegetation type and VZA in the virtual dataset, and the very coarse spatial resolution of the final virtual product ( $0.5^\circ$ ).

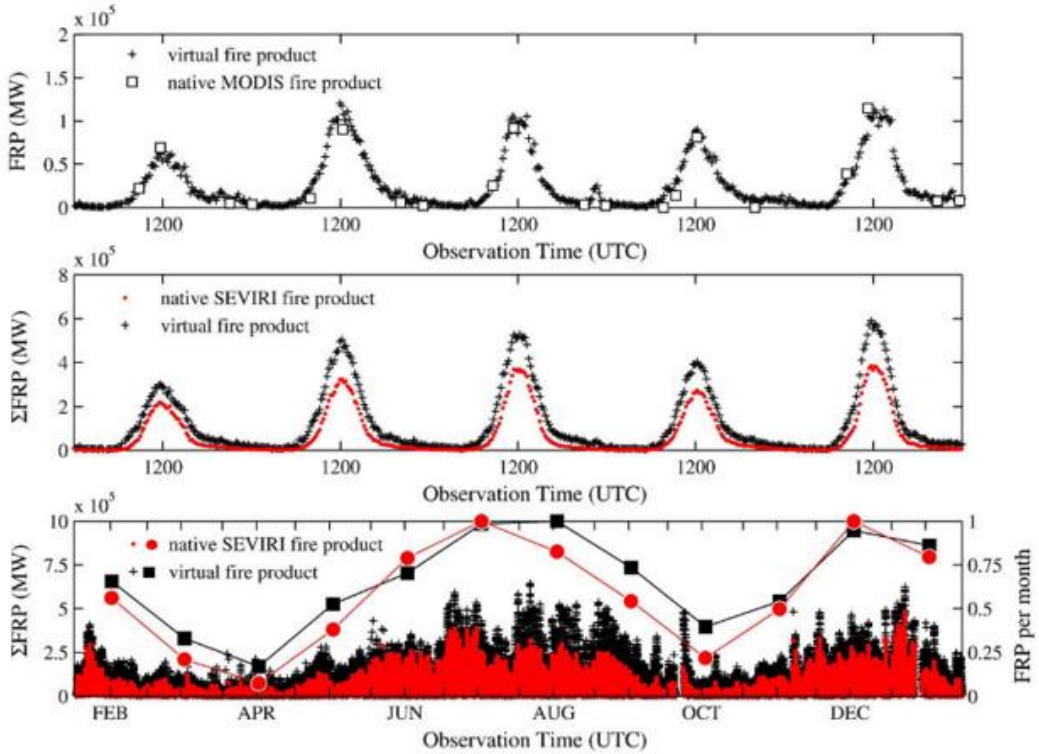


**Figure 2.6** A comparison of the native SEVIRI FRP and MODIS FRP products with the virtual FRP generated by the empirical f-D distribution database of Freeborn et al. (2009)

This approach was extended by Andela et al. (2015) who explored some of the potential drivers related to the shape of diurnal cycles found in Giglio (2007). For example, land cover and climatology as well as aspects of the fire regime such as fire size and total annual FRE. Their results are compared with SEVIRI FRP and the study concludes by highlighting the importance of diurnal fire dynamics in the estimation of accurate FRE measures. Notably however, the impact of anthropogenic activities on the fire ignition cycle was not considered in their work.

It is clear from the range of above-described methods, that substantial work has been done to address both the spatial and temporal limitations of remote sensing data used in the characterizations of biomass burning and fire emissions. Despite this, it is still unclear what an optimal approach should be, and the propagation of (not always known) uncertainties in the data used in these methods along with uncertainties introduced by the methodologies themselves continue to pose a challenge. Assessments of the performance of these different

approaches are also not always easy to make due to the changing nature of fire activity and the difficulty in obtaining good quality independent data.

## 2.4 Fire Emission Inventories

This section describes the methods used in converting satellite observations of BA, AF detections and FRP into estimates of gas and aerosol species emissions from biomass burning. It presents the two main methods used for fire emission inventory generation and details several specific fire emissions inventories commonly used in the research community.

The variety of FRP, AF and BA satellite data available, at varying temporal and spatial resolutions (see **Section 2.3**), presents the potential for many different approaches to produce biomass burning emission inventories. The variations in these inventories and their main sources of uncertainty will be determined both by the type, and spatio-temporal resolution of satellite data used, as well as the assumptions introduced when estimating emissions. Methods to estimate fire emissions can generally be categorised as either bottom-up or top-down. Top-down methods have traditionally been those of atmospheric inversion – where observations of a particular atmospheric species (e.g. CO) are inverted to estimate the amount of CO emitted in a particular region (e.g. Kopacz et al., 2010). Bottom-up methods on the other hand rely on observations of purely surface phenomena, most commonly BA, turned into estimates of total fuel consumption,  $FC_T$  (in kg) using various other information (e.g. model-based estimates of fuel consumption per unit area). These estimates of total fuel consumption can then be multiplied by biome-specific emission factors (EFs) to obtain the amounts of a trace gas or aerosol species emitted. More recently, fire emissions estimation approaches that only use satellite data of the atmosphere and of the fire itself (in terms of its FRP) have also been termed top-down (Ichoku and Ellison, 2014). These bypass the conversion of the satellite data to  $FC_T$  and relate the FRP or FRE measures directly to emissions of a given atmospheric species. This is done using a smoke emission coefficient,  $C_e$  (in g MJ<sup>-1</sup>), that is geographically or vegetation-type-specific and derived using satellite observations of atmospheric phenomena (e.g. AOD). A summary of several commonly used fire emissions inventories is detailed in **Table 2.2** (Zhang et al., 2014) giving information on the EO data sources used and

spatio-temporal resolution of each inventory. Four of these inventories and the general approach used in bottom-up and top-down emissions estimation are described in more detail in this Section.

**Table 2.2** Summary of several bottom-up and top-down fire emissions inventories which are regularly used in biomass burning research.

Category	Method	Data	Resolution	Fire data source	References	Fields
Bottom-up approaches	Fuel consumption and burned area based	FLAMBE	1 ~ 5 km, hourly	MODIS/ GOES	Reid <i>et al</i> (2009)	PM <sub>2.5</sub>
		FINNv1.0	~1 km <sup>2</sup> , daily	MODIS	Wiedinmyer <i>et al</i> (2011)	BC, OC, PM <sub>2.5</sub> , etc
	FRP-based with land cover specific conversion factors and emission factors	GFEDv3.1	0.5° × 0.5° Monthly	TRMM-VIRS/ ATRS; MODIS	van der Werf <i>et al</i> (2010)	BC, OC, PM <sub>2.5</sub> , etc
		GFASv1.0	0.5° × 0.5°, daily	MODIS	Kaiser <i>et al</i> (2012)	BC, OC, PM <sub>2.5</sub> , etc
		GBBEP-Geo	3 ~ 4 km, hourly	GOES (SEVIRI in Africa)	Zhang <i>et al</i> (2012)	Total dry mass
Top-down approaches	FRP-based with satellite AOD constraint	FEER- SEVIRIv1.0	1° × 1°, hourly	MODIS/ SEVIRI	Ichoku and Ellison (2013)	Total parti- culate matter
		QFEDv2.4	0.25° × 0.3125°, or 0.1° × 0.1° daily	MODIS	Darmenov and da Silva (2013)	BC, OC, PM <sub>2.5</sub> , etc

## 2.4.1 Bottom-up Fire Emission Inventories

Most bottom-up approaches estimate fire emissions from the relation:

$$M_x = FC_T \times EF_x \quad [2.7]$$

where  $M_x$  is the mass of species  $x$  emitted (in g),  $FC_T$  is the total dry fuel consumed (in kg) and  $EF_x$  is the mass of species  $x$  emitted per kg of fuel consumed (in g kg<sup>-1</sup>). Emission factors are typically based on laboratory experiments or in-situ field measurements of fire emissions (Andreae and Merlet, 2001; Akagi et al., 2011; Andreae, 2019). Crucial to this approach is the conversion of BA, AF detections or FRP to total fuel consumed,  $FC_T$ .

When using BA satellite data the method first proposed by Seiler and Crutzen (1980) is used to estimate  $FC_T$  from BA measures:

$$FC_T = BA \times FL \times CC \quad [2.8]$$

where  $BA$  is the burned area ( $\text{m}^2$ ),  $FL$  is the pre-burn fuel load ( $\text{kg m}^{-2}$ ) and  $CC$  is the combustion completeness (unitless). Fuel load (the mass of dry fuel per area) and combustion completeness are challenging to determine either by remote sensing or from in-situ measurements at ground level. They are therefore typically estimated from a combination of landcover maps and vegetation growth models coupled with empirical relationships linking meteorological variables related to fuel moisture (Potter et al., 1993; Ito and Penner, 2004; van der Werf et al., 2006, 2017). The dependence of  $FC_T$  on the parametrisation of  $FL$  and  $CC$  causes large variations in  $FC_T$  estimates and this is a key source of uncertainty in the BA approach to emissions estimation (Reid et al., 2005b; Zhang et al., 2008; Reid et al., 2009a). As discussed in **Section 2.2**, BA measures are not significantly impacted by the temporal resolution of satellite observations since burn scars are detectable for quite some time after a fire has burned. However, burn scars are typically only mapped after a fire has ceased to burn (or at least not commonly mapped in real time) and this limits the use of BA based emissions inventories in near-real time applications.

Where FRP observations are available,  $FC_T$  can be estimated from the linear relationship between FRP and the rate of fuel consumption (Wooster, 2002; Wooster et al., 2005) and an analogous relationship exists between FRE and  $FC_T$  which are the temporal integrals of FPR and the rate of fuel consumption respectively. This relation of FRE to  $FC_T$  removes the requirement for the highly variable parameters of  $FL$  and  $CC$  thus providing an alternative route to  $FC_T$  - though a FRE-to- $FC_T$  conversion factor must still be estimated. This has mostly been done from in-situ field measurements (Wooster et al., 2005; Van Leeuwen et al., 2014), but these are by necessity generally made on quite small fires that may not be so applicable to larger fires and to spaceborne FRP measures. The FRE route to estimating  $FC_T$  enables emissions estimates to be generated in near-real time due to the ready availability and low latency of FRP data streams. However, estimates of  $FC_T$  are strongly influenced by the temporal resolution of FRP observations since FRE must be temporally integrated from FRP observations (see **Section 2.3**).

Bottom-up emissions inventories are generally more widely used than top-down inventories, likely due to the latter being more recently developed. Several of the most commonly used bottom-up fire emissions inventories are described here in more detail, though other emissions inventories do exist, such as FLAMBE (Reid et al., 2009a) and GBBEP-Geo (Zhang et al., 2012).

#### 2.4.1.1 The Global Fire Emissions Database - GFED

The Global Fire Emissions Database (GFED; Van Der Werf et al., 2006, 2010, 2017) is a bottom up inventory that provides monthly and daily fire emissions with a global coverage and which are derived from the MODIS MCD64A2 500 m BA product (Giglio et al., 2013). MODIS BA is mapped at  $0.25^\circ \times 0.25^\circ$  and  $FC_T$  is derived at this spatial resolution from the application of **Equation 2.8**. The global biogeochemical Carnegie-Ames-Stanford-Approach model (CASA; Potter et al., 1993 and updates; Van Der Werf et al., 2006, 2010, 2017) is used to estimate fuel loads, and fuel consumption per unit area is derived from this, plus vegetation characteristics and combustion completeness (CC) based on antecedent meteorological conditions. Finally, the *EFs* of Andreae and Merlet (2001) and Akagi et al. (2011) are applied to  $FC_T$  estimates to generate fire emissions of trace gases and aerosols. **Figure 2.7** shows the global distribution of mean burned area fraction, fuel consumption per unit area and total carbon emissions per unit area between 1997 and 2014 as determined by GFEDv4s.

As was discussed in **Section 2.2.1**, typically more than ~ 20% of a BA pixel must be fire affected in order for it to be detected (Giglio et al., 2006), and this results in small burn areas not being identified in the MODIS BA product (Tsela et al., 2014; Hawbaker et al., 2017; Roteta et al., 2019). In the most recent version of the inventory, GFEDv4s (van der Werf et al., 2017), a ‘small fire’ boost is applied to MODIS BA measures to account for the considerable number of small fire burns which are not detected in the 500 m MCD64A2 product. These dominantly occur in agricultural regions (Randerson et al., 2012), though small burns that are not detected by MODIS exist in every biome. The small fire boost introduced in GFEDv4s has been shown to account for these small agricultural fires during some time periods, however, it also causes a false positive biases in others periods (Zhang et al., 2018).



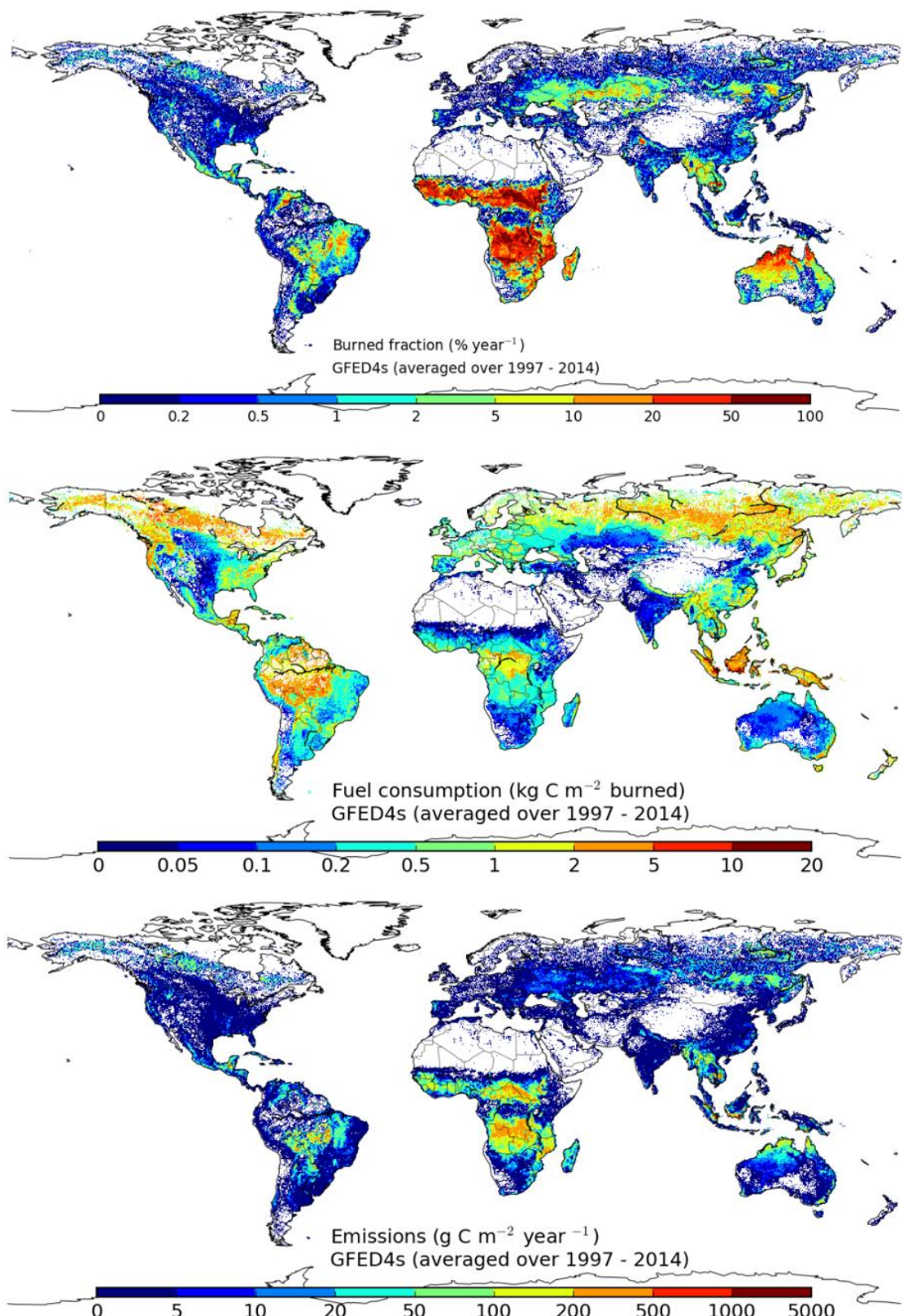


**Figure 2.7** Mean burned area fraction, fuel consumption and total carbon emissions per unit area between 1997 and 2014, as determined by GFEDv4s (van der Werf et al., 2017)

These unobserved small fires and the uncertainties in the parameters of  $FL$  and  $CC$  which can be as high as 50% (Reid et al., 2009a) are the main sources of uncertainty in the GFED emission inventory. A further limitation is that, since GFED relies on BA satellite data it cannot be used in near-real time forecasting of air quality. Despite this, its temporal range - starting from the beginning of the MODIS era (circa 1997) – and its widespread use and long-term comparison to other datasets makes it a very popular choice for providing fire emissions estimates in climatological studies (e.g. Aldersley et al., 2011; Keywood et al., 2013; Morton et al., 2013) and it is regularly used in other research related to biomass burning emissions (Yurganov et al., 2008; Huijnen et al., 2012; Pechony et al., 2013; Paugam et al., 2016; Reddington et al., 2016; Cusworth et al., 2018; Kiely et al., 2019; Zhang et al., 2020).

#### 2.4.1.2 The Global Fire Assimilation System - GFAS

The Global Fire Assimilation System (GFAS; Kaiser et al., 2012) generates emissions estimates from FRP data. GFAS exists as part of the Copernicus Atmosphere Monitoring Service (CAMS) and uses the MODIS MOD14/MYD14 1 km AF products to provide FRP data used to map daily global  $FC_T$  at a spatial resolution of  $0.1^\circ \times 0.1^\circ$  daily. The method described in Andela et al. (2015) is used to model the diurnal trajectory of FRP from the four daily MODIS FRP observations and FRE is calculated from this scaled Gaussian diurnal FRP. Gridded  $FC_T$  is obtained through the multiplication of FRE by biome specific FRE-to- $FC_T$  conversion factors which are generated from relations between FRP and historic GFED-derived  $FC_T$  estimates (Heil et al., 2010; Kaiser et al., 2012). Finally, emission fluxes of 40 trace gas and aerosol species are generated from these  $FC_T$  estimates through multiplication with the  $EFs$  of Andreae and Merlet (2001).

The use of MODIS FRP enables the near-real time generation of fire emission estimates and this is a key advantage of the GFAS emission inventory. Key sources of uncertainty include the requirement for the temporal integration of FRP and the potential for AFs to be undetected, either because they are not burning at the time of the MODIS overpass, or because their FRP is below that of the MODIS detection FRP threshold (see **Section 2.3.1**). Further, the uncertainty in the FRE-to- $FC_T$  conversion factor is not only significant (Kaiser et al., 2012; Van

Leeuwen et al., 2014) but also relies on the  $FC_T$  estimates of GFED, so is directly linked to  $FL$  and  $CC$  parameters, and GFAS estimates are not independent of GFED (Andela et al., 2013).

Despite these limitations, GFAS is widely used by the research community (Huijnen et al., 2012; Baldassarre et al., 2015; Inness et al., 2015; Koplitz et al., 2016; Heymann et al., 2017; Rémy et al., 2017; Reddington et al., 2019) and in particular its real-time nature means it is the input source of fire emissions in the Copernicus Atmosphere Monitoring Service (CAMS).

#### 2.4.1.3 The Fire Inventory from NCAR – FINN

The Fire Inventory from NCAR (FINNv1; Wiedinmyer et al., 2011) provides daily global fire emissions estimates and uses the same MODIS MOD14/MYD14 1 km AF product as is used in GFAS. However, instead of using the FRP measures provided in the product, FINN rather uses the time and location of AF detections in an approach that applies **Equation 2.8** to generate a pseudo-BA based emission inventory. MODIS AF pixels (which have a nadir resolution of 1 km) are used to generate estimates of BA based on the assumption that when an AF pixel is detected, this corresponds to a 1 km<sup>2</sup> burned area. Cases of multiple daily AF detections in the same location are accounted for as well as partial vegetation cover in some pixels using landcover maps. These estimates of daily BA are then multiplied by fuel loads from Hoelzemann et al. (2004) and combustion completeness from Ito and Penner (2004) with updates from Wiedinmyer et al. (2006) to generate estimates of  $FC_T$ . Finally, emission factors from Andreae and Merlet (2001) and Akagi et al. (2011) are applied to generated fire emissions for various different gas and aerosol species.

FINN produces fire emissions estimates at a higher spatial resolution than either GFAS or GFED (the native resolution of MODIS – 1 km at nadir) and due to its use of MODIS AF detections, it can be produced in near-real time. It does however have some significant sources of uncertainty, key of which are the assumptions made in the estimation of BA from AF pixels. The strong thermal signal produced by an active fire in MIR allows AF detection algorithms to detect fires covering as little as  $10^{-4}$  of a pixel's area (see **Section 2.2.2**), therefore, the assumption that the burned area of an AF pixel is the same as the pixel's footprint area may result in significant overestimations of BA. It is suggested that this overestimation of BA may

be balanced by missing detections of AF that are burning either outside of the MODIS overpass or below the MODIS FRP detection threshold (Wiedinmyer et al., 2011). As with GFED and GFAS, uncertainty in FINN estimates also come from the parameters of  $FL$  and  $CC$  used to convert BA to  $FC_T$ .

FINN has been widely used in fire emissions research (Amnuaylojaroen et al., 2014; Guerrette and Henze, 2016; Reddington et al., 2016, 2019; Vongruang et al., 2017; Mehmood et al., 2018; Kiely et al., 2019; Shi et al., 2020), particularly in regional air-quality modelling using the WRF-Chem model due to an accessible user tool developed for integrating FINN into this model (NCAR, 2020).

## 2.4.2 Top-down Approaches

Top-down fire emissions inventories using FRP data remove the requirement for either a FRE-to- $FC_T$  conversion factor or  $FL$  and  $CC$  parameters. They do this by using the direct relation between FRE and satellite-based atmospheric observations related to fire emissions, thus bypassing conversions to  $FC_T$ . This relation is quantified through a smoke emission coefficient which is either geographically or biome specific (Ichoku and Kaufman, 2005; Ichoku and Ellison, 2014; Mota and Wooster, 2018; Lu et al., 2019) and is given by:

$$M_x = C_e^x \times FRE \quad [2.9]$$

where  $M_x$  is the mass of species  $x$  emitted (g),  $C_e^x$  is the smoke emission coefficient for species  $x$  ( $\text{g MJ}^{-1}$ ) for a given location or biome and FRE is the fire radiative energy (MJ). This smoke emission coefficient,  $C_e^x$ , also applies to the relation between FRP and the rate of emission of species  $x$ ,  $R_x$  (in  $\text{g MJ}^{-1} \text{s}^{-1}$ ). Emissions or emission rates for any other chemical species,  $y$ , can be easily calculated from the multiplication **Equation 2.9** with the ratio of the emission factors of species  $x$  and species  $y$  ( $EF_y/EF_x$ ; no units). Values of  $C_e$  are calculated from FRP satellite data and observations of fire emissions, for example, aerosol optical depth (AOD) or total column measurements of trace gases, or from modelled concentration fields of similar species (Darmenov and da Silva, 2015). Crucially, this route to fire emissions can be applied in real time and removes the reliance on the highly uncertain parameters used in bottom-up

emissions inventories (Reid et al., 2005b; Zhang et al., 2008; Reid et al., 2009a; Van Leeuwen and van der Werf, 2011).

#### 2.4.2.1 The Fire Energetics and Emissions Research $C_e$ product - FEER

The Fire Energetics and Emissions Research product (FEER; Ichoku and Ellison, 2014) is a global  $1.0^\circ \times 1.0^\circ$   $C_e$  product for Total Particulate Matter (TPM) and was produced using the ‘top-down’ methodology first proposed by Ichoku and Kaufman (2005). FEER uses 7 years’ worth of the MODIS MOD14/MYD14 1 km AF product and the MODIS MOD04/MYD04 10 km AOD product to generate a dataset of fires (from FRP observations) and matching smoke plumes generated by those fires (from AOD observations). The rate of emission of TPM,  $R_{sa}$  (in  $\text{kg s}^{-1}$ ), in each plume is calculated from the AOD anomaly (summed AOD of the plume above the non-plume background AOD), modelled wind fields and the aerosol mass extinction efficiency,  $\beta_e$  (in  $\text{m}^2 \text{g}^{-1}$ ). The fire-plume matchup dataset is mapped to a  $1.0^\circ$  grid and the relationship between FRP and TPM emission rate in each grid cell is used to determine the  $C_e$  value of that grid cell. **Figure 2.8** shows these fire-plume matchups for a single grid cell (Ichoku and Ellison, 2014) where the  $C_e$  of the grid cell is given by the slope of the line-of-best-fit between  $R_{sa}$  and FRP - in this case  $0.0231 \text{ kg s}^{-1} \text{ MW}^{-1}$ . These linear regressions between  $R_{sa}$  and FRP were applied in each  $1.0^\circ$  grid cell to generate a global  $C_e$  map relating FRP to emissions of TPM (**Figure 2.9**). Global fire emissions are generated through the application of **Equation 2.9** to MODIS FRP data, with additional multiplication by  $(EF_y/EF_{TPM})$  to generate emissions of any other species,  $y$ , using the emission factors of Andreae and Merlet (2001) and its updates (Akagi et al., 2011; Andreae, 2019).

FEER can be applied to FRP data and can therefore generate near-real time emissions. Uncertainties in the method stem from; the use of simultaneous observations of MODIS FRP and AOD (Mota and Wooster, 2018); the use of a single value for the aerosol mass extinction efficiency,  $\beta_e$ , which varies, with relative humidity and age of smoke (Chin et al., 2002; Abel et al., 2005); and the use of the MODIS 10 km AOD which has limited performance over thick smoke (Levy et al., 2013; Livingston et al., 2014).

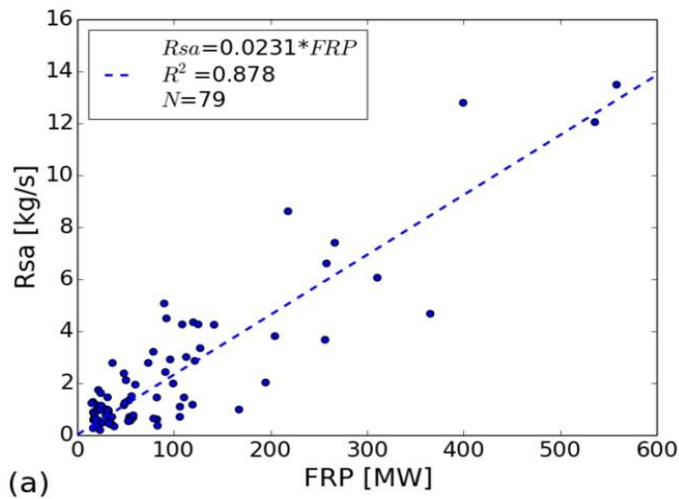


**Figure 2.8** The relationship between the emission rate of TPM in a smoke plume and the FRP of the fire associated with that plume, for all fires in a single  $1.0^\circ$  grid cell (Ichoku and Ellison, 2014).

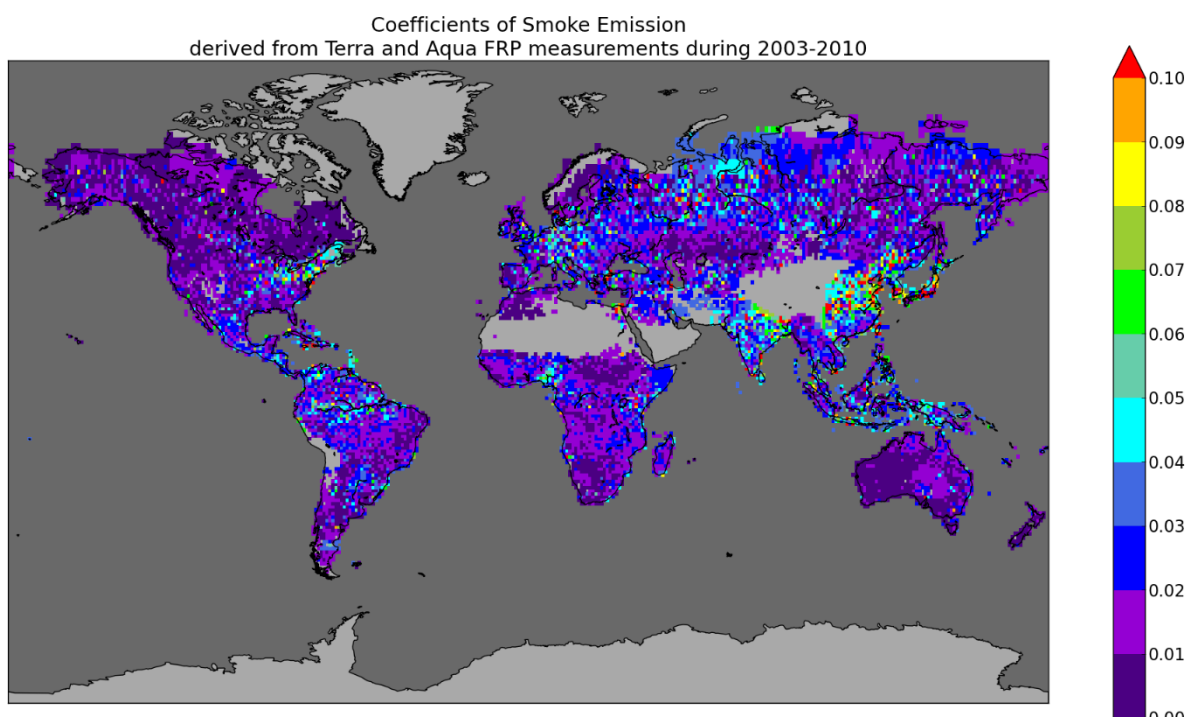


**Figure 2.9** The FEER global TPM smoke emission coefficient product with a spatial resolution of  $1.0^\circ$  with which  $C_e$  values (in  $\text{kg s}^{-1} \text{MW}^{-1}$ ) can be used to directly generate emission of TPM from FRP data (Ichoku and Ellison, 2014).

#### 2.4.2.2 The Fire Radiative Energy Emissions - FREM

The Fire Radiative Energy Emissions (FREM; Mota and Wooster, 2018)  $C_e$  product provides a top-down route to high temporal resolution emissions. It was developed and applied over southern hemisphere Africa (SHAF) at around  $0.05^\circ$  spatial resolution using the geostationary SEVIRI FRP-PIXEL product and MODIS MOD04/MYD04 10 km AOD product. FREM uses a comparable approach to derive  $C_e$  values as described by Ichoku and Kaufman (2005) and Ichoku and Ellison (2014) with some key adaptations including the use of geostationary FRP data rather than MODIS FRP and derivation of biome-specific smoke emission coefficients,  $C_{biome}$ , as an intermediary step to the final  $C_e$  product.

FRP observations of fires identified in the SEVIRI FRP product are matched with MODIS AOD observations of the matching smoke plumes generated by these fires. The FRE of each fire is calculated through the temporal integration of 15-minute SEVIRI FRP observations from the start of fire activity on a given day, to the time of the MODIS AOD observation. The TPM emitted by each of these fires is calculated from AOD observations of the smoke plume in the same approach used by Ichoku and Kaufman (2005) – though using a region specific value for  $\beta_e$ . The GLOBCOVER 2009 landcover map derived from 300 m ENVISAT MERIS data is used to identify and classify five distinct biomes in SHAF and FRE-TPM matchups are assigned to these biomes based on the majority biome in which FRP pixels were observed for each fire. The relation between FRE and TPM in each of these biomes, where the majority of FRP pixels came from a single biome, were plotted and biome specific smoke emission coefficients,  $C_{biome}$ , were taken as the slope of a line-of-best-fit between FRE and TPM. **Figure 2.10** shows the TPM of each fire-plume matchup against its FRE for each biome. A regional  $C_e$  product was generated from these five  $C_{biome}$  values at the spatial resolution of the SEVIRI product from a weighted average of  $C_{biome}$  values based on a SEVIRI pixel's fractional coverage of each biome. The resulting FREM  $C_e$  was used to generate TPM fire emissions for SHAF through application of **Equation 2.9** to a full six-year SEVIRI FRP-PIXEL dataset and emissions for trace gas species were generated through the multiplication of these emissions by biome specific emission factor ratios.

Mota and Wooster (2018) apply a 'small' fire adjustment to SEVIRI FRE data (when generating final emissions, not during  $C_{biome}$  derivation) to account for small fires with an FRP below the

FRP detection limit of SEVIRI, which is higher for geostationary sensors compared to polar-orbiting sensors due to their lower spatial resolution (see **Section 2.3**). FRE are upscaled by a factor of 1.46 based on studies comparing the SEVIRI and MODIS FRP products (Roberts et al., 2015). However, this upscaling may be overestimated or unnecessary in FREM since derived  $C_{biome}$  values may inherently account for these low FRP fires which are undetected in the SEVIRI product. On the other hand, the use of the 10 km MODIS AOD products during the derivation of the  $C_{biome}$  values meant that there was a focus on large fires that might have been less affected by undetected low FRP AF pixels. The aerosols from undetected small fires will still contribute to the observed MODIS AOD anomaly (and calculated TPM) but will not contribute to FRE, thereby introducing an intrinsic ‘boost’ in  $C_{biome}$  values and, in turn, FREM emissions. Additionally, this scaling factor may vary with satellite view zenith angle (VZA), due to the increasing SEVIRI footprint pixel area as a function of VZA.

Due to the fact that FREM applies the SEVIRI product at its native spatio-temporal resolution it can produce the highest spatio-temporal resolution emission inventory currently available for SHAF (up to 15-minute at approximately  $0.05^\circ$ ). This is a key strength of the approach compared to FEER, GFAS and GFED which have spatial resolutions at least twice as coarse. Some of the sources for uncertainty present in the FEER are reduced in FREM, for example FREM addresses the issue of simultaneously observed FRP and AOD in FEER by utilising SEVIRI FRP to quantify the fire activity leading up the time of the AOD observation. The mass extinction efficiency,  $\beta_e$ , used in FREM is also more region specific. Uncertainties in FREM, as with FEER, come mainly from the variability of the aerosol mass extinction efficiency,  $\beta_e$ , with smoke age and relative humidity and the use of the MODIS 10 km AOD product which is not optimised for observation of smoke plumes (and from underestimation of the FRP due to non-detection of low FRP AF pixels). The MODIS 10 km AOD product is not very suited to the observation of smoke plumes due to its relatively coarse spatial resolution (Remer et al., 2013; He et al., 2017), its’ very conservative cloud masking which removes many smoke affected pixels (Levy et al., 2013; Livingston et al., 2014) and the variability of AOD at wide MODIS VZA in the product (Sayer et al., 2015). Indeed, Mota and Wooster (2018) suggest the use of higher spatial resolution AOD observations as an key area for further work. Due to its use of geostationary FRP data FREM is not available with global coverage, however, the FREM

methodology could be applied to the suite of FRP products available from other geostationary sensors, such as those shown in **Figure 2.5**. These combined satellite datasets could be used to produce a high temporal resolution top-down fire emission inventory for the mid-latitudes.

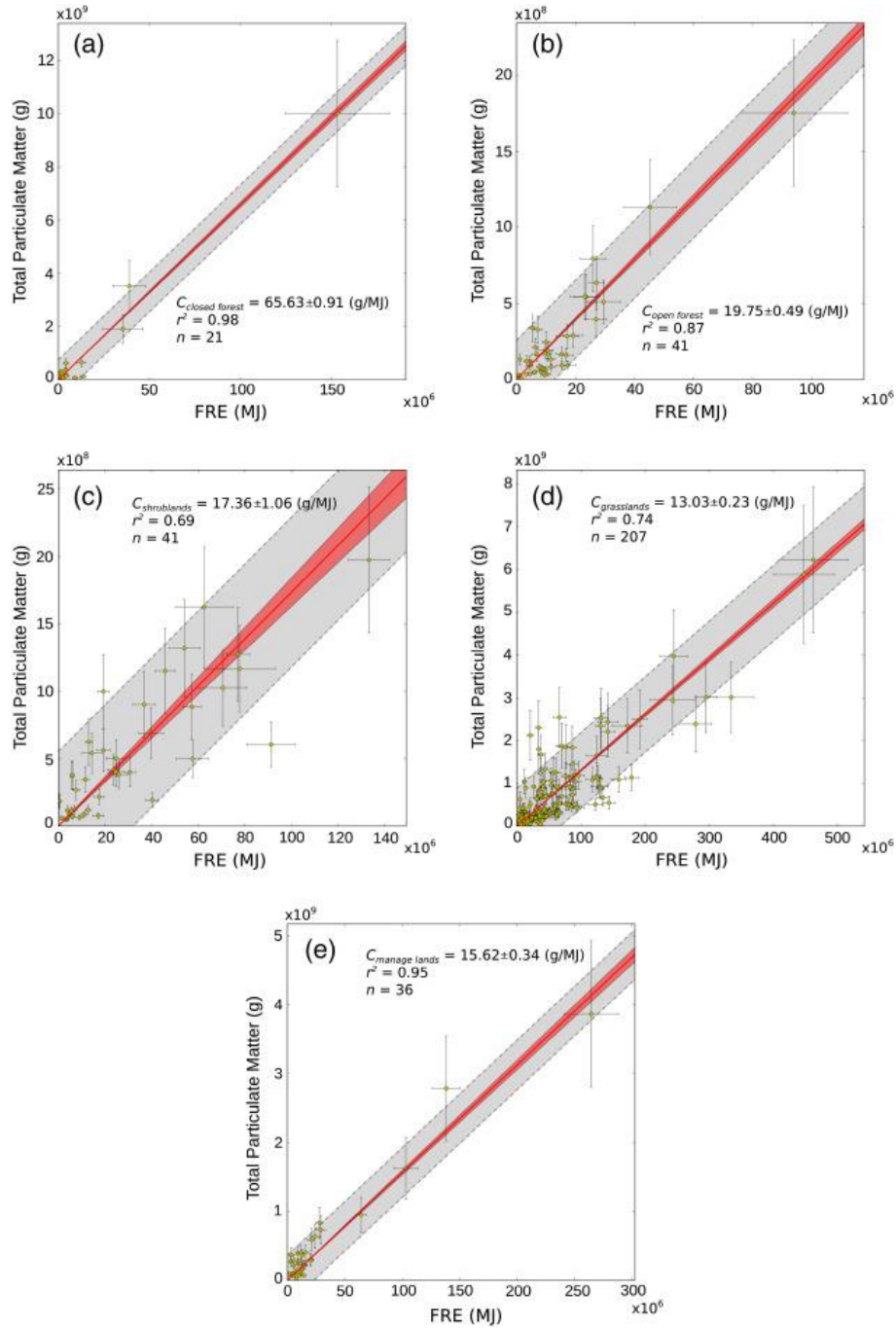


**Figure 2.10** The relationship between FRE and TPM from fire-plume matchups observed in each of the five biomes defined with the GLOBCOVER 2009 landcover map. The slope of these gives the  $C_{biome}$  value for a) closed canopy forest b) open canopy forest/woody savanna c) shrublands d) grasslands and e) managed land.

## 2.5 Validation and Assessment of Fire Emissions Estimates

This section discusses methods used in the validation of fire emission inventories, key of which is the use of atmospheric modelling. It details the challenges associated with evaluating estimated fire emissions and describes in more detail the use of atmospheric modelling for this purpose. The main considerations and limitations of such approaches are highlighted as well as previous work that has been carried in this area.

The explicit and direct validation of fire emission inventories is rendered extremely difficult due to the lack of exact ‘ground truth’ observations with which to compare emissions estimates—no single type of observation is available that gives the full spatio-temporal and chemical extent of fire emissions. As such, the assessment of fire emissions inventories must use fire-related observations such as those listed in **Table 2.1** from (Ichoku et al., 2016). Individual components of fire emissions inventories can be assessed - for example BA and FRP satellite products are regularly compared with other higher resolution satellite observations as a means of evaluation (Roy et al., 2008; Tansey et al., 2008; Freeborn et al., 2014; Roberts et al., 2015; Giglio et al., 2016) and satellite derived observations of AOD and trace gases such as CO and CH<sub>4</sub> are validated using satellite and ground-based observations (Lyapustin et al., 2011; Liu et al., 2014; Deeter et al., 2017; He et al., 2017). Emission factors which are typically produced from laboratory or in-situ field measurements are highly variable and are generally collated and mean values for different vegetation types are used (Andreae and Merlet, 2001; Akagi et al., 2011; Andreae, 2019).

In general, the evaluation of the final fire emissions inventories themselves relies either on simple comparisons between emissions inventories to quantify the relative correctness of an inventory (e.g. Wiedinmyer et al., 2011; Kaiser et al., 2012; Ichoku and Ellison, 2014), or emissions are used as input in chemical transport models (CTM) to simulate the evolution of emissions which can then be compared with ground-based and satellite-based observations of aerosols and gases.

### 2.5.1 An Overview of Atmospheric Modelling

Atmospheric modelling involves the numerical simulation of meteorological and atmospheric processes to reproduce or forecast the chemical composition of the atmosphere. In its broadest definition an atmospheric model can refer to a very wide range of models - from the highly complex Atmosphere-Ocean General Circulation Models (AOGCMs) used to study Earth's climate and atmospheric composition on decadal and millennial time scales (e.g. CCMS3; Collins et al., 2006) to Lagrangian particle dispersion models used in, for example, tracking the evolution of volcanic plumes (e.g. Prata et al., 2007). National and international meteorological services often produce and make available results from global atmospheric models that provide information on the chemical composition of the atmosphere, for example the EU Copernicus Atmospheric Monitoring Service (CAMS) provide global 3-hourly atmospheric composition at  $0.75^\circ \times 0.75^\circ$  resolution in their EAC4 reanalysis model (Inness et al., 2019). These global chemistry models can be used as initial and boundary conditions in regional meteorology-driven chemical transport models (CTMs) to gain localised high spatio-temporal resolution chemical concentration fields. Hereafter, atmospheric modelling or air quality (AQ) modelling will refer specifically to the use of these regional-scale CTMs.

CTMs are typically coupled to numerical weather prediction (NWP) models and the meteorological fields simulated in the latter are used to drive the chemical and physical processes of the CTM. Using the NWP metrological fields, CTMs simulate the transport and chemical and microphysical processes of aerosols and gases through the atmosphere based on equations of mass conservation and chemical reactions. NWP models and CTMs allow users to fine-tune model parameters and configurations related to meteorology and chemistry thereby providing tailored simulation results for specific research questions.

Fire emission inventories can be used as input in CTMs to investigate or forecast the impact of biomass burning emissions on the atmosphere and on air quality (e.g. Tie et al., 2007; In et al., 2009), to study the chemical or physical processes taking place after emission (e.g. Jost, 2003; Su et al., 2017) and to evaluate fire emission inventories or the underlying EO data themselves (e.g. Baldassarre et al., 2015; Ichoku et al., 2016; Reddington et al., 2016, 2019).

This approach to assess the performance of fire emission inventories is one of the only methods generally available to assess their quantitative accuracy. However, the use of CTMs for emission inventory evaluation and validation introduces significant sources of uncertainty when model results are compared to observations. The evolution of concentration fields and the final simulation output of a CTM will be impacted by several experimental choices and model features which are discussed here.

### 2.5.1.1 NWP Model and CTM Model Selection

There are many open access CTMs available for carrying out AQ simulations, each of which will generate simulation results with variations in modelled concentration fields. The variation in model output will largely be dependent on the complexity of the model and the various assumptions made in representing components of the atmospheric system (Derwent et al., 2010).

As mentioned above, AQ models consist of a NWP model coupled to a CTM and how these models are coupled can be realised in two ways – *on-line* or *off-line*. Off-line modelling (or one-way interactive models) consist of a CTM which is driven by meteorological input data that have been pre-produced by a NPW model whereas in on-line modelling systems (or two-way interactive models) there is a two-way feedback between the NWP model and the CTM at designated model time-steps. The schematic in **Figure 2.11** details these two different approaches to model coupling. On-line chemistry allows for the consideration of air pollution feedbacks such as from aerosol and greenhouse gases on meteorological processes and climate forcing (Li et al., 2017) thereby providing improved representations of modelled concentrations. However, online coupled models require substantially higher computational resources, and this can be a determining factor in the selection of which AQ model is used.

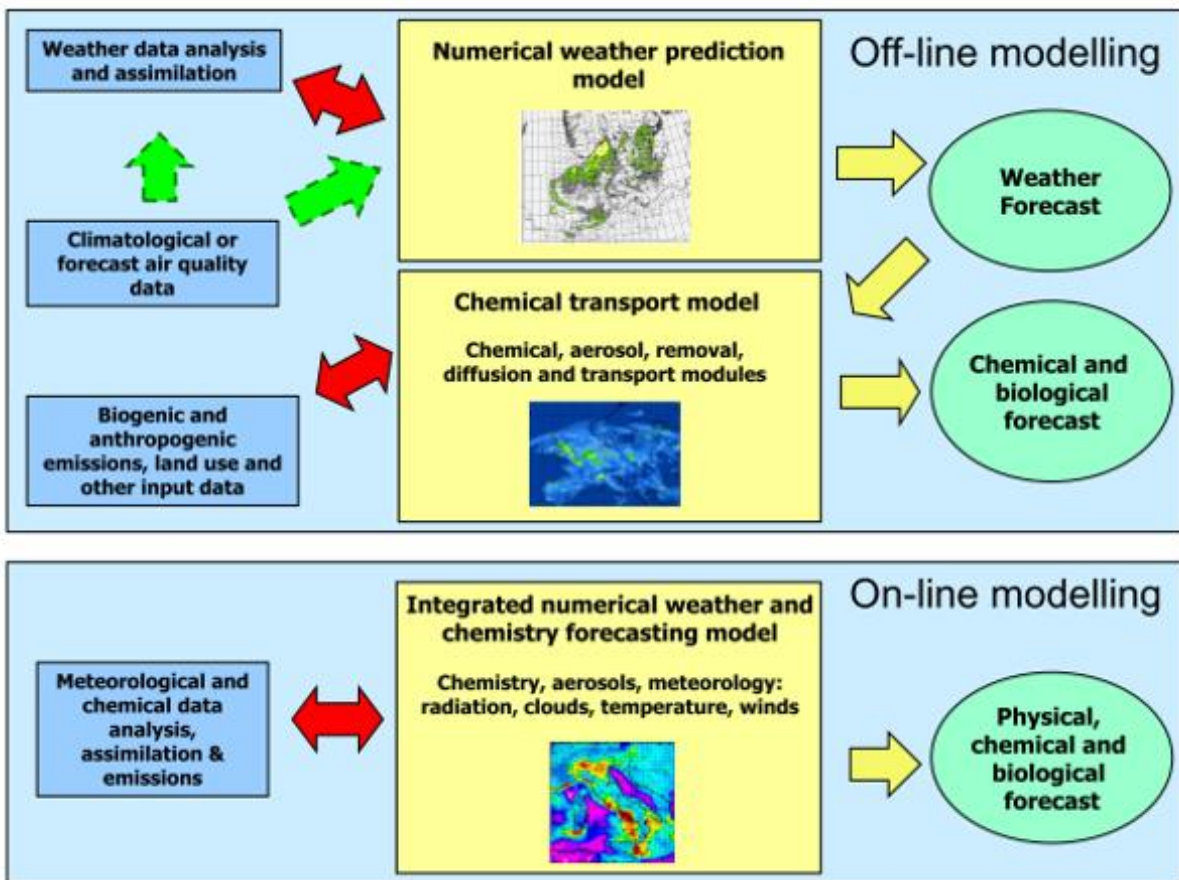


**Figure 2.11** Schematic describing the different approaches to NWP and CTM coupling in on-line and off-line modelling systems (Kukkonen et al., 2012)

One on-line model commonly used in air quality research is the WRF-Chem model (e.g. Yang et al., 2013; Kochanski et al., 2016; van der Velde et al., 2020), and off-line models commonly used include WRF-CMAQ (e.g. Cheng et al., 2014; Baldassarre et al., 2015; Vongruang et al., 2017) and GEOS-Chem (Henze et al., n.d.; Chen et al., 2009; Zhang et al., 2011). A review of modelling systems used operationally in Europe is presented in Kukkonen et al. (2012) along with a detailed investigation into the sensitivities, uncertainties and biases of these various different models, and the average impact these have on simulated concentrations.

### **2.5.1.2 Model Configuration and Domain Set-up**

Further to the choice of specific NWP model and CTM used, the parameterisation schemes selected for various physical and chemical processes in the two models introduces a further source of variation in simulated model output. In the case of the NWP model these processes include the selection scheme to use for cloud microphysics, convective parameterisation and planetary boundary layer (PBL) behaviour, while in the CTM these include schemes for dry and wet deposition, diffusion as well as the chemical package and aerosol package used. The latter two respectively determine the set of chemical reaction equations that are applied in the model, and the representation of aerosols in terms of their size distribution and microphysical processes including aggregation, nucleation, and chemistry (Binkowski, 1999). The performance of a specific NWP model configuration can be especially dependant on the validation study region, for example, a specific set of meteorological schemes will be suitable for a domain in the tropics but not a domain in northern Europe. Similarly, the specific chemical or aerosol species that are of interest may have improved representation in one chemical/aerosol scheme than another. As with the on-line and off-line nature of the NWP-CTM coupling, the complexity of the schemes selected will impact the computational resources required to run simulations, as will the size of the model domain in terms of grid cells and vertical layers.

### **2.5.1.3 Initial and Boundary Conditions**

In most regional AQ models initial conditions (IC) for meteorology (for the NWP model) and chemistry (for the CTM) must be provided in the first simulation time-step and boundary conditions (BC) must be provided to determine the flux of material and energy in and out of the model domain throughout the simulation. The source of IC and BC for both the meteorology and chemistry tend to be taken from global weather or chemistry models which have a lower spatio-temporal resolution than the final NWP-CTM model output. IC and BC for meteorology may be taken from global weather datasets such as the NCEP FNL reanalysis (<https://rda.ucar.edu/datasets/ds083.2/>) or the ECMWF ERA5 reanalysis (<https://www.ecmwf.int/en/forecasts/datasets/reanalysis-datasets/era5>), while IC and BC for chemistry may use datasets such as WACCM (<https://www2.acom.ucar.edu/gcm/waccm>) or

the previously mentioned ECMWF EAC4 reanalysis. Since these global models differ between each other, the selection of which global dataset is used for ICs and BCs will influence the results generated by the NWP-CTM coupled model, particularly in the earlier model time-steps.

#### **2.5.1.4 Non-fire Emission Inventories**

Whether the focus of an AQ modelling study is to investigate urban pollution, agricultural burning or any other pollution episode, all potential sources of gas and aerosol emissions in the domain must be accounted for. This is especially important when model results are compared with observations, since observed concentration fields will measure the pollutants from all sources. As with fire emission inventories, there are a number of anthropogenic, biogenic and dust emissions inventories available and the selection of each will impact the magnitude and spatio-temporal distribution of gases and aerosols modelled by the CTM. For example, dust emissions will influence model estimates of AOD and CO pollution from industry will contribute to measured CO values in some areas.

#### **2.5.2 CTMs for Fire Emissions Evaluations**

In the evaluation of fire emissions inventories, despite the limitations and sources of uncertainty described above, atmospheric modelling provides the only method available to compare estimated fire emissions with observations of emissions. In general, fire emissions inventories are used as input in a CTM and the simulation results are compared with satellite-based or ground based observations of, for example, AOD, CO and/or PM<sub>2.5</sub>. Several studies that apply this method of fire emission inventory assessment are described below.

In a comparative study of GFASv1.1, GFASv1.0, and emissions derived from the Wildfire Automated Biomass Burning Algorithm (WF\_ABBA) and the SEVIRI FRP-PIXEL product, WRF-CMAQ was used to simulate changes in AOD caused by a large forest fire near Antalya in 2009 (Baldassarre et al., 2015). Simulation results were compared to MODIS 10 km AOD observations and CO and NH<sub>3</sub> observations from the Infrared Atmospheric Sounding Interferometer (IASI). The work highlighted the importance of correct emission estimates not

only in terms of the magnitude of emissions but also in terms of their temporal structure and vertical distribution in order to accurately replicate AOD observations. A comparison of the WRF-CMAQ modelled AOD fields using these different fire emissions inputs compared to MODIS AOD measures is shown in **Figure 2.12**.

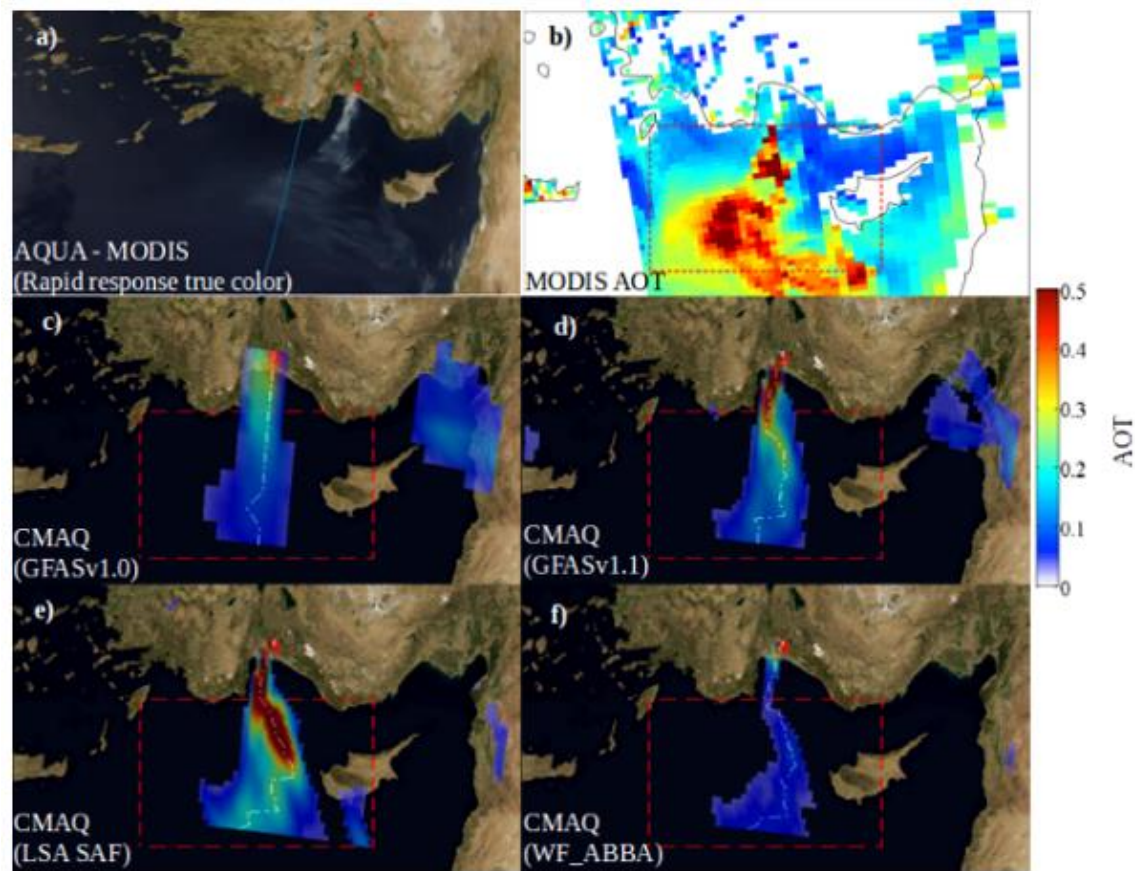


**Figure 2.12** GFASv1.0, GFASv1.1, SEVIRI FRP-PIXEL based and SEVIRI WF\_ABBA based fire emissions used as input in CMAQ compared with MODIS true colour imagery and MODIS AOD observations of smoke resulting from a fire near Antalya on 1<sup>st</sup> August 2008 at 14:30 UTC.

The GFAS fire emissions inventory described in **Section 2.4.1.2** is detailed in Kaiser et al. (2012) and in that work GFAS is used as input in the ECMWF MACC modelling system. The results from these simulations are compared to MODIS AOD as part of the evaluation procedure for the inventory. Kaiser et al. (2012) find that GFAS underestimates aerosols by a factor of between 2.2 and 4.1 (depending on region) compared to 10 km MODIS AOD observations and recommend GFAS emissions be multiplied by a region-averaged factor of 3.4 before being used as input in atmospheric modelling.

The FEERv1 top-down emission inventory described in **Section 2.4.2.1** is evaluated against 10 km MODIS AOD in Northern Sub-Saharan Africa (NSSA) by comparing AOD observations with WRF-Chem model results which used FEER fire emissions as input (Ichoku et al., 2016). Comparisons showed severe underestimation of modelled AOD compared to satellite observations and the work highlights the sometimes contradictory conclusions of different studies which confuse the identification of the main source of uncertainty in such assessments - emissions, model error or the modelled geographic region (Ichoku et al., 2016).

One study compares the emissions estimates of seven different fire emission inventories over the NSSA region using WRF-Chem (Zhang et al., 2014), four of which have been discussed in detail in **Section 2.4**. The emissions inventories used in that study are summarised in **Table 2.2**, and simulated organic carbon (OC), black carbon (BC) and PM<sub>2.5</sub> fields using each inventory as input in WRF-Chem are shown in **Figure 2.13**. **Figure 2.13** demonstrates the large differences between emission inventories both in terms of localised emissions estimates, and overall magnitudes. Indeed, Zhang et al. (2014) show that over the modelled domain total smoke emissions in February 2010 vary by up to a factor of 7 and at local scales this increases to factors of up to 33. They show that the uncertainties in fire emissions have the largest impact on modelled atmospheric composition at local and hourly-to-daily scales, highlighting the need for the mitigation of these uncertainties, particularly in regions of high fire activity.

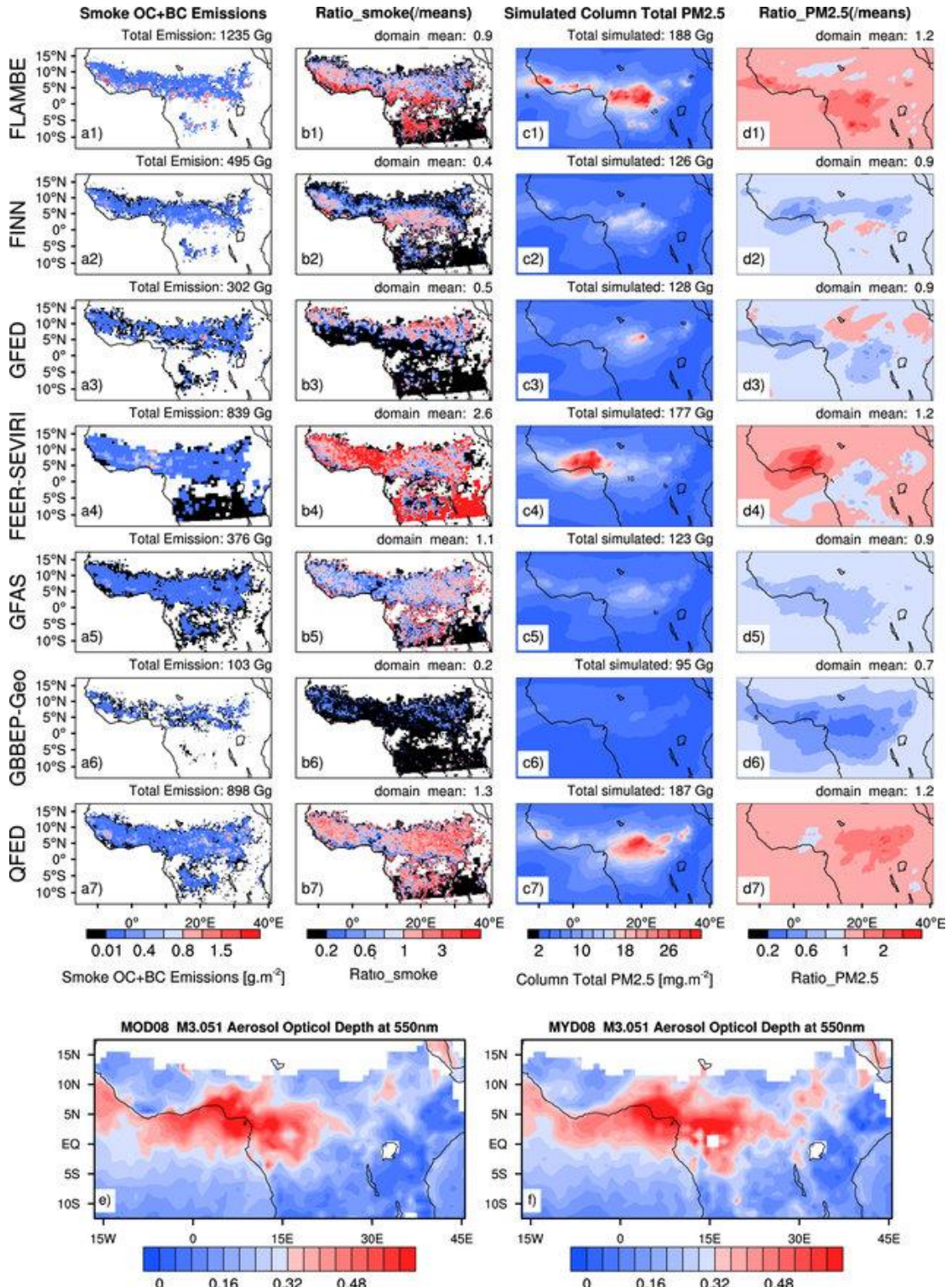


**Figure 2.13** Comparisons between FLAMBE, FINNv1.0, GFEDv3.1, FEER-SEVIRIv1.0, GFASv1.0, GBBEP-Geo and QFEDv2.4 for (a1-a7) monthly total smoke OC+BC emissions (unit:  $\text{g m}^{-2}$ ) during February 2010; (b1-b7) the ratio of individual smoke emissions to their means among different inventories; (c1-c7) February mean column total PM2.5 (unit:  $\text{mg m}^{-2}$ ); (d1-d7) the ratio of PM2.5 from different emission inventories to their means simulated by WRF-Chem. (e and f) MODIS AOD (from Terra and Aqua) at 550 nm as plotted within the NASA Giovanni. Taken from (Zhang et al., 2014)

## 2.6 Summary and Research Objectives

This overview of the current state-of-the-art in fire emission estimation using satellite remote sensing has highlighted some of the key uncertainties and limitations that are relevant in current approaches. The physical principles on which the two main fire detection and quantification methods – BA and AF/FRP - are based were described in **Section 2.2** along with the limitations of each of these approaches. Alternative fire-related variables that can be determined via remote sensing were also briefly highlighted. **Section 2.3** discussed the satellite platforms and specific sensors used in the satellite based detection of fire and provided further detail on the benefits and disadvantages of polar-orbiting and geostationary based data sources, key of which are related to the spatial and temporal limitations of each. Methods which have been proposed to merge these different data types were also discussed in this section. Approaches used in the transformation of remote sensing BA, AF and FRP measurements into actual estimates of fire emitted gas and aerosol species were detailed in **Section 2.4**. This section presented several specific bottom-up and top-down fire emissions inventories and described the specific satellite datasets they use and the main sources of uncertainty in each, thereby highlighting the potential sources for difference between emissions inventories. Finally, **Section 2.5** discussed how fire emissions inventories can be evaluated using atmospheric modelling and independent ground-based or satellite-based observations of fire-related variables. This section provided an overview of some key features of atmospheric models which pertain to the simulation results used in emission inventory assessment. The body of research discussed in this section demonstrates that, despite being the only available method of assessment, atmospheric modelling of fire emissions introduces further uncertainty into estimates of fire generated gas and aerosol concentrations.

Based on this review, a clear area for further research is the mitigation of uncertainty in current fire emission inventories. The spatial and temporal resolution of satellite products play a key part in variations between emissions estimates, and this includes active fire methods that are the only ones capable of providing real-time information. Though several works have identified the impact of sensor viewing geometry on fire detection performance for polar-

orbiting sensors, limited work has been done on characterizing the impact of sensor geometry on fire detection in geostationary based active fire products. Top-down approaches to fire emission estimation that eliminate the use of parameters such as fuel load and combustion completeness or a FRE-to- $FC_T$  conversion factor have been proposed using both polar-orbiter based (FEER) and geostationary based (FREM) FRP datasets. However, these top-down approaches apply a MODIS AOD product, which in fact appears to have limited suitability in analysing fire generated smoke plumes.

Based on this information, the specific research objectives of this thesis are as follows:

**Objective 1:** To investigate the impact of sensor view zenith angle (VZA) on the detection of AF and characterization of FRP in geostationary satellite active fire products – specifically the FRP-PIXEL product generate by the two SEVIRI sensors operating onboard Meteosat-11 (MSG) and Meteosat-8 (MSG-IODC) which image Africa from different locations using different view zenith angles (addressed in **Chapter 3**).

**Objective 2:** To develop methodological improvements to the FREM top-down approach for landscape fire emissions estimation (Mota and Wooster, 2018) which address its key sources of uncertainty and limitations, and to apply these developments to produce an updated fire emission inventory for Africa (addressed in **Chapter 4**).

**Objective 3:** To conduct an evaluation of the fire emission inventory developed in Chapter 4 via its use within a chemical transport model (CTM) and comparison of the output simulated atmospheric fields with independent ground-based and satellite-based data (addressed in **Chapter 5**).

# Chapter 3 Assessing the View Zenith Angle (VZA) and Vegetation Dependencies of Meteosat SEVIRI FRP Retrievals

## 3.1 Introduction

This Chapter presents an evaluation of the active fire (AF) detections and Fire Radiative Power (FRP) retrievals made in the SEVIRI FRP-PIXEL product from Meteosat-11 and Meteosat-8 (Indian Ocean Data Coverage; IODC), which are different versions of the Meteosat Second Generation (MSG) satellite. These FRP retrievals are contained within the Meteosat FRP-PIXEL products being produced operationally from both systems by the EUMETSAT LSA SAF (<https://landsaf.ipma.pt/>). In this Chapter they are compared both against each other and against the MODIS MYD14/MOD14 Active Fire products. The near simultaneous data from Meteosat-11 and Meteosat-8 are used to investigate the impact and interaction of vegetation type and view zenith angle (VZA) on the detection of AF pixels and the characterisation of their FRP, both at the locations individual fires and at the regional scale. A key aim is to identify the factors that should be considered when developing a coherent and consistent FRP dataset from multiple geostationary platforms.

Geostationary satellites offer the highest temporal resolution available for AF detection. Imaging sensors aboard operational satellites such as GOES, Himawari-8 and Meteosat-11 provide full disk images at between 10- and 15-minute resolution (see **Section 2.3.2**). The suite of geostationary imaging instruments centred over different equatorial locations around the globe offers the opportunity to produce a combined, high-temporal resolution global (or near global since high latitudes are not well viewed) dataset – providing satellite-based monitoring

of both fire and a suite of other environmental parameters. For example, the Satellite ClOud and Radiation Property retrieval System (SatCORPS) provided by NASA produces global geostationary retrievals of cloud properties at an hourly resolution (<https://satcorps.larc.nasa.gov/>). A key challenge in generating this type of dataset is integrating the observations of products from different instruments, on different platforms, and accurately accounting for their individual biases. This is particularly important for AF characterisation, where other natural factors affect the retrieval of FRP at different locations. For example, the vegetation type being burned, cloud cover, and the time of day, or year. These are in addition to sensor or product specific attributes such as the sensor spatial resolution and the AF detection and FRP retrieval algorithm itself (see **Section 2.2**).

The AF detection products derived from the measurements of the SEVIRI sensor aboard Meteosat-11 are vital in monitoring biomass burning over Europe, Africa and the Middle East. First launched in 2002, the SEVIRI radiometer measures radiances and/or brightness temperature in eleven spectral channels, ranging from  $0.6 \mu\text{m}$  to  $14 \mu\text{m}$  (Aminou et al., 1997). With a view of Africa - the most fire intense continent on the planet - SEVIRI is optimally positioned to contribute significantly to global fire monitoring. Several AF detection algorithms have been developed to characterise fires from raw SEVIRI brightness temperature measurements (Prins et al., 1998; Joro et al., 2008; Amraoui et al., 2010). The most commonly used, with the best performance (Roberts et al., 2015), is the SEVIRI FRP-PIXEL product (Roberts and Wooster, 2008; Wooster et al., 2015). Once AFs have been detected and confirmed by the Fire Thermal Anomaly (FTA) detection algorithm (Roberts et al., 2005), their FRP is retrieved using the MIR radiance method of Wooster et al. (2003, 2005) described in **Section 2.2.2**.

A number of evaluations of the FTA and MIR radiance FRP retrieval algorithms as applied to Meteosat SEVIRI have been conducted (Wooster et al., 2005; Roberts and Wooster, 2008; Freeborn et al., 2014; LSA SAF, 2015; Roberts et al., 2015; Hall et al., 2019) in all cases using SEVIRI data from the MSG satellite positioned over  $0^\circ \text{N}$ ,  $0^\circ \text{E}$ . Different Meteosat satellites have taken up this position over the lifetime of the MSG mission, and currently Meteosat-11 provides the operational full disk service from this location (with Meteosat-12 waiting in orbit as a backup in case failure should occur).

In October 2016 the first of the MSG series (Meteosat-8) which had provided the operational full disk service from 2004 was moved out of its then position into a new location over the Indian Ocean. The SEVIRI FRP-PIXEL product for this new ‘Indian Ocean Data Coverage’ (IODC) location ( $0^{\circ}$  N,  $41.5^{\circ}$  E) became operational from February 2017, whilst Meteosat-11 continued to generate the same FRP-PIXEL product from its location at  $0^{\circ}$  N,  $0^{\circ}$  E. The SEVIRI instrument aboard both satellites image the whole of Africa from different view zenith angles. A true colour image showing the full disk view of SEVIRI aboard both Meteosat-11 and Meteosat-8 is shown in **Figure 3.1**.

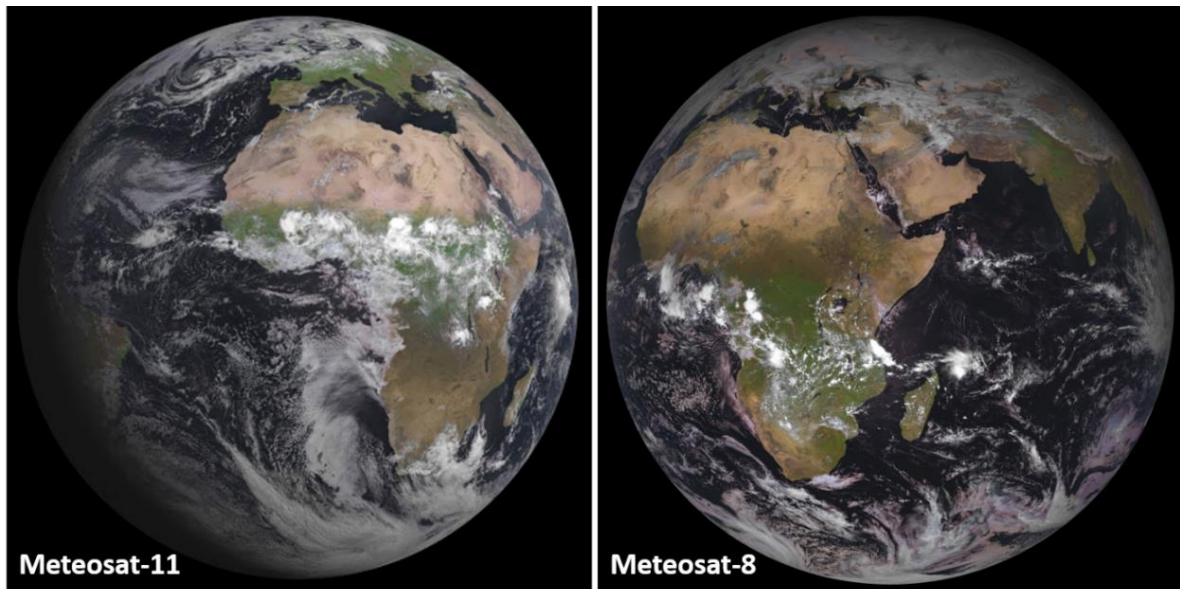


**Figure 3.1** True colour image taken by the SEVIRI sensors operating aboard Meteosat-11 (Left) and Meteosat-8 (right) - showing the full disk imagery collected from their respective positions centred over  $0^{\circ}$  N,  $0^{\circ}$  E and  $0^{\circ}$  N,  $41.5^{\circ}$  E. (Images adapted from EUMETSAT: <https://www.eumetsat.int/website/home/>).

The new position of Meteosat-8 and the occurrence of two near identical instruments whose data are used to produce the same FRP-PIXEL product using the same algorithm allows for the first time the possibility to simultaneously observe fires burning in Africa from different viewing angles with the same sensor (**Figure 3.1**). As discussed in **Chapter 2**, pixel footprint area is a limiting factor in AF detection and FRP estimation (Freeborn et al., 2011, 2014; Kumar et al., 2011). The size of the minimum detectable AF increases with pixel area, and pixel footprint area increases non-linearly with view zenith angle (VZA) for both geostationary and

polar-orbiting sensors. For example, MODIS pixel areas at the edge of the swath (close to 65° VZA) increase by up to 8 times compared to nadir and overlap by up to 50% in the along-track direction (Masuoka et al., 1998; Wolfe et al., 1998) - a feature known as the MODIS ‘bow-tie’ effect. **Figure 3.2** shows the growth in SEVIRI pixel area as a function of VZA, showing that the pixel area almost triples at VZA > 70° and even at VZA of around 30° there is roughly a 25% increase in pixel area.

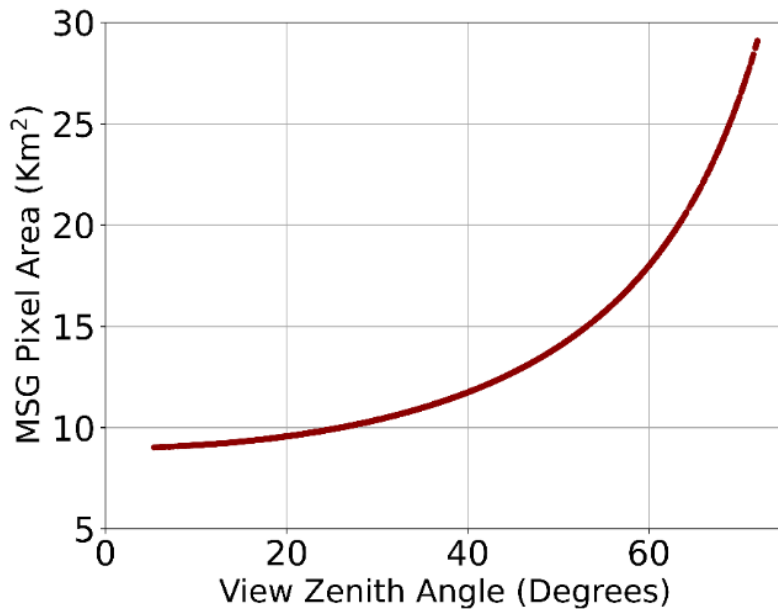


**Figure 3.2** Growth in SEVIRI pixel footprint area as a function of VZA as assumed in the FRP-PIXEL product algorithm detailed in Wooster et al. (2015) which is used to generate the Met-8 and Met-11 FRP-PIXEL products analysed herein. The data for this plot were derived from the AF pixels in the Met-11 SEVIRI FRP-PIXEL products collected between 1<sup>st</sup> January and 31<sup>st</sup> December 2018.

As described in **Chapter 2** the amount of vegetation being burned strongly influences the radiative output of a fire due to the fuel available for combustion, and indeed FRP measurements are used to estimate the rate of fuel consumption as was discussed in **Section 2.4**. The type of vegetation also impacts the measurement of FRP from satellite sensors, for example tree canopy cover can intercept radiation emitted by surface fires (Freeborn et al., 2014; Roberts et al., 2018). Despite biome and VZA having an impact on FRP measurements (Crutzen and Andreae, 1990; Andreae and Merlet, 2001; Heil et al., 2010; Freeborn et al., 2011, 2014), limited work has focused on this topic in the scope of geostationary sensors, and very little on the combined effect and possible interaction of these impacts in general.

This Chapter will be the first to provide an evaluation of the Meteosat-8 SEVIRI FRP-PIXEL product and compare its FRP data to those from Meteosat-11 and MODIS. It aims primarily to identify significant differences between the SEVIRI FRP-PIXEL products coming from Meteosat-8 and Meteosat-11 in terms of their characterisation of fire over Africa, particularly with respect to VZA and vegetation type.

## 3.2 Methodology

### 3.2.1 Datasets

Three satellite products were compared over the period 1<sup>st</sup> January 2018 to 31<sup>st</sup> December 2018:

- The operational Indian Ocean Data Coverage (IODC) SEVIRI FRP-PIXEL product, which is available from the EUMETSAT LSA SAF archive (<https://landsaf.ipma.pt/en/>) and which is generated from SEVIRI aboard Meteosat-8 having a sub-satellite position of (0° N, 41.5° E). This dataset has a nadir pixel sampling distance (spatial resolution) of 3 km, a temporal resolution of 15 minutes, and is hereafter referred to as M8.
- The operational ‘standard’ MSG SEVIRI FRP-PIXEL product also available from the EUMETSAT LSA SAF archive which is generated from SEVIRI aboard Meteosat-11, having the same spatio-temporal resolution as M8 (3 km at nadir; 15 minute) but from a sub-satellite nadir position of (0° N, 0° E). This product is hereafter referred to as M11.
- The Level 2 Collection 6 MOD14/MYD14 Active Fire Product, generated using data collected by the MODIS instruments onboard both Terra and Aqua (Giglio et al., 2016) available from <https://earthdata.nasa.gov/>. These products include the detection of AF pixels and their FRP retrieval, the latter performed using the same MIR radiance method as used in the Meteosat FRP-Pixel products (Wooster et al., 2003). The MOD14/MYD14 product comprises two daytime and two night-time observations, made at approximately 10:30 and 22:30 (Terra) and 13:30 and 02:30 (Aqua) local solar time (these are the equatorial crossing times and the actual solar time of the observation at any particular latitude depends on e.g. its location within the MODIS swath) at a spatial resolution of 1 km at nadir. The selection of the MOD14/MYD14 fire products as a ‘benchmark’ dataset for

comparisons against the two SEVIRI FRP products was based on (i) the existence of a number of validation studies comparing the SEVIRI FRP-PIXEL product (from the current location of Meteosat-11) to these MODIS AF products (Roberts et al., 2005, 2015; Calle et al., 2008; Roberts and Wooster, 2008; Freeborn et al., 2014) (ii) the validation studies of the MODIS AF product itself (Morisette et al., 2005; Schroeder et al., 2008; Giglio et al., 2016) and (iii) the common use of the MODIS products in fire emission inventories such as GFAS (Kaiser et al., 2012), FINN (Wiedinmyer et al., 2011) and FLAMBE (Reid et al., 2009b). To account for the impact of the MODIS sensor's 'bow-tie' effect on AF detection at wide swath angles (detailed by Schroeder et al., 2008; Freeborn et al., 2011; Kumar et al., 2011; Giglio et al., 2016), the MODIS AF detections used in the comparisons in this study were limited to those at  $VZA \leq 18.3^\circ$ . The fire detection performance of MODIS within this VZA range has been well characterised using comparisons against simultaneously acquired very high spatial resolution ASTER observations (Morisette et al., 2005; Csiszar et al., 2006), and a similar VZA restriction was applied to MODIS AF data in Freeborn et al. (2014). The MODIS-retrievals of FRP were adjusted for the atmospheric attenuation of the fire-emitted thermal signal using the same procedure conducted in the SEVIRI FRP-PIXEL algorithm (Wooster et al., 2015). Essentially, the atmospheric transmittance of the atmospheric path between each fire and the MODIS sensor was calculated using MODTRAN-5 (Berk et al., 2004) and the Total Column Water Vapor (TCWV) field from the ECMWF ERA-Interim reanalysis (<https://apps.ecmwf.int/datasets/data>). The full procedure is detailed in Wooster et al. (2015).

### 3.2.2 Study Region and Biome Classification

The primary focus of this thesis is on African fires, and therefore the FRP observations from SEVIRI were limited to the region of interest shown in red in **Figure 3.3a**. The sub-satellite location of Meteosat-11 and Meteosat-8 and the expected VZA bounds for the SEVIRI sensor aboard each satellite are also shown. To investigate the relationship between FRP measurements and vegetation type, a biome map of Africa was produced using the ESA Climate Change Initiative (CCI) Landcover map (<http://maps.elie.ucl.ac.be/CCI/>). The ESA

CCI landcover map is derived from PROBA-V observations, that have a spatial resolution of 300 m. Analogous to the biome classification described in **Chapter 4**, landcover classes over Africa were aggregated into five distinct vegetation types (excluding bare area, urban area and water bodies) from the 36 original CCI landcover classes - these are *grassland*, *shrubland*, *woodland savanna*, *managed land* and *closed canopy forest*. It has been shown that FRP measurements from fires in closed canopy forest and certain woodland savannas can be affected by tree canopy interception of surface-emitted FRP (Freeborn et al., 2009, 2014; Roberts et al., 2018). So, to further stratify the five vegetation types with respect to tree cover, the woodland savanna biome was separated into two classes based on percentage tree cover (above 5 m height). Percentage tree cover was taken from the 30 m spatial resolution Landsat Vegetation Continuity Fields (VCF) product for 2015 (<https://lcluc.umd.edu/metadata/global-30m-landsat-tree-canopy-version-4>). The woodland savanna biome was separated into *high-woodland savanna* (percentage tree cover > 20%) and *low-woodland savanna* (percentage tree cover < 20%). These biomes were mapped to a  $0.5^\circ \times 0.5^\circ$  grid, and their spatial distribution is shown in **Figure 3.3b**.

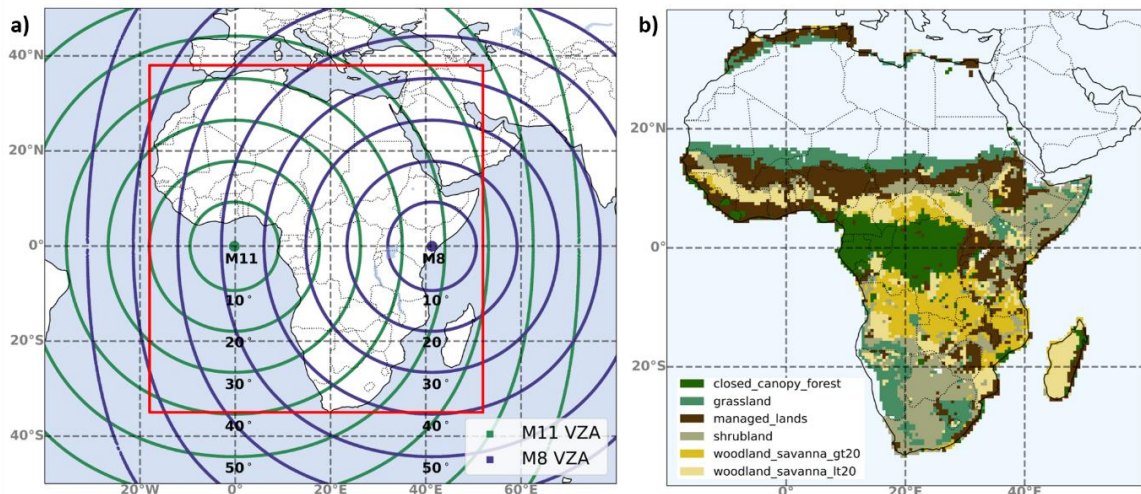


**Figure 3.3** (a) Region of interest (outlined in red) within which MODIS and SEVIRI observations were limited to in this study. Also shown are the nadir positions of the SEVIRI sensor operating aboard Meteosat-8 and Meteosat-11, and the spatial distribution of VZA for each. (b)  $0.5^\circ \times 0.5^\circ$  gridded vegetation map derived from CCI Landcover (from 300m PROBA-V measures) and 30 m Landsat VCF percentage tree cover above 5 m as detailed in **Section 3.2.2**.

### 3.2.3 M8 and M11 Validation with MODIS

For each MODIS MOD14/MYD14 granule available over the study period, a subset of concurrent and co-located SEVIRI AF pixels was identified by temporally and spatially filtering the FRP-PIXEL Products' AF pixels to only include those that (i) were acquired within  $\pm 5$  minutes of the MODIS overpass and (ii) were spatially located within the convex hull of available MODIS AF pixels. This spatial filtering method, (ii), is discussed further in **Section 3.3.4**. Each subset of M8, M11 and MODIS AF pixels were then used firstly to assess the AF detection performance of the M8 and M11 products against MODIS-detected active fires, and secondly to compare FRP measurements of each SEVIRI product against MODIS FRP via three different comparison methods.

#### 3.2.3.1 Active Fire Detection performance

To assess the AF detection performance of M11 and M8, the values for the errors of commission and errors of omission were calculated relative to detected MODIS AF pixels. This was carried out using an adapted version of the method of Freeborn et al. (2014). In previous validations, SEVIRI pixels were matched to MODIS by remapping MODIS pixels to the image coordinates of the SEVIRI disk at a fixed sub-satellite position (Freeborn et al., 2014; Roberts et al., 2015). The centre latitude and longitude of each MODIS pixel was assigned to a SEVIRI pixel based on its inclusion in the ground footprint of the SEVIRI thermal pixel. Due to the higher spatial resolution of the MODIS product, several MODIS AF pixels may be assigned to the same SEVIRI pixel.

Initial exploration of M8 data found that unlike the newer Meteosat-11, which is relatively stable in its orbit, the older Meteosat-8 is prone to drift from its designated nadir position at  $0^{\circ}\text{N}$ ,  $41.5^{\circ}\text{E}$ . **Figure 3.4** shows the variation in the Meteosat-8 nadir position in 2018. The geographic nadir coordinates shown in **Figure 3.4** were derived from close-to-nadir AF pixels –M8 AF pixels from 2018 with  $\text{VZA} < 0.5^{\circ}$  were collated and their average pixel centre latitude and longitude values were assumed to approximate the daily Meteosat-8 nadir position. Over the year, the longitude of the Meteosat-8 nadir position varies only slightly - by up to a degree, however the latitude of the nadir position varies much more substantially by up to  $10^{\circ}$ . A

small portion of this variation can be attributed to the locations of the 'nadir' pixels (with VZA  $< 0.5^\circ$ ) used to determine the nadir position, but a significant drift in the satellite position is still clear. Nadir position plots cannot be replicated by this method for Meteosat-11 data due to the sub-satellite position being stationed over ocean, where no AF pixels exist.

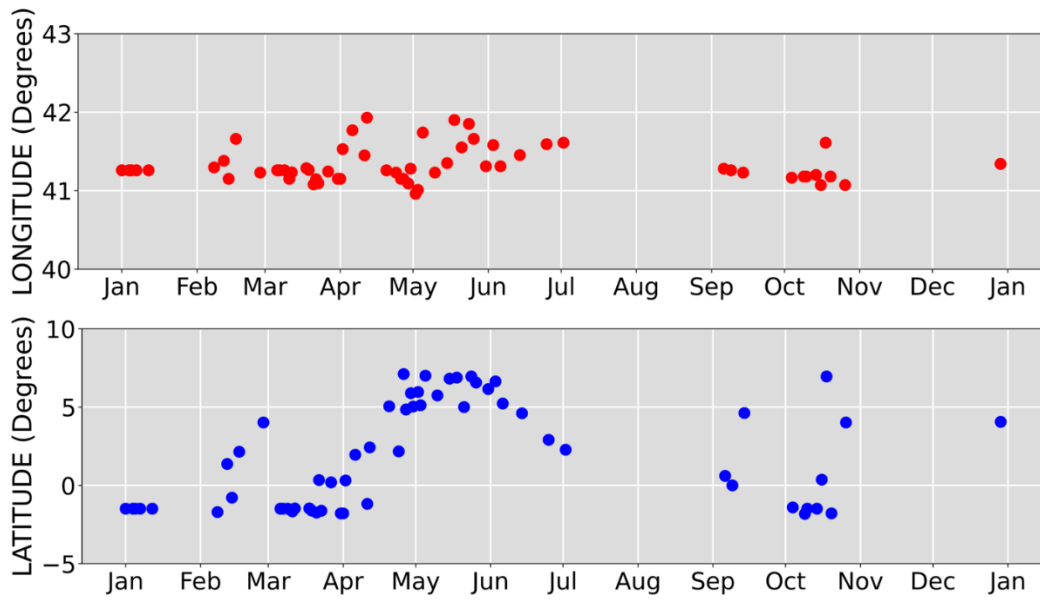


**Figure 3.4** Mean latitude and longitude of nadir pixels in the M8 SEVIRI FRP product during 2018, calculated from close-to-nadir AF pixels (VZA  $< 0.5^\circ$ ). These data show a significant latitudinal shift of the satellite view occurs over the year, resulting in the nadir position varying by up to  $10^\circ$ .

The drift associated with M8 data is of importance with respect to an assessment of SEVIRI AF detection because MODIS pixels mapped to a stationary SEVIRI Meteosat-8 grid cannot be compared directly to the image coordinates of the actual M8 FRP pixels, due to this drifting of Meteosat-8 nadir. To address this, the AF detection performance evaluation and per-fire FRP comparison described in **Section 3.2.3.2** map both MODIS AF pixels and M8 AF pixels to an 'ideal' stationary Meteosat-8 SEVIRI image centred at ( $0^\circ$ N,  $41.5^\circ$ E). Searches for matching AF pixels between M8 and MODIS were carried out relative to their ideal M8 SEVIRI disk coordinates.

Despite the remapping described above - when applied to a stationary SEVIRI disk - the designation of a fire location is still uncertain to some extent due to the differing pixel shape, orientation and overlap of the point spread function and instantaneous geometric field of view (IGFOV) of both instruments (Freeborn et al., 2014; Roberts et al., 2015). To reduce the impact of these effects on the spatial accuracy and the calculations of the errors of commission and omission, a  $3 \times 3$ -pixel window was used when searching for matching SEVIRI AF and MODIS AF pixels. A correct or false detection was then confirmed based on the presence or absence of a match between pixels from the two fire products within this  $3 \times 3$  window. **Figure 3.5** illustrates the three possible classifications – correct detections, errors of omission and errors of commission - and how they were assigned. This AF detection performance analysis was carried out for both M8 and M11 pixels against the MODIS AF product, with percentages of each type of error calculated for each SEVIRI product over the study period.

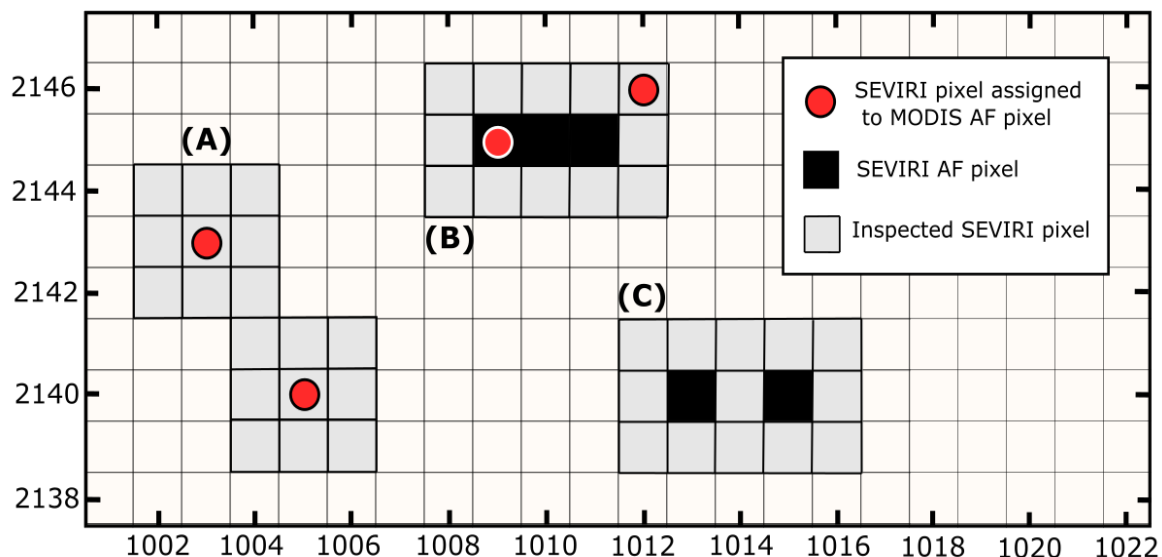


**Figure 3.5** Schematic showing the three potential AF pixel classifications in the detection performance analysis conducted herein, and how they were classified. A) errors of omission – no SEVIRI AF pixels were detected within a  $3 \times 3$  pixel window surrounding a MODIS AF pixel B) correct detections – a SEVIRI AF pixel is detected at or within the  $3 \times 3$  pixel window surrounding a MODIS AF pixel and C) errors of commission – no MODIS AF pixels were detected within  $3 \times 3$  pixels of a SEVIRI AF pixel. The axes in this diagram represent the image line and columns of the SEVIRI full disk image.

### 3.2.3.2 FRP Measurement Analysis

The spatio-temporally filtered subsets of M8, M11 and MODIS FRP pixels for each MODIS granule were compared in terms of AF pixel counts and FRP via three comparison methods:

- Total Areal – all FRP pixels in the spatio-temporal subset were summed to get the total pixel count and total FRP observed by each fire product at that given time over the spatial extent of the MODIS granule.
- Per-Area – all FRP pixels in the spatio-temporal subset were mapped to a  $0.5^\circ \times 0.5^\circ$  grid based on their geographic pixel centres, total pixel counts and FRP were calculated for each individual grid cell for each fire product.
- Per-Fire – all FRP pixels in the spatio-temporal subset were passed through a clustering algorithm to identify individual fires. A fire was defined as a group of coincidental and spatially contiguous AF pixels. Fire clusters were matched between sensors and the pixel count and total FRP for each matched cluster was calculated for each fire product. The method used to cluster FRP pixels into fires in per-fire comparisons applies a similar method to that first used by Roberts et al. (2005) and later by others (Zhukov et al., 2006; Roberts and Wooster, 2008; Xu et al., 2010). As in the procedure for calculating errors of AF detection omission and commission, MODIS pixels were mapped to the SEVIRI disk and for comparisons with M8, SEVIRI pixels were also mapped to the ideal Meteosat-8 disk, centred at  $0^\circ$  N,  $41.5^\circ$ E (see **Section 3.2.3.1**). Due to its higher spatial resolution, multiple MODIS AF pixels could fall within a single SEVIRI disk AF pixel footprint. In these cases where MODIS AF pixels were summed and total pixel counts and FRP values were propagated. A connected component labelling algorithm (Wu et al., 2005) was then used to identify contiguous groups of pixels in each satellite product. Once individual clusters have been identified from each product independently, fire clusters were matched between products based on the overlap between clusters expanded by a pixel wide buffer to account for geolocation offsets following Roberts and Wooster (2008). The FRP of an individual fire as observed by each satellite product was taken as the sum of the FRP from all AF pixels in that fire cluster and fire clusters were retained, only if a match between both AF products was found.

Least-squared best-fits with forced intercepts through zero were used to parameterise the relationship between the resulting data points generated using the above three methods. The coefficients and statistical measures from these regressions were used to evaluate the agreement between the MODIS and SEVIRI AF products. The data were also aggregated in time, and in the case of per-area comparisons, in space, to gain further insight into overall trends.

### 3.2.4 M8 and M11 Comparison

In addition to their evaluation against MODIS, M8 and M11 FRP measurements were directly compared against each other using the same three comparison methods; total areal, per-area and per-fire. The two SEVIRI products were compared at their native temporal resolutions and the pixels were spatially filtered to only those falling inside the region of interest (ROI) outlined in **Figure 3.3a**. In per-fire comparisons, the M8 pixel centre coordinates were mapped to the M11 SEVIRI disk matching fire clusters between the two products were identified via the same process as used in **Section 3.2.3.2**. Mean VZAs were calculated for each AF cluster and for each grid cell in per-fire and per-area companions respectively. In per-area comparisons the biome map described in **Section 3.2.2** and shown in **Figure 3.3b** was used to determine the majority vegetation type of each  $0.5^\circ \times 0.5^\circ$  grid cell.

### 3.2.5 VZA and Biome Effect on FRP

The simultaneous observation of FRP in the M11 and M8 FRP-PIXEL products allows measurements of the same fire, using the same sensor and detection algorithm, at a different VZA. Therefore, in theory, the differences in observed FRP between the two products at any given location should primarily be due to the differing pixel footprint characteristics at that location. To further investigate this hypothesis the interaction between VZA and FRP was considered in terms of VZA difference,  $VZA_{DIFF}$ , and FRP difference,  $FRP_{DIFF}$ . These were calculated for each  $0.5^\circ \times 0.5^\circ$  grid cell from per-area comparisons and for each fire cluster from per-fire comparisons as:

$$VZA_{DIFF} = VZA_{M8} - VZA_{M11} \quad [3.1]$$

$$FRP_{DIFF} = FRP_{M8} - FRP_{M11} \quad [3.2]$$

As defined above, if a grid cell or fire has a negative  $VZA_{DIFF}$  value, it is closer to the Meteosat-8 nadir position and a positive  $VZA_{DIFF}$  means it is closer to the Meteosat-11 nadir position. The closer a pixel is to nadir, the smaller the VZA and the smaller the pixel footprint area is (**Figure 3.2**), and because of the latter the lower the minimum FRP detection limit of that pixel. Negative  $FRP_{DIFF}$  values correspond to the FRP of that grid cell or fire being higher in the M11 product than the M8 product, whereas the opposite is true for positive values of  $FRP_{DIFF}$ . The distributions of these variables and least-squares fits between them were used to quantify the effect of VZA on FRP.

The biome map in **Figure 3.3b** was used to categorise the grid cells from per-area comparisons between M8 and MODIS, M11 and MODIS and also between M8 and M11 themselves. The statistical significance of the difference in the FRP values assessed in the six different biomes was evaluated using a Kruskal-Wallis H test, and least-squares best-fits were applied to biome subsets to examine how these vary. The Kruskal-Wallis H test was used because of the non-parametric nature of the FRP data statistics. The interaction between vegetation type, VZA and FRP was investigated, again using the variables of  $VZA_{DIFF}$  and  $FRP_{DIFF}$  to determine if there was a significant difference between the response of FRP to VZA in different biomes.

## 3.3 Results

### 3.3.1 M8 and M11 Validation using MODIS FRP

Results obtained in direct comparisons between the two SEVIRI FRP products and the MODIS FRP product are presented here and are compared to previous validation studies of the SEVRIRI FRP-PIXEL product. Validations of the SEVIRI FRP-PIXEL product have been conducted using FRP products other than MODIS (e.g. Hall et al., 2019), however the studies discussed here are limited to those that use the same MOD14/MYD14 AF products as were used in this study (Roberts et al., 2005, 2015; Roberts and Wooster, 2008; Freeborn et al., 2014; LSA SAF, 2015). Details of these past studies are shown in **Table 3.1**. The study period and geographic extent of the validation studies listed in **Table 3.1** vary, as do the VZA thresholds applied to MODIS FRP observations and the way which the FRP products are compared and the results reported (e.g. total areal, per-area or per fire). These variations are likely to impact to some extent the results obtained in each study, therefore direct comparisons of this study with previous works should be treated with care.

**Table 3.1** Summary of previous MODIS-based SEVIRI-FRP Pixel product evaluation studies, including their spatio-temporal extent and other characteristics of importance .

Study	MSG Satellite	Time period	Duration	Region	MODIS VZA limit (degrees)	Time window (minutes)
Roberts et al. 2005	Meteosat-8	September (2003)	4.5 days	Southern Africa	±45.0	±12
Roberts et al. 2008	Meteosat-8	May (2003)	6 days (2 nights)	Africa	±55.0	±6
Freeborn et al. 2014	Meteosat-9	October - April (2008/9)	6 months	Central African Republic	±18.3	±8
Roberts et al. 2015	Meteosat-9	August (2008)	1 month	Southern Africa	±30.0	±6
LSASAF 2015	Meteosat-11	July (2015)	1 month	Southern Africa	±30.0	±6
This work	Meteosat-8 & Meteosat-11	January - December (2018)	1 year	Africa	±18.3	±5

### 3.3.1.1 FRP Characterisation Analysis

All the MOD14 and MYD14 granules retrieved over the ROI (**Figure 3.3a**) for the period 1<sup>st</sup> January to 31<sup>st</sup> December 2018 were collated - totalling 8815 MYD14 granules and 8702 MYD14 granules. At 15-minute temporal resolution there were 34896 and 34974 SEVIRI disk images available in this period from M8 and M11 respectively. For inter-comparisons with MODIS, SEVIRI pixels from these products were restricted to pixels acquired within a ± 5-minute window of a MODIS observation and falling within the convex hull of the available MODIS AF pixels. **Table 3.2** provides a summary of the FRP pixels from each SEVIRI product which coincided with a MODIS overpass and which were observed within the spatial extent of each set of MODIS AF pixels.

**Table 3.2** Summary of concurrent and co-located SEVIRI and MODIS AF pixel detections made in the region of interest bounded in red in **Figure 3.3a** between January 1st and December 31st 2018.

	M11 SEVIRI	M8 SEVIRI	MODIS (Aqua & Terra)
Number of AF Pixels	103716	125462	576667
Sum of FRP (TW)	7.71	9.84	15.99
Minimum Pixel FRP (MW)	7.7	7.0	2.5
Maximum Pixel FRP (MW)	822	1474	2174
Mean Pixel FRP (MW)	63.9	69.3	23.7
Median Pixel FRP (MW)	47.7	50.7	13.2

When the M8 and M11 SEVIRI FRP measurements are limited to times and locations where MODIS observations (with VZA ≤ 18.3°) are available, MODIS is able to detect many more AF pixels than either of the SEVIRI products. This is to be expected as MODIS has a lower minimum FRP detection threshold (~ 5 to 8 MW at nadir) than SEVIRI (~ 30 to 40 MW at nadir) due to its smaller nadir pixel size, meaning it can detect lower FRP fires (Roberts et al., 2015). **Table 3.2** shows that MODIS' summed FRP for the geographic region is thus around double that of the summed FRP from either SEVIRI product and mean, median and minimum FRP pixel values are also all lower for MODIS than for SEVIRI. The maximum pixel FRP of MODIS

is higher than that of SEVIRI, because MODIS has a relatively high saturation brightness temperature ( $\sim 500$  K) in its Band 21 (MIR) channel used to derive FRP (Giglio et al., 2016), which compares to the SEVIRI MIR channel which saturates at a brightness temperatures of  $\sim 335$  K (Roberts et al., 2005, 2015; Wooster et al., 2015). This difference is offset somewhat by SEVIRI pixels being far larger than those of MODIS (at nadir) – so the same FRP fire will result in a lower MIR brightness temperature in SEVIRI than in MODIS. However, this does not fully make up for the very large difference in the two sensors saturation temperatures, resulting in MODIS being able to measure far higher FRP fires.

It is clear from the summarised results in **Table 3.2** that over the year the M8 SEVIRI FRP-PIXEL product detects more AF pixels and measures a higher overall summed FRP than does the M11 product (by around 28% more in terms of total FRP). Interestingly, the M8 FRP maxima is nearly double that of the M11 product (1474 MW compared to 822 MW). The spatial distributions of total FRP from all the pixels included in **Table 3.2** for each satellite product are shown in **Figure 3.6**. **Table 3.2** and **Figure 3.6** show that MODIS captures much more fire activity than SEVIRI when limited to the area of MODIS spatio-temporal coverage. However, when the full spatio-temporal extent of the SEVIRI product is considered (**Table 3.6** and **Figure 3.10**) total FRP measurements are much higher. This highlights the value of the high temporal resolution measurements of FRP provided from geostationary orbit, which contrasts with the sometimes limiting requirement for extreme temporal interpolation when using polar-orbiting FRP datasets (e.g. Vermote et al., 2009; Kaiser et al., 2012).

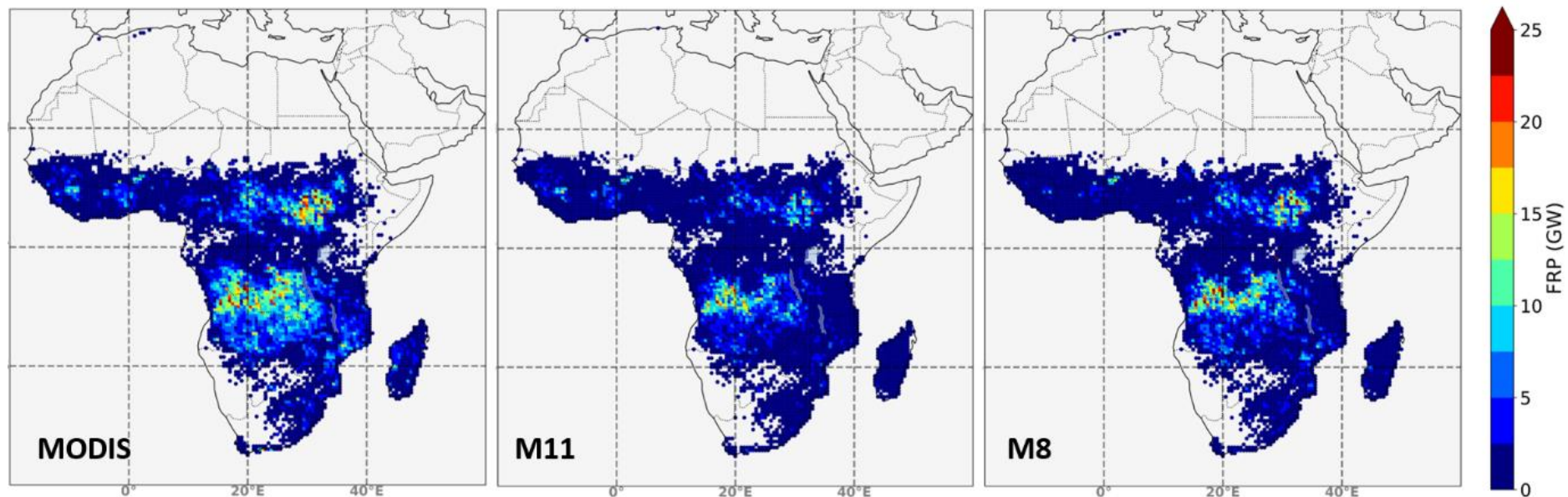


**Figure 3.6** Total FRP (GW) measured in each  $0.5^\circ \times 0.5^\circ$  grid cell by MODIS and by SEVIRI, as calculated from all the SEVIRI FRP-PIXEL product AF pixels available within  $\pm 5$  minutes of a MODIS overpass and which were within the spatial extent of the MODIS AF observations made between VZA of  $\pm 18.3^\circ$  and between 1<sup>st</sup> January and 31<sup>st</sup> December 2018.

Results from an ordinary least-squares (OLS) linear best-fit to the data from the three comparison approaches (total areal, per-area and per-fire) described in **Section 3.2.3.2** are shown in **Figure 3.7** for both the M8 and M11 datasets against MODIS. The full datasets generated by per-area and per-fire comparisons are very large - containing tens of thousands of temporally matched grid cells and fire clusters. The points in the total areal comparisons comprise all the MODIS granules in 2018 that contained AF pixels over the ROI (**Figure 3.3a**). Summary statistics for the regression relationships found with these data are shown in **Table 3.3**.

Both SEVIRI products detect lower FRP than MODIS, ranging between 36% and 40% lower for M8 (depending on the comparison method) and 51% lower for M11 in all comparison methods. Despite the relatively large RMSE values found during the per-fire comparisons (405 MW for M8 *vs.* MODIS and 449 MW for M11 *vs.* MODIS), the bias is relatively low with values of -8 MW and 38 MW respectively for M8 and M11. These biases are within the range of those obtained in previous evaluations of the standard SEVIRI FRP-PIXEL product (**Table 3.4**). In all three comparison methods applied, M8 SEVIRI detects more AF pixels, and measures higher summed FRP than does M11 SEVIRI, and the slopes of the OLS linear best fit to the M8 and MODIS data are consistently closer to unity than are that from the M11 and MODIS data.

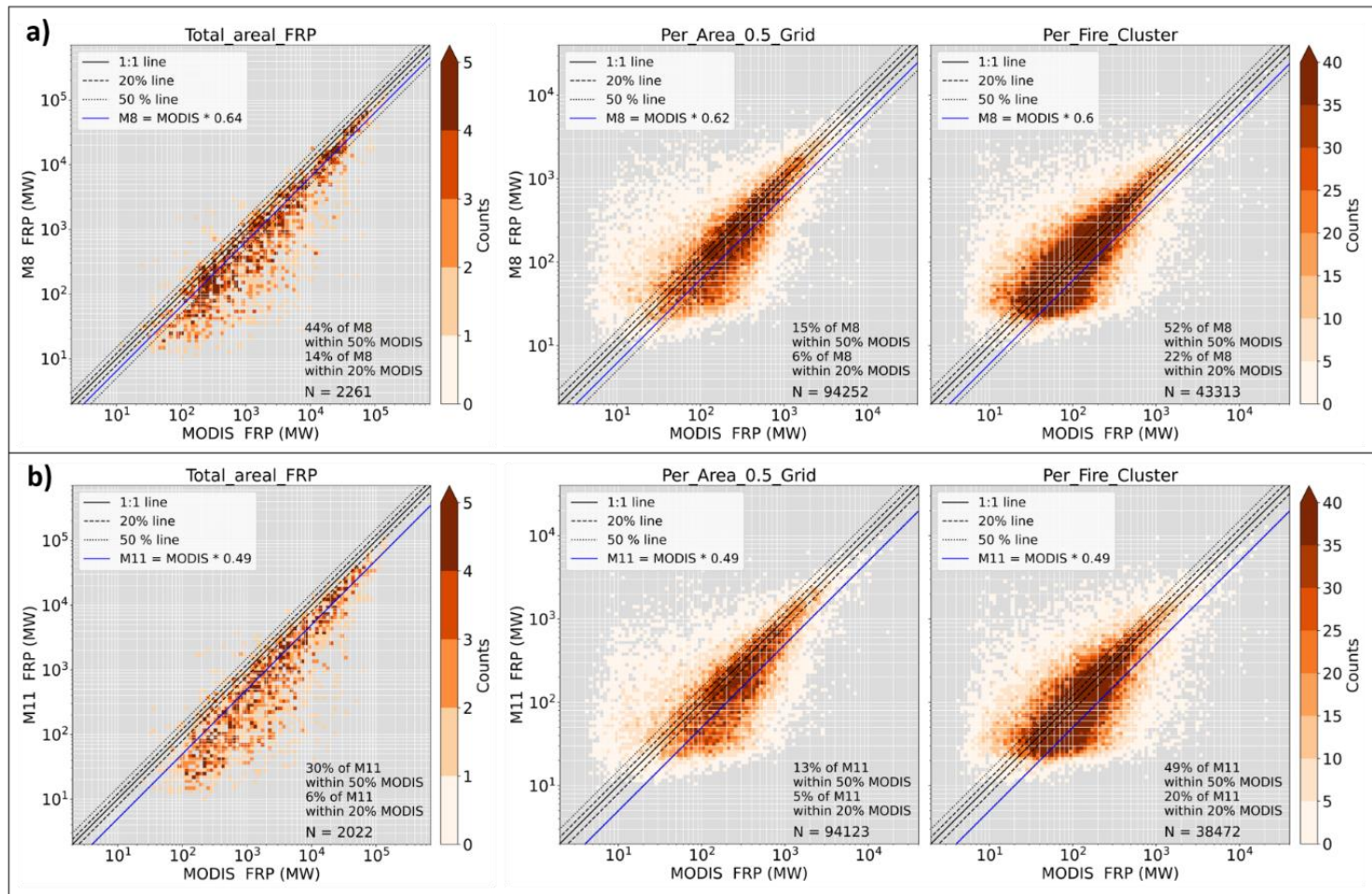


**Figure 3.7** Relationship between SEVIRI and MODIS FRP derived from spatially and temporally matched AF pixels identified over Africa in 2018. Three different comparison methods described in **Section 3.2.3.2** are used, total areal, per-area and per-fire. (a) M8 SEVIRI in relation to MODIS (b) M11 SEVIRI in relation to MODIS. In each comparison plot, the least-squares linear best fit is shown (blue) along with the 1:1 line (black solid), 50% line and 20% line (black dashed). The density of points in each case is represented by the colour bar for ease of visualisation. The results of the above least-square fits are summarised in **Table 3.3**.

**Table 3.3** Summary of the OLS linear best fit parameters and statistics derived when comparing M8 and M11 SEVIRI FRP retrievals against those made from MODIS via three methods – total areal, per-area and per fire.

Comparison method	M8 SEVIRI			M11 SEVIRI		
	Total areal	Per-Area	Per-Fire	Total areal	Per-Area	Per-Fire
N	2261	94252	43313	2022	94123	38471
Slope	0.64	0.62	0.6	0.49	0.49	0.49
Standard Error	0.005	0.002	0.003	0.005	0.001	0.003
Uncentred R <sup>2</sup>	0.86	0.59	0.53	0.85	0.59	0.48
RMSE (MW)	7339	293	405	9653	304	449
Bias (MW)	2985	63	-8	4422	88	38

Comparing **Table 3.3** to results from other validation studies (**Table 3.4**), the current study indicates an overall poorer performance of the SEVIRI products against MODIS than previous studies have reported, particularly for the M11 SEVIRI product which was obtained from the standard Meteosat operating position. It is, however, crucial to note some important differences in this study compared to other works. Firstly, the temporal and spatial extent of this study covers a longer period and larger area than any past study. In most cases other studies include FRP data from a few days to a few weeks, with Freeborn et al. (2014) being the only exception to this. Freeborn et al. (2014) use 6 months of matched SEVIRI and MODIS data, but only include observations from the region covering Central African Republic - a far smaller region of interest than used in this work and a particularly fire affected part of Africa. There are also differences in the VZA restrictions applied to the MODIS observation. In this study a very stringent VZA threshold of  $\pm 18.3^\circ$  is applied to the MODIS data, based on the fact that Morisette et al. (2005) showed that FRP is well characterised across Southern Africa within this swath range. Within this view angle range, the MODIS pixel area grows only slightly, from  $1 \text{ km}^2$  at nadir to  $1.2 \text{ km}^2$  at  $\pm 18.3^\circ$ . Most studies reported in **Table 3.4** use far more inclusive limits than applied in this work, up to  $\pm 55.0$  (see **Table 3.1**). Only Freeborn et al. (2014) use the same  $\pm 18.3^\circ$  limit as used here. The larger spatio-temporal scale of this study has therefore, captured far more of the variability in performance between the SEVIRI and MODIS fire products than have previous works. When the more restrictive VZA threshold

applied to MODIS FRP observations in this work is also considered, the results show that SEVIRI's performance against MODIS (close to nadir) has likely been slightly overestimated, in terms of per-area FRP measures - this may be by 38% to 51% (**Table 3.4**). Studies that have included more MODIS off-nadir observations have, by definition, used data where MODIS performs more poorly due to the pixel areas of these off-nadir MODIS data being larger and thus, the minimum FRP detection limit being higher than for MODIS' close-to-nadir data (Freeborn et al., 2011; Kumar et al., 2011).

To gain an understanding of the M8 and M11 SEVIRI FRP performance over the year, the datasets presented in **Figure 3.7** and **Table 3.3** are temporally and spatially aggregated to obtain median daily FRP values - plotted in **Figure 3.8**. When aggregated to these daily medians, total areal and per-area comparisons yield the same data, and as such daily per-area and daily total areal plots are identical. Results from these daily median comparisons show that per-area comparisons yield similar results to those of the full dataset, and only fractionally improve the agreement between both SEVIRI products and MODIS FRP – increasing the slope of the OLS linear best-fit from 0.62 to 0.65 for M8 and from 0.49 to 0.5 for M11 for example. Conversely, daily per-fire median values give slopes of 0.96 and 0.73 for M8 and M11 fires respectively. This shows that when aggregated over the two MODIS overpasses and over Africa as a whole, both M8 and M11 SEVIRI per-fire measurements show improved agreement with MODIS, particularly M8. However, the M11 FRP of a fire is still 'on average' 27% lower than when measured by MODIS. Unlike in per-area data, the per-fire comparisons do not include fires for which no corresponding matchup is found between the SEVIRI product and MODIS product. That per-fire comparisons present a better performance of SEVIRI than the per-area comparisons, confirms that when a fire is detected by both MODIS and SEVIRI, FRP is reasonably well characterised by SEVIRI. Hence, the largest contribution to the lower total regional FRP measures made by SEVIRI comes from that fact that many lower FRP fires identified by MODIS remain undetected by SEVIRI completely. This trend was also observed by Roberts et al. (2015). Since per-fire comparisons show the lowest bias in full dataset comparisons (**Table 3.3**), the per-fire measures between daily median M8 FRP and MODIS FRP and daily median M11 FRP and MODIS FRP were used in direct comparison to the agreement obtained between SEVIRI FRP and MODIS in previous studies (**Table 3.4**).

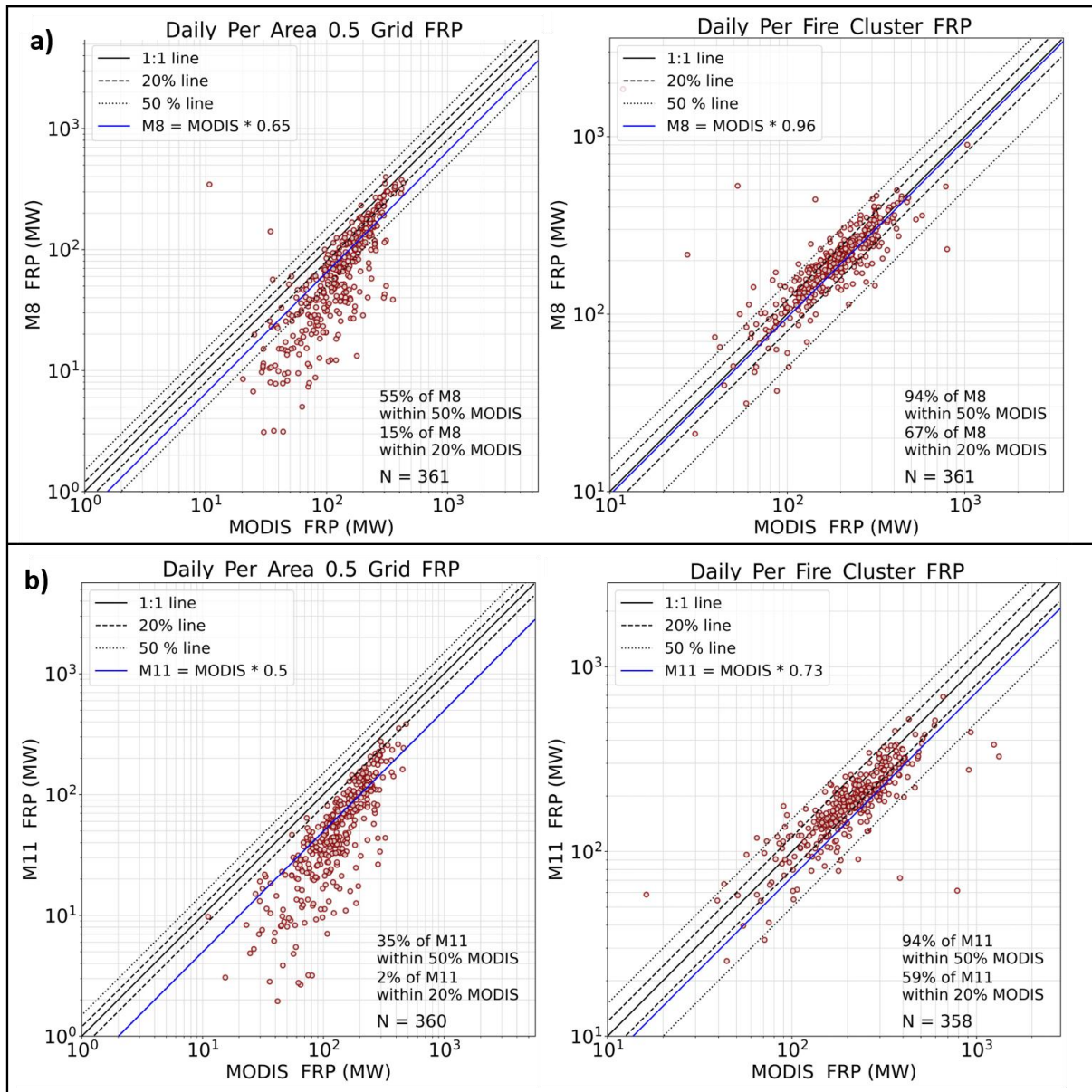


**Figure 3.8** Relationship between M8 and M11 FRP and FRP from the matching MODIS observations for the same per-area and per-fire data as shown in **Figure 3.7**, aggregated in space and time to get daily median comparisons. (a) M8 SEVIRI relation to MODIS b) M11 SEVIRI relation to MODIS. In each comparison plot the least- squares line-of-best-fit is shown (blue) along with the 1:1 line (black solid), 50% line and 20% line (black dashed). The results of the least-square fits for per fire comparisons are summarised in **Table 3.4** along with the results of previous studies.

**Table 3.4** Summary of the results from previous works which have compared SEVIRI and MODIS FRP. Also shown are results obtained from this study for the daily averaged per-fire comparisons shown in **Figure 3.8**.

Study	Slope	R <sup>2</sup>	N of points	Bias (MW)	RMSD (MW)
Roberts et al. 2005	1	0.83	139	-20	214
Roberts et al. 2008	1	0.62	277	4	178
Freeborn et al. 2014	1	0.61	282	-14	-
Roberts et al. 2015	0.97	0.94	153	88	88
LSASAF 2015	0.97	0.74	-	-	-
This study M8	0.96	0.96	361	-9	116
This study M11	0.73	0.87	358	40	107

### 3.3.1.2 Errors of Omission and Commission

The assessment of the AF detection performance finds that the M8 and M11 products have very similar errors of omission. 70% and 71% of MODIS' AF detections having no corresponding SEVIRI pixels at the same time in the M8 and M11 data respectively. Errors of commission between M8 and M11 are more dissimilar, with 9% of M8 pixels having no matching MODIS observation, compared to M11 where this is 20% of all AF pixels. Previous validation studies obtained between 8% and 25% for error of commission rate, and between 53% and 71 % for error of omission rate by comparison (**Table 3.5**). Bearing in mind the VZA restrictions applied to MODIS pixels in this work compared to others (**Table 3.1**), these errors of omission and commission are within what might be expected.

**Table 3.5** Summary of the AF errors of omission and commission obtained in previous validation studies, along with those from this study comparing M8 and M11 AF detections against those of MODIS in 2018.

Study	Errors of Omission (%)	Errors of Commission (%)
Roberts et al. 2008	57	8
Freeborn et al. 2014	53	25
Roberts et al. 2015	71	11
LSASAF 2015	71	13
This study - M8	70	9
This study - M11	71	20

The SEVIRI errors of omission and commission were also analysed as a function of SEVIRI VZA range, to determine if there is any significant change in detection performance as VZA varies away from the nadir sub-satellite point (SSP). At higher SEVIRI VZAs the pixel footprint area increases (see **Figure 3.2**), the fire thermal emissions are viewed from a more oblique angle (Freeborn et al., 2014) – this also causes the atmospheric path length to increase. The latter means the atmospheric transmission is typically lowered, in turn lowering the contrast of a particular fire signal and its background in terms of MIR brightness temperature.

The results of this analysis applied to M8 and M11 SEVIRI FRP data are shown in **Figure 3.9**. Both SEVIRI products show an overall increase in the AF percentage of errors of commission and errors of omission as VZA increases, up to  $\sim 40^\circ$ . However, at VZA beyond around  $40^\circ$  this appears to stabilise and errors of omission and commission appear not to grow further (up to the maximum VZA considered of  $\sim 70^\circ$ ). For M8 however, the errors of commission presented here are slightly misleading, and this topic is discussed further in **Section 3.3.4**.

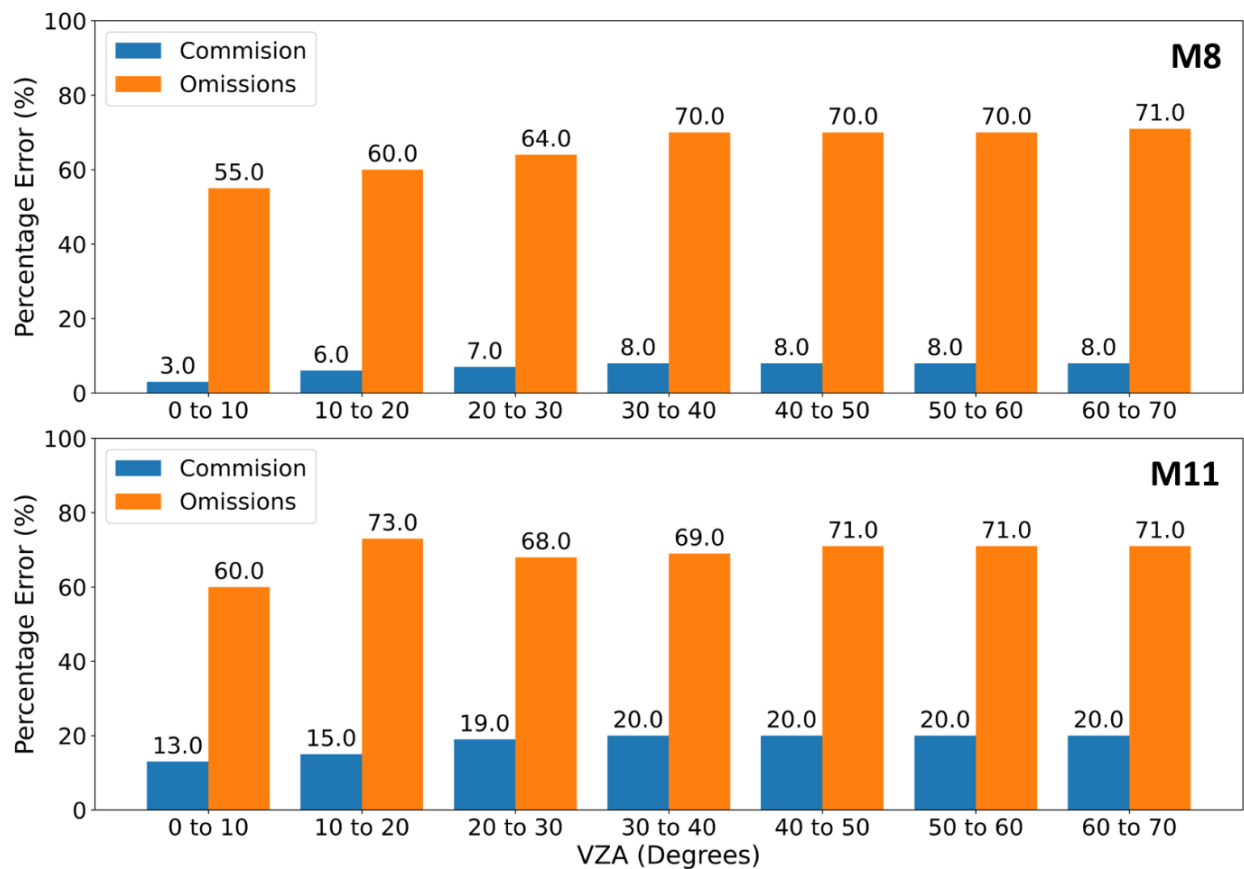


**Figure 3.9** Errors of omission and commission for the M8 and M11 SEVIRI FRP-PIXEL products in relation to MODIS, calculated at different SEVIRI VZA ranges.

### 3.3.2 M8 and M11 SEVIRI Inter-comparison

Simultaneous data from M8 and M11 allows the observation of fires using the same sensor and identical retrieval algorithms from two different viewing positions. The direct comparisons between M8 and M11 at their full temporal resolution are reported here. The SEVIRI FRP-PIXEL products from both sensors are compared every 15-minutes using the same total areal, per-area and per-fire metrics detailed in **Section 3.2.3.2**. Due to the high temporal resolution of SEVIRI, each type of comparison contains many more data points than for the SEVIRI-MODIS comparisons. AF pixels from 34,874 SEVIRI product files from each of M8 and M11 were used in the comparisons, and the spatial distribution of the total summed FRP observed by each SEVIRI sensor over 2018 is shown in **Figure 3.10**. A summary of all these FRP data is provided in **Table 3.6**.

**Figure 3.10** clearly shows that, in general, the spatial patterns are similar between the M8 and M11 FRP products but that there are some distinct differences, particularly in the region outlined in red over the north western Sahara. FRP magnitudes also differ in the regions outlined in yellow. Both these features are further highlighted in **Figure 3.14a** and are discussed in more detail in **Section 3.3.3** and **Section 3.3.4**.

The impact of SEVIRI's high temporal resolution on total annual measures of FRP is clear when **Figure 3.10** is compared with the summed total FRP when it is restricted to SEVIRI observations acquired within  $\pm$  5-minutes of a MODIS overpass (**Figure 3.6**). SEVIRI at its full temporal resolution captures far more instantaneous FRP than does MODIS, and this demonstrates why FRP measurements from polar-orbiting sensors must be temporally extrapolated over the day to realistically quantify fire activity (e.g. Vermote et al., 2009; Kaiser et al., 2012).

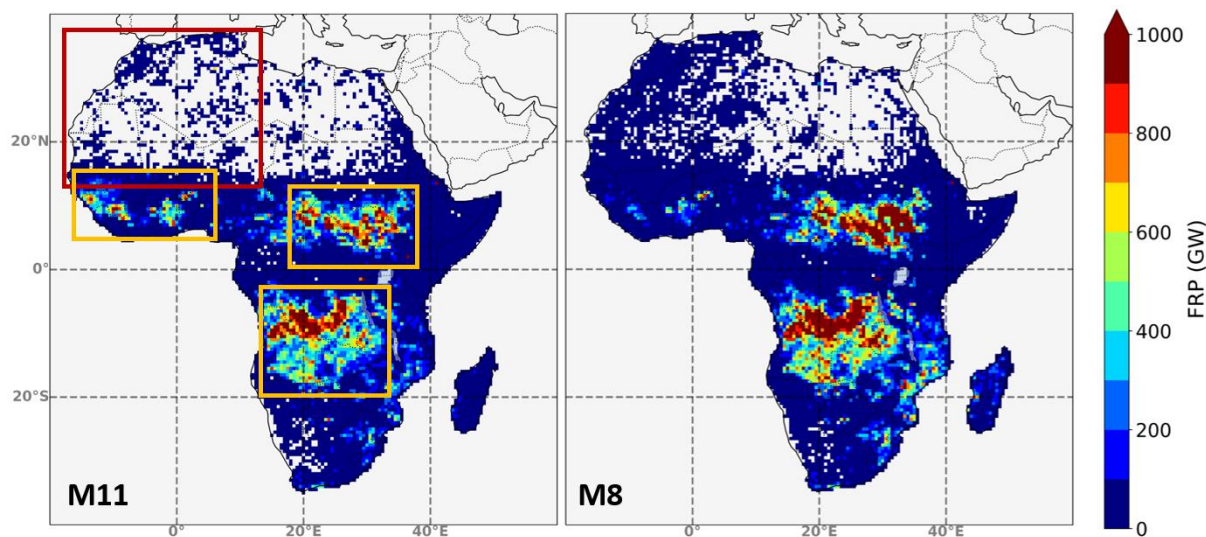


**Figure 3.10** Total summed FRP (in GW) measured in each  $0.5^\circ \times 0.5^\circ$  grid cell in the per-area comparisons made using both SEVIRI products over Africa between 1<sup>st</sup> January and 31<sup>st</sup> December 2018. The region outlined in red indicates an area where many false AF detections occur in M8 (see **Section 3.3.4**). The regions outlined in yellow are areas encompassing some of the highest fire activity over the year where the impact of SEVIRI VZA is most obvious (see **Section 3.3.3**).

**Table 3.6** Summary of SEVIRI AF pixels detected by M8 and M11 in the region of interest bounded in red in **Figure 3.3** between January 1st and December 31st, 2018.

	M11 SEVIRI	M8 SEVIRI
Number of AF Pixels	$16.0 \times 10^6$	$18.4 \times 10^6$
Sum of FRP (PW)	1.04	1.33
Minimum Pixel FRP (MW)	5.6	5.3
Maximum Pixel FRP (MW)	1845	2608
Mean Pixel FRP (MW)	56.0	55.7
Median Pixel FRP (MW)	33.3	33.5

**Table 3.6** shows that minimum, mean and median FRP pixel values throughout the year are very similar between the M8 and M11 products. M8 detects about 2.4 million more AF pixels than does M11, and this results in it having a summed FRP about 0.3 PW greater than M11. The similarity of mean and median FRP pixel values between the products indicates that differences in measured FRP at larger scales between the two products originate in M8 detecting more AF pixels, rather than M8 measuring higher individual pixel FRPs.

The results from comparisons between M8 and M11 are shown in **Figure 3.11a**. Similarly to **Section 3.3.1** - where M8 yielded total areal, per-area and per-fire comparisons with greater agreement to MODIS FRP than provided by M11 (**Table 3.2** and **Table 3.3**) - M8 measured FRP here is higher than that of M11 in both the total areal and per-fire comparisons, by 31% and 7% respectively (). Conversely, per-fire comparisons show M11 FRP to be higher than M8 by 8%, however, the coefficient of variation ( $R^2 = 0.64$ ) is lower than for the other two types of comparison -  $R^2$  is 0.96 and 0.77 for total areal and per-area comparisons respectively. Again, the per-area and per-fire datasets are extremely large, each containing several million points which are summed to calculate 3-day FRP totals over the year (**Figure 3.11b**). **Figure 3.11b** shows that from June onwards (the start of the Southern African fire season), M8 measured FRP is consistently higher than M11 FRP. Earlier in the year - in the Northern African fire season - when fires are closer to the M11 nadir position, M11 and M8 measure FRP more similar in magnitude and in fact, between March and May M11 generally measures higher FRP than does M8.

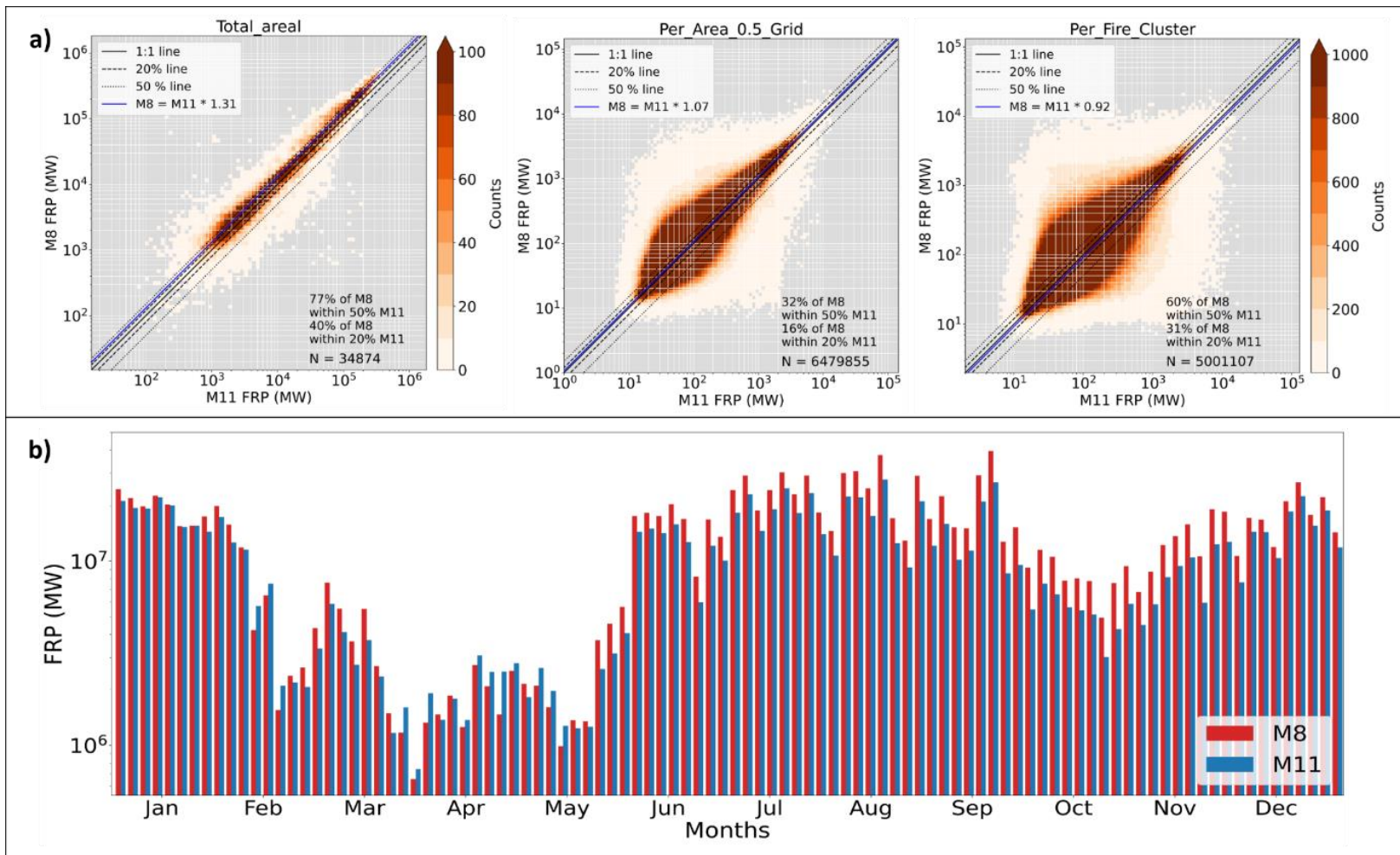


**Figure 3.11** Comparison of M8 and M11 FRP data. a) Relationship between M8- and M11-derived FRP from 1<sup>st</sup> January to 31<sup>st</sup> December 2018 as compared using three different methods – total areal, per-area and per-fire. In each comparison plot the least-squares line of best fit is shown (blue) along with the 1:1 line (black solid), 50% line and 20% line (black dashed) and the density of points in each case is represented by the colour bar for ease of visualisation. b) 3-day total FRP measured in the total-areal comparisons, plotted over the year for each SEVIRI product.

The data of **Figure 3.11a** are averaged to get daily median FRP (**Figure 3.12**) and the regression analyses in **Figure 3.11a** and **Figure 3.12** are summarised in **Table 3.7**. When measurements between the two products are compared in terms of daily median FRP, the reduction in the spread of points results in comparisons having an increased weighting towards M8, generating slopes of 1.32 and 1.20 for per-area and per-fire comparisons respectively in OLS best fits. The RMSE is relatively low in daily averages at around 24 MW. Per-area and per-fire comparisons both show a negative bias of -16 MW and -20 MW respectively. As with the SEVIRI-to-MODIS inter-comparisons, the fact that the slope is closer to unity in daily per-fire data compared to per-area data indicates that some component (~12%) of the higher FRP measured by M8 results from FRP pixels in M8 that have no matching fires at all in M11.

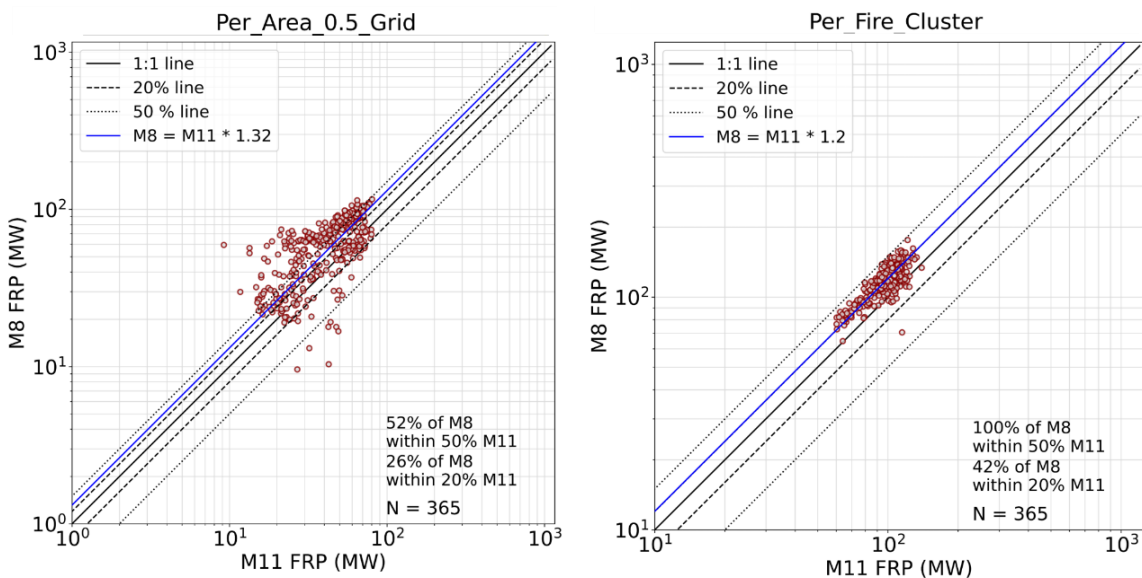


**Figure 3.12** Daily averaged (median) FRP for the per-area and per-fire dataset shown in **Figure 3.11a**. The least-squares line of best fit is shown (blue) along with the 1:1 line (black solid), 50% line and 20% line (black dashed) and regression statistics are reported in **Table 3.7**.

**Table 3.7** Summary of the linear-best-fit plots between M8 and M11 measurements of FRP over Africa made between Jan 1st 2018 to 31st Dec 2018 (**Figure 3.11a** and **Figure 3.12**).

Comparison method	Full Dataset		Daily Median		
	Total areal	Per-Area	Per-Fire	Per-Area	Per-Fire
N	34873	$6.47 \times 10^6$	$5.00 \times 10^6$	365	365
Coefficient	1.31	1.07	0.92	1.32	1.20
Standard Error	0	0	0	0.02	0.01
Uncentred R-squared	0.962	0.771	0.64	0.91	0.99
RMSE (MW)	23995	228	293	25	23
Bias (MW)	-8217	-44	-39	-16	-20

### 3.3.3 FRP Sensitivity to Observation VZA

A Spearman Rank Correlation test for the per-area data shows the correlation between FRP and VZA in M8 and M11 data to be significant - with a *p*-value approaching zero - and in both datasets VZA and FRP have a weak negative correlation coefficient of -0.28 and -0.20 (for M8 and M11 respectively). The distributions of the full dataset of grid cell from per-area comparisons in terms of their FRP and VZA are shown in **Figure 3.13**. Noting the log axis in the distribution of grid cell FRP, the majority of grid cells have FRP totals of between 0 to 2500 MW in both M8 and M11. Grid cells with FRP totals above this are consistently seen with higher frequency in M8 than in M11, especially in the case of grid cells with FRP totals above 17500 MW. The distribution of M8 and M11 grid cell VZA in **Figure 3.13** shows that grid cells are overall observed at lower VZA by M8 than by M11 - with many more grid cells with a VZA of between 10° and 30° for M8 than M11. This means that the grid cells most dominated by fire activity in 2018 lie closer to the nadir point of M8 than M11, and thus would have been observed at a higher spatial resolution (and with a higher atmospheric transmission) in M8 than in M11. This could be a key reason for the overall higher FRP measured by M8.

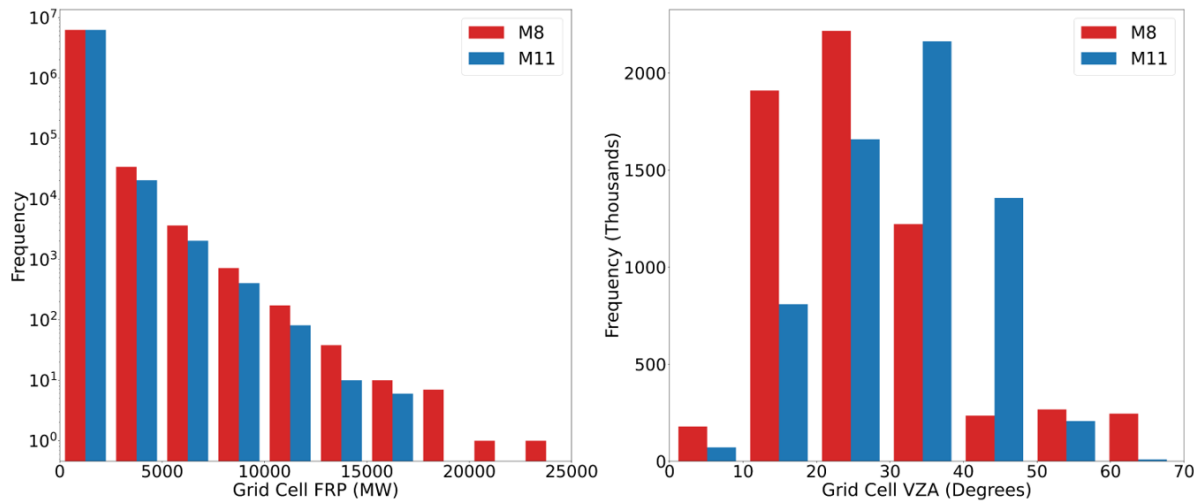


**Figure 3.13** Distributions of FRP (left) and VZA (right) of grid cells used in the per-area comparisons made with M8 and M11 active fire datasets. The FRP of a single grid cell at any given observation time is calculated from the sum of all the FRP pixels falling within that cell, whilst the cell's VZA is the mean VZA of any SEVIRI pixel having a centre point in that grid cell.

As described in **Section 3.2.5**,  $VZA_{DIFF}$  and  $FRP_{DIFF}$  are used to further investigate the impact of SEVIRI VZA on measured FRP. Defined as it is in **Equation 3.1**, negative  $FRP_{DIFF}$  values correspond to M11 measuring a higher FRP than M8, with the opposite true for positive values. While based on **Equation 3.2**, negative  $VZA_{DIFF}$  values correspond to a fire or grid cell being closer to the M8 nadir position, and therefore having a higher spatial resolution (smaller pixel area) in M8 than M11, and the opposite applied for positive values of  $VZA_{DIFF}$ . The distributions of  $FRP_{DIFF}$  and  $VZA_{DIFF}$  in per-area and per-fire comparisons are shown in **Figure 3.14**, each count being an individual fire cluster or  $0.5^\circ$  grid cell at a single SEVIRI scan time. Note that the distribution of  $FRP_{DIFF}$  is plotted with a log scale used for grid cell and fire counts.

The distribution of grid cells (per-area) and individual fires (per-fire) are similar in terms of  $FRP_{DIFF}$ . Both per-area and per-fire distributions have a higher frequency of positive  $FRP_{DIFF}$  values, i.e. higher observed FRP in M8, which has already been shown by other results (**Figure 3.11**, **Figure 3.12** and **Table 3.7**). The distribution of grid cell and individual fire  $VZA_{DIFF}$  is highly asymmetrical and differs substantially between grid cells (per-area) and fires (per-fire). Many more individual fires are located closer to the Meteosat-8 nadir position than the Meteosat-11 nadir position and this effect is even greater for per-area grid cells. Of

particular note is a large peak of grid cells with  $VZA_{DIFF}$  values around  $40^\circ$  (i.e. locations close to the M11 sub-satellite position). This feature differs from patterns seen so far, where more AFs are detected and higher overall FRP is measured by the satellite whose nadir point is closer to the given fire (or grid cell). This is discussed further in **Section 3.3.4** and is related to a large number of false detections over the north western region of Africa.

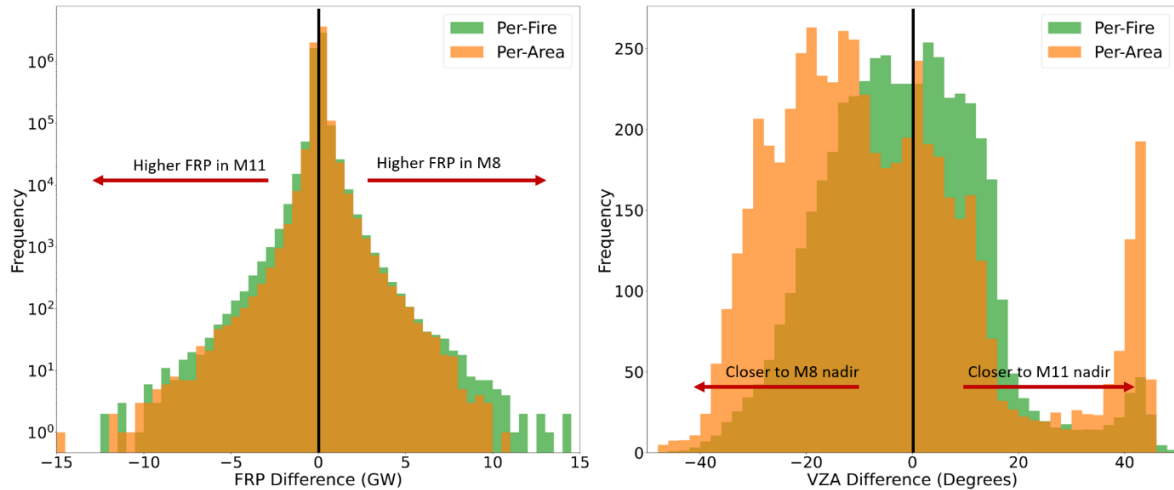


**Figure 3.14** Distributions of  $FRP_{DIFF}$  (left) and  $VZA_{DIFF}$  (right) in grid cells (per-area) and individual fires (per-fire). Frequency is presented on a log scale in the  $FRP_{DIFF}$  distributions while  $VZA_{DIFF}$  frequency is shown in thousands.

The spatial distribution of  $VZA_{DIFF}$  and median  $FRP_{DIFF}$  over the year seen in **Figure 3.15** shows clearly that in Sub-Saharan Africa, very positive  $FRP_{DIFF}$  values generally coincide with negative  $VZA_{DIFF}$  values in areas with high fire activity (outlined in yellow in **Figure 3.10**) and vice-versa for extreme negative  $FRP_{DIFF}$  values. This supports the argument that the proximity of a given region to the SEVIRI sub-satellite point position has a significant influence on the FRP measured in that region over the year. This results from the higher spatial resolution of the SEVIRI sensor closer to nadir, and therefore the lower FRP detection limit. In **Figure 3.15a**, exceptions to this trend occur to some extant along the west coast of southern Africa and over the Horn of Africa, but most notably over the north western Sahara (outlined in red in **Figure 3.10**), an area in which relatively little fire occurs naturally as it composes primarily bare ground. This occurrence is associated with the already-mentioned false AF detections made in the M8 FRP-PIXEL product over this region, which appear to be potentially caused by issues with the SEVIRI cloud mask applied to data from M8 (see **Section 3.3.4**).

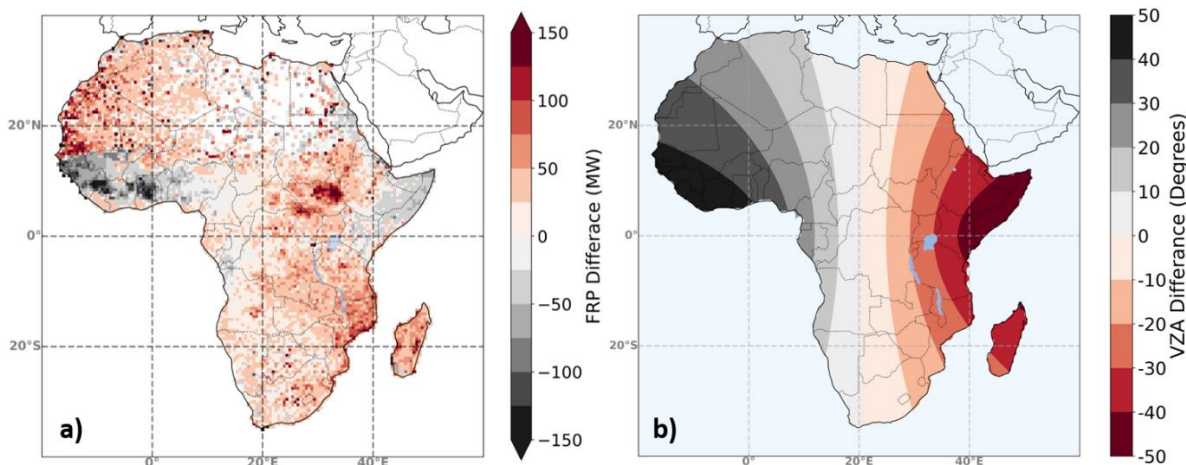


**Figure 3.15**. Spatial distribution of  $FRP_{DIFF}$  (a) calculated as the difference between M8 and M11 median FRP values over the year for each grid cell and  $VZA_{DIFF}$  (b) calculated as the difference between M8 and M11 mean VZA for each grid cell.

**Figure 3.16** shows the relationship between M8 and M11 grid cell summed FRP over the year for both per-area and per-fire comparisons, plotted as a function of  $VZA_{DIFF}$  (colour scale). The mean latitude and longitude of per-fire clusters were gridded to the same  $0.5^\circ \times 0.5^\circ$  grid used in the per-area comparisons to aggregate clusters by geographic location. **Figure 3.16** shows that in per-area comparisons, when a grid cells' annual total FRP exceeds approximately 10,000 MW, in either sensor its relative proximity to the nadir positions strongly determines which SEVIRI product observes higher total FRP. Conversely, grid cells with total FRP below around 5000 MW in either sensor show the opposite relationship. These lower FRP grid cells are typically associated with false detections in the previously mentioned region of the western Sahara. Similar patterns where the proximity-to-nadir determines which SEVIRI product detects higher FRP are seen for large fires in per-fire comparisons in **Figure 3.16**. The inverse relationship for low FRP fires seen in per-area comparisons is removed in per-fire comparisons, because fires which are only observed by a single product are removed - i.e. only fires with matches in both products are retained and the apparent false M8 AF detections over the western Sahara are thus removed.

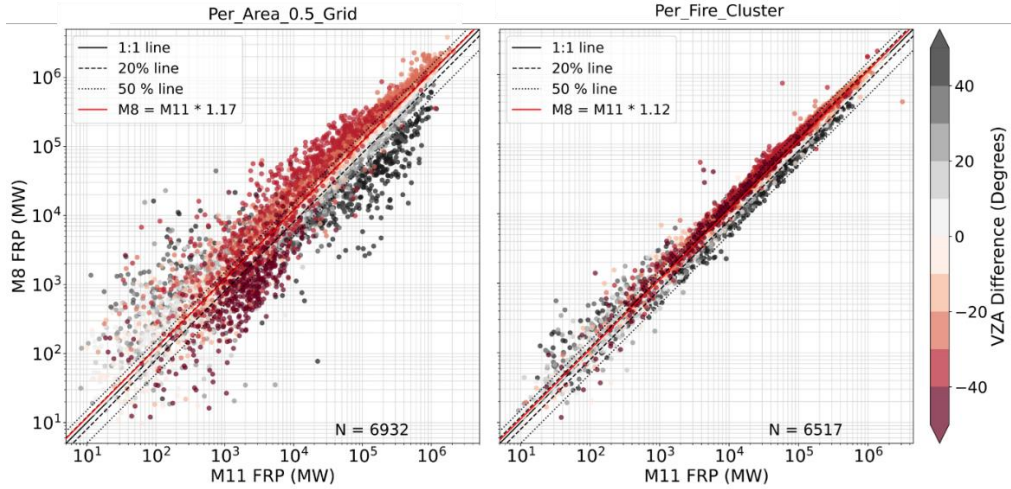


**Figure 3.16** Relationship between M8 and M11 total grid cell FRP calculated as the summed FRP of each  $0.5^\circ \times 0.5^\circ$  grid cell between 1<sup>st</sup> January and 31<sup>st</sup> December 2018 in per-area comparisons and in per-fire comparisons. The  $VZA_{DIFF}$  of each grid cell is represented in the colour scale.

Least-squares linear best fits of  $VZA_{DIFF}$  against  $FRP_{DIFF}$  for the median grid cell FRP for the per-area and per-fire data are shown in **Figure 3.17**. The relation of these two variables can be used to quantify explicitly how measurements of FRP change between the two SEVIRI products as a function of VZA. Per-area data give an intercept of 11.5 MW and slope of -0.69 MW per VZA degree, while per-fire data give a more positive intercept of 32.8 MW and a more negative slope of -1.21 MW per degree. Since in per-fire data false fire detections by either product are somewhat removed, the coefficients from its regression will give a more accurate indication of VZA effects. The regression coefficients from per-fire data can be interpreted as i) the FRP of a fire measured in a grid cell by M8 is, on aggregate, 32.8 MW higher than is measured by M11, and ii) with each degree closer to either sensor's nadir position, that sensor measures a fire's FRP to be 1.21 MW higher than does the other sensor. Although the aim of applying a OLS linear best fit to these data is to more qualitatively understand the impact of SEVIRI's VZA on FRP measures, the coefficient of variation ( $R^2$ ) for these fits are very low (0.06 and 0.05 for per-fire and per-area data respectively). Additionally, other features of this data, such as the weakly heteroscedastic residuals indicate that coefficients obtained from a simple least-squares regression should be treated with extreme caution. Nevertheless, the general shape of the patterns seen in **Figure 3.17** do seem visually to lend these relationships some credence (i.e. a generally negative and approximately linear relationships between FRP difference and VZA difference).

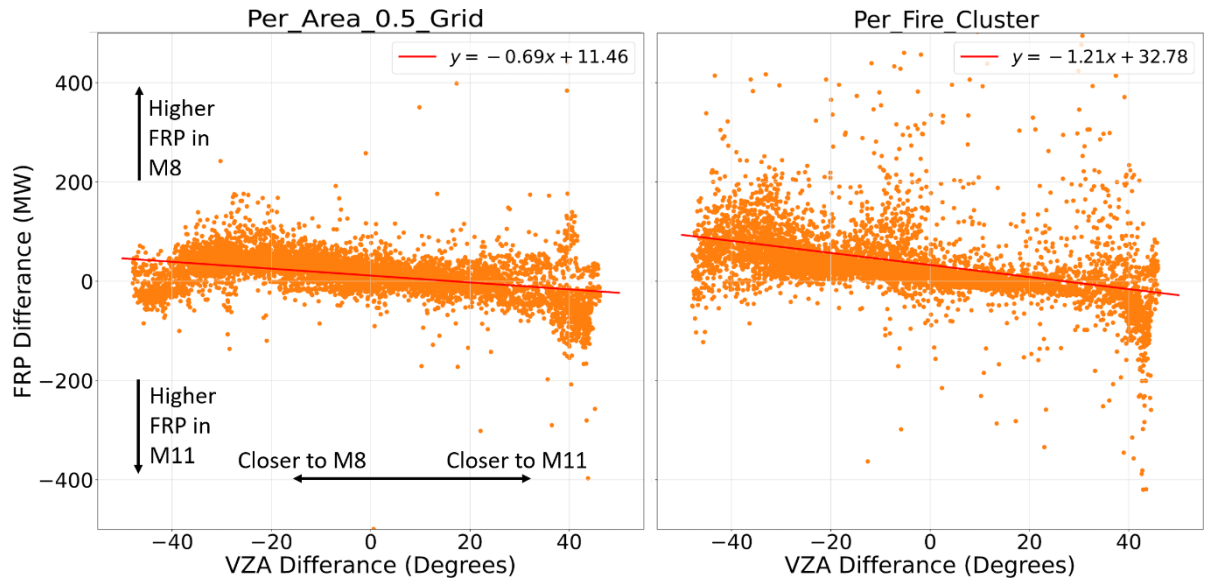


**Figure 3.17** Least-squares linear best fit of  $FRP_{DIFF}$  and  $VZA_{DIFF}$  calculated from median FRP values in each grid cell from the per-area and per-fire datasets.

### 3.3.4 M8 SEVIRI False AF Detections

Based on the results presented in **Section 3.3.1**, particularly those of **Table 3.5** and **Figure 3.9** showing the errors of omission and commission, it would not be unreasonable to conclude that M8 SEVIRI is performing in line with previous validation efforts (**Table 3.4**). Apart from the unexpected feature of M8 consistently measuring higher FRPs than M11, the M8 results obtained in **Section 3.3.1** are not dissimilar to those of other studies in terms of OLS fit and errors of commission and omission. However, the results from direct comparisons between M8 and M11 FRP, which include SEVIRI FRP observations at their full temporal resolution, highlight that many AF pixels are being detected by M8 that are not present in M11 data – in particular over large areas of north western Africa (**Figure 3.15a**). Many of these AF pixels are likely false fire detections, as neither M11 nor MODIS observe the same magnitude of FRP over this region. Furthermore, the per-fire and per-area histograms of  $VZA_{DIFF}$  in **Figure 3.14** show that at a  $VZA_{DIFF}$  around  $40^\circ$  there are many more fire-containing grid cells than matched individual fires. Since per-fire comparisons do not include AF pixels for which matches between products were not found, this indicates that many fires observed in that region are only being detected by M8 and not by M11 or by MODIS. This feature points to

probable false fire detections in the M8 FRP-PIXEL product that have not been characterised in the error of commission analysis carried out in **Section 3.3.1.2**.

The error of commission analysis described in **Section 3.2.3.1** fails to identify these false M8 AF detections due to an assumption made in the procedure used to screen and match MODIS granules with coincident and collocated SEVIRI FRP pixels. Rather than using the MODIS swath MOD03/MYD03 geolocation files to identify the spatial extent of MODIS granules, an assumption that the convex hull of observed MODIS AF pixels can be used to spatially bound potential SEVIRI pixels was used. This procedural choice was made to reduce the amount of computational resources and additional datasets needed in processing this large dataset, and follows the methodology used by Freeborn et al. (2014). However, it results in areas which have no MODIS AF pixels present are not being screened for false AF detections in the SEVIRI datasets.

Through manual inspection of individual SEVIRI Quality Product files it appears that the false AF detections in the M8 FRP-PIXEL product occur at the edges of clouds and at a relatively wide VZA ( $> \sim 40^\circ$ ). **Figure 3.18** shows the M8 SEVIRI Quality Product for a region over Sierra Leone on 6<sup>th</sup> September 2018, 19:45 UTC. This period is well outside the northern African fire season and no active fires were observed by either MODIS or VIIRS in the region on this day. From the quality mark descriptions provided alongside **Figure 3.18**, it can be seen that around interspersed cloud edges (quality mark = 8) the SEVIRI FRP-PIXEL algorithm in M8 data assigns a mixture of quality mark 1 (active fire), 6 (unable to define background signal) and 7 (signal not sufficiently above background). Since M11, MODIS and VIIRS do not observe these AF the M8 fires assigned here are therefore most likely false fire detections, and although there may only be a handful of such false AFs per SEVIRI image; at 15-minute resolution over the course of a day/days this leads to a substantial overall number of false detections (**Figure 3.15**).

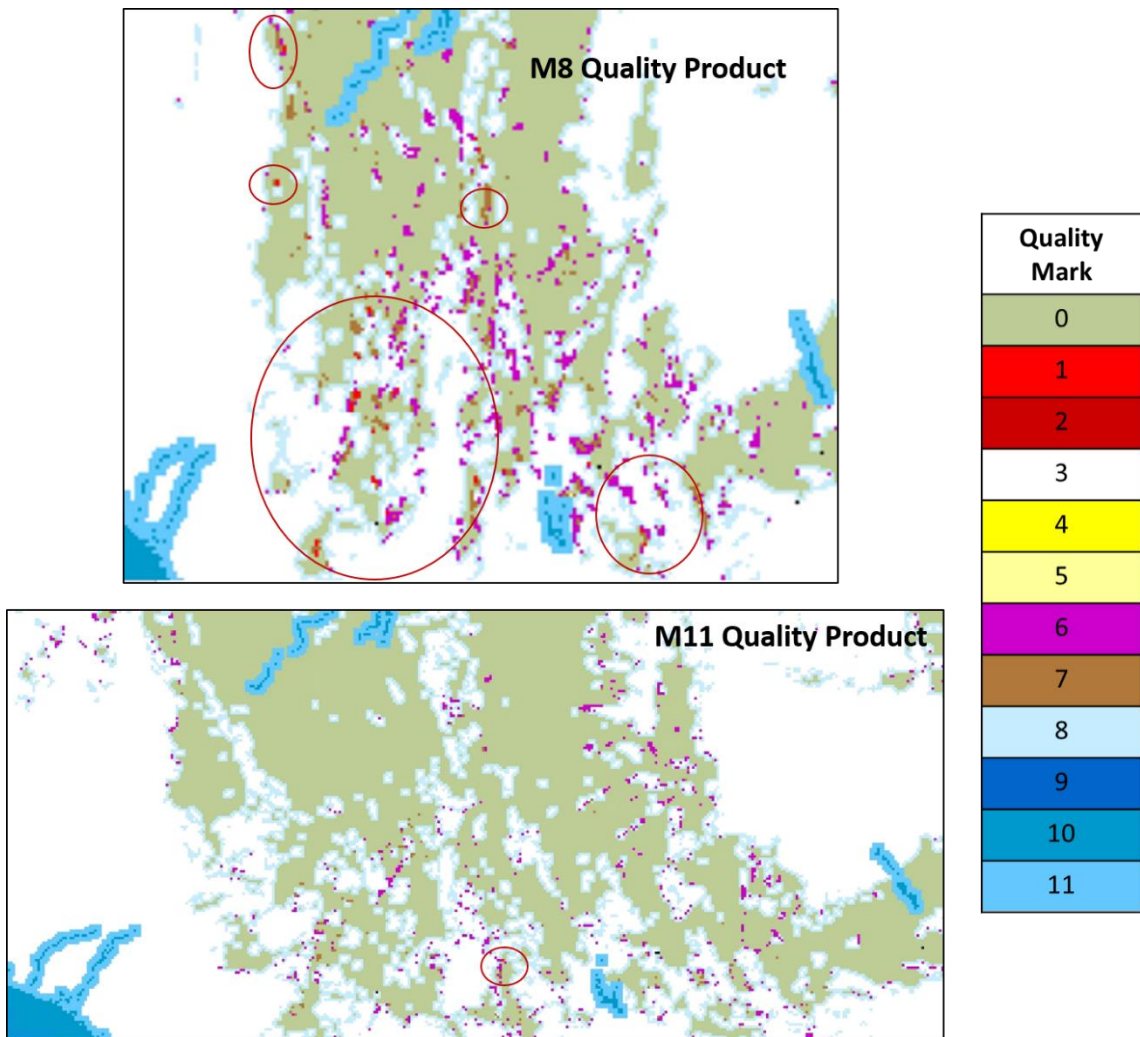


**Figure 3.18** Matching Meteosat-8 and Meteosat-11 SEVIRI FRP-PIXEL Quality products from 6<sup>th</sup> September 2018 19:45 UTC – shown over a region covering Sierra Leone and Guinea (10.6° N, 11.3° W). Shown alongside is the key each quality mark value. Groups of SEVIRI pixels classed as active fires (Quality mark = 1) are circled in red. Full details of the quality mark values are available in (Wooster et al., 2015).

**Figure 3.19** shows the mean month of 2018 in which fires were observed in  $0.5^\circ \times 0.5^\circ$  grid cells by M8. In the region in question (the same as outlined in red in **Figure 3.10**), a clear distinction can be seen between when true fires and false fires are detected. False detections in the western Sahara, and particularly just below 20° N, are detected between May and August - a period far outside the north African fire season which normally occurs between November and February. This distinction in the time of year when false detections occur and clear relationship with the SEVIRI cloud mask (**Figure 3.18**) points to the influence of seasonal effects pertaining to meteorological clouds and their identification and cloud masking.

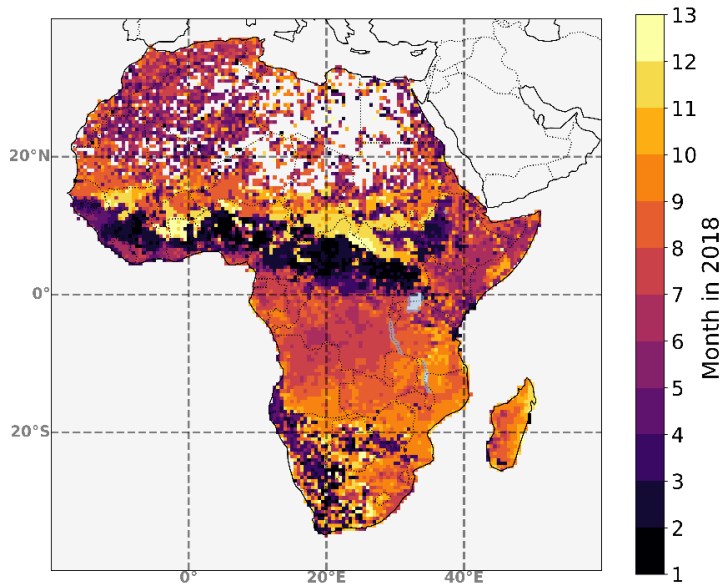


**Figure 3.19** Per-area grid cells as shown in **Figure 3.10**, categorised by the mean month of 2018 in which M8-detected fires in each grid cell were observed.

Further work is needed to improve the method for characterising errors of commission to quantify more explicitly the scale of this M8 product issue, however current M8 pixel observations at wide swath should treated with caution and the work herein has contributed to communications with the LSA SAF regarding this issue and its potential remediation. The SEVIRI cloud mask has been designed and optimised for operations when the satellite is in the operational position on the equator at  $0^{\circ}$  E, and perhaps the cloud mask does not perform so well for data captured at high VZA from the Meteosat IODC position. This finding is coherent with Freeborn et al. (2014), who have shown that the SEVIRI FRP-PIXEL algorithm is strongly affected by the product cloud mask in terms of AF detection.

### 3.3.5 Biome Effect on FRP and Interaction with VZA

The vegetation type being burned in a fire dictates in part the amount of fuel available for combustion – for example fires in forests typically burn more fuel per unit area than fires in grasslands (Van Leeuwen et al., 2014). The amount of fuel burned is a key determinant in the thermal energy released from a fire (Wooster et al., 2003), but also in the amount of fire radiative energy (FRE) quantified using the time-series of FRP observations made from

geostationary satellites (Freeborn et al., 2014; Roberts et al., 2018). The majority vegetation cover of each  $0.5^\circ \times 0.5^\circ$  grid cell from per-area comparisons was determined using the biome map described in **Section 3.3.2** and shown **Figure 3.3b**. A Kruskal-Wallis H Test was applied to the M8 and M11 SEVIRI full dataset from the per-area data of **Figure 3.7**. This test is applied to non-parametric datasets to assess whether categories have median values that are statistically significantly different.

Results of this test showed that in both M8 and M11 datasets, the grid cell FRP of all biome categories were statistically different ( $p$ -values approaching zero), except for the managed land and closed canopy forest biomes which were statistically similar to one another (**Table 3.8**). The results of this test applied to the MODIS grid cell FRP dataset presented in **Figure 3.7**, determines that the same does not apply for MODIS, in which all groups are statistically distinct except for shrubland and low-woodland savanna. Grid cell median FRP over the year was separated by biome in M8 and M11 comparisons against MODIS and per-area comparisons of M8 and M11, these are shown in **Figure 3.20**. Both the average grid cell FRP and the spread of FRP differ between biomes, for example grid cells within high-woodland savanna have the highest median FRP and are clustered more closely. Conversely, grid cells in managed land exhibit lower overall FRP and show a much broader spread in all three products and the agreement between FRP products also varies by biome.

**Table 3.8** Results from a Kruskal-Wallis H test of grid cell FRP measurements from per-area comparisons where grid cells are categorised by their majority vegetation cover. This test was applied to M8, M11 and MODIS AF products separately. A *p*-value between groups of less than 0.05 indicates that two groups are statistically distinct, whereas groups whose *p*-values are greater than 0.05 are highlighted in orange.

Biome group 1	Biome group 2	M11 SEVIRI		M8 SEVIRI		MODIS	
		H-statistic	p-value	H-statistic	p-value	H-statistic	p-value
Closed canopy forest	Managed land	1.3	0.3	0.1	0.8	20.7	0.0
Closed canopy forest	Shrubland	38.6	0.0	10.9	0.0	321.5	0.0
Closed canopy forest	Grassland	181.0	0.0	164.9	0.0	38.3	0.0
Closed canopy forest	Low-woodland savanna	430.4	0.0	377.4	0.0	395.8	0.0
Closed canopy forest	High-woodland savanna	904.8	0.0	945.8	0.0	664.4	0.0
Managed land	Shrubland	44.5	0.0	25.5	0.0	722.6	0.0
Managed land	Grassland	238.5	0.0	214.7	0.0	104.7	0.0
Managed land	Low-woodland savanna	584.7	0.0	631.3	0.0	918.3	0.0
Managed land	High-woodland savanna	1267.3	0.0	1445.2	0.0	1442.8	0.0
Shrubland	Grassland	318.6	0.0	207.1	0.0	36.8	0.0
Shrubland	Low-woodland savanna	207.5	0.0	194.7	0.0	1.3	0.2
Shrubland	High-woodland savanna	655.5	0.0	725.9	0.0	61.2	0.0
Grassland	Low-woodland savanna	743.6	0.0	712.2	0.0	47.9	0.0
Grassland	High-woodland savanna	1042.1	0.0	1088.9	0.0	110.5	0.0
Low-woodland savanna	High-woodland savanna	226.6	0.0	373.7	0.0	56.8	0.0

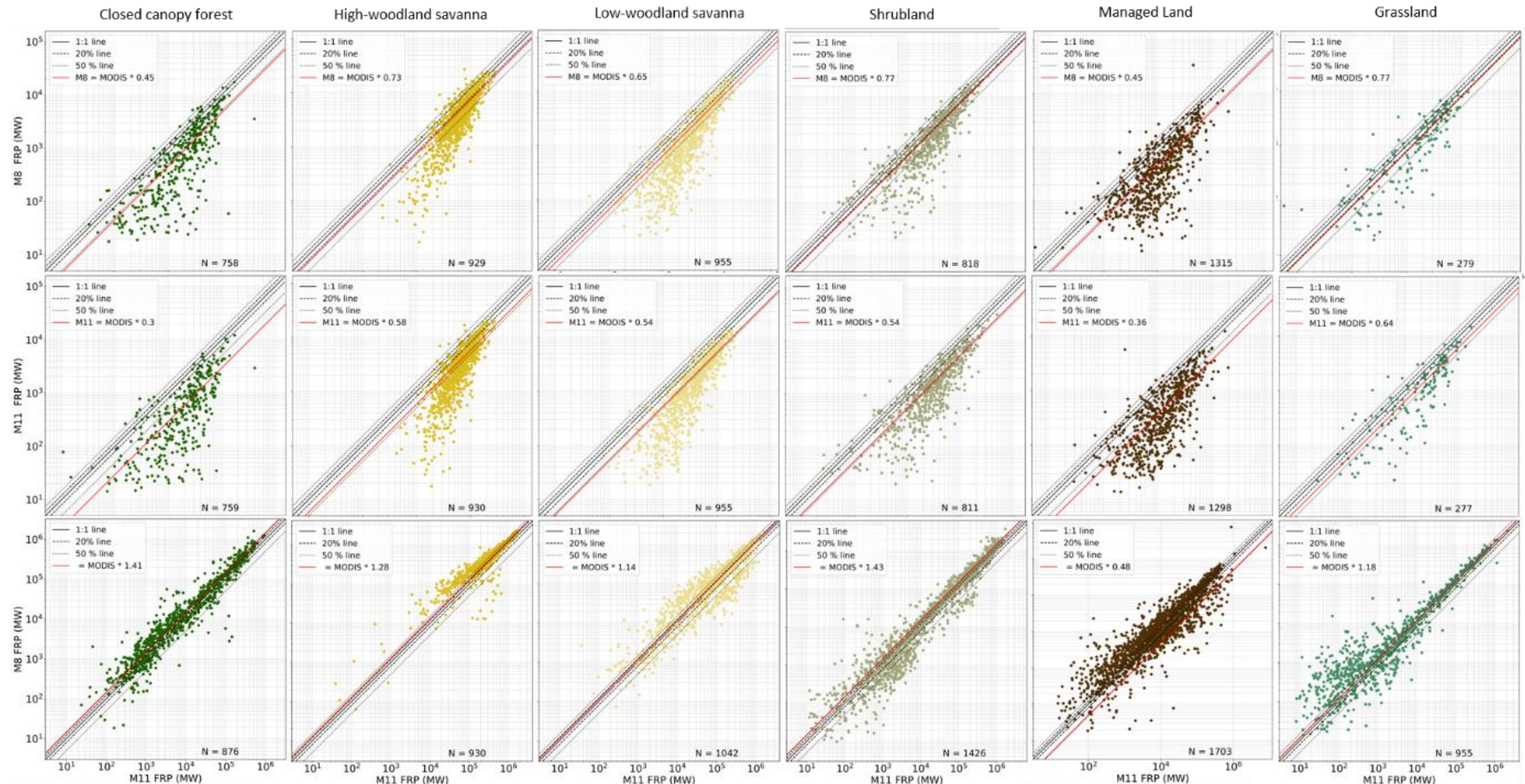


**Figure 3.20** Per-area grid cell comparisons, separated by biome between (top row) M8-MODIS, (middle row) M11-MODIS and (bottom row) M8-M11.

Using the definitions of  $VZA_{DIFF}$  and  $FRP_{DIFF}$ , the per-area data presented in **Figure 3.17** were separated by vegetation type to gain an understanding of how different biomes are impacted by VZA with respect to FRP characterisation. **Figure 3.21** shows  $FRP_{DIFF}$  plotted against  $VZA_{DIFF}$  for grid cells in the six different biomes. Interpreting the coefficients derived from least-squares linear best fits of the points in each biome, high-woodland savanna - having the most negative slope – appears to be most strongly impacted by SEVIRI VZA according to this analysis. Conversely grassland appears to be minimally impacted by VZA, having a slope close to zero (0.35 MW per Degree). All biomes yield a positive intercept ranging between 3.7 and 73.4 MW, pointing again to the overall higher grid cell FRP measured by M8 compared to M11. As already highlighted, the coefficients obtained in this regression should be treated with caution. However, the results do provide a helpful indication of the relative magnitude of the biome impact of VZA on FRP measures.

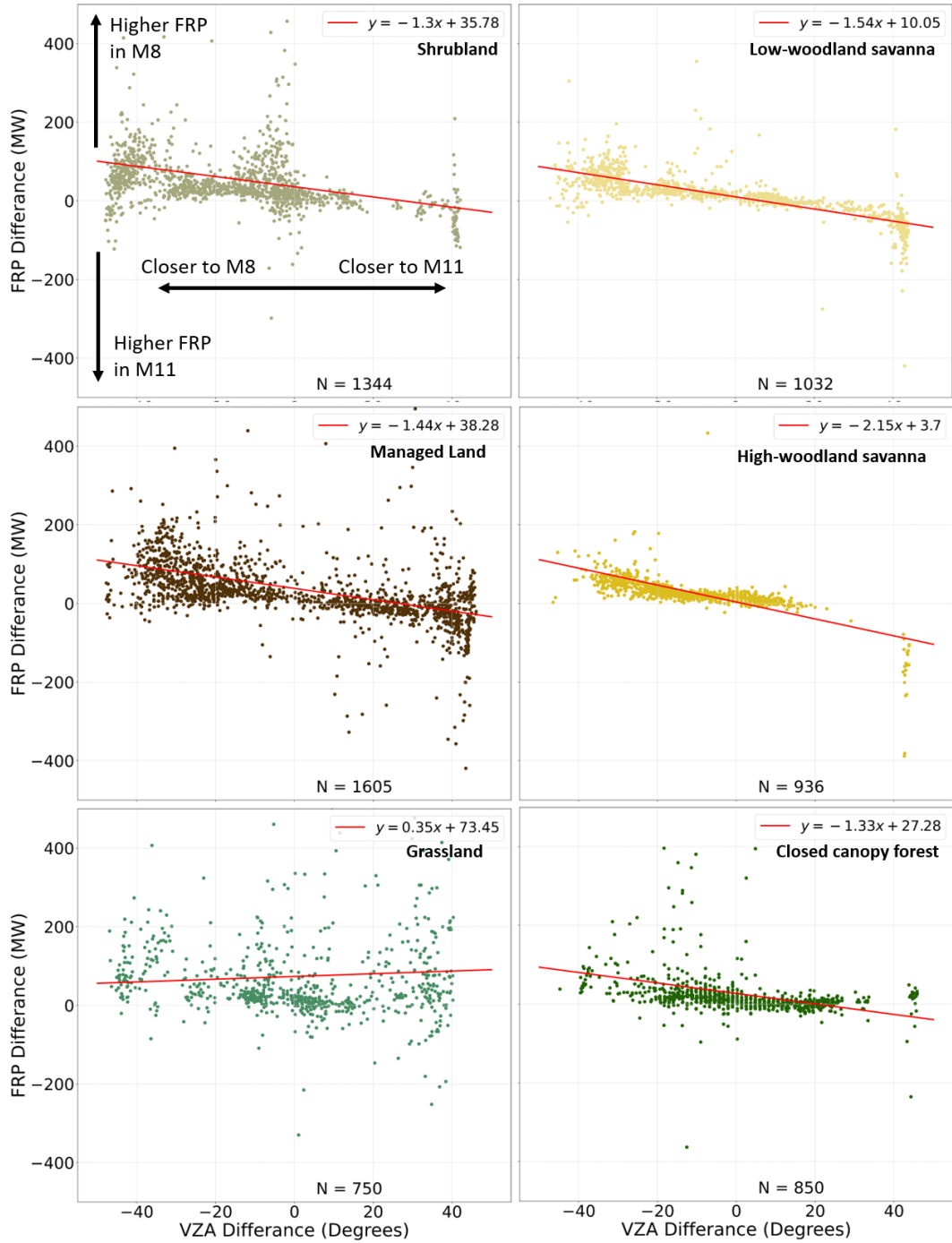


**Figure 3.21** Least-squares linear best fits between data of grid cell  $FRP_{DIFF}$  and  $VZA_{DIFF}$ , split by the majority vegetation coverage in each grid cell using the biome map in **Figure 3.3b**.

## 3.4 Discussion

### 3.4.1 M8 Measurements of FRP

Throughout the analysis conducted in this work, M8 consistently measures higher FRP values than M11 in all three comparison methods used (total areal, per-area and per-fire). The novelty of this study in carrying out an assessment of the SEVIRI FRP-PIXEL product generated from Meteosat-8 operating at the Indian Ocean sub-satellite position of 0° N, 41.5° E means that there is no precedent to suggest what the expected impact of the new viewing position might be on measurements of FRP over Africa. Indeed, as this is the first known inter-comparison of the SEVIRI FRP-PIXEL product from the same SEVIRI sensor operating from different locations, the inferences as to the reason for the variations seen between the two products are primarily drawn from the analysis carried out herein. In this context, two probable causes are proposed for overall higher FRP measurements in M8 when compared to M11:

- i) The relative size of SEVIRI pixel footprints (and atmospheric transmittance) in regions which have the greatest fire activity which is determined by SEVIRI pixel VZA.
- ii) False fire detections by M8 arising from issues related to the SEVIRI cloud mask implementation at certain VZA within the SEVIRI M8 data.

Both i) and ii) are related to VZA, and both effects have varying strengths over specific regions of Africa. In the case of i) the impact of pixel footprint area on the minimum detection limit of many satellite FRP products has been shown already (Freeborn et al., 2011, 2014; Kumar et al., 2011; Li et al., 2020). In this work, **Figure 3.13** and **Figure 3.14** clearly show that active fires occur with the highest frequency between 10° and 40° VZA in the M8 FRP-PIXEL product and between 20° and 50° in the M11 FRP-PIXEL product. Therefore, M8 images an area with smaller pixels, and with a higher general atmospheric transmissivity, over the regions with the most active fire. From the spatial distributions of total summed FRP (**Figure 3.10**) it can be seen that many regions with the highest total FRP, such as the two eastern most regions outlined in yellow, lie closer to the M8 sub-satellite (nadir) position. Therefore, these regions

will have a lower AF detection threshold in M8 than in M11, meaning that more small (lower FRP) fires will be detected in M8 than in M11.

The feature of false fire detections described in ii) has yet to be reported in other studies and is most probably not a systemic problem with the SEVIRI FRP-PIXEL algorithm, but rather an issue with the implementation of the Meteosat IODC operational product. Qualitatively the cumulated false AF detections can clearly be seen in **Figure 3.10** (outlined in red) and **Figure 3.15**, and individual false detections at a single SEVIRI acquisition can be seen in the SEVIRI Quality Product files from M8 and M11 acquired on 9<sup>th</sup> September 2018 19:45 UTC (**Figure 3.18**). Due to assumptions made in the MODIS-SEVIRI pixel screening procedure described in **Section 3.2.3.1**, a more explicit quantification of the scale of the problem is not currently available. As previous validations have not carried out analyses on the errors of commission and omission of SEVIRI at different VZA, whether these false detections are unique to the M8 product is difficult to determine. However, the negative values of  $FRP_{DIFF}$  in **Figure 3.15a** over the Horn of Africa indicate that this may also occur for M11, though to a much lesser extent than seen in M8. Further validation work is recommended in the future to further investigate SEVIRI AF detection performance at different VZA. Particularly studies expanded beyond the African continent to capture fires viewed from wider VZA by M11 SEVIRI would be of value. This will be an important step if there is a desire to build a synergetic dataset combining M8 and M11 FRP data together.

### 3.4.2 Vegetation Type and VZA Effect on FRP

The results of the Kruskal-Wallis H Test presented in **Section 3.3.5 (Table 3.8)** give clear confirmation that, even when viewed from different VZA, the FRP signal of different vegetation types is distinct in both SEVIRI products and in the MODIS product.

Two cases occurred in which biome FRP data were shown to not to be statistically different; closed canopy forest and managed lands in SEVIRI FRP data and shrubland and low-woodland savanna in the MODIS FRP data. The similar FRP signals for closed canopy forest and managed land are unexpected, but could result from causes such as seasonal effects, uncertainties in land cover classification, or them simply having similar FRP signals. The latter

is quite probable as these biomes also have a relatively low H-statistic in the MODIS FRP data (**Table 3.8**). In the case of shrubland and low-woodland savanna, these are shown to also have similar fire emission coefficients relating FRP to emission rates of Total Particulate Matter (TPM) (see **Chapter 4**), indicating that their FRP signals are potentially close in nature.

The effect of tree canopy cover on the interception of the FRP signal observed by satellites has been indicated by previous SEVIRI validation studies (Freeborn et al., 2014; Hall et al., 2019) and has been characterised explicitly by Roberts et al. (2018) who show through simulations that measured FRP decreases in direct proportion to percentage canopy cover. Since tree canopy has the effect of intercepting the surface emitted FRP signal from reaching the sensor, it follows that the angle at which a fire is viewed from by the sensor will have a collective effect on the interception of this signal. This idea is represented in **Figure 3.22**, which illustrates how the vegetation cover and VZA could combine either to amplify or reduce the interception of FRP at the sensor. This idea is investigated through the OLS fits of  $FRP_{DIFF}$  and  $VZA_{DIFF}$  in different biomes (**Figure 3.21**).

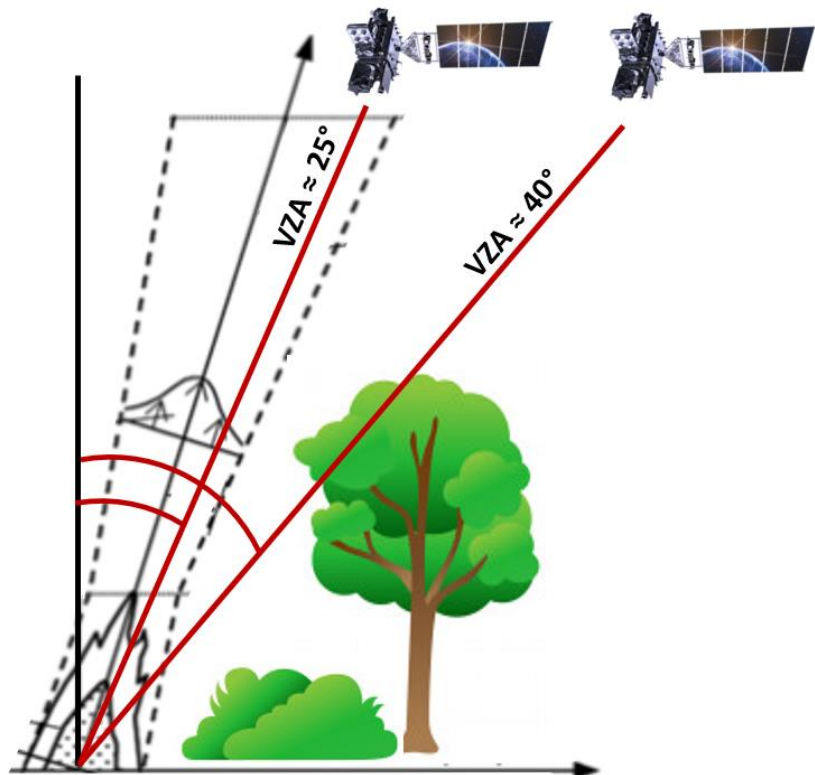


**Figure 3.22** Schematic showing the interception of the FRP signal from a surface fire measured by satellite in an area of significant tree canopy, and the potential impact of sensor VZA in amplifying this effect (adapted from Wang et al., 2009)

What might be expected if this conjecture holds true is that biomes which have taller vegetation (such as closed canopy forest, and the woodland savanna biomes) will have a more negative slopes in OLS regressions between  $FRP_{DIFF}$  and  $VZA_{DIFF}$ . By contrast, biomes which have little or no tall vegetation ( e.g. grassland and shrubland) will have relatively flat (close to zero) slopes in OLS fits between  $VZA_{DIFF}$  and  $FRP_{DIFF}$  as they are defined in **Section 3.2.5**. **Figure 3.21** shows that, in general, this is observed in the FRP per-area dataset with slopes of 0.35, -1.30, -1.44, -1.33, -1.54, and -2.15 (MW per VZA degree) for grassland, shrubland, managed land, closed canopy forest, low-woodland savanna and high-woodland savanna respectively. The closed canopy forest biome does not show conformation to this trend, and in fact has a very similar slope to that of shrubland and managed land. The Kruskal-Wallis H test described in **Section 3.3.5** showed closed canopy forest and managed land FRP measured by SEVIRI to not be statistically significant and this gives further evidence that these two biomes are closely related in terms of how their FRP signals may be affected by VZA. Despite the anomaly of closed canopy forest, the slopes of the other biomes in **Figure 3.21** support the conjecture that biomes with low tree cover (e.g. grassland) are less impacted by SEVIRI VZA variations than biomes with an increased components of canopy cover - such as high-woodland savanna and low-woodland savanna.

Factors such as the overall higher FRP measurements of M8 and the appropriateness of a least-squared regression test applied to this weakly heteroscedastic dataset could also attribute to uncertainties in the slopes derived. There is, therefore, room for further investigation into this interaction between biome type and VZA and their combined effect on FRP measures.

## 3.5 Summary and Conclusions

This work has used the MODIS MOD14 and MYD14 active fire products to carry out an evaluation of the SEVIRI FRP-PIXEL product – both that from Meteosat-8 centred over the Indian Ocean (Meteosat IODC) and Meteosat-11 centred over west Africa (the standard Meteosat position). Direct comparisons between the FRP measures of these two SEVIRI FRP products were also conducted. Data used were acquired between 1<sup>st</sup> January and 31<sup>st</sup>

December 2018 – focusing over Africa. The work here represents the first known assessment of the SEVIRI product from Meteosat IODC, and the first known comparison of the SEVIRI FRP-PIXEL product generated from sensors stationed at different positions.

In evaluations against MODIS, the AF error of omission rate for both SEVIRI products is found to be around 70%. M8 and M11 SEVIRI underestimate FRP compared to coincident MODIS FRP by between 36%-40% and 51% depending on the comparison method – total areal, per-area or per-fire. However, comparisons of individual fires simultaneously observed by SEVIRI and MODIS (per-fire comparisons), averaged over the day, show a less significant underestimation by SEVIRI (underestimation of 6% by M8 and 27% by M11) and a similar improved performance of individual fire FRP measures was observed by Roberts et al. (2015).

Measured FRP from the M11 satellite compared to the MODIS fire product (**Table 3.4**) shows a greater underestimation by SEVIRI than found in other works (Roberts et al., 2005, 2015; Roberts and Wooster, 2008; Freeborn et al., 2014). Based on the spatial and temporal scale of these previous studies (**Table 3.1**) it is probable that, due to the longer study period and larger study region used in this work, greater variation in the performance of SEVIRI products against the MODIS product is captured in the validation conducted here.

In comparisons against MODIS, M8 has an AF error of commission rate of 9% and for M11 this is far higher at 20%. However, direct comparisons between M8 and M11 showed that the error of commission rate for M8 is likely much higher and is underestimated in the procedure used herein (see **Section 3.3.4**). Putting to one side the false detections in M8, when separated by VZA the AF errors of omission and errors of commission generally increase as a function of the SEVIRI sensor VZA between 0° and 40°. But the errors do not change significantly between 40° and 70° (**Figure 3.9**).

When FRP measurements of M8 SEVIRI and M11 SEVIRI are compared directly, M8 has consistently higher measured FRP than M11. An assessment of the distribution of fire activity with respect to VZA shows that higher FRP in M8 is probably caused by a combination of false fire detections in M8 and the sub-satellite position of M8 being closer to regions of high fire activity. The result of the latter, is M8 observations having a higher spatial resolution and higher atmospheric transmission than M11 observations in areas of high fire activity.

Comparisons between the calculated variables of  $VZA_{DIFF}$  and  $FRP_{DIFF}$  give a least-squares linear best fit with a slope of -1.21 MW per VZA Degree and intercept of 32.8 MW, which can be interpreted as follows;

- i) For each degree of VZA that a fire is closer to SEVIRI nadir, it will have a retrieved grid cell FRP on aggregate, 1.21 MW higher.
- ii) On aggregate, over Africa and over the year, when fires are mapped to a  $0.5^\circ \times 0.5^\circ$  grid, M8 grid cells contain 32.8 MW more FRP than do M11 grid cells.

The quantification of VZA effects on FRP will be impacted by the issue of false AF detections in M8, and more work is needed to understand the statistical robustness of the coefficients derived in the OLS best fits used in this study. A similar analysis applied to specific vegetation types shows that fires in biomes with an element of canopy height have a measured FRP which is more strongly affected by VZA than for biomes which have relatively low vegetation heights.

In the wider scientific context of the effort to monitor fire from space, the findings of this chapter have two key implications. Firstly, in evaluations against the MODIS MOD14 and MYD14 fire products and in comparisons against each other, the SEVIRI FRP-PIXEL product from Meteosat-8 and Meteosat-11 observe different magnitudes of FRP over the continent of Africa in 2018 from their differing viewing positions. These differences are partly due to the spatial distribution of fire activity over the continent relative to the view provided by the two sensors, and partly due to false detections in the M8 product. Per-fire comparisons which remove some of the bias from these false detections, indicate that M8-retrieved FRP is between 7% and 20% higher than retrieved by M11. If these two products were to be incorporated into a merged geostationary fire product, significant consideration of these differences should likely be taken. The results from this Chapter guide the below recommendations for future work:

- i) Address and remove false detections from the M8 SEVIRI FRP-PIXEL product and ascertain definitively whether M11 suffers the same issue at wide VZA beyond Africa.

- ii) In reporting the FRP for any given region, the SEVIRI product in which the region has the smaller VZA will likely give a more accurate characterisation of fire and should be used preferentially.
- iii) Depending on the application, for both SEVIRI products considered here there may be a need for a “small fire” (low FRP) correction to – on aggregate – compensate for fires burning below the minimum FRP detection threshold of SEVIRI, and this correction should likely vary with VZA.

Secondly, results from this chapter also show that SEVIRI VZA impacts the characterisation of FRP and that the extent to which this is true varies by biome, due possibly to the level of interception by tree canopies. The effect being that vegetation types with an element of tree canopy are more strongly impacted by VZA than vegetation types that have minimal height. The full FRP grid cell datasets show that, as observed by satellite, the FRP measures from each of the six biomes defined in this Chapter are distinct, suggesting that the separation of vegetation classes presented here is appropriate for future work that might aim to distinguish the FRP signal and e.g. fire emissions of the biomes. This is with the exception of closed canopy forest and managed land which, in SEVIRI, produce apparently statistically similar FRP distributors. There may, however, be other factors involved - such as seasonal effects or the spatial distribution of these biomes with respect to the SEVIRI sub-satellite position

# Chapter 4 Advances in the Estimation of High Spatio-Temporal Resolution Pan-African Top-Down Biomass Burning Emissions made using Geostationary Fire Radiative Power (FRP) and MAIAC Aerosol Optical Depth (AOD) Data

## 4.1 Introduction

This Chapter presents updates to the ‘top-down’ Fire Radiative Energy Emissions’ (FREM) approach to biomass burning emissions calculations of Mota and Wooster (2018), which bypasses the estimation of fuel consumption - a major source of uncertainty in widely used ‘bottom up’ approaches. Elements of the research presented here have been published in a peer reviewed publication (Nguyen and Wooster, 2020), however, updates to the derived emission coefficients of that work are presented here with additional details not included in that publication.

Most widely used fire emission inventories use a ‘bottom-up’ approach, in which estimates of total fuel consumed,  $FC_T$ , are generated from EO-derived metrics of burned area (BA), active fire (AF) counts and/or fire radiative power (FRP) as was discussed in **Section 2.4.1**. These  $FC_T$  estimates are multiplied by biome-specific emission factors (EFs) to relate each kilogram of burned dry matter to the amount of a trace gas or aerosol released into the atmosphere. EFs are mostly derived from small scale laboratory experiments or ground-based field measurements (e.g. Andreae and Merlet, 2001; Akagi et al., 2011; Andreae, 2019), and more

rarely through airborne sampling of fire smoke plumes (e.g. Abel et al., 2003; Lavrov et al., 2006; Quennehen et al., 2012). Several bottom-up emissions inventories were discussed in detail in **Section 2.4.1** including GFED (van der Werf et al., 2006, 2010, 2017), GFAS (Kaiser et al., 2012) and FINN (Wiedinmyer et al., 2011). Biases and uncertainties present in these landscape fire inventories stem primarily from:

- i) Limitations of the original satellite observations and the fire detection and characterisation algorithms applied to them to generate fire metrics (see **Section 2.2** and **Section 2.3**). Compromises are generally made between spatial and temporal resolution, and algorithm errors of omission and commission impact the precision and accuracy of the satellite-derived fire measures (Boschetti et al., 2004; Freeborn et al., 2009; Randerson et al., 2012).
- ii) Assumptions associated with estimating fuel consumption per unit area ( $\text{kg.m}^{-2}$ ) or any alternative scalar required to turn satellite-derived metrics into an estimate of burned dry matter (**Section 2.4.1**, Kasischke and Penner, 2004; Reid et al., 2009; Wooster et al., 2011; Kaiser et al., 2012)
- iii) Limitations and uncertainties in the EFs used to convert between burned dry matter and the final emissions of aerosols and trace gases (Van Leeuwen and van der Werf, 2011).

Top-down methodologies such as those of Ichoku and Ellison (2014) and Mota and Wooster (2018) have taken to deriving landscape fire emissions estimates directly from satellite-derived FRP measures to address ii). These approaches bypass the fuel consumption estimation step altogether and reduce the number of assumptions required during the fire emissions calculation. In these approaches, a biome dependant or geographically dependent scalar (smoke emission coefficient;  $C_{biome}$  or  $C_e$ , in  $\text{g.MJ}^{-1}$ ) captures the relationship between the FRP of fires and their associated total particulate matter (TPM) emissions (see **Section 2.4.2**). These coefficients are derived from a series of matchup fires where FRP data and satellite-based aerosol optical depth (AOD) observations are available. Once this scalar is determined, the need to calculate fuel consumption is removed when deriving further smoke emissions estimates from the FRP data of observed fires.

Whilst these top-down approaches successfully bypass the fuel consumption step, in both the Fire Energetics and Emissions Research (FEER; Ichoku and Ellison, 2014) and Fire Radiative Energy Emissions (FREM; Mota and Wooster, 2018) approach, the coarse 10 km spatial resolution of the MODIS AOD product used to derive in-plume TPM, and performance issues related to this AOD product in thick-smoke affected environments, can introduce significant uncertainties when deriving the  $C_e$  values.

The aim of this Chapter is to develop a series of improvements to the FREM methodology of Mota and Wooster (2018) – hereafter termed FREMv1 - and to use this updated FREMv2 method to produce a new SEVIRI FRE-based fire emissions inventory for TPM and carbonaceous gases for Africa. Key of these developments is the exploitation of a far higher spatial resolution (1 km) MODIS AOD product (Lyapustin et al., 2018) that offers improved performance in heavily smoke impacted environments. Secondary aims of this Chapter are to compare the FREMv2 emission inventory developed here with other widely used emissions inventories (GFAS, GFED and FEER) and to back-calculate total fuel consumption estimates using high resolution burned area data.

## 4.2 Limitations in Current Top-down Methodologies

### 4.2.1 MODIS AOD Observations

In all previous remote sensing based top-down methodologies, biome dependant (e.g. FREMv1 and Lu et al., 2019) and geographically dependant (e.g. FEER; Ichoku and Kaufman, 2005; Ichoku and Ellison, 2014) smoke emission coefficients have been derived using satellite-based FRP observations and the 10 km AOD (MOD/MYD04) MODIS Level 2 product (Levy et al., 2013) from Terra and Aqua. The outputs of two different AOD retrieval algorithms are available in this MODIS product;

- i) Dark Target (DT) - designed to work over dense vegetation.
- ii) Deep Blue (DB) -developed for desert surfaces but updated to apply to most cloud free land.

Output from Dark Target was used by Ichoku and Kaufman (2005) and Ichoku and Ellison (2014), whereas FREMv1 and Lu et al. (2019) use the Deep Blue AOD retrieval (introduced in Collection 6; Levy et al., 2013) since it showed better agreement with AREONET AOD observations across southern Africa (Sayer et al., 2014).

The MODIS 10 km AOD (MxD04) product and its updates (Tanre et al., 1997; Hsu et al., 2004, 2006, 2013; Remer et al., 2005; Levy et al., 2013) has been produced for more than 15 years, is widely used within the air quality community (Remer et al., 2013), and has been extensively characterised and validated (Holben et al., 2001; Chu et al., 2002; Ichoku et al., 2002, 2003; Sayer et al., 2013; Livingston et al., 2014; Xiao et al., 2016; Jethva et al., 2019). However, its use in top-down fire emissions inventories introduces some key uncertainties and limitations. These include issues associated with its relatively low 10 km spatial resolution (Lyapustin et al., 2011; Raffuse et al., 2013; Remer et al., 2013; He et al., 2017), the cloud mask implemented in both the DT and DB versions (Levy et al., 2013; Raffuse et al., 2013; Remer et al., 2013; Livingston et al., 2014), and MODIS view-angle effects (Sayer et al., 2015). The more recent 3 km MODIS AOD product which applies the same DT retrieval algorithm (Remer et al., 2013) also suffers from distortions at wide swath angles and erroneous cloud masking over thick smoke.

AOD retrievals in the MxD04 product are produced at 10 km resolution to improve the signal-to-noise ratio of the input reflectance data (Tanre et al., 1997). In the DB product (henceforth referred to as MxD04\_DB) raw 1 km pixels are arranged into 10×10 pixel blocks and screened to remove those affected by cloud. The remaining pixels in each 10 km block are then used to obtain the AOD retrieval (Hsu et al., 2013), and the number of 1 km<sup>2</sup> pixels used in each 10 km<sup>2</sup> pixel accompanies the final 10 km AOD estimates within the product files. When targeting smoke plumes, investigations carried out in this Chapter and those of other studies (Levy et al., 2013; Livingston et al., 2014) show that the conservative cloud mask used by both the DT and DB algorithms result in cases of (i) the 10 km AOD pixels at the locations of the thickest smoke being completely masked out, and (ii) the 10 km AOD pixels in areas of thick smoke being retrieved from only a fraction of the 1 km pixels present within the ~ 10 km × 10 km box. **Figure 4.1a** and **Figure 4.1b** show an example of a smoke plume where some MxD04\_DB pixels use as little as 40% of the original one hundred MODIS 1 km pixels to

retrieve a single 10 km AOD value. A comparison with the 500 m MODIS true colour image for the same area (**Figure 4.1c**) demonstrates how the low spatial resolution of the MxD04\_BD product introduces further uncertainty into the determination of the plume boundary, particularly when compared with the alternative 1 km MAIAC AOD product (**Figure 4.1d**) discussed further in **Section 4.3**.

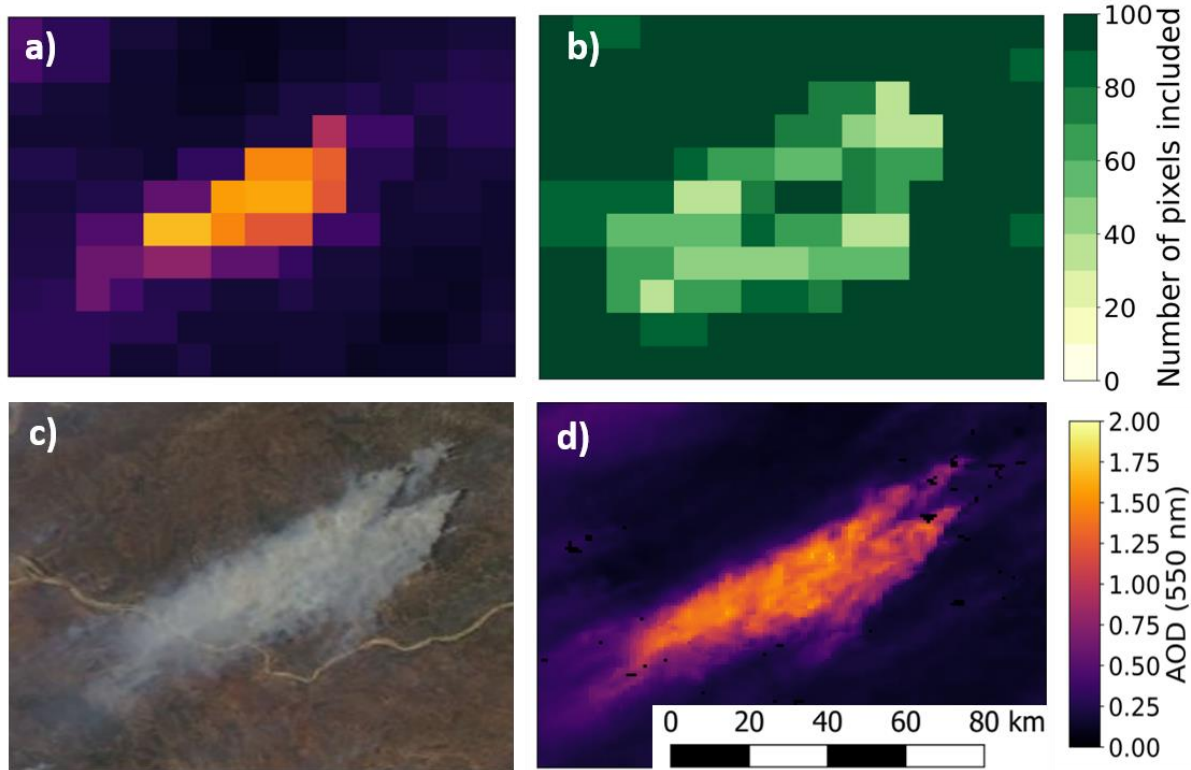


**Figure 4.1** Example plume from a large fire burning north of the Save River (Mozambique), imaged on 8<sup>th</sup> October 2015 at 11:15 UTC via (Aqua) MODIS sensor (at a VZA 40.6°). (a) 10 km MxD04\_DB AOD product; (b) MxD04\_DB field showing the number of 1 km reflectance pixels (out of 100) used to retrieve each 10 km AOD pixel value; (c) 500 m MODIS Corrected Reflectance (True Colour) image; and (d) 1 km MCD19 MAIAC AOD product derived from the same MODIS imagery shown in (c). The colour scale shown in (d) is also relevant for (a). The plume is far more easily distinguished in the 1 km than the 10 km AOD product and better matched to the smoke spatial distribution shown in the MODIS true colour image of (c). Unlike the 1 km AOD product of (d), the 10 km MxD04\_BD AOD data of (a) rather poorly defines the plume bounds and some pixels in this product are heavily impacted by the cloud mask which removes AOD pixels over the thickest smoke (b). Some erroneous masking does occur in the 1 km product of (d), shown as the black pixels, but this is minimal and addressed via the interpolation described in **Section 4.3**.

The extreme masking of smoke affected 1 km pixels as cloud in the MxD04\_DB algorithm, as demonstrated in **Figure 4.1**, introduces uncertainty and probably bias into any estimates of total particulate matter (TPM) derived from the 10 km MxD04 AOD observations. Since the excluded pixels are mainly located over the thickest smoke, their exclusion is likely to significantly affect the final retrieved 10 km AOD, and therefore TPM measures. Additionally, the complete masking of 10 km pixels in some cases limits the number of plumes that can be identified and used in deriving the smoke emission coefficients,  $C_e$ . Both Mota and Wooster (2018) and Lu et al. (2019) take measures to minimise the effect of completely masked MxD04\_DB pixels. Mota and Wooster (2018) retain MxD04\_DB pixels with quality mark  $\geq 2$ , resulting in the inclusion of MxD04\_DB pixels using as little as 40% of the native 1 km pixels being used in  $C_e$  derivation (e.g. in **Figure 4.1b**), and they also excluded plumes comprising any completely masked 10 km pixels. Lu et al. (2019) use a nearest neighbour method to fill gaps in the MxD04\_DB data over plumes caused by erroneously ‘cloud masked’ AOD pixels.

Another source of uncertainty introduced when using either the MODIS DT or DB MxD04 product comes from the MODIS ‘bow-tie’ effect (detailed in **Section 2.3.1**) that results from the MODIS design and scan geometry and the Earth’s curvature (Wolfe et al., 1998). Above view zenith angles (VZA) of  $\sim 20^\circ$ , two key distortions occur with respect to MxD04\_DB - (i) growth of the MODIS 10 km AOD pixel area from about  $10 \times 10$  km at nadir to around  $20 \times 40$  km at the scan edge, and (ii) the overlap of successive scans towards the scan edge meaning features are duplicated in adjacent pixels (Wolfe et al., 1998). These features result in an AOD data product which has a dependency on the location of the AOD pixels within the MODIS swath, and there are indications that this may influence the statistics of the AOD retrievals towards the scan edges (Sayer et al., 2015; Mhawish et al., 2019). This potentially introduces bias into top-down methodologies that use the MxD04 AOD products without limiting the VZA of observations used in the derivation of  $C_e$  values.

A further limitation of the MxD04 AOD products relate to their fundamentally low 10 km nadir spatial resolution (see **Figure 4.1**), which is unable to resolve smoke plumes from many smaller fires or plumes from fires which are not sufficiently isolated from other aerosol sources (primarily other nearby fires). In both cases, differences between the in-plume AOD and the background AOD (i.e. the AOD anomaly) may not be significant enough to define the

AOD pixels that represent the plume. This places a limit on the minimum fire size used to derive  $C_e$  or  $C_{biome}$  values and makes the sampling of fires over certain areas during periods of peak fire activity difficult, as their plumes often merge together (Mota and Wooster, 2018).

#### 4.2.2 Other Limitations

Separate from the MxD04 AOD product issues, differences in the method chosen to calculate the value of an AOD background exist between top-down methodologies. In all top-down inventories discussed in this work, the equations proposed by Ichoku and Kaufman (2005) (see **Section 4.4.2**) are used to convert AOD to the emitted TPM of an individual fire. The fire emitted AOD for a given smoke plume is defined as the summed total AOD of the smoke plume above the AOD background. It is clear then, that the choice of AOD background value used in these calculations impacts the final TPM estimate, and therefore the  $C_e$  or  $C_{biome}$  values derived from matchups between TPM and FRE. Ichoku and Kaufman (2005) and Ichoku and Ellison (2014) select background AOD values based on pixels immediately up-wind of individual smoke plumes, whereas Mota and Wooster (2018) take background AOD values to be the 20<sup>th</sup> percentile AOD of all values within set 500 km<sup>2</sup> regions of interest bounding a smoke plume. The background AOD values estimated from this large-scale averaging in FREMv1 may not be fully representative of the true background into which smoke from a fire is emitted.

The above problematic characteristics of the MxD04 products, and the FREMv1 and FEER methodologies, contribute to uncertainty and possibly bias in the smoke emission coefficients derived, and thus in the resultant smoke emissions estimates.

### 4.3 Developments to the FREM Approach

The methodology proposed here builds on the original FREMv1 approach of Mota and Wooster (2018) to address the limitations described above. The main advance is use of an alternative MODIS AOD product that offers substantial advantages over the MxD04 products when used in smoke-affected areas. This alternative AOD product is based on the Multiangle Implementation of Atmospheric Correction (MAIAC) algorithm, developed to retrieve

surface bidirectional reflectance factor (SBRF), internal cloud mask and AOD over land (Lyapustin et al., 2011). The MAIAC AOD product (Collection 6 MCD19A2; Lyapustin et al., 2018) provides combined Aqua and Terra AOD retrievals at 1 km resolution over both dark and bright surfaces, and has been shown to improve the resolvability of atmospheric smoke and dust features compared to the 10 km MxD04 product (Emili et al., 2011; Lyapustin et al., 2011, 2012; Jethva et al., 2019; Mhawish et al., 2019). At AERONET station locations, both Emili et al. (2011) and Jethva et al. (2019) show that the MAIAC AOD product provides more than double the number of AOD retrievals compared to MxD04\_DB, due to its higher spatial resolution and improved cloud masking. In fact, the MAIAC algorithm explicitly includes a ‘smoke test’ to discriminate biomass burning smoke from clouds (Lyapustin et al., 2012). Other evaluations have compared the MAIAC product to the VIIRS 750 m spatial resolution IP AOD product, to AERONET AOD measurements, and to surface measurements of particulate matter (Hu et al., 2014; Arvani et al., 2016; Martins et al., 2017; Superczynski et al., 2017). They have shown its improved coverage compared to the standard VIIRS AOD product and its good agreement with ground-based AOD and particulate matter measures.

In addition to its higher spatial resolution and improved cloud mask, some key features of the MAIAC product address issues related to the dependence of AOD retrievals on VZA in the MxD04 product. These include the gridding of L1B MODIS bands to 1 km resolution prior to AOD retrieval using an area-weighted method (Wolfe et al., 1998), and the calculation of surface BRF using a dynamic spectral regression coefficient (SRC) (Lyapustin et al., 2011). The former results in an improved representation of any given 1 km grid cell by appropriately weighing the contribution of observations falling within that cell, and this is especially important at the swath edge where the MODIS pixel area is up to eight times larger than at nadir. The dynamic SRCs, are calculated from a time series analysis of previous AOD retrievals for each 1 km pixel. Therefore, when VZA are well sampled in the preceding retrieval times series (multiple cloud free observations per pixel), SRC values represent well the angular component of surface BRF (full details can be found in Lyapustin et al., 2011). The final MAIAC AOD product is reported on a 1 km grid in the MODIS sinusoidal projection (Lyapustin et al., 2018) and Mhawish et al. (2019) show VZA-dependant bias to be the lowest in MAIAC AOD retrievals compared to the output of the MxD04 DT and DB algorithms.

**Figure 4.2a** shows fire emitted TPM estimates for a series ( $n=635$ ) of African smoke plumes, as derived from the MxD04\_DB AOD product and the MAIAC AOD product, all calculated via multiplication of the plume-integrated AOD anomaly (accounting for pixel area) by the smoke mass extinction coefficient (see **Equation 4.1** and **Equation 4.2**). Whilst the MAIAC-derived TPM estimates appear consistent across all VZA's, those from MxD04\_BD increase significantly at  $VZA > 40^\circ$ . Inclusion of plumes observed at high VZA values in the MxD04\_DB product used by Mota and Wooster (2018) could lead to artificially high in-plume TPM estimates, and therefore a high bias in the derived  $C_{biome}$  values in FREMv1. When a comparison is made between MxD04\_BD and MAIAC estimated TPM from plumes with  $VZA < 20^\circ$  (**Figure 4.2b**), MAIAC-based TPM estimates are typically higher (on average by  $\sim 26\%$ ) than those of MxD04\_BD. This likely results from the less conservative MAIAC cloud masking and the increased number of valid AOD retrievals available over the thickest smoke when compared to MxD04\_BD.

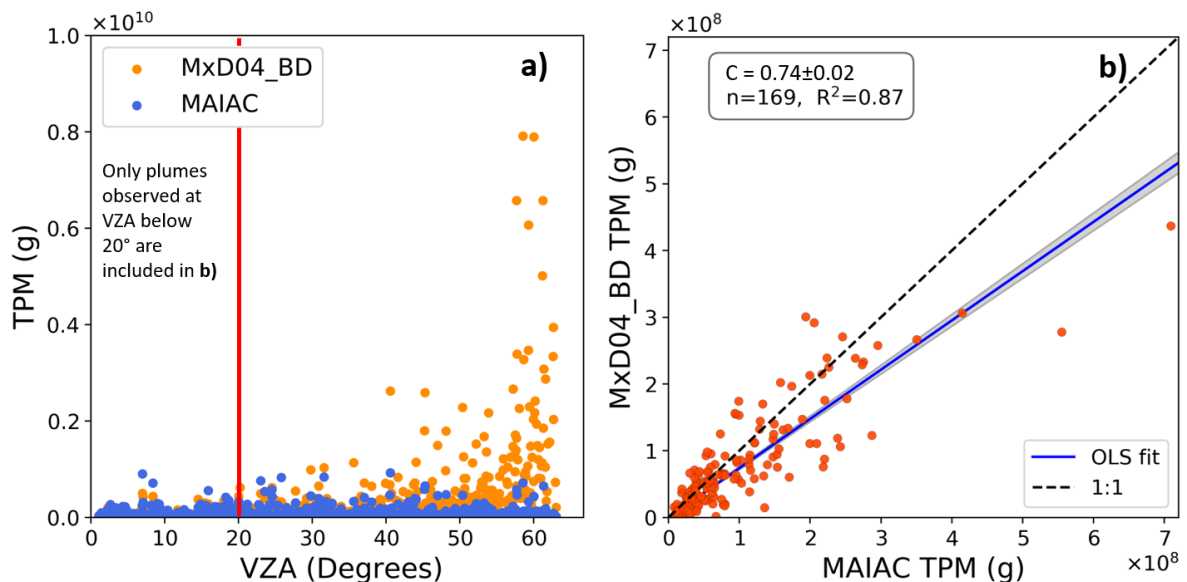


**Figure 4.2** (a) Estimated fire emitted Total Particulate Matter (TPM) in 635 individual smoke plumes, as derived from the 10 km MxD04\_DB AOD product (orange) and the 1 km MAIAC AOD product (blue), shown as a function of sensor view zenith angle (VZA). (b) Direct comparison of the matching MxD04\_DB and MAIAC-derived TPM values for each plume in (a), restricted to those observed at  $VZA \leq 20^\circ$ .

Another update performed in FREMv2 compared to FREMv1 is an improved method for calculating the background AOD value of smoke plumes. FREMv2 applies a localised value for background AOD, as opposed to the large-area-average value applied in FREMv1. The minimum AOD pixel within a buffered area of the smoke plume is, in most cases, up-wind of the targeted plume and is used as the background AOD value. This approach is more similar to that adopted by Ichoku and Kaufman (2005) and Ichoku and Ellison (2014), and is justified by the argument that (i) background AODs derived from large scale averaging could be biased by reflectance anomalies or aerosol changes far from the plume, for example dust in the averaging area, and (ii) a large-area-averaged background will also be insensitive to the immediate local AOD background of the plume (e.g. during periods of high fire activity when local atmospheric particulate matter concentrations are likely to be already high).

Other developments in the FREMv2 methodology described in this Chapter include the consideration of relative humidity in the estimation of fire generated TPM using the smoke mass extinction efficiency, expansion of the study region to the entirety of Africa, and the inclusion of more up-to-date land cover map and use of tree canopy percentage cover information to delineate more precisely the fire-relevant biomes.

## 4.4 Smoke Emission Coefficients, $C_{biome}$ , Derivation

### 4.4.1 Geographic Area and Biome Classification

The FREMv2 smoke emission coefficients,  $C_{biome}$ , and final emissions estimates presented in this Chapter expand the Southern Hemisphere Africa (SHAF) region studied in FREMv1 to include Northern Hemisphere Africa (NHAF). The SHAF dry season is normally from July to September, and in NHAF it is from November to April. These periods also represent the primary fire seasons in these regions. The dense tropical forests close to the equator (e.g. in northern D.R.C and Gabon) are wetter and less susceptible to large-scale fires compared to those dominated by deciduous and herbaceous vegetation further north and south. These woody savannah and shrubland/grassland areas also host a large portion of Africa's biomass burning. In addition to expanding FREMv2 to include the whole of Africa, an updated

landcover map that provides more detailed biome classification was developed. This updated map is also used in **Chapter 3** to investigate the impact of VZA on SEVIRI FRP measures in different biomes. The 2015 European Space Agency (ESA) Climate Change Initiative (CCI) Landcover map (Validated in ESA, 2017) - derived from 300 m spatial resolution PROBA-V observations and comprising 36 landcover types - is used to define five distinct biome classes in this work. Similar to FREMv1, grassland and woodland savanna are classified as separate biomes as suggested by Korontzi et al. (2004) for fire-related GHG emission reporting. Details of the CCI land cover class codes assigned to FREMv2 biomes are shown in **Table 4.1**. The five biomes were defined by the main vegetation types of *closed canopy forest*, *woodland savanna/open forest*, *grassland*, *shrubland* and *managed lands*. Since the biome classes of FREMv1 were based on the GLOBCOVER 2009 landcover map (<http://due.esrin.esa.int/>), which differs from the 2015 CCI landcover map in some respects, the spatial distribution of the biome classes in this work also differs from those of FREMv1, for example over the Kalahari region of southern Africa. To provide further biome discrimination, this work includes use of percentage tree cover (above 5 m height), taken from the 30 m Landsat Vegetation Continuous Fields (VCF) product of 2015 (<https://landsat.gsfc.nasa.gov/>) which is shown for Africa in **Figure 4.3a**.

Woodland savanna is by far the largest contributing biome to FRE release over Africa (**Figure 4.4**) and correct assessment of its smoke emissions is critical to the overall accuracy of biomass burning emissions estimates. Areas of woodland savanna are dominated by surface fires (Van Leeuwen et al., 2014). Where vegetation height is an additional component, these biomes have the potential to produce smoke plumes more influenced by surface litter and woody debris (Heil et al., 2010). They may also be more affected by canopy interception of surface-emitted FRP as was suggested in **Chapter 3** and other works (Freeborn et al., 2014; Roberts et al., 2018). Hence, to improve the precision of  $C_{biome}$  values for woodland savanna fires, this class was separated into *low-woodland savanna* and *high-woodland savanna* using a 20% VCF tree cover threshold (**Figure 4.3b**). This threshold was selected based on the similarly high  $r^2$  values obtained from these split datasets in  $C_{biome}$  derivation using ordinary least-squares (OLS) regression (see **Figure 4.7**).

**Table 4.1** CCI landcover classes assigned to the FREMv2 biomes in this study and the Landsat VCF tree cover threshold used to separate the woodland savanna class. CCI class codes are detailed in **Appendix A**.

FREMv2 Biome	Assigned CCI class codes	Landsat VCF Tree Cover above 5 m
Closed canopy forest	50,180,160,170	-
Low-woodland savanna	60,61,62,70,90,100,110	< 20 %
High-woodland savanna	60,61,62,70,90,100,110	> 20 %
Shrubland	120,122,121	-
Grassland	130,150,151,152,153	-
Managed land	10,11,12,20,30,40,190	-

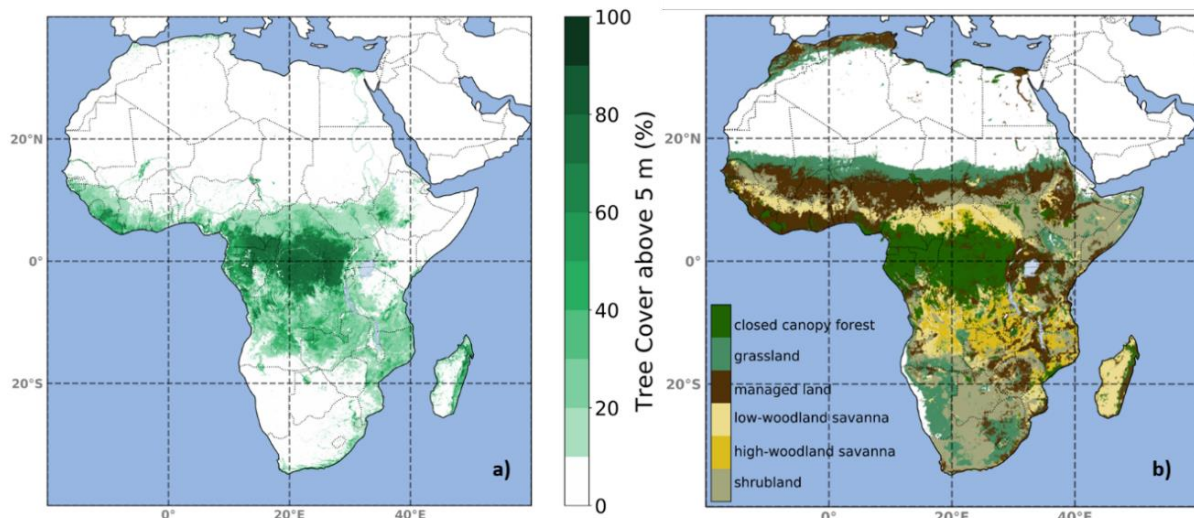


**Figure 4.3** (a) Mapped percentage tree cover above 5 metres, as determined from the 30 m spatial resolution Landsat Vegetation Continuous fields (VCF) product for 2015. (b) FREMv2 biome map for Africa derived from the 2015 ESA CCI Landcover map (itself derived from 300 m PROBA-V imagery) and the Landsat VCF product. Biomes were aggregated from the 36 land cover types defined in the original CCI map, with the two woodland savanna biomes separated using (a) (see **Table 4.1**).

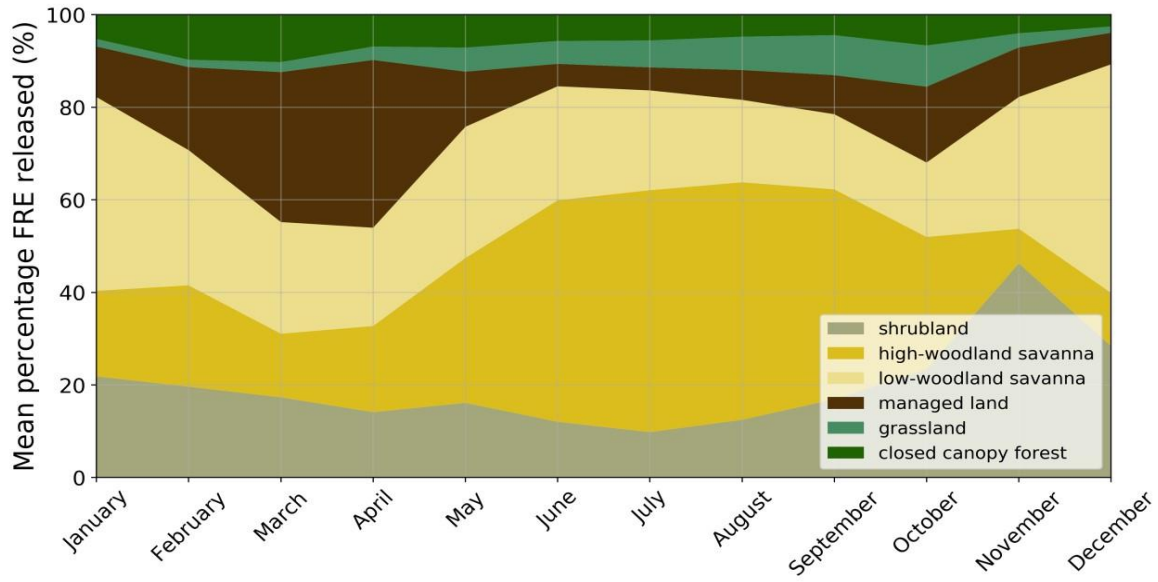


**Figure 4.4** Mean percentage contribution of different biomes to the fire radiative energy (FRE) released by fires between 2013 and 2018. FRE measures are derived from the SEVIRI FRP-PIXEL product. On average woodland savanna fires contribute the greatest total FRE throughout the year, except for in November, and this means their determination is especially important for overall smoke emission estimate accuracy. The importance and abundance of fires in this biome is reflected in the high numbers of fire-plume matchups identified for both the *low-* and *high-woodland savanna* biomes (see **Section 4.4.3**).

The FREMv2 biome map was re-projected and aggregated to the ‘standard’ Meteosat SEVIRI full disk projection, such that each SEVIRI pixel was assigned a sub-pixel fraction of each biome, with the overall pixel class assigned to the majority fraction (**Figure 4.3b**). Locations of the closed canopy forest, low-woodland savanna and high-woodland savanna biomes (the main classes having vegetation above 5 m height) broadly match the tree cover spatial distribution of the VCF tree cover product (**Figure 4.3a**), and also agree well with tree cover maps derived from MODIS data (e.g. Hansen et al., 2002; Sexton et al., 2013; Kobayashi et al., 2016).

#### 4.4.2 FRP and AOD 2015 Datasets and Fire Matchups

The geostationary Meteosat SEVIRI FRP-PIXEL product of Wooster et al. (2015) was the primary FRP data input for derivation of the  $C_{biome}$  values in FREMv2. The full spatio-temporal resolution (15 min, 3 km at nadir) FRP-PIXEL product covering NHAF and SHAF during 2015 was acquired from the EUMETSAT Land Surface Analysis Satellite Applications Facility (LSA SAF: <http://landsaf.meteo.pt>). The AOD product used was the Terra and Aqua combined MODIS MAIAC 550 nm 1 km product (Collection 6 MCD19A2; Lyapustin and Wang, 2018) previously described in **Section 4.3**. Fire activity from the SEVIRI FRP-PIXEL product was assigned to MAIAC AOD measurements of smoke plumes in what is here referred to as ‘fire matchup selection’.

First, a blob detection procedure (difference of Gaussian; Lindeberg , 1998) commonly used in computer vision was applied to each MAIAC AOD image to identify regions of interest (ROIs) containing potential smoke plumes. These ROIs were filtered to keep only those with matching active fires in SEVIRI data - spatially contiguous FRP pixels observed between 00:00 local time and the MODIS overpass time. To ensure complete sampling of all fire activity contributing to a given smoke plume, the SEVIRI FRP-PIXEL Quality Product detailed in Wooster et al. (2015) was used to filter out fires that were cloud-obscured leading up to the MODIS overpass time. In cases when both Aqua and Terra MAIAC AOD data were available, the Aqua data – which are acquired closer in-time to the peak of fire diurnal cycles in Africa (Giglio, 2007; Andela et al., 2015) - were preferentially used. This subset of candidate fire matchups was subject to a final manual check to remove any erroneously identified or poorly defined plumes. Each remaining ROI containing a smoke plume had the AOD boundary of the plume defined via histogram thresholding of AOD pixel values (**Figure 4.5a** and **Figure 4.5b**). The convex hull of the plume feature was used to define the plume edges and all FRP pixels measured within this bound, between 00:00 hrs and the MODIS overpass time of the AOD image, were categorised as being from the fire which contributed smoke to the plume (**Figure 4.5c**). In most cases FRP pixels were not observed until 08:00 local time. The 1 km resolution of the MAIAC data meant analysis of plume RBG imagery was not needed to help define plume features, unlike with the 10 km MxD04\_DB data used in FREMv1 (Mota and Wooster, 2018).

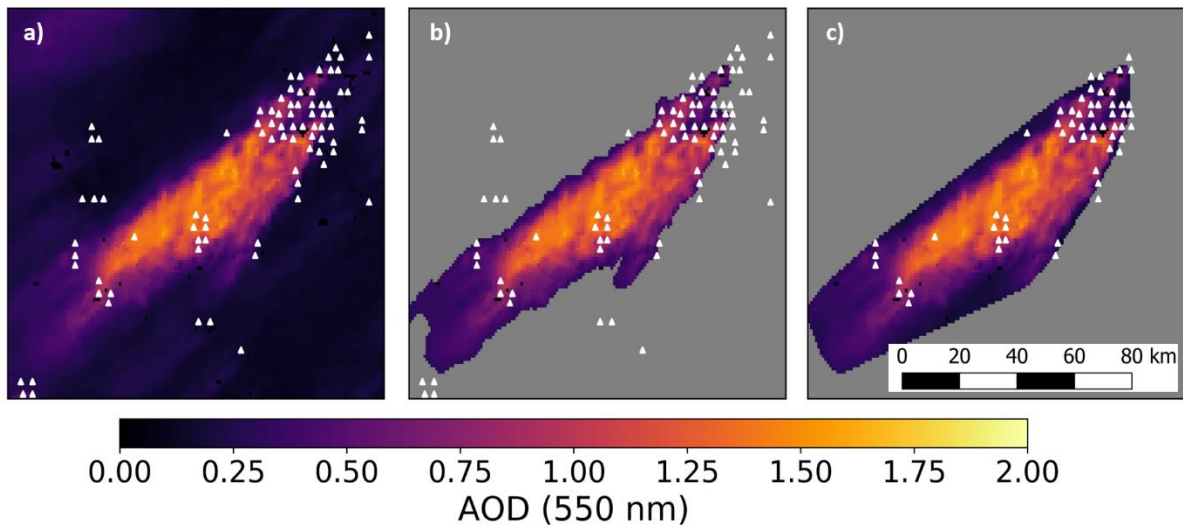


**Figure 4.5** Example region of interest (ROI) containing the fire shown in **Figure 4.1** along with matchup active fire pixels (*white triangles*) from the SEVIRI FRP-PIXEL product detected between 00:00 local time and the MODIS overpass time. (a) MAIAC 1km AOD and SEVIRI active fire (AF) pixels; (b) histogram thresholding to discriminate the plume from the surrounding ‘ambient’ background. (c) SEVIRI AF pixels detected within the convex hull of the plume are considered to come from the same ‘fire’ that produced the smoke plume. The fire radiative energy (FRE) of the causal fire is then calculated from these observations and used to match to the AOD-derived total particulate matter (TPM) (see **Figure 4.7**).

Only fire matchups for which a single FREMv2 biome represented more than 50% of the observed FRP pixels in a fire were retained. In some cases, the MAIAC AOD cloud mask did screen out some pixels within the smoke plume (e.g. pixels in black in **Figure 4.1d**), though the impact was far less than for the 10 km MODIS MxD04 AOD data. To preserve the accuracy of fire emitted TPM estimates, matchup fires were limited to plumes having MAIAC AOD retrievals at more than 95% of their pixels, and a Radial Basis Function (RBF) interpolation was used to fill gaps from the relatively few missing AOD pixels. A sensitivity analysis was carried out to assess the impact of this interpolation on the calculated TPM values. To do this additional AOD pixels were purposely removed from plumes and their values were then re-estimated via the RBF interpolation. Minimal impact was shown due to the quality of the interpolation procedure and the fewer than 5% of in-plume AOD pixels missing. A comparison of TPM values calculated from plumes where the interpolation was and was not applied is shown in **Figure 4.6**.

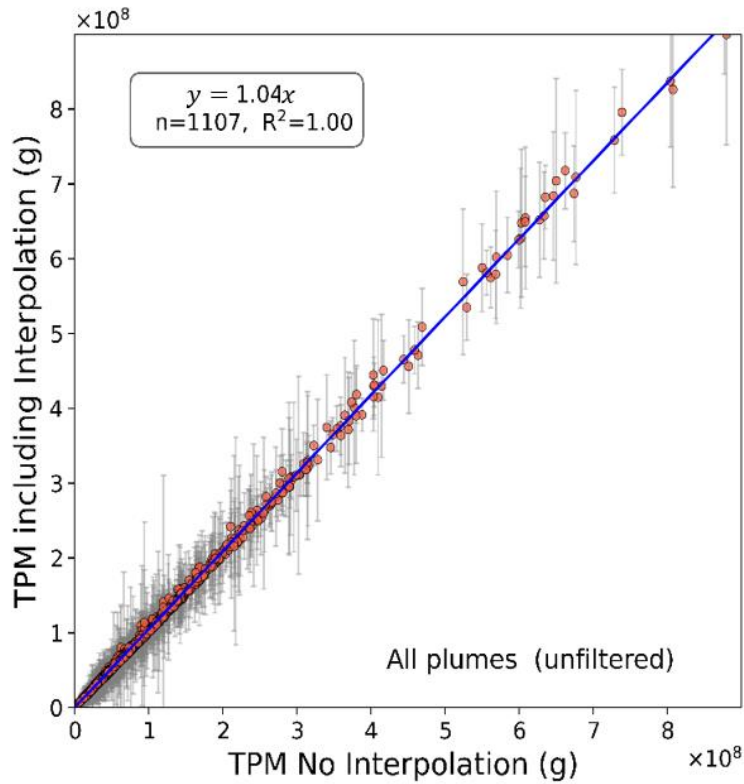


**Figure 4.6** Sensitivity analysis of the RBF interpolation procedure applied to plumes to account for the, up to 5% , missing MAIAC AOD pixels in fire-plume matchups.

After the pre-processing and data screening described above, 968 fire matchups remained for  $C_{biome}$  derivation. Each fire-plume matchup had its FRE and column integrated mass of TPM estimated, the former from the temporal integration of FRP from the start of fire activity on the day of the fire to the time the MAIAC AOD data were acquired. The latter were calculated following the same approach as Ichoku and Kaufman (2005). The fire emitted AOD,  $AOD_{550}^f$ , of each plume is defined as:

$$AOD_{550}^f = \sum_{i=1}^{N^f} (AOD_{550,i}^t - AOD_{550}^b) \cdot A_i \quad [4.1]$$

where  $AOD_{550,i}^t$  is the total AOD of pixel  $i$ , in the plume convex hull,  $AOD_{550}^b$  is the AOD background value (taken as the minimum AOD value in the plume convex hull),  $A$  is the aerosol pixel area and  $N^f$  is the number of aerosol pixels in the plume convex hull with  $AOD_{550}^t \geq AOD_{550}^b$ . The fire emitted TPM of a plume can then be estimated from the division of  $AOD_{550}^f$  by the smoke aerosol mass extinction coefficient,  $\beta_e$  (in  $m^2.g^{-1}$ ):

$$TPM = \frac{AOD_{550}^f}{\beta_e} \quad [4.2]$$

The mass extinction coefficient,  $\beta_e$ , can be measured *in situ* and its value depends on several factors including relative humidity, the age of the smoke and the wavelength used in measurements. Reid et al. (2005) provide a detailed review of values for  $\beta_e$  in smoke plumes that range between 3.8 - 4.5 m<sup>2</sup>.g<sup>-1</sup>, and combining these with the values of Abel et al. (2005) for South African fires that range from 2.22 – 3.37 m<sup>2</sup>.g<sup>-1</sup> an intermediary  $\beta_e$  of 3.5±1.0 m<sup>2</sup>.g<sup>-1</sup> was assumed for this work. The  $\beta_e$  value of smoke has been shown to increase with aerosol ageing (Formenti et al., 2003; Abel et al., 2005) and also with relative humidity (RH) (Chin et al., 2002; Koppmann et al., 2005). The RH for each of the plumes used in this work was estimated from the ERA-Interim reanalysis at 762 m altitude (Balsamo et al., 2015; <https://www.ecmwf.int/en/forecasts/datasets/reanalysis-datasets/era-interim>), and all matchup plumes showed coincident RH values < 70%. A minimal effect of RH on  $\beta_e$  is therefore expected in the plumes used, since below a RH of 70% inflation of  $\beta_e$  for smoke generated from biomass burning is typically less than 10% (Chin et al., 2002; Reid et al., 2005b). The  $\beta_e$  of fresh smoke aerosol has been shown to increase by 20 to 50% as it ages after 1 - 4 days (Reid et al., 1998; Abel et al., 2005). However, for the majority of the fire matchups in this work, significant AFs were not observed until 08:00 hrs or later, resulting in the oldest smoke in these plumes being around 7 or 8 hours old and thus limiting the extent to which  $\beta_e$  grows due to plume ageing. The uncertainty range attached to this value also includes these potentially higher bounds. However, this is a clear source of uncertainty in this methodology and further investigation into the potential for biome-dependent variability and the effect of aging on  $\beta_e$  is recommended for future work.

#### 4.4.3 Derivation of Smoke Emission Coefficients ( $C_{biome}$ )

Fire matchups were used to derive a set of smoke emission coefficients (**Table 4.2** and **Figure 4.7**) for each of the biomes defined in **Section 4.4.1**, based on an (OLS) regression. Uncertainties in TPM and FRE are plotted in **Figure 4.7** which were calculated from the

combined AOD uncertainty measures provided in the MAIAC product, the uncertainty in  $\beta_e$ , and the FRP uncertainties provided in the FRP-PIXEL product (Wooster et al., 2015).

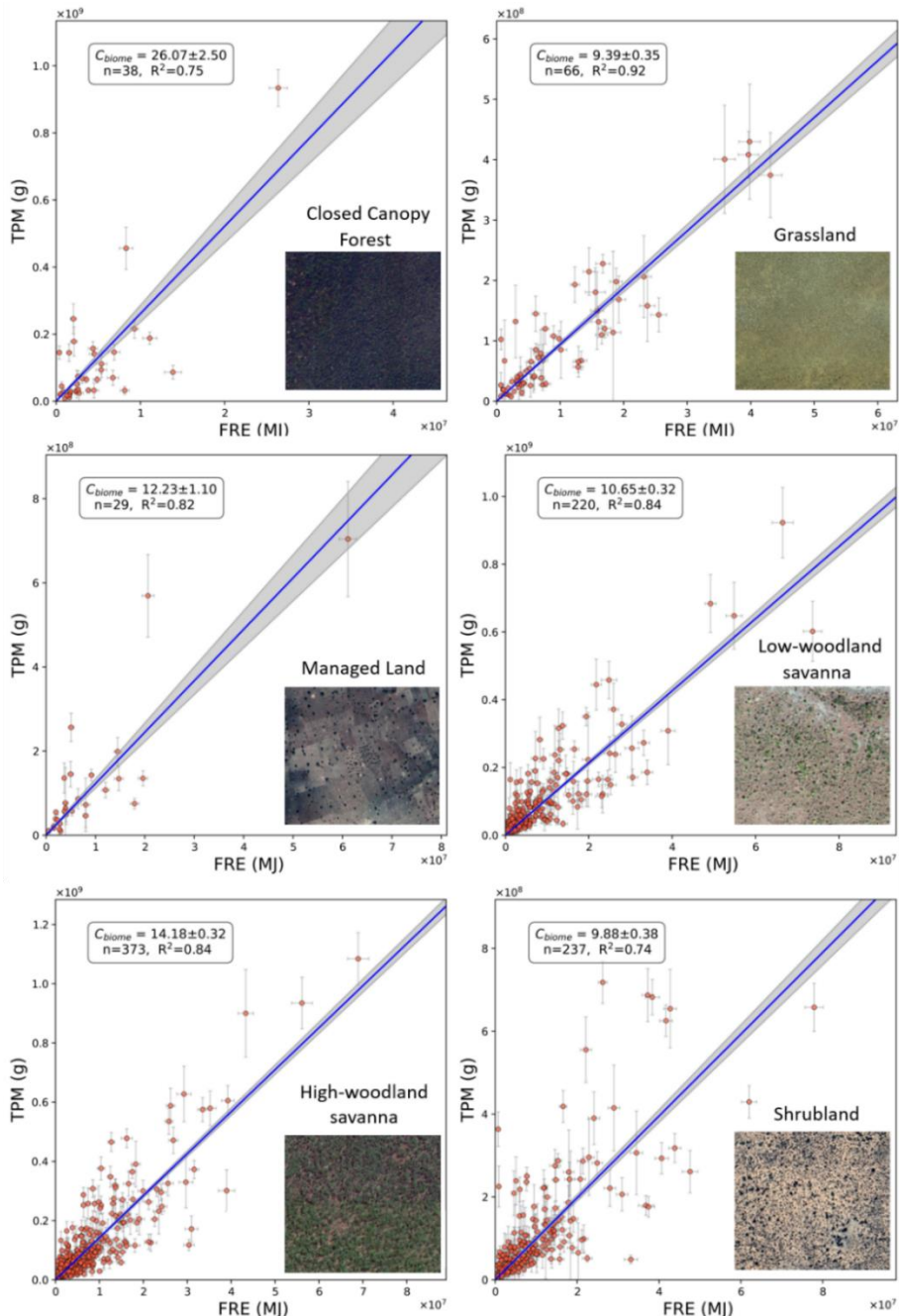


**Figure 4.7** Smoke emission coefficients ( $C_{biome}$ ; in  $\text{g.MJ}^{-1}$ ) for the six African fire-affected biomes defined in **Section 4.4.1**, each derived from the slope of an ordinary least-squares (OLS) regression between data of fire-emitted total particulate matter (TPM) and matching fire radiative energy (FRE). The grey shaded area defines the 95% probability prediction interval of the OLS-derived slope. Each scatterplot is accompanied by an illustrative insert that depicts the typical landcover for the biome as seen in Google Earth (example locations are Closed Canopy Forest  $10.359^\circ \text{S}, 19.086^\circ \text{E}$ ; Grassland  $21.180^\circ \text{S}, 19.560^\circ \text{E}$ ; Managed Land  $10.495^\circ \text{N}, 7.586^\circ \text{E}$ ; Low-Woodland Savanna  $7.085^\circ \text{N}, 27.095^\circ \text{E}$ ; High-Woodland Savanna  $12.523^\circ \text{S}, 23.323^\circ \text{E}$ ; Shrubland  $23.055^\circ \text{N}, 22.242^\circ \text{E}$ ).

**Table 4.2** Biome-dependent smoke emission coefficients ( $C_{biome}$ ) and accompanying uncertainties for the African fire-affected biomes mapped in **Figure 4.3b** and calculated from FREMv2 and from FREMv1 (reported in Mota and Wooster, 2018). Matching FEER-equivalent coefficients are also shown, based on the geographical location of fire matchups and the FEER  $C_e$  ( $1^\circ \times 1^\circ$ ) product of Ichoku and Ellison (2014).

Biome Type	FREMv2 $C_{biome}$ (g MJ $^{-1}$ )	FREMv1 $C_{biome}$ (g MJ $^{-1}$ )	FEER $C_{biome}$ (g MJ $^{-1}$ )
Closed canopy forest	26.07±2.50	65.63±0.91	16.34
Managed land	12.23±1.10	15.62±0.34	15.80
Grassland	9.39±0.35	13.03±0.23	10.98
Shrubland	9.88±0.38	17.36±1.06	10.97
Low-woodland savanna	10.65±0.32	19.75±0.49	12.78
High-woodland savanna	14.18±0.32	19.75±0.49	13.81

These FREMv2 smoke emission coefficients were compared to those of FREMv1 (Mota and Wooster, 2018) and FEER (Ichoku and Ellison, 2014) which are also shown in **Table 4.2**. In FEER,  $C_e$  values are derived for each individual  $1^\circ$  grid cell using the MODIS archive of that cell (see **Section 2.4.2.1**), as opposed to being defined by biome. Therefore, to derive FEER-equivalent  $C_{biome}$  values for comparison in this work, all the FREMv2 fire matchups were intersected with the FEER  $1^\circ C_e$  product (see **Figure 4.8b** and **Figure 4.8d**) and the mean FEER  $C_e$  for each of the biomes were calculated from these intersecting FEER grid cells.

FREMv2  $C_{biome}$  values range from  $9.39 \pm 0.35$  g MJ $^{-1}$  (grassland) to  $26.07 \pm 2.50$  g MJ $^{-1}$  (closed canopy forest) and in all biomes, are lower than those of FREMv1 - with an average decrease of 39% across all biomes. These differences relate to a combination of factors. Primarily the far more appropriate MAIAC AOD product, but also the improved method for background AOD estimation, the updated and extended biome mapping, and the inclusion of fire matchups from NHAF as well as SHAF. Since plume TPM values are most strongly influenced by the AOD product used, the application of MAIAC AOD in this work is likely to have the most significant impact on  $C_{biome}$  values. The MAIAC product's characteristics may both increase and decrease TPM values compared to the use of MxD04. As discussed in **Section 4.2.1** and demonstrated in **Section 4.3**, MxD04 AOD retrievals are VZA dependent and bias can be seen at the swath edges (Sayer et al., 2015), meaning TPM estimates for plumes observed at wide

VZA can be significantly inflated (**Figure 4.2a**). In the FREMv1 methodology such plumes were not omitted during  $C_{biome}$  derivation, and this likely resulted in overestimated TPM values and thus FREMv1  $C_{biome}$  values. The MAIAC AOD product uses an area-weighted method to grid L1B MODIS pixels to a 1 km pixel grid prior to AOD retrieval, providing finer detail and improved plume distinction at VZA > 20°, allowing the inclusion of smaller fires in the matchup dataset. One feature of the MAIAC AOD product likely to increase estimates of TPM and thus FREMv2  $C_{biome}$  values is its less conservative cloud masking, which resulted in MAIAC-derived TPM estimates being ~26% higher than the equivalent MxD04\_BD values when plumes observed at VZA < 20° were considered (**Figure 4.2b**). These characteristics of the MAIAC AOD product have a combined effect but cause an overall reduction in final  $C_{biome}$  values in FREMv2 compared to FREMv1.

The number of fire matchups identified in both the closed canopy forest and managed land biomes are significantly fewer than for the other biomes, largely because of fewer identifiable fires in the AOD product and the fact that many did not meet the matchup selection criteria. The lower number of matchups means that the  $C_{biome}$  coefficients for these two biomes have significantly larger uncertainties – roughly 3× and 7× higher for managed land and closed canopy forest respectively - than the uncertainty of other biomes. As was discussed in **Section 2.3.2**, the SEVIRI FRP-PIXEL product has a minimum AF detection limit of around 30 - 40 MW, and fires burning below this threshold will often remain undetected until they or other fires within the same pixel cause the pixel's FRP total to exceed this value. Agricultural fires in managed lands are typically quite small (Zhang et al., 2017), and in closed canopy forests surface fires, burning on the forest floor, are likely to be partially obscured by the tree canopy (Roberts et al., 2018). Both these effects may result in a lower FRE total being measured than might be expected, and hence higher  $C_{biome}$  values than should be determined in these biomes.

FREMv2 coefficients are on average only 6% lower than FEER-equivalent  $C_{biome}$  values, with FREMv2  $C_{high-woodland savanna}$  (which has the largest matchup sample sizes) showing very good agreement with its FEER- equivalent (14.18±0.32 g MJ<sup>-1</sup> and 13.81 g MJ<sup>-1</sup> respectively). FREMv2  $C_{low-woodland savanna}$ ,  $C_{shrubland}$  and  $C_{grassland}$  values are also all within 11% of their FEER-equivalents.  $C_{closed canopy forest}$  shows the greatest divergence being around 37% higher

than the FEER-equivalent, perhaps likely stemming from the relatively small sample size ( $n=38$ ) which is strongly affected by one or two high TPM-FRE points.

The newly derived FREMv2  $C_{biome}$  values of **Table 4.2** were used to generate a SEVIRI per-pixel smoke emissions coefficient ( $C_e$ ) product for Africa for subsequent use in FREMv2 fire emissions estimation. The  $C_e$  value of each SEVIRI pixel across Africa was calculated based on the weighted mean of the relevant  $C_{biome}$  values and the per-pixel biome fractional coverage derived in **Section 4.4.1**. Figure 4.8a shows the resulting FREMv2  $C_e$  product, along with the FEER  $C_e$  ( $1^\circ \times 1^\circ$ ) product (Figure 4.8b; Ichoku and Ellison, 2014) and their difference, averaged to  $1^\circ$  spatial resolution (Figure 4.8c). As previously detailed, FEER  $C_e$  values are calculated for each  $1^\circ$  grid cell from matchup fires within that cell (rather than per biome) so the spatial variability of FEER  $C_e$  values is far higher than the biome-driven FREMv2  $C_e$  product of **Figure 4.8a**. Across Africa, FEER  $C_e$  are on average higher than those of FREMv2 by 3.22 g.MJ<sup>-1</sup>, and this difference is dominated by regions where the FEER  $C_e$  values are significantly higher than FREMv2, for example over Nigeria (**Figure 4.8c**). Regions with the most similar values are generally those well sampled by fire matchups in FREMv2 (**Figure 4.8d**), whereas those with the highest differences tend to have few or no fire matchups in FREMv2 due primarily to relatively low fire activity being recorded there but also frequent cloud cover in 2015 obscuring fires. Future work on FREMv2 should extend the fire matchup sampling period to multiple years to obtain additional matchups in regions and biomes currently relatively poorly sampled by FREMv2 plumes.

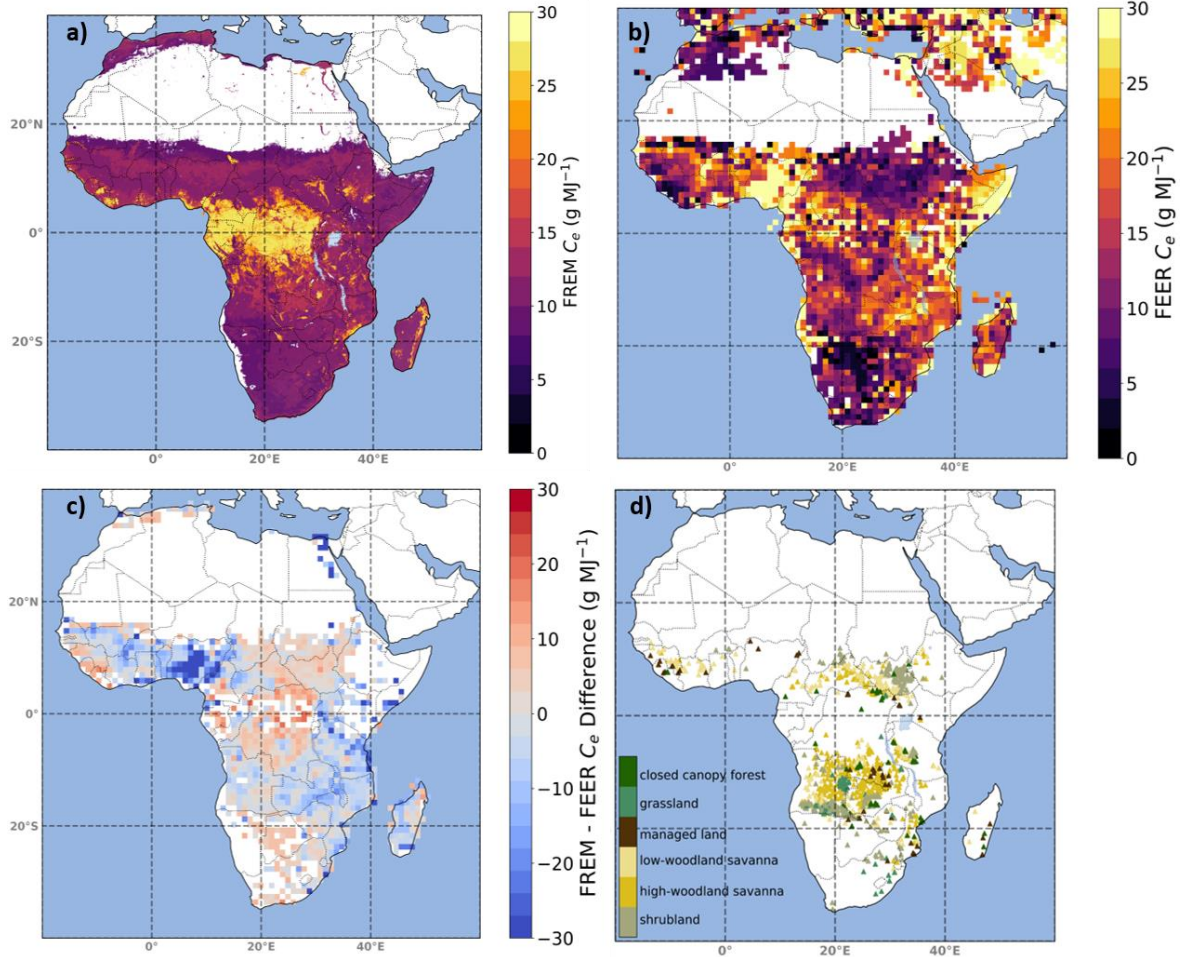


Figure 4.8 (a) FREMv2 smoke emission coefficient ( $C_e$ ) mapped at  $0.05^\circ$ ; (b) the matching  $1^\circ$  FEER  $C_e$  product; and (c) the difference between (a) and (b). In (c), FEER grid cells whose value was derived from gap-filling or which were calculated from less than 15 samples were removed (see Ichoku and Ellison (2014) for full details). (d) Shows the spatial distribution of the fire matchups used to derive the FREMv2  $C_{biome}$  values of Figure 4.7.

## 4.5 FREMv2 Emissions Inventory Development

### 4.5.1 Total Particulate Matter (TPM) Emissions

The FREMv2  $C_e$  product in **Figure 4.8a** was used to convert data of the Meteosat SEVIRI FRP-PIXEL product (Wooster et al., 2015) into the highest spatio-temporal resolution TPM emissions inventory yet available over Africa (15 min,  $0.05^\circ \times 0.05^\circ$ ). These emissions were then compared to a set of other emission inventories widely used by the research and operational communities. Hourly averages of SEVIRI FRP (in MW) multiplied directly by the

FREMV2  $C_e$  product provide mapped instantaneous TPM emission rates (in kg s<sup>-1</sup>), whereas multiplication by FRE gives emission totals for the defined FRP temporal integration period (in kg). **Figure 4.9** presents total monthly TPM emissions estimates from FREMV2, GFASv1.2 (Kaiser et al., 2012; <https://apps.ecmwf.int/datasets/data/cams-gfas/>), GFEDv4.1s (van der Werf et al., 2017); [www.globalfiredata.org/](http://www.globalfiredata.org/)), along with FEERv1.0-GFAS1.2 (the FEER  $C_e$  product applied to GFASv1.2 FRP estimates, Ichoku and Ellison, 2014 ; [www.feer.gsfc.nasa.gov/](http://www.feer.gsfc.nasa.gov/)) and FEERv1.0-SEVIRI (the FEER  $C_e$  product applied to SEVIRI FRP-PIXEL product).

FREMV2 determines mean annual TPM emissions for Africa at  $27.34 \pm 1.57$  Tg yr<sup>-1</sup> for the five years studied - 38% of this is generated from fires in NHAF, and 62% from fire in SHAf. Pan-African totals are 80% and 43% higher than GFASv1.2 and GFEDv4.1s respectively, with estimates from SHAf fires showing greater divergence in both cases. The FREMV2 values are within 7% of the FEER-GFASv1.2 and FEER-SEVIRI top-down inventories, agreeing with Ichoku and Ellison (2014) who also show FEER-GFAS to be higher than GFASv1 and GFEDv3 by similar factors over NHAf and SHAf. Kaiser et al. (2012) report that GFASv1.2 smoke aerosol emissions must be multiplied by a global scaling factor of 3.4 before being used as input into atmospheric models to provide modelled AODs in line with satellite observations of AOD. This provides evidence that Africa's TPM emissions are indeed higher than GFAS (and GFED) currently estimate.

As demonstrated by Wooster et al. (2015) and Hall et al. (2019), at the time of their overpasses, polar-orbiter based AF products detect more 'small' (i.e. low FRP) fires compared to the SEVIRI FRP-PIXEL product as a result of their finer pixel size and thus lower minimum FRP detection limit. This effect is amplified at as SEVIRI VZA increases due to the growth of SEVIRI pixel footprint area (see **Figure 3.2**). However, it was also shown that over the course of several days, the far more frequent data available from SEVIRI allows an increased number of AF detections overall (Roberts et al., 2015; Hall et al., 2019). The SEVIRI-derived FREMV2 emissions agree well with those of FEER which are derived from MODIS FRP data matchups that have a significantly lower minimum FRP detection limit than SEVIRI (Roberts et al., 2015). This suggests that FREMV2 accounts for the smoke emission contribution from a proportion of the active fire pixels remaining undetected by SEVIRI. This is likely because, whilst SEVIRI

fails to detect the lowest FRP fires, the smoke they generate has contributed to the AOD in the 1 km MAIAC product used to generate the  $C_{biome}$  values from fire matchups. Thus, FREMv2  $C_{biome}$  and  $C_e$  values contain an inherent ‘boost’ from the TPM emitted from undetected low-FRP active fire pixels. Further, the 1 km spatial resolution of MAIAC AOD enables the distinction and use of many more smaller smoke plumes than the higher resolution MxD04 product.

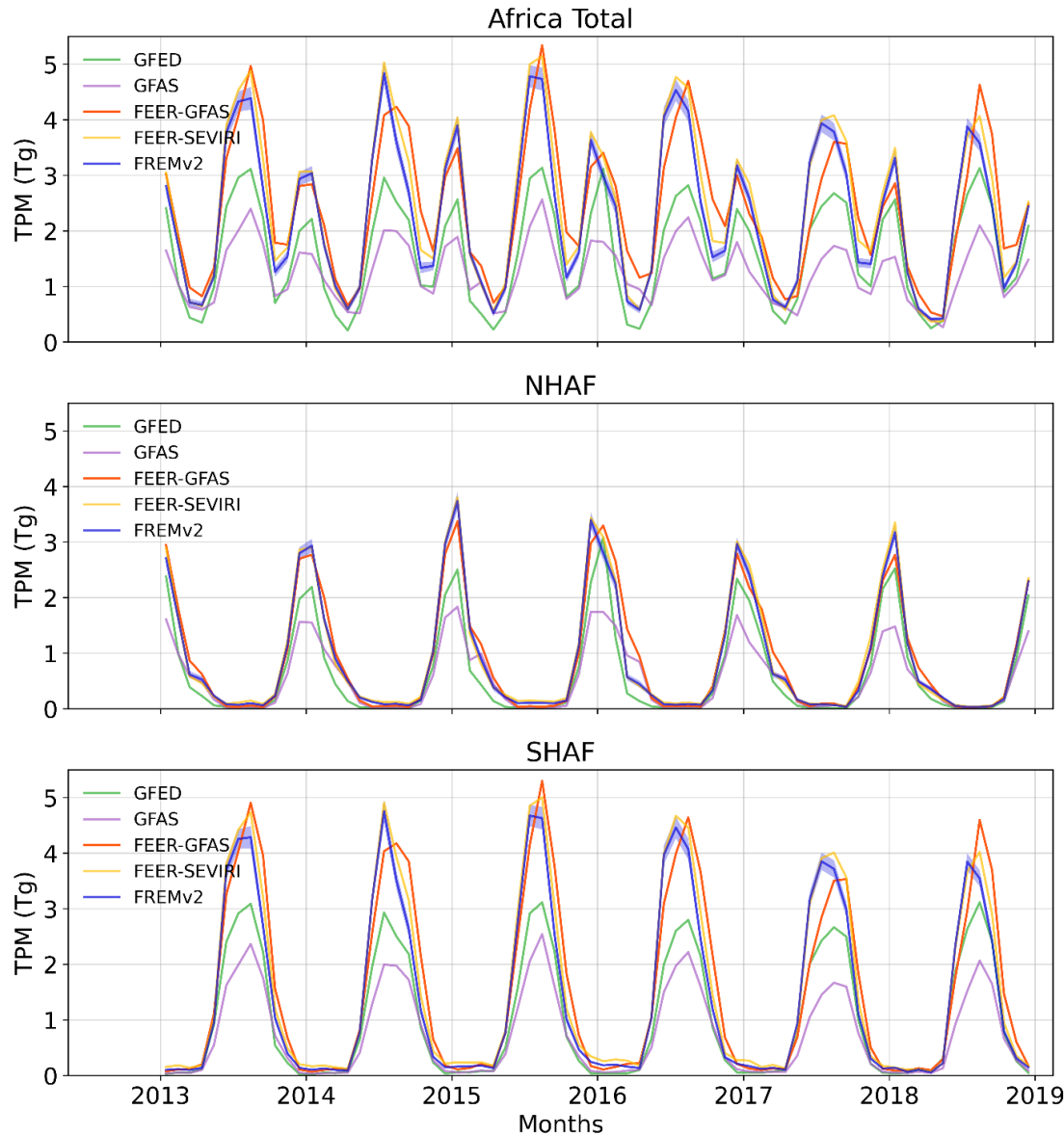


**Figure 4.9** Monthly total particulate matter (TPM) emissions from landscape fires for 2013 to 2018, as derived using the FREMv2 methodology (blue) applied to the Meteosat FRP-PIXEL product of Wooster et al. (2015). Corresponding monthly TPM emissions are shown from GFEDv4.1s (green), GFASv1.2 (purple), and the FEERv1.0 coefficients applied to the GFASv1.2 FRP (red) and SEVIRI FRE data (yellow).

The five inventories of **Figure 4.9** show similar temporal patterns of TPM emissions, with clearly identifiable NHAF and SHAF burning seasons and annual peaks and minima occurring in the same years. Like FREMv1, FREMv2 predicts an earlier peak in TPM emissions over SHAF than do the other inventories. Peak smoke emission in FREMv2 occurs in July in every year but one, whereas in all other inventories (except FEER-SEVIRI, which has peak TPM split equally between July and August) this occurs in August. A potential cause may be the splitting of high and low woodland savanna biomes in FREMv2. High-woodland savanna is mainly concentrated just below the equator (**Figure 4.3b**) in a region that burns earlier than the dominant southern African fire season. Therefore, due to FREMv2 discriminating between high and low woodland savanna and grasslands, the dominant  $C_e$  values applied to the SEVIRI FRP-PIXEL data vary not only by biome, but also over time due to the seasonal progression of fire activity across the continent. Due to the FREMv2 biome map being based on land cover and VCF data from 2015, changes in land cover in the 2013 to 2018 period are not accounted for. However, canopy changing crown fires are very rare in low and high-woodland savanna, shrublands and grasslands – which are dominated by surface fires (Van Wilgen et al., 1990; Heil et al., 2010; Van Leeuwen et al., 2014) - and so fire-related change in tree canopy cover is very limited in these biomes (Zhou et al., 2019). However, FREMv2 may require more regular updates of the biome map of **Figure 4.3b** to account for anthropogenically driven land cover change occurring in this period.

The similar TPM estimates generated by FEER-GFASv1.2 (which indirectly uses MODIS FRP) and FEER-SEVIRI (and FREMv2, which both use SEVIRI FRP), compared to the far lower values of GFASv1.2 (also based on MODIS FRP) indicate that the higher annual-scale TPM emissions of the top-down approaches stem dominantly from the  $C_e$  values applied to FRP measures, and less from the source of the FRP observations used. That said, in the case of FEER-GFASv1.2 it is worth noting that whilst the FEER  $C_e$  values are derived from MODIS FRP observations, the MODIS FRP data used within GFAS undergoes several stages of processing and thus presents different FRP values to those originally provided by the MODIS MOD14/MYD14 products (Kaiser et al., 2012). The similarity between TPM emissions estimates generated by FREMv2 and the two FEER inventories supports the case that higher

emissions estimates come mainly from the magnitude of  $C_e$  values, since the FREMv2 and FEER  $C_e$  values agree well in general (**Table 4.2** and **Figure 4.9**).

FREMv2 TPM emissions for 2016 are generated at  $0.05^\circ$  across Africa - a spatial resolution  $\times 5$ ,  $\times 2$  and  $\times 2$  times higher than GFEDv4.1s, GFASv1.2 and FEER-GFASv1.2 respectively. TPM emission density ( $\text{g m}^{-2}$ ) for 2016 is presented for each inventory in **Figure 4.10**, both for the whole of Africa and a smaller  $20^\circ \times 20^\circ$  region outlined in red on the GFEDv4.1s plot in **Figure 4.10**. The FEER  $C_e$  product with its  $1^\circ$  grid cell resolution can, in theory, be applied to the native SEVIRI FRP-PIXEL product as has been done for the FEER-SEVIRI dataset shown in **Figure 4.10**. However, the spatial resolution of the FEER  $C_e$  product is 20 times lower than that of SEVIRI FRP observations, so these FEER-SEVIRI derived emissions estimates do not account for the finer detail of inter-biome spatial variations that FREMv2 does. Additionally, the appropriateness of applying FEER  $C_e$  values, (which are derived from 'raw' MODIS FRP data) to 'raw' SEVIRI FRP data is unclear, particularly when their different minimum-FRP detection limits are considered.

In general, the spatial distribution of the African TPM emissions is somewhat similar across all five inventories. In line with the temporal trends seen in **Figure 4.9**, notably higher TPM emission densities are observed for the three top-down emission inventories. The high spatial resolution of FREMv2 provides more detailed spatial information on smoke emissions than do the other inventories, which may be relevant for supporting improved local scale air quality modelling. FREMv2 features a region of distinctly higher total TPM emissions in northern Angola and D.R.C. compared to the other emissions inventories and this region is dominated by high-woodland savanna (**Figure 4.3b**) and also features partial coverage of closed canopy forest (**Appendix C**). The unexpectedly high emissions totals here demonstrate the impact of the more spatially resolved biome classification used in FREMv2 (through the separation of high and low woodland savanna) and the potentially overestimated  $C_{biome}$  value for closed canopy forest that results from its small sample size in  $C_{biome}$  derivation (**Figure 4.7**).

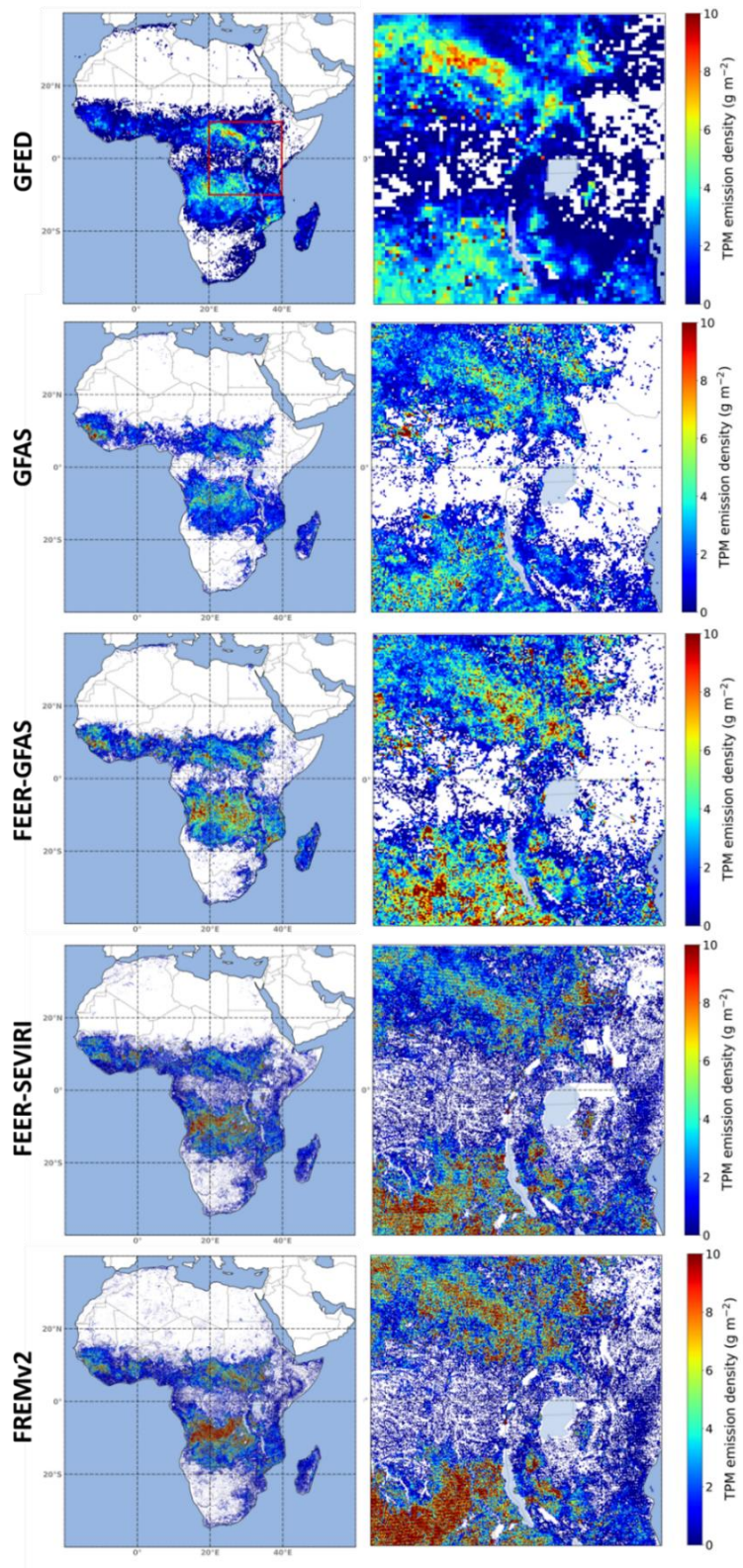


**Figure 4.10** Total particulate matter (TPM) emission density ( $\text{g.m}^{-2}$ ) across Africa for 2016 as determined by GFEDv4.1s ( $0.25^\circ$  grid cells), GFASv1.2 ( $0.1^\circ$  grid cells), FEERv1.0-GFASv1.2 ( $0.1^\circ$  grid cells), FEERv1.0-SEVIRI ( $0.05^\circ$  grid cells), and FREMv2 inventory derived herein ( $0.05^\circ$  grid cells). The red  $20^\circ \times 20^\circ$  region outlined in the top left GFED plot is shown magnified for each inventory in the right-hand column.

The distribution of biomes across NHAF and SHAf has a significant impact on the contribution each biome has to the total TPM emissions of each region (**Figure 4.11**). Both closed canopy forest and grassland show a similar percentage contribution to total TPM emissions in each hemisphere, with mean annual emissions totals within 2% of each other and a combined mean contribution of 17% and 20% of total TPM emissions for NHAF and SHAf respectively. In NHAF, fires from managed lands and shrublands contribute most to annual TPM emissions, though their fractional contributions exhibit significant seasonal variations - varying by 45% and 38% across the year respectively. In SHAf these two biomes show a narrower range across the year and an overall lower contribution to total TPM emissions, which are instead dominated by high-woodland savanna fires between May and November. In both NHAF and SHAf, the highest monthly contribution of emissions from managed lands occurs outside the primary burning season (November-April in NHAF and July-September in SHAf), potentially due to deliberate post-harvest or end-of-growing season burning (Yevich and Logan, 2003).

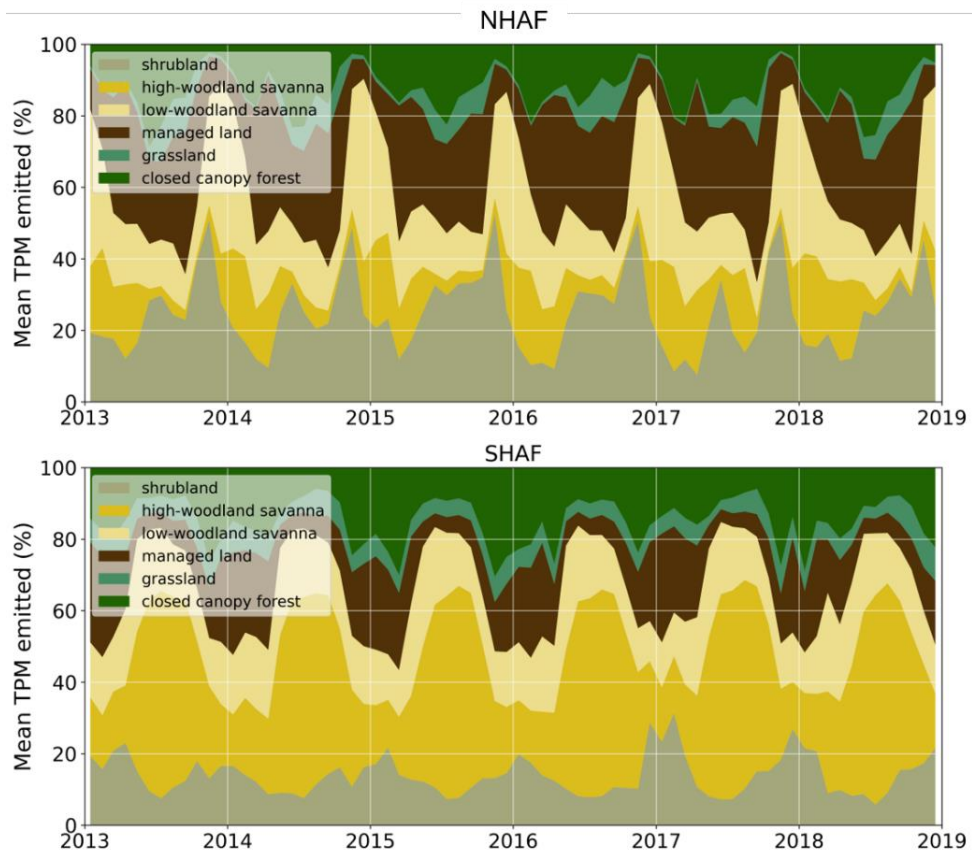


**Figure 4.11** Mean monthly contribution (%) of fires to total particulate matter (TPM) emissions in each of the six FREMv2 biomes from 2013 to 2018 in (a) Northern Hemisphere Africa and (b) Southern Hemisphere Africa.

#### 4.5.2 Trace Gas and Total Carbon Emissions

Trace gas emissions estimates are derived from FREMv2 outputs via application of the updated standard emission factors (EFs) of Andreae (2019) whereas GFEDv4.1s, GFASv1.2 and FREMv1 use the EFs detailed in Andreae and Merlet (2001). Unlike the bottom-up approaches in which EFs are multiplied by total fuel consumption estimates, in the FREM methodology trace gas emissions are estimated directly from FRP-generated FRE measures using a set of trace gas emissions coefficients. The approach is similar to that of Huijnen et al. (2016) who estimated CO<sub>2</sub> and CH<sub>4</sub> emissions from fire-emitted CO estimates. The trace gas emission coefficients in FREMv2 are calculated using the EF ratios between the relevant gas and TPM, which are then multiplied by the TPM  $C_{biome}$  values derived in **Section 4.4.3** and reported in **Table 4.2**. Emission coefficients for each gas, and each biome are calculated via:

$$C_x^{biome} [g.MJ^{-1}] = \frac{EF_x^{biome} [g.kg^{-1}]}{EF_{TPM}^{biome} [g.kg^{-1}]} \cdot C_{TPM}^{biome} [g.MJ^{-1}] \quad [4.3]$$

Where  $C_x^{biome}$  is the emission coefficient for species  $x$  in a specific *biome*,  $EF_x^{biome}$  is the emission factor for species  $x$  in that biome,  $EF_{TPM}^{biome}$  is the emission factor for TPM in that biome and  $C_{TPM}^{biome}$  is the smoke emission coefficient for TPM in that biome as determined in the FREMv2 (**Figure 4.7**). These coefficients are multiplied directly by geostationary FRE values to estimate trace gas emissions. Trace gas emissions coefficient derivation for each SEVIRI pixel uses an area-weighted mean of the biome-specific EF ratios (similarly to the  $C_e$  product derivation in **Section 4.4.3**), thereby generating an emission coefficient map for each gas. The biomes defined in Andreae (2019) are less detailed than those of FREMv2, resulting in all but the closed canopy forest and managed land biomes using a single set of EF ratios (savanna and grassland EF). This relative lack of EF detail affects all the fire emission inventories compared in this work, and points to the potential need for more research focused on further distinction of EFs with respect to vegetation type.

Monthly CO<sub>2</sub>, CH<sub>4</sub> and CO emissions are shown in **Figure 4.12**, which exhibit a similar seasonal pattern to TPM emissions (**Figure 4.9**), and mean annual totals are shown in **Table 4.3**. Direct retrieval of CO atmospheric concentrations is carried out using data from instruments such as MOPITT (Worden et al., 2010) and TROPOMI (Veefkind et al., 2012), and comparisons of GFEDv2 and GFEDv3 CO emissions with MOPITT-derived CO measures have suggested that GFED underestimates fire emitted CO over Africa by up to 50% (Chevallier et al., 2009; Kopacz et al., 2010; Pechony et al., 2013). Comparisons of the different GFED versions shows that for NHAF and SHAf, GFEDv4.1s CO emissions were around 30% lower than GFEDv3 (van der Werf et al., 2017), pointing to significant underestimation of CO emissions by GFEDv4.1s over Africa. The substantially higher CO emissions provided by FREMv2 and by the other top-down approaches may therefore be more realistic than the lower values provided by the bottom up inventories of GFEDv4.1s (and GFAS). Studies showing African burned area to be far higher when mapped using high resolution imagery than with the 500 m MCD64A1 product used in GFED supports this argument (Tsela et al., 2014; Hawbaker et al., 2017; Roteta et al., 2019).

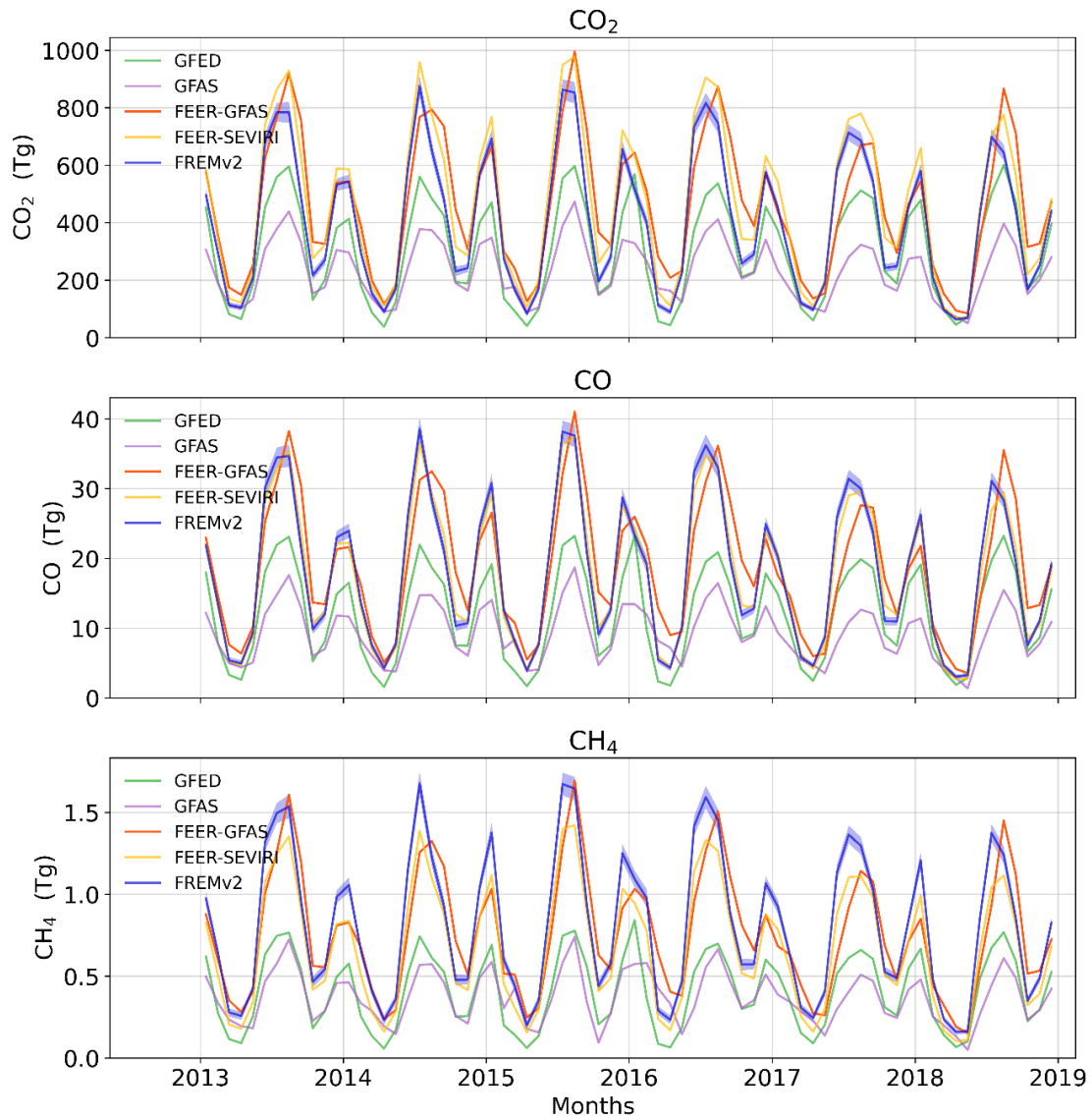


**Figure 4.12** Monthly total emissions (Tg) of (a) CO<sub>2</sub>; (b) CO; and (c) CH<sub>4</sub> for African landscape fires as estimated by FREMv2 (blue) between 2013 and 2018. Corresponding values from GFEDv4.1s (green), GFASv1.2 (purple), FEERv1.0-GFASv1.2 (red) and FEERv1.0-SEVIRI (yellow) are shown for comparison.

FREMv2 emissions of total carbon were calculated from the summed carbon content in the CO<sub>2</sub>, CO and CH<sub>4</sub> emissions, which typically contribute more than 99% of total carbon release in savanna/grassland and tropical forest fires (Andreae, 2019). Estimates of total fuel consumption in terms of dry matter consumed (DMC) were then calculated on the assumption of a 50% dry matter fuel carbon content (van der Werf et al., 2010, 2017) with mean annual totals reported in **Table 4.3**.

**Table 4.3** Mean annual total carbon and trace gas emissions for 2013 to 2018, along with dry matter consumed (DMC) totals (Tg.yr<sup>-1</sup>), for Northern and Southern Hemisphere Africa (NHAF and SHAf) as estimated by the different fire emissions inventories compared herein including FREMv2

	GFAS		GFED		FEER-GFAS		FEER-SEVIRI		FREMv2	
	NHAF	SHAf	NHAF	SHAf	NHAF	SHAf	NHAF	SHAf	NHAF	SHAf
C (Tg)	346	470	398	651	588	1007	594	1023	529 ± 59	890 ± 37
CO <sub>2</sub> (Tg)	1188	1619	1368	2242	2018	3457	2045	3525	1803 ± 207	3034 ± 135
CO (Tg)	48	63	55	88	83	141	78	135	81 ± 9	135 ± 6
CH <sub>4</sub> (Tg)	2.0	2.4	1.9	3.0	3.4	5.7	3.0	5.2	3.7 ± 0.4	6.0 ± 0.3
Dry matter consumed (Tg)	693	941	796	1303	1177	2014	1187	2046	1059 ± 118	1780 ± 74

#### 4.5.3 Fuel Consumption per Unit Area ( $F_c$ ) from Burnt Area Observations

As discussed in **Section 2.4.1**, the poorly constrained fuel load and combustion completeness parameters contribute a significant part of the uncertainty in bottom up estimates of fuel consumption per unit area ( $F_c$ , in kg.m<sup>-2</sup>), and unmapped small burns missed by the 500 m MCD64A1 MODIS burned area (BA) product (Tsela et al., 2014; Hawbaker et al., 2017; Roteta et al., 2019) add further uncertainty and possibly bias into the final derived fuel consumption estimates (Reid et al., 2009a; Vermote et al., 2009; Van Leeuwen and van der Werf, 2011). As demonstrated by Mota and Wooster (2018), it is possible to generate FREM-derived estimates of  $F_c$  through an inversion of the original Seiler and Crutzen (1980) BA-based approach to fire carbon emissions estimation (see **Equation 2.8** and **Section 2.4.1**). The 500 m MODIS MCD64A1 BA product used in GFED (van der Werf et al., 2017) – which is in turn used in the calibration of GFAS (Kaiser et al., 2012) - was used in mapping  $F_c$  across southern Africa in FREMv1. In this work the far higher spatial resolution (20 metre) FireCCISFD11 African BA product (Roteta et al., 2019) derived from Sentinel-2 data for 2016 is used to estimate  $F_c$ . This BA product has been shown to map up to 60% more BA in some areas compared to MCD64A1(Roteta et al., 2019). Fuel consumption is mapped across Africa at 0.25° spatial resolution (**Figure 4.13a**) by mapping FREMv2 dry matter consumed (DMC) data for 2016 (calculated in **Section 4.5.2**) and dividing this by the matching BA measures calculated from the approximately 1.5×10<sup>6</sup> potential FireCCISFD11 pixels falling in each 0.25° grid cell. Note that these per-pixel  $F_c$  values apply only to the burned area patch inside a given pixel, and not the 0.25° pixel as a whole.

Compared to  $F_c$  from the model-based GFEDv4.1s values (**Figure 4.13b**), around a third of 0.25° grid cells have significantly higher  $F_c$  in FREMv2. This result is somewhat expected based on the overall higher carbon emissions of the former (**Figure 4.12** and **Table 4.3**). In the remaining 0.25° cells the two inventories provide similar values (see difference map in **Figure 4.13c**). There are some unprocessed tiles in the FireCCISFD11 product (see Roteta et al., 2019), resulting in a minority of 0.25° grid cells having unreported or unrealistically high  $F_c$  values in excess of 10 kg.m<sup>-2</sup>. After removing these anomalous cells, biome-specific  $F_c$  frequency distributions and statistics based on grid cells were derived (**Figure 4.14**) – using grid cells where a single biome covered at least 80% of the cell and where more than 5% of the cell was

burned. Distributions are heavy-tailed and show a spatial variability somewhat similar to that derived by Roberts et al. (2011) using an alternative FRE and BA based approach. There are relatively few fuel consumption databases derived from field measurements, but van Leeuwen et al. (2014) provides summary statistics for African savannah burns and the low woodland savannah and shrubland median values in **Figure 4.14** are very close to the 0.34 kg.m<sup>-2</sup> mean fuel consumption found in that study.

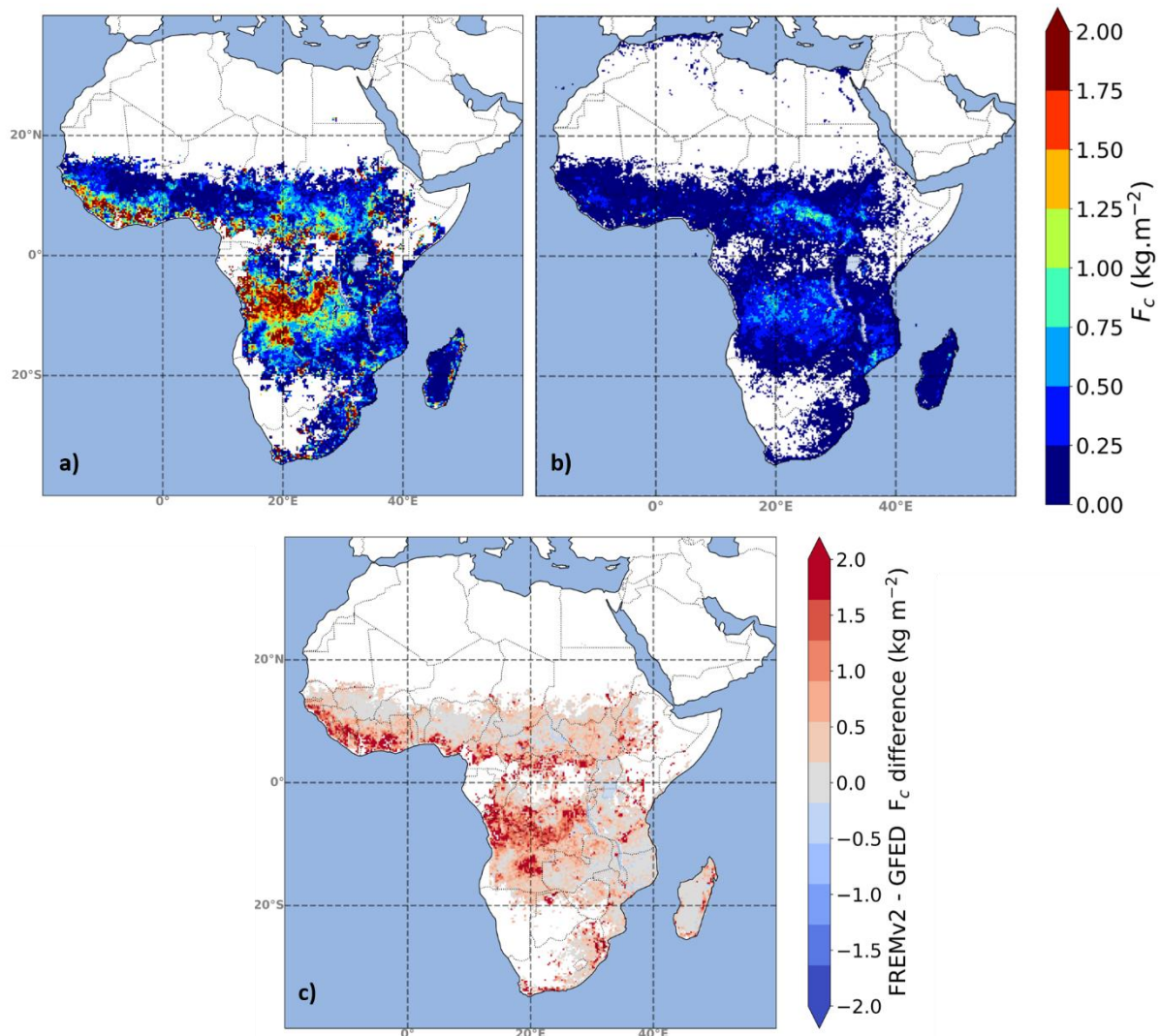


**Figure 4.13** Fuel consumption per unit area ( $F_c$ , kg.m<sup>-2</sup>) mapped at 0.25° from (a) 2016 FREMv2 dry matter consumed (DMC) totals and the FireCCISFD11-estimated burned area, and (b) GFEDv4.1s. (c) difference in fuel consumption per unit area ( $F_c$ , kg.m<sup>-2</sup>) calculated from a) and b). Note that  $F_c$  values in (a) apply only to the burned area patch inside a given pixel, and not the 0.25° pixel as a whole.

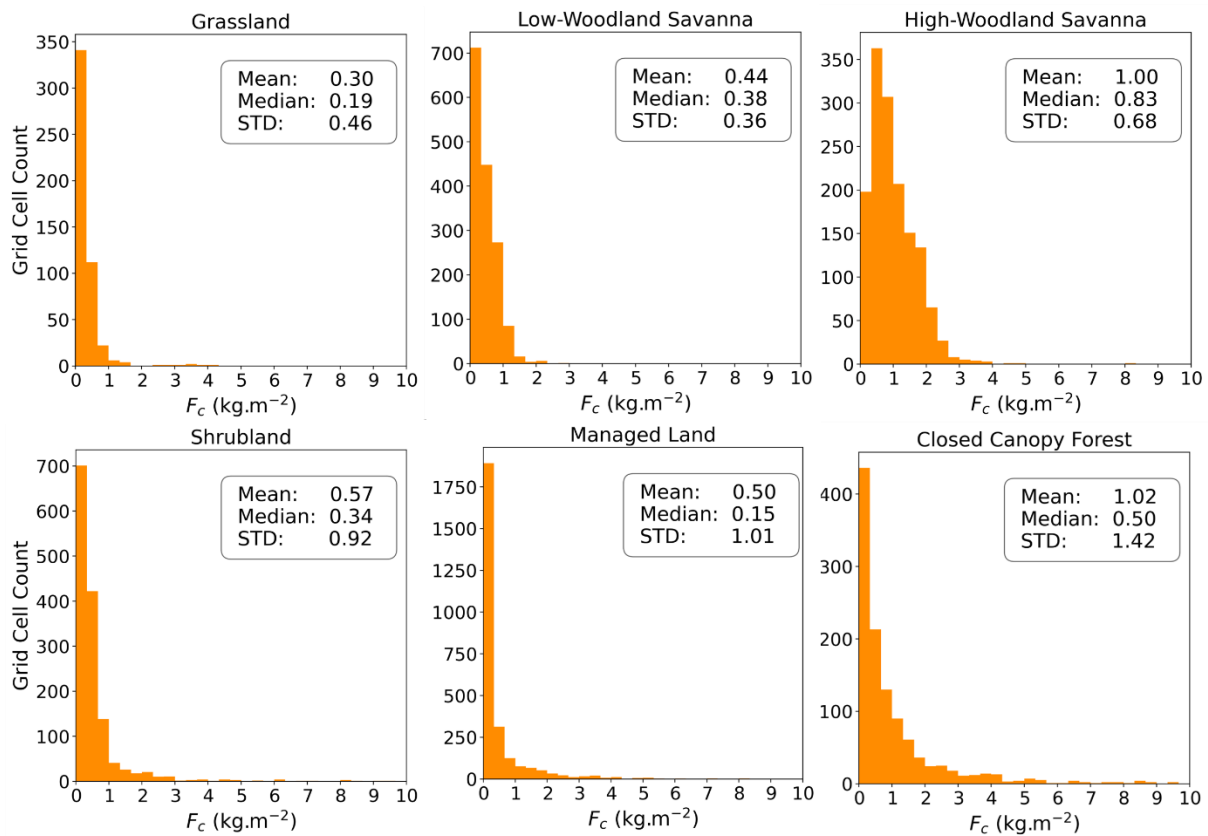


**Figure 4.14** Per-biome FREMv2  $F_c$  frequency distributions and derived means, medians and standard deviations calculated from the fuel consumption per unit area map of **Figure 4.13a** and the biome map of **Figure 4.3b** using pixels with more than an 80% fractional coverage of a single biome and more than 5% pixel burned area according to the FireCCISFD11 product.

## 4.6 Summary and Conclusions

This chapter details developments to the fully top-down ‘Fire Radiative Energy Emissions’ (FREMv1) landscape fire emissions methodology of Mota and Wooster (2018) which is here termed FREMv2. This new methodology is used to develop the highest spatio-temporal resolution African landscape fire emissions inventory currently available.

The FREM approach bypasses the total fuel consumption step of ‘bottom-up’ fire emissions methodologies, recognised as a key source of uncertainty (Reid et al., 2005b; Zhang et al., 2008; Reid et al., 2009a; Van Leeuwen et al., 2014). The method generates smoke emissions estimates directly from satellite retrievals of FRP and relies on a set of biome-dependent smoke emission coefficients ( $C_{biome}$ , g.MJ<sup>-1</sup>) that are derived from almost one thousand fire matchups between Meteosat SEVIRI FRP-based Fire Radiative Energy (FRE) estimates and in-plume total

particulate matter (TPM) estimates made using the 1 km MAIAC AOD product. The FREMv2 methodology introduces significant improvements to all stages of the FREMv1 approach, most particularly those associated with the use of the 10 km MODIS MxD04 AOD product for TPM estimation.

Issues with use of MxD04 included, masking of thick smoke as cloud (Levy et al., 2013; Raffuse et al., 2013; Remer et al., 2013; Livingston et al., 2014), the impact of sensor VZA dependence on AOD retrieval (Sayer et al., 2015; Mhawish et al., 2019), and the products' relatively low spatial resolution making smoke plumes difficult to discriminate (Lyapustin et al., 2011; Raffuse et al., 2013; Remer et al., 2013; He et al., 2017) and requiring a focus on the largest fires when deriving the FREMv1 coefficients. Additional improvements include a more up to date and detailed fire-relevant mapping of pan-African biomes using CCI Land Cover 2015 (ESA, 2017) and Landsat-derived percentage tree cover information (**Figure 4.3**). The latter enables improved specification of the smoke emission coefficients in the woodland savanna biome, which annually contributes the most to Africa's fire radiative energy release (**Figure 4.4**). Expansion of the FREMv2 inventory to include both NHAF and SHAF enabled many more FRE-AOD matchup fires to be included in the smoke emissions coefficient generation compared to FREMv1, including many more small fires whose plumes can be discriminated using the 1 km MAIAC AOD product. This also enabled localised values of plume background AOD to be selected in a more representative manner than in FREMv1. The impact of relative humidity on the smoke mass extinction coefficient used was also accounted for in FREMv2.

The evolutions reported in this Chapter result in a set of FREMv2 biome-dependent smoke emission coefficients,  $C_{biome}$ , for TPM (**Table 4.2**) that are between 22% and 60% lower than those of FREMv1. The FREMv2 coefficients are far closer to the biome equivalent coefficients of the FEER top-down methodology (Ichoku and Ellison, 2014) than FREMv1, particularly in the case of high-woodland savanna which contributes a considerable proportion of smoke emissions in SHAF. Some significant differences between the coefficients in FREMv2 and FEER do remain, but mostly in regions showing relatively fewer fires and thus which are poorly sampled by FREMv2 fire matchups (Figure 4.8). A significant advantage of FREMv2 over FEER is that the spatial mapping of the final  $C_e$  product for Africa is easily derived from

the six FREMv2  $C_{biome}$  values reported in **Table 4.2** and the SEVIRI-pixel biome coverage, this means that FREMv2  $C_e$  product updates to account for landcover changes can be easily calculated simply using an updated landcover map. In the FEER methodology of Ichoku and Ellison (2014),  $C_e$  values are mapped for 1° grid cell from fire matchups observed within each cell using more than a decade of data from the MODIS record, and landcover change related updates would thus require a complete new collection of a set of fire matchups and re-derivation of the geographically dependant  $C_e$  product.

Whilst this FREMv2 approach addresses some of the principal uncertainties and biases in the original FREMv1 (and indeed the FEER) methodology, there remain sources of uncertainty and limitations that would benefit from further investigation. These include:

- i) Elucidation of the effect of small fires having an FRP below the minimum geostationary active fire detection limit, and the extent to which these are now accounted for via the ability to include smaller fire matchups during  $C_{biome}$  derivation via use of the 1km MAIAC AOD product (**Section 4.5.1**)
- ii) Further investigation of the smoke mass extinction coefficient ( $\beta_e$ ) used to estimate column-integrated TPM from AOD, and the impact of smoke ageing effects in the time between emission and observation of aerosols (typically < 8 hrs here).
- iii) Improvement of the smoke emissions coefficients for closed canopy forest and managed land, which are currently derived from a relatively small number of matchup fires compared to the other biome classes.

With respect to (iii) an increased number of fire matchups are needed to address this issue. The number of matchups could be increased by including multiple years of data and focusing on improving automation of the fire match-up process, for example through use of the MAIAC Quality Assessment product's 'smoke mask' (Lyapustin et al., 2012) and machine learning techniques, to help increase the range and efficiency of the matchup process and thus the number of matchups used.

The FREMv2 African biomass burning emission inventory for 2013 to 2018 was compared to GFASv1.2, GFEDv4.1s and two versions of FEER - FEER-GFASv1.2 and FEER-SEVIRI (**Figure 4.9, Figure 4.10, Figure 4.12** and **Table 4.3**). FREMv2 provides the highest levels of spatio-

temporal detail ( $0.05^{\circ}$  spatially, updated 4 times per hour) as it can exploit the native geostationary FRP data resolutions. Monthly FREMv2 TPM emission totals agreed well with both FEER-GFASv1.2 and FEER-SEVIRI, and are significantly higher than those of GFEDv4.1s and GFASv1.2 which past studies have suggested tend to underestimate NHAF and SHAf aerosol emissions (Chevallier et al., 2009; Kopacz et al., 2010; Kaiser et al., 2012; Pechony et al., 2013; Tosca et al., 2013; Reddington et al., 2019). Trace gas and carbon emissions are similarly also higher than GFEDv4.1s and GFASv1.2, and close to those of FEER. Recent development of a 20 m African burned area (BA) product (FireCCISFD11; Roteta et al., 2019) and other studies (Tsela et al., 2014; Hawbaker et al., 2017) have shown a likely cause of this to be the underestimation of BA by as much as 50% in some regions of Africa by the MODIS MCD64A1 500 m BA product, upon which GFED fire emissions estimates are based. GFAS is also indirectly dependant on this BA product through its calibration against GFED (Kaiser et al., 2012).

Using FREMv2 carbon emissions, estimates of dry matter consumed (DMC) were derived through an inversion of the Seiler and Crutzen (1980) BA approach to emission estimation. By dividing FREMv2 DMC by the FireCCISFD11 20 m BA product, one of the first data-driven mappings of fuel consumption per unit area ( $F_c$ ) across Africa was generated (**Figure 4.13**). These fuel consumption estimates produce higher  $F_c$  in many areas compared to the modelled-based GFEDv4.1s values.

Future developments to the FREM emission inventory may include its application to FRP data from other geostationary satellites which use the same baseline algorithm which is applied to generate the Meteosat FRP-PIXEL product used in this work (Roberts et al., 2015; Wooster et al., 2015) - for example data from Himawari-8 (Xu et al., 2017), Meteosat (IODC) and GOES (Xu et al., 2010). Since direct validation of large-scale fire emissions estimates remains challenging, future work will also use the final FREMv2 smoke emissions estimates within an atmospheric model to generate trace gas concentration and AOD fields for comparison to ground-based and satellite-based measures, exploiting a validation strategy similar to that previously used for evaluating other large scale fire emissions estimates (e.g. Baldassarre et al., 2015; Ichoku et al., 2016; Reddington et al., 2016).

# Chapter 5 Validation of the FREMv2 Fire Emission Inventory using WRF-CMAQ, AERONET and MAIAC Observations of AOD and Sentinel-5P Measurements of CO

## 5.1 Introduction

This chapter presents an evaluation of the FREMv2 fire emission inventory presented in **Chapter 4**. FREMv2 emissions of gas and aerosols are used as input in the WRF-CMAQ atmospheric transport model, and simulated outputs of aerosol optical depth (AOD) and carbon monoxide (CO) concentration are compared to ground-based (AERONET) and satellite-based (MODIS MAIAC) AOD data and satellite-based (Sentinel-5P TROPOMI) CO data.

As was discussed in **Section 2.5**, although inter-comparisons between different fire emissions inventories can be used to gauge their relative biases (e.g. Van Der Werf et al., 2010; Wiedinmyer et al., 2011; Andela et al., 2013; Mota and Wooster, 2018; Nguyen and Wooster, 2020), the actual validation of emissions inventories is really only possible through the use of atmospheric modelling. Fire emissions are used as input in a chemical transport model (CTM), and the resulting simulated output is compared to independent observations of atmospheric trace gas and aerosol concentrations (e.g. Andela et al., 2013; Baldassarre et al., 2015; Ichoku et al., 2016; Reddington et al., 2016).

Several factors are likely to impact the simulation outputs in addition to the fire emissions inventory used as input, these include the specific numerical weather prediction (NWP) and

CTM used, the various configurations of both of these (Kukkonen et al., 2012), the initial and boundary conditions used for meteorology and chemistry and any other emissions inventories (e.g. for industry) used as input. These were discussed in detail in **Section 2.5.1**. These selections along with model resolution can not only impact the simulations themselves, but they also determine the computational cost associated with running the model (Sobhani, 2018). In using atmospheric transport models to evaluate emissions inventories, the above factors contribute to model error which can make it challenging to determine the source of any differences seen between model results and observations (Ichoku et al., 2016). Nevertheless, measures of fire-related variables coming from both ground-based and remote sensing instruments (such as those described in **Section 2.2.3**) can be used in the comparisons to CTM results to assess the accuracy of simulations and thus of the fire emissions inventories used as input in the CTM.

The primary objective of this Chapter is to assess the FREMv2 emission inventory – doing so by using it within a CTM and comparing the model output to independent observations of AOD and CO column amounts over southern Africa during the fire season. The validation aims to assess FREMv2 performance and to quantify bias in the emission inventory. Results will be used in future work to guide developments in fire emission estimation via top-down approaches that build on FREMv2.

## 5.2 Methods

### 5.2.1 Model Description and Setup

The modelling simulations in this study were realised using the Advanced Research Weather Research and Forecasting model (WRF-ARW v4.1.1; Skamarock et al., 2019; <https://www2.mmm.ucar.edu/wrf/>) and the Community Multiscale Air Quality model (CMAQ v5.3; EPA, 2019; <https://www.epa.gov/cmaq>). The latter provides off-line chemistry simulations in which feedbacks from gases and aerosols on meteorological processes are not included (see **Section 2.5.1**). Aerosols can have a significant impact on radiative fluxes and PBL height (Li et al., 2017), however the computational resources available for this work

guided the use of an off-line chemistry approach which was computationally less intensive. Irrespective of its lack of feedbacks between chemistry and meteorology, WRF-CMAQ is commonly used in both operational AQ systems (Kukkonen et al., 2012) and in many other research studies including those related to fire emissions and smoke-contaminated air (e.g. In et al., 2009; Cheng et al., 2014; Baldassarre et al., 2015; Hu et al., 2016; Syrakov et al., 2016; Vongruang et al., 2017; Koplitz et al., 2018; Choi et al., 2019). Simulations were carried out for an  $\sim 3000 \text{ km}^2$  region of Southern Hemisphere Africa (SHAF). The SHAF fire season occurs annually during the region's dry season – roughly between July and September.

The WRF-CMAQ simulated domain is shown in **Figure 5.1** along with the location of the AERONET sites used to provide the ground-based comparison data, and the regions of interest (ROIs) used in comparisons between the WRF-CMAQ output and the satellite AOD and CO datasets (see **Section 5.2.3**). The WRF-CMAQ domain had a spatial resolution of 9 km, with 35 vertical model layers over a  $347 \times 319$  grid. Simulations were conducted from 15<sup>th</sup> June 2019 to 29<sup>th</sup> August 2019 and were carried out in two separate simulations to reduce the divergence of model results on long model runs - the second simulation was started from 29<sup>th</sup> July 2019. In both simulations a period of 24 hours was allowed for the model to spin-up and stabilise – data from these spin-up periods are not reported in results.

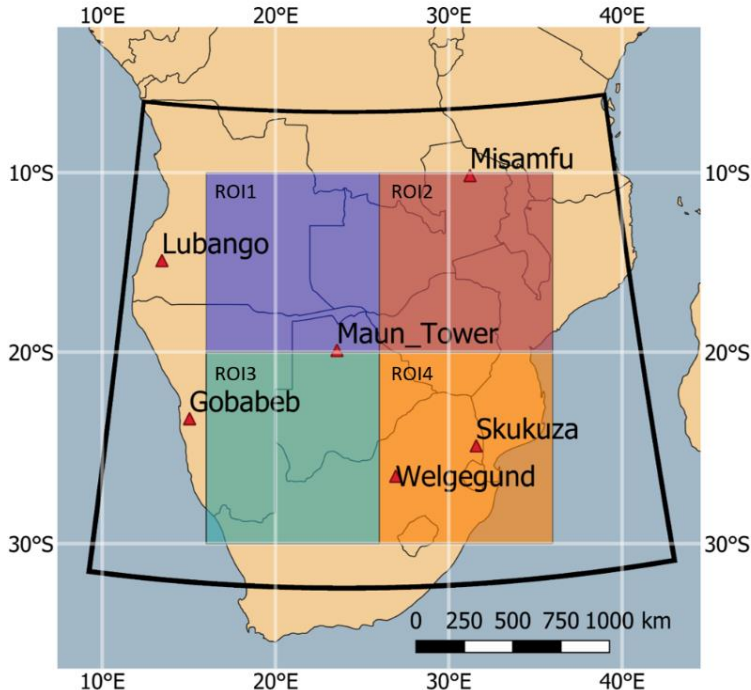


**Figure 5.1** The WRF-CMAQ model domain covering southern hemisphere Africa, along with the locations of the AERONET sites used for comparison to the model output. The coloured boxes indicate smaller regions of interest (ROIs) which were used in comparisons of model output to satellite observations (S5P CO and MODIS MAIAC AOD).

The model configuration and set of physical schemes used in WRF were selected based on previous AQ simulations over Southern Africa which used the WRF-Chem model (Yang et al., 2013; Zhang et al., 2014; Kuik et al., 2015). Gas-phase chemistry was simulated in CMAQ with the third revision of the Carbon Bond 2006 mechanism (Emery et al., 2015) and the AERO7 aerosol module (Appel et al., 2018) - together referred to as CB6r3\_ae7. Initial conditions (IC) and boundary conditions (BC) for meteorological fields were provided from the NCEP FNL global reanalysis (<https://rda.ucar.edu/datasets/ds083.3/>) and chemistry IC and BC came from the WACCM chemistry and aerosol model (<https://www.acom.ucar.edu/waccm/>). Details of model configuration and setup for the WRF-CMAQ simulations are summarised in **Table 5.1**, and a schematic detailing the various model inputs, processing stages and model components are illustrated in **Figure 5.2**.

**Table 5.1** Summary of WRF-CMAQ model configuration

General features	
Domain extent	10°E - 44 °E, 5°S -32°S
Modelled time period	15 <sup>th</sup> June to 28 <sup>th</sup> July, and 29 <sup>st</sup> July to 29 <sup>st</sup> Aug 2019
Resolution	9 km × 9 km, 35 vertical levels (top layer at 5 kPa)
WRF configuration	
	Scheme
cloud microphysics	Lin et al.
radiation (shortwave)	Goddard
radiation (longwave)	Rapid Radiative Transfer Model (RRTM)
boundary layer physics	Mellor-Yamada-Janic (MYJ)
land surface processes	Noah LSM
cumulus convection	Grell 3-D
CMAQ configuration	
Chemistry mechanism	CB6r3
aerosol module	AERO7
Dust emissions	inline
Biogenic emissions	inline BEIS3
Initial and boundary conditions	
Metrology	NCEP FNL, 0.25° × 0.25°, 26 levels, 6 hour
Chemistry	WACCM, 0.9° × 1.25°, 88 levels, 3 hour

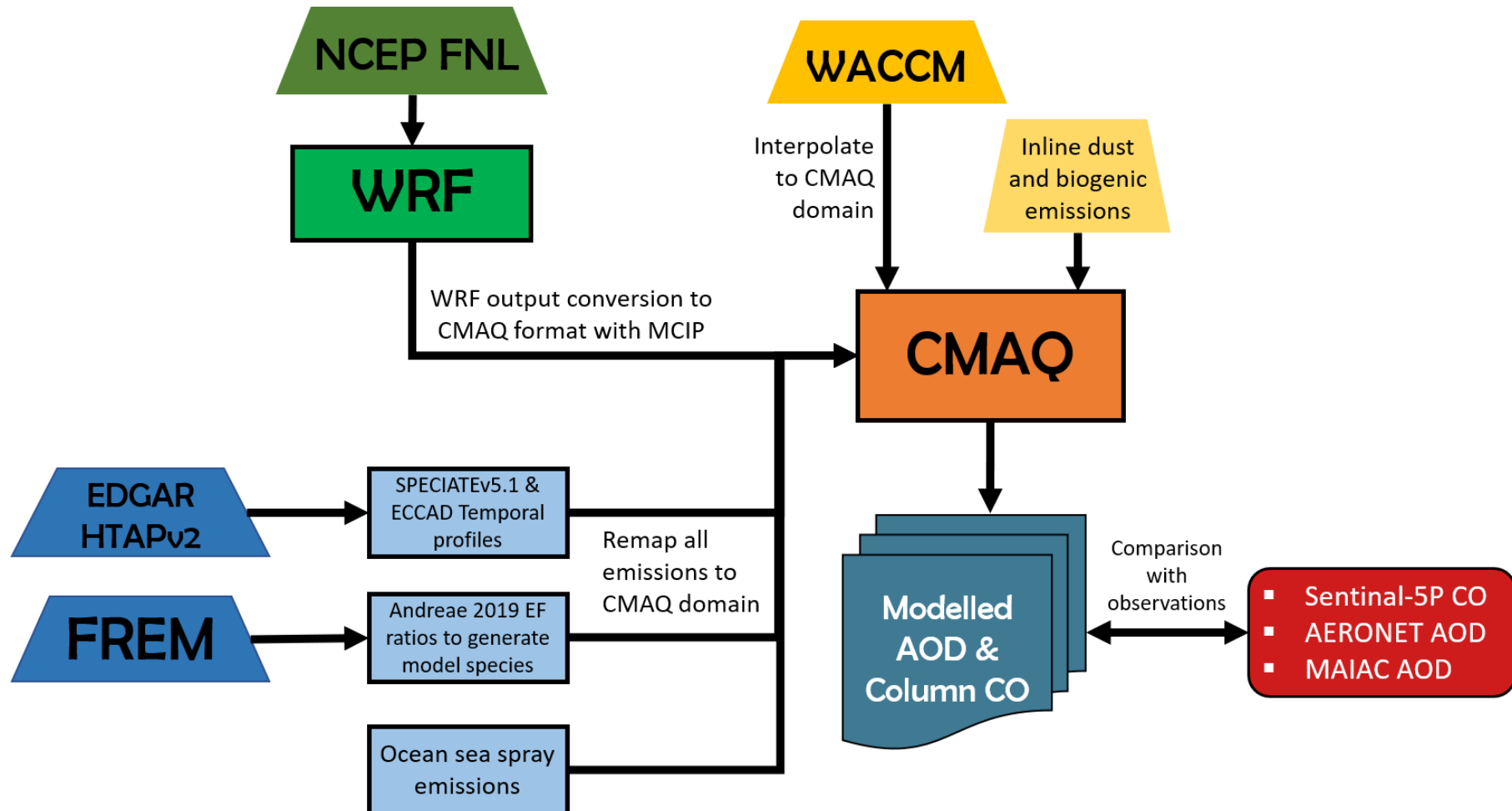


Figure 5.2 Flowchart depicting the input datasets, pre-processing stages and model components of the WRF-CMAQ setup used in this validation study.

## 5.2.2 Emissions

### 5.2.2.1 Anthropogenic emissions

Anthropogenic emissions were taken from the EDGAR-HTAPv2 inventory (EDGAR: Emission Database for Global Atmospheric Research of the Joint Research Centre of the European Commission, in collaboration with the Task Force on Hemispheric Transport of Air Pollution, TF HTAP, organized by the United Nations Economic Commission for Europe's Convention on Long- range Transboundary Air Pollution; [https://edgar.jrc.ec.europa.eu/htap\\_v2/](https://edgar.jrc.ec.europa.eu/htap_v2/)). EDGAR-HTAPv2 provides monthly emissions from the energy, residential, agricultural, industrial and transport sectors for CH<sub>4</sub>, CO, SO<sub>2</sub>, NO<sub>x</sub>, NMVOC, NH<sub>3</sub>, PM<sub>10</sub>, PM<sub>2.5</sub>, BC and OC and includes annual emissions from the shipping and aviation sectors. These monthly and annual anthropogenic emissions (0.1°×0.1° spatial resolution) were fractioned by month, day-of-week and hour-of-day using the Copernicus Atmospheric Monitoring Service (CAMS) global temporal profiles available via Emissions of atmospheric Compounds and Compilation of Ancillary Data (ECCAD; <https://eccad.aeris-data.fr/>) Unlike gases such as CO and CH<sub>4</sub>, anthropogenic pollutant emissions comprised of grouped species such as NMVOCs , PM<sub>2.5</sub> and PM<sub>10</sub> cannot be directly used as input into the CMAQ model. These must first be converted into chemical species that are defined in the CB6r3\_ae7 chemistry mechanism of CMAQ (see species listed in **Appendix B**). The mass composition of these grouped pollutants varies by sector, and for this dis-aggregation, speciation profiles from SPECIATEv5.1 were used to fractionate emissions. SPECIATEv5.1 is a repository of organic gas and particulate matter (PM) profiles of air pollution sources made available by the US EPA (<https://www.epa.gov/air-emissions-modeling/speciate>). Anthropogenic emissions from agricultural burning included in EDGAR-HTAPv2 were removed to avoid double counting of these emissions when combined with other fire emissions information. Finally, emissions were re-mapped to the WRF-CMAQ domain and converted to the specific file format required by the CMAQ model.

### 5.2.2.2 Fire emissions

The fire emissions used as input come from the FREMv2 emission inventory described in **Chapter 4**. As with the FREMv2 inventory, the Meteosat-11 SEVIRI FRP-PIXEL product available from the EUMETSAT Land Surface Analysis Satellite Applications Facility (LSA SAF; <http://landsaf.meteo.pt/>) was used to generate the emissions dataset. Hourly averages of FRP were calculated from the 15-minute temporal resolution SEVIRI FRP-PIXEL product, which were then multiplied by the FREMv2 smoke emissions coefficient  $C_e$  product (Figure 4.8a) to provide mapped Total Particulate Matter (TPM) emission rates ( $\text{kg s}^{-1}$ ). Emission factor ratios were calculated from the emission factors (EFs) of Andreae (2019). Emission coefficients for a number of different trace gas and aerosol species were then obtained via the same equation used to derive carbonaceous gases in **Section 4.5.2 (Equation 4.3)**. This equation was applied to obtain biome-specific emission coefficients for 32 gas and aerosol species that are defined in the CMAQ CB6r3\_ae7 chemical mechanism (**Appendix B**). The biomes in FREMv2 are more stratified than those described in Andreae (2019) and as a result the  $EF_x^{biome}$  values used to calculate CMAQ species emission coefficients for fires in high-woodland savanna, low-woodland savanna, grassland and shrubland biomes use same the EF value - though different  $C_{TPM}^{biome}$  values. The fractional coverage of each biome within a SEVIRI pixel was used to calculate the per-pixel emission coefficient for each species ( $C_e^x$ ), with gases first converted to mol  $\text{MJ}^{-1}$ , whilst aerosols remained in g  $\text{MJ}^{-1}$ . These emission coefficient maps were then multiplied by hourly SEVIRI-derived FRP values to obtain emissions rates of gases (in  $\text{mol s}^{-1}$ ) and aerosols ( $\text{g s}^{-1}$ ). **Figure 5.3** shows the total carbon emissions (in Gg) for each month of the simulation period to illustrate the general spatial distribution and magnitude of the fire emissions. Total C emissions were calculated from the summed carbon content of the FREMv2-estimated CO<sub>2</sub>, CO and CH<sub>4</sub> emissions which contribute more than 99% of carbon released by fires in savanna and tropical forests (Andreae, 2019). FREMv2 emissions in their native SEVIRI projection were mapped to the WRF-CMAQ domain and prepared in the correct file format for ingestion into the model. Fire emissions were divided and emitted equally at the seven lowest model levels which span from the surface up to 950 m altitude.

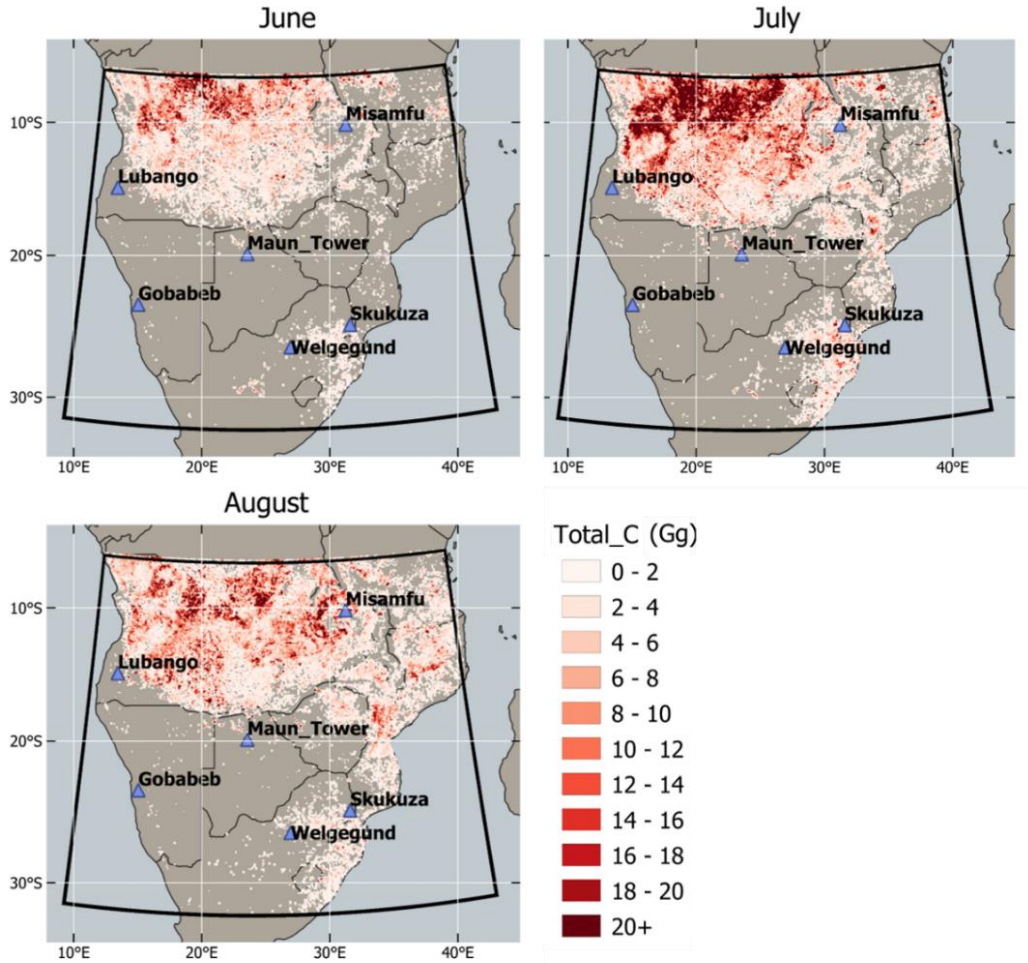


**Figure 5.3** FREMv2 summed total carbon emissions (Gg) in each month of the simulation period between 15<sup>th</sup> June and 29<sup>th</sup> August 2019 calculated from the summed carbon content of CO, CO<sub>2</sub> and CH<sub>4</sub> emissions. The location of the six AERONET sites are also shown.

### 5.2.3 Validation Datasets

WRF-CMAQ simulation results are compared with three independent datasets to quantify the performance of the model and its inputs. Agreement between each of the validation datasets and model results is quantified using the Pearson's correlation coefficient ( $r$ ) and the normalised mean bias function (NMBF) described by Yu et al. (2006). This NMBF has been specifically developed for comparisons between modelled and observed concentrations in air quality modelling and reduces the inflation in bias that may be caused by low values of the observed quantities (see Yu et al., 2006). NMBF is defined as:

$$NMBF = \frac{(\Sigma M - \Sigma O)}{|\Sigma M - \Sigma O|} \left[ \exp \left( \left| \ln \frac{\Sigma M}{\Sigma O} \right| \right) - 1 \right]$$

where  $M$  and  $O$  are modelled and observed values of the variable in question. As defined above, a positive NMBF indicates an overestimation of the model by a factor of  $1 + NMBF$ , while a negative NMBF indicates that the model underestimates observations by a factor of  $1 + (1 - NMBF)$ . Hence, a NMBF value of 0.10 is a 10% overestimation by the model, and a NMBF value of -0.10 is a 10% underestimation.

WRF metrological fields of 2 metre temperature and 10 metre wind speed and direction are compared to the global weather reanalysis model, ERA-Interim, which is available from ECMWF (Dee et al., 2011; <https://www.ecmwf.int/en/forecasts/datasets/reanalysis-datasets/era-interim>). It has a spatial resolution of  $0.75^\circ \times 0.75^\circ$  and 60 vertical levels.

### 5.2.3.1 Sentinel-5P TROPOMI CO

The TROPOMI instrument aboard ESA's Sentinel-5 Precursor (S5P) Mission is a hyperspectral spectrometer covering the ultraviolet-visible (UV-VIS), near infrared (NIR) and shortwave infrared (SWIR) wavelengths with a  $7 \text{ km} \times 7 \text{ km}$  spatial resolution (Veefkind et al., 2012). Data are available from ESA (<https://s5phub.copernicus.eu/dhus/#/home>) and include daily global measurements of important tropospheric trace gases such as ozone,  $\text{CH}_4$ ,  $\text{NO}_2$  and CO, amongst others. Total Column CO measurements are obtained from raw spectra via the shortwave infrared CO retrieval algorithm (SICOR; Landgraf et al., 2016), and the results have been validated against both total column CO measurements made from ground-based spectrometers (Borsdorff et al., 2018b) and the ECMWF assimilation system (Borsdorff et al., 2018a). In this study, Level 2 Sentinel-5P total column CO measurements, hereafter referred to as S5P CO, are compared with CMAQ modelled total column CO. The S5P acquisition of column CO ( $\text{g m}^{-2}$ ) occurs over the model domain daily between approximately 12:00 and 14:00 UTC. Daily S5P retrievals of column CO comprise 1 or 2 S5P swath products and these are combined and compared with the mean of column CO from CMAQ between 12:00 and 14:00 UTC. Both modelled CO and S5P CO are mapped to a  $0.1^\circ \times 0.1^\circ$  grid for ease of comparison.

S5P CO was compared to modelled CO both in terms of the CO values over the full domain extent, over the ROIs indicated in **Figure 5.1**, and in terms of the measured CO of individual smoke plumes identified in the S5P CO product. Individual plumes were manually identified through visual inspection and drawing polygons around S5P CO pixels which were clearly associated with fire emissions. These polygons were matched to the CMAQ model output and a 0.1° grid cell buffer was added to account for any differences in the spatial distribution of plumes. The total column CO contained within each plume polygon in the S5P CO product was matched and compared to the total CO contained in the same area in the CMAQ CO output.

### 5.2.3.2 AERONET AOD

AERONET provides a global network of ground-based sun photometers that provide retrievals of aerosol optical properties, including Angström exponent, fine mode-fraction, aerosol refractive index, and aerosol optical depth (AOD) at various different wavelengths (340 nm, 380 nm, 440 nm, 500 nm, 675 nm, 870 nm, 1020 nm) as well as precipitable water retrievals. The AERONET network comprises more than 800 measurement sites around the world and across the network, instruments are standardized, along with the calibration, processing and distribution procedure applied to data outputs (Holben et al., 2001; Giles et al., 2019). AERONET data is available at three quality levels; Level 1.0 (unscreened), Level 1.5 (cloud-screened and quality controlled), and Level 2.0 (quality-assured). In this study Level 2.0 data is used and data from six AERONET sites within the model domain are compared to the output of the WRF-CMAQ runs. The AERONET sites used are Maun Tower ( $19.9^{\circ}\text{S}$ ,  $23.55^{\circ}\text{E}$ ), Lubango ( $15.0^{\circ}\text{S}$ ,  $13.4^{\circ}\text{E}$ ), Misamfu ( $10.2^{\circ}\text{S}$ ,  $31.2^{\circ}\text{E}$ ), Gobabeb ( $23.6^{\circ}\text{S}$ ,  $15.0^{\circ}\text{E}$ ), Welgegund ( $26.6^{\circ}\text{S}$ ,  $26.9^{\circ}\text{E}$ ) and Skukuza ( $35.0^{\circ}\text{S}$ ,  $31.6^{\circ}\text{E}$ ). AOD data is available for the full simulation period from each of these sites, with the exception of Misamfu and Welgegund that have data available from 15<sup>th</sup> June until 29<sup>th</sup> July and 13<sup>th</sup> August respectively. The locations of these six sites within the WRF-CMAQ domain are shown in **Figure 5.1**. CMAQ produces modelled AOD fields at several different wavelengths (294 nm, 303 nm, 310 nm, 316 nm, 333 nm, 381 nm, 550 nm and 607 nm). AERONET AOD observations at 380 are used in comparisons to WRF-CMAQ modelled AOD at 381 nm (only calculated during local daylight

hours) because this pair of wavelengths are the closest together of the modelled and measured values.

### 5.2.3.3 MAIAC MODIS AOD

WRF-CMAQ modelled AOD at 550 nm was compared to the MODIS MAIAC 550 nm 1 km product (Collection 6 MCD19A2; Lyapustin et al., 2018) - the same AOD product used in the derivation of FREMv2 emission coefficients. This product is referred to as MAIAC AOD hereafter. The MAIAC AOD product is provided in the MODIS sinusoidal projection (Wolfe et al., 1998) and the WRF-CMAQ domain is covered by nine 1200 km<sup>2</sup> tiles of this projection who's daytime Aqua and Terra overpasses occur approximately between 08:00 and 10:00 UTC daily. The CMAQ AOD between 08:00 and 10:00 UTC is averaged and used in comparisons to these MAIAC observations and both modelled and observed AOD are remapped to a 0.1°×0.1° grid for ease of comparison.

As in S5P CO comparisons, model-determined and observed AOD were compared firstly in terms of their values over the full domain and the ROIs depicted in **Figure 5.1** and secondly in terms of individual smoke plumes identified in the MAIAC AOD product. Individual plumes were again manually identified and defined using polygons bounding the plume feature in the MAIAC AOD product (in its original 1 km spatial resolution). These polygons were mapped and matched to the CMAQ model domain, a 0.1° grid cell buffer was added, and the mean AOD of the fire emitted smoke was calculated for both the MAIAC observed plumes and the CMAQ modelled plumes via the same method described by Ichoku and Ellison (2014) and detailed in **Equation 4.1** and smoke plumes were compared on this basis.

## 5.3 Results

### 5.3.1 WRF Meteorological Fields Compared to ERA-Interim

The accuracy of the wind fields in WRF are particularly important to this study as it will effect (i) the time taken for fire generated AOD to reach the AERONET validation site locations (and will impact the physical processes which particles undergo in between) and (ii) the spatial distribution of individual fire plumes which are matched between the model and observed Sentinel-5P CO and MAIAC AOD data.

Comparison of WRF meteorological variables are carried out against the ERA-Interim reanalysis data detailed in **Section 5.2.3** which has a spatial resolution of  $0.75^\circ$ . **Figure 5.4** shows monthly mean 2 metre temperature ( $^{\circ}\text{C}$ ) and 10 metre wind speed ( $\text{m s}^{-1}$ ) and direction. For ease of visualisation WRF 10 m wind speed has been averaged to 54 km spatial resolution, however temperature remains at the model's native 9 km resolution. Overall, the temperature distribution of the WRF model output captures similar features to those present in ERA-Interim and represents monthly changes in temperature relatively well. The higher spatial resolution of the WRF simulations demonstrates how localised features can be characterised when a global meteorology model is used as input in a regional scale NWP model. Of particular note are features related to topography that are not observed in the  $0.75^\circ \times 0.75^\circ$  ERA-Interim data, for example in the north east of the domain. A similar difference is seen in comparisons between wind speed and direction - this same north eastern region has peaks and troughs of high north westerly wind in WRF which are not observed in ERA-Interim and in which the area is far more homogeneous in terms of wind speed. In both WRF and ERA-Interim the dominant wind direction in the northern part of the domain is north westerly and has an increased westerly component towards the west of the domain. In the south of the domain the opposite is true, and the dominant wind direction is southerly, and has an increased easterly component in the south east of the domain.

Overall, meteorological fields in WRF and ERA-Interim reanalysis match well, but WRF results gives more regional detail which ERA-Interim is not capable of distinguishing due to its coarse resolution.

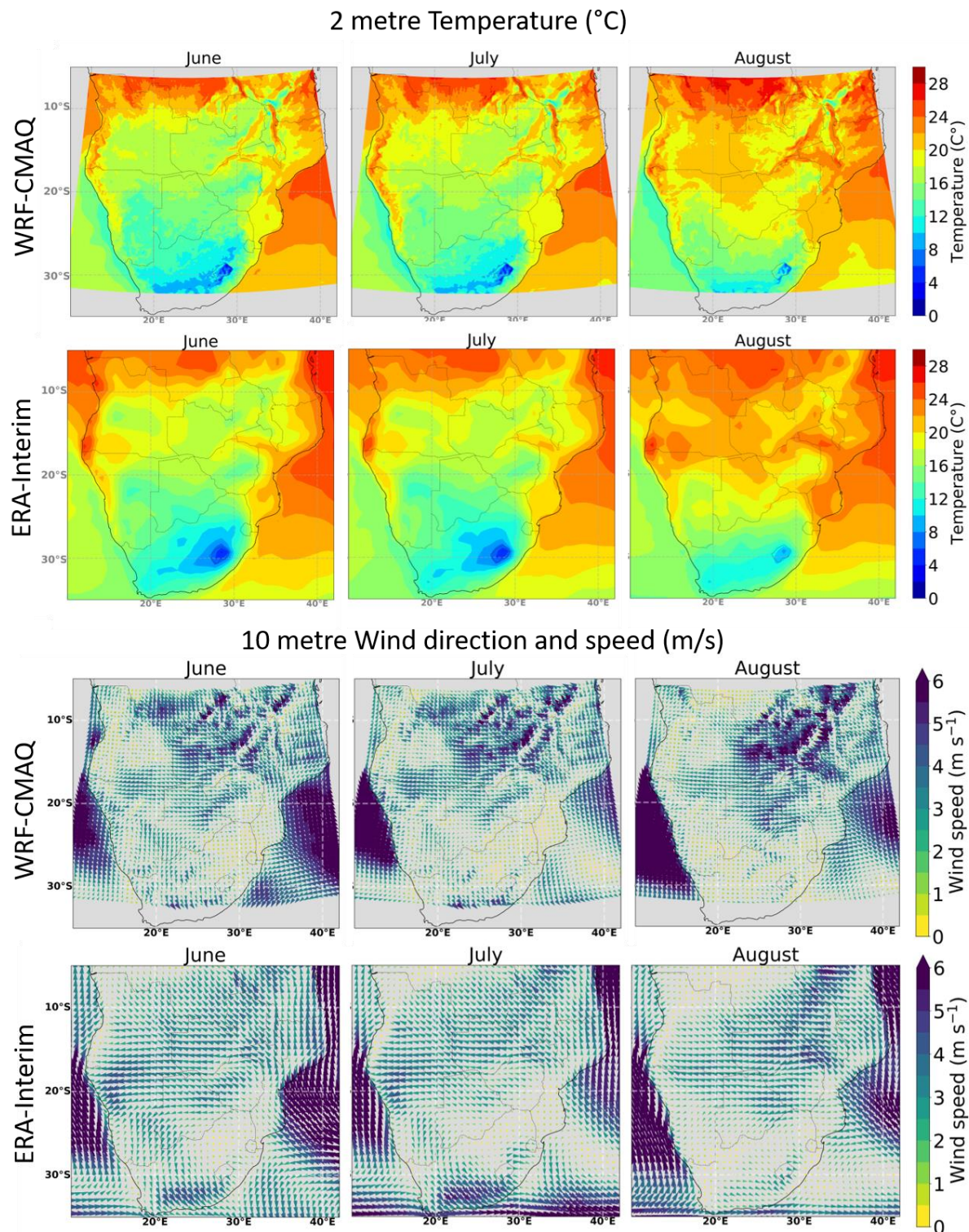


**Figure 5.4** Selected metrological variables comparing monthly means for June, July and August over the simulation period. Comparison of WRF-CMAQ with ERA-Interim in terms of 2 metre temperature ( $^{\circ}\text{C}$ ) and 10 metre wind speed ( $\text{m s}^{-1}$ ) and direction.

### 5.3.2 CMAQ Column CO Comparisons with Sentinel-5P CO

#### 5.3.2.1 Full Domain and ROIs

CMAQ total column CO was compared with total column CO measurements from the S5P product, and mapped monthly mean CO for CMAQ and S5P are shown in **Figure 5.5** along with the percentage difference between S5P and CMAQ CO. In all months of the simulation a region of high CO is observed over the north western region of the domain. The migration of fire activity southwards is observed in both modelled and observed CO, as increased values of CO are seen over the south eastern areas of the domain from June through to August. In June and July CMAQ modelled CO is up to 60% higher than S5P column CO in the aforementioned north western region, while in much of the rest of the domain modelled column CO is between 1% and 30% lower than S5P. An improved agreement between CMAQ and S5P CO is seen in August (i.e. the level of both over and underestimation of modelled CO compared to S5P CO in the domain are reduced).

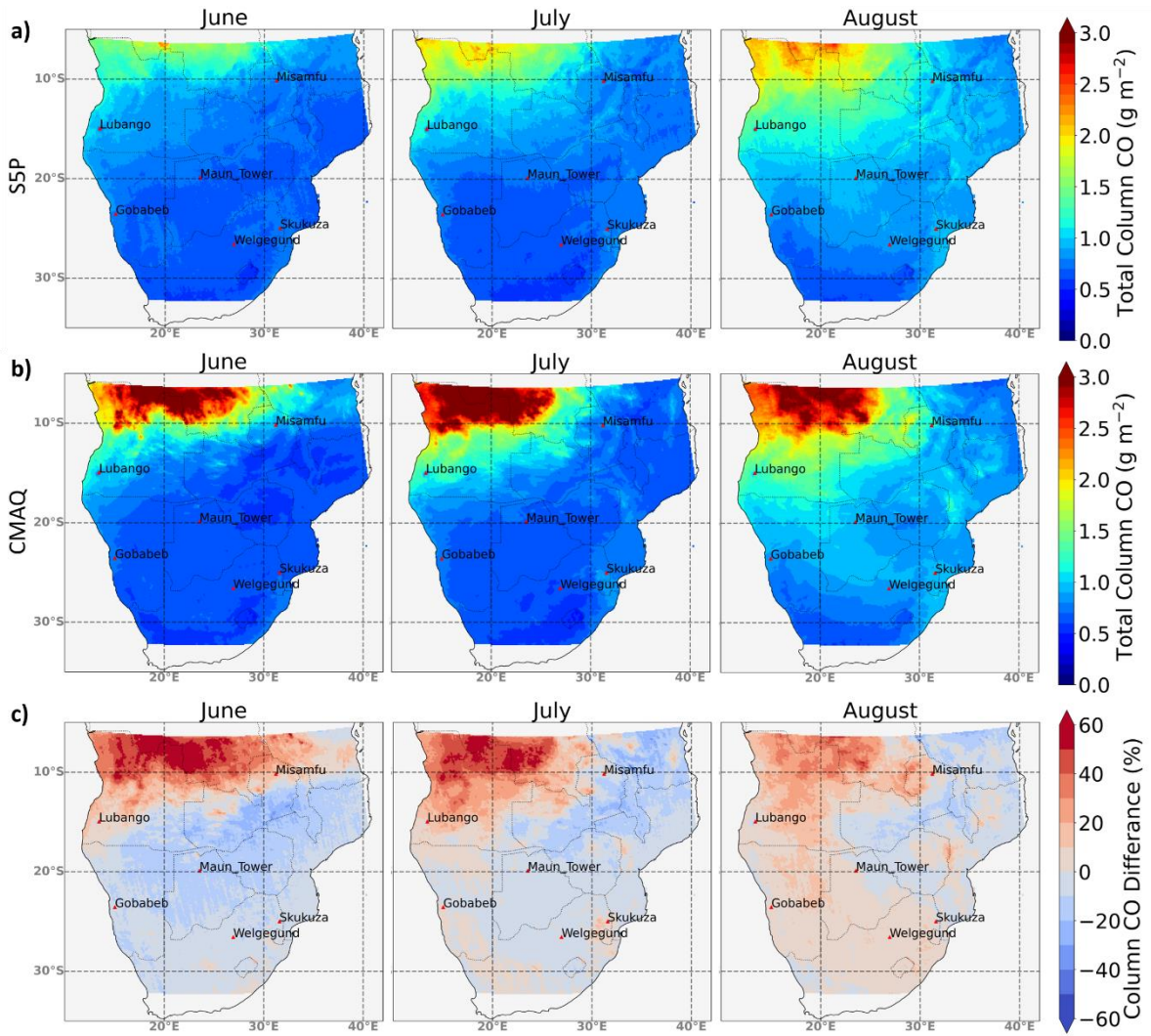


**Figure 5.5** Mapped mean monthly total CO from a) S5P and b) CMAQ during the simulation period from 15<sup>th</sup> June to 29<sup>th</sup> August 2019. c) shows the percentage difference between S5P and CMAQ AOD

Model and observed daily summed total column CO (Gg) are shown in **Figure 5.6** for the full domain extent and for each of the four regions of interest (ROIs) labelled in **Figure 5.1**. Temporal patterns of summed column CO are well replicated by CMAQ indicating that (i) detections of active fires are being reasonable well captured temporally in the SEVIRI FRP product and (ii) the meteorological fields of WRF, particularly wind, are performing well. ROI1, which includes much of the north western region of the domain, shows the largest difference between modelled and observed CO with modelled CO up to 1 Gg higher than observed CO in early August. This might be expected if the FREMv2-determined CO emissions used as input were even slightly overestimated, since this region has some of the

highest fire activity and Total C emissions (**Figure 5.3**). Both modelled and observed summed CO in the full domain is dominated by the high values of column CO in ROI1. For ROI2, ROI3, and ROI4 during the first few days of each of the two CMAQ model run simulations (starting 15<sup>th</sup> June and 29<sup>th</sup> July, respectively – marked by vertical blue line) S5P CO tends to be higher than modelled CO. Based on the bias towards higher modelled CO during most other periods, this indicates that a longer spin up time may be needed (beyond the 24 hours currently used) for the model to stabilise

The relation between daily summed total column CO in each ROI as determined by the model and by S5P is shown in **Figure 5.7** and monthly mean total column CO values are detailed for the same ROIs and full domain extent in **Table 5.2** along with the Pearson's correlation coefficients and NMBF between the datasets by month.

**Figure 5.7** shows again that, of the four ROIs, ROI1 summed total CO has the largest bias towards modelled CO (NMBF = 0.13 – a 13% overestimation by CMAQ compared to S5P). The three other ROIs have NMBF values close to zero (between 0.0 and -0.03) and both the full domain and all ROIs show a strong correlation between modelled and observed CO (all  $r \geq 0.83$ ). Daily summed CO from the full domain includes CO from all four ROIs and the additional area within the domain not included in any ROIs (see **Figure 5.1**). Importantly, this includes the complete north western region of the domain in which the largest differences between modelled and observed CO occurs (**Figure 5.5**) and results in summed CO being 13% higher in CMAQ than S5P. Despite these differences, overall, comparisons of modelled CO with S5P show very good agreement with monthly NMBF for all ROIs (**Table 5.2**) ranging between -0.8 and 0.16 (a 8% underestimation and 16 % overestimation of modelled CO relative to S5P CO) and Pearson's correlation coefficients are between 0.93 and 0.67. Over the full domain, the lowest bias (9% overestimation by model CO) occurs in August, and this is also the case for all the ROIs excluding ROI1. The negative NMBF values in June and July for ROI2, ROI3, and ROI4 indicate that at certain periods – mainly when fire emissions are low - the CMAQ model underestimates CO. This underestimation may be partly inherited from the WACCM chemistry used for initial and boundary conditions and may also be caused by artefacts from S5P CO observations – tracks from the satellite can be seen in **Figure 5.5c** in June over parts of Botswana.

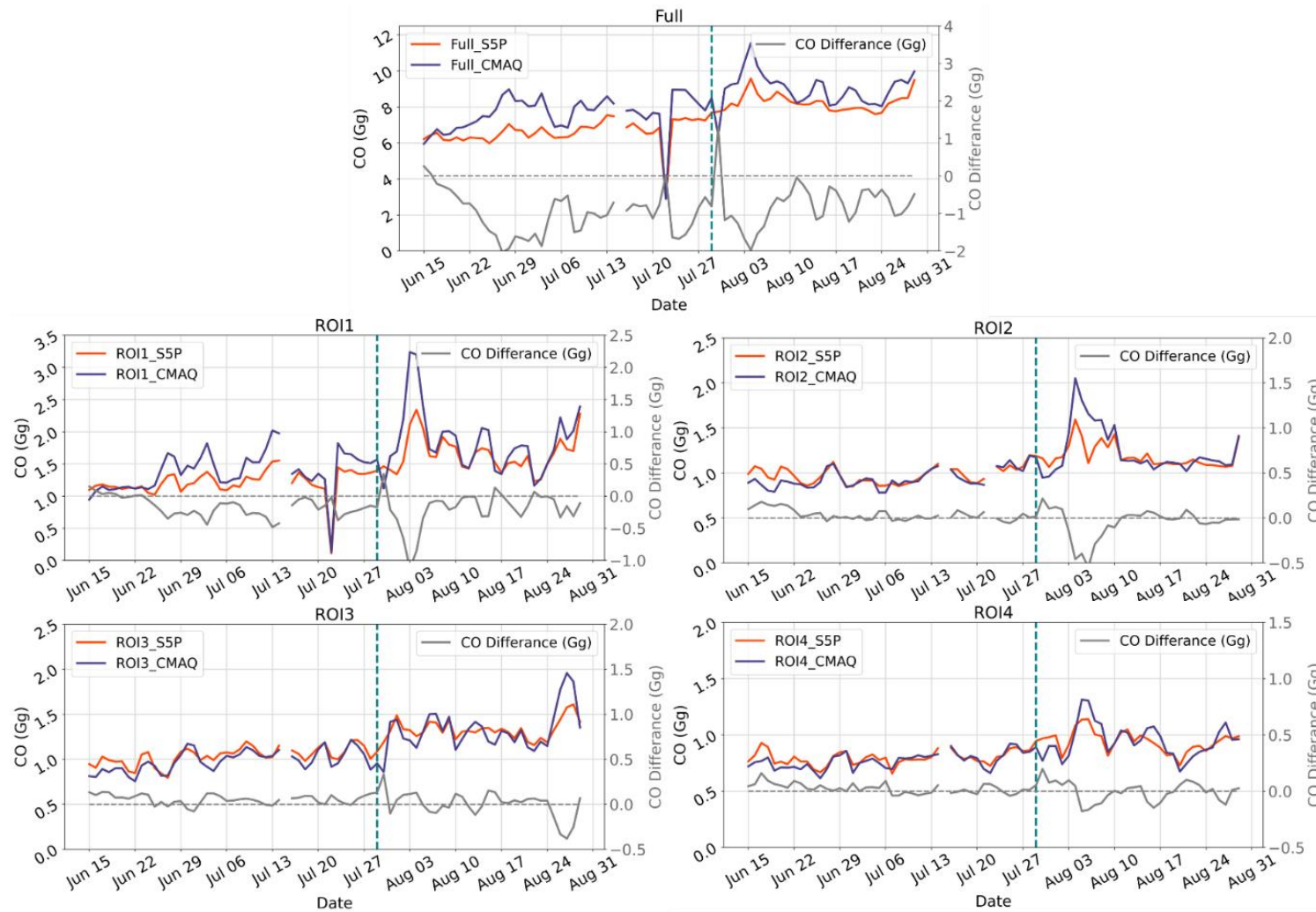


**Figure 5.6** Daily total CO averaged over the full domain extent and the ROIs shown in **Figure 5.1** as determined by CMAQ and observed in the S5P product. The difference between modelled and observed total CO is plotted by a solid grey line and a vertical dotted line on 29<sup>th</sup> July indicates the start of the seconds simulation

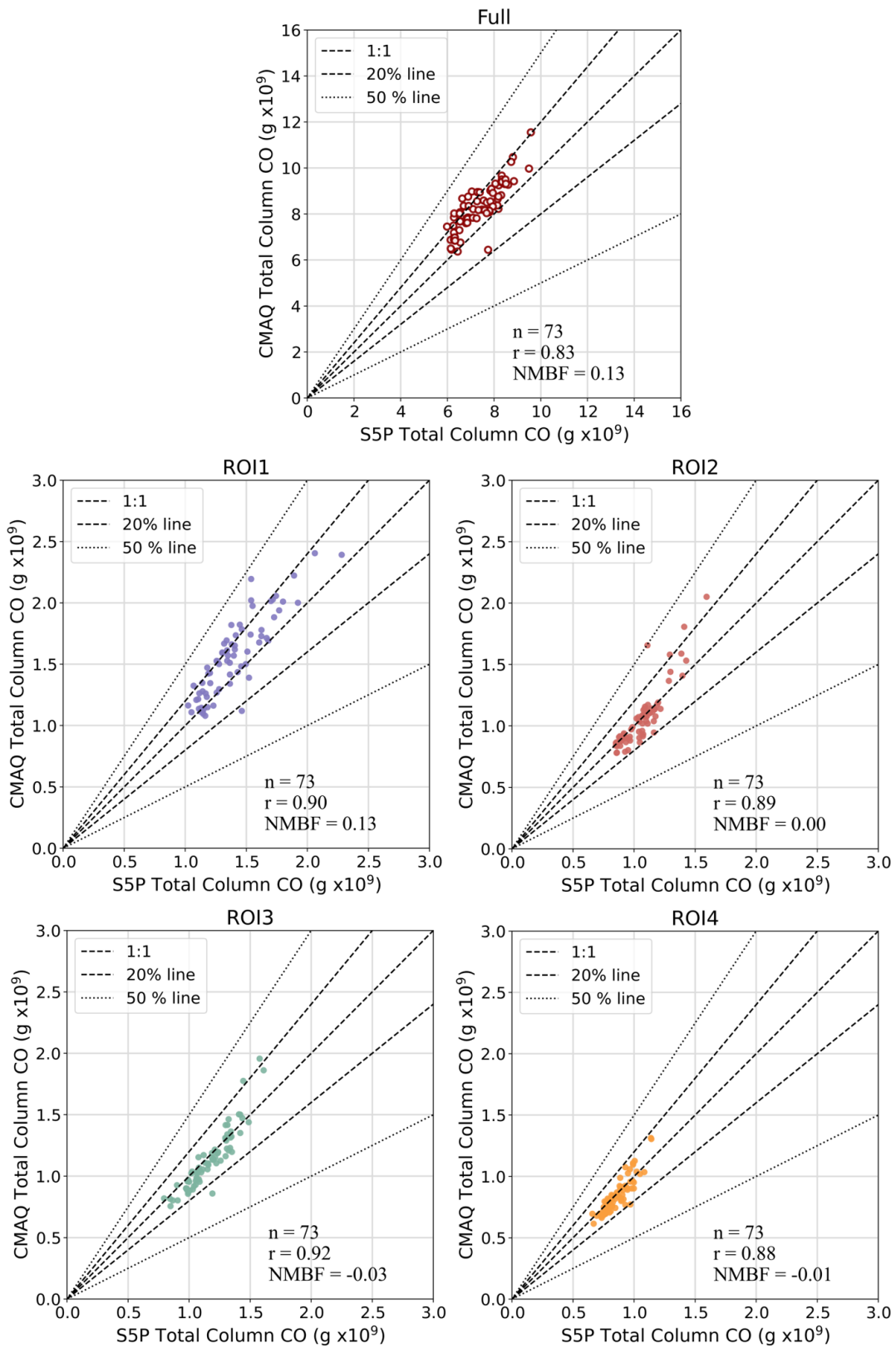


**Figure 5.7** The relationship between daily CMAQ total column CO and S5P total column CO in the full domain extent and the four ROIS shown in **Figure 5.1**. The Pearson's correlation and NMBF of each dataset is shown and dotted lines show the 1:1, 20% and 50% lines. Results of these plots are summarised in **Table 5.2**.

**Table 5.2** Monthly means of daily CMAQ and S5P total column CO, in the full extent of the domain and the ROIs shown in **Figure 5.1**, the NMBF of daily CMAQ CO with respect to observations and the temporal Pearson's correlation coefficient of daily CO over each month and the whole modelled period (15th June to 29th August 2019).

	Month	CMAQ Mean	S5P Mean	NMBF	Pearson's Correlation
<b>Full</b>					
CO ( $\text{g} \times 10^6$ )	June	7.45	6.38	0.16	0.67
	July	8.03	7.01	0.14	0.75
	August	9.10	8.49	0.10	0.87
	All	8.19	7.38	0.13	0.83
<b>ROI1</b>					
CO ( $\text{g} \times 10^6$ )	June	1.26	1.15	0.09	0.75
	July	1.51	1.31	0.16	0.91
	August	1.88	1.74	0.13	0.90
	All	1.60	1.42	0.13	0.91
<b>ROI2</b>					
CO ( $\text{g} \times 10^6$ )	June	0.90	0.97	-0.08	0.68
	July	0.97	0.99	-0.02	0.89
	August	1.40	1.28	0.05	0.84
	All	1.06	1.06	0.00	0.89
<b>ROI3</b>					
CO ( $\text{g} \times 10^6$ )	June	0.91	0.97	-0.06	0.82
	July	1.06	1.11	-0.05	0.93
	August	1.31	1.34	0.00	0.89
	All	1.13	1.16	-0.03	0.94
<b>ROI4</b>					
CO ( $\text{g} \times 10^6$ )	June	0.73	0.78	-0.07	0.83
	July	0.81	0.82	-0.02	0.85
	August	0.99	0.99	0.01	0.86
	All	0.85	0.86	-0.01	0.90

### 5.3.2.2 Individual CO Plumes

Individual fire-generated CO plumes identified in the S5P product were compared with CMAQ CO equivalent plumes. Modelled and observed total CO were calculated for each plume as the summed column CO within a bounding polygon containing the plume (plus a  $0.1^\circ$  grid cell buffer). The average location of plumes and polygons used to define them are shown in **Figure 5.8**.

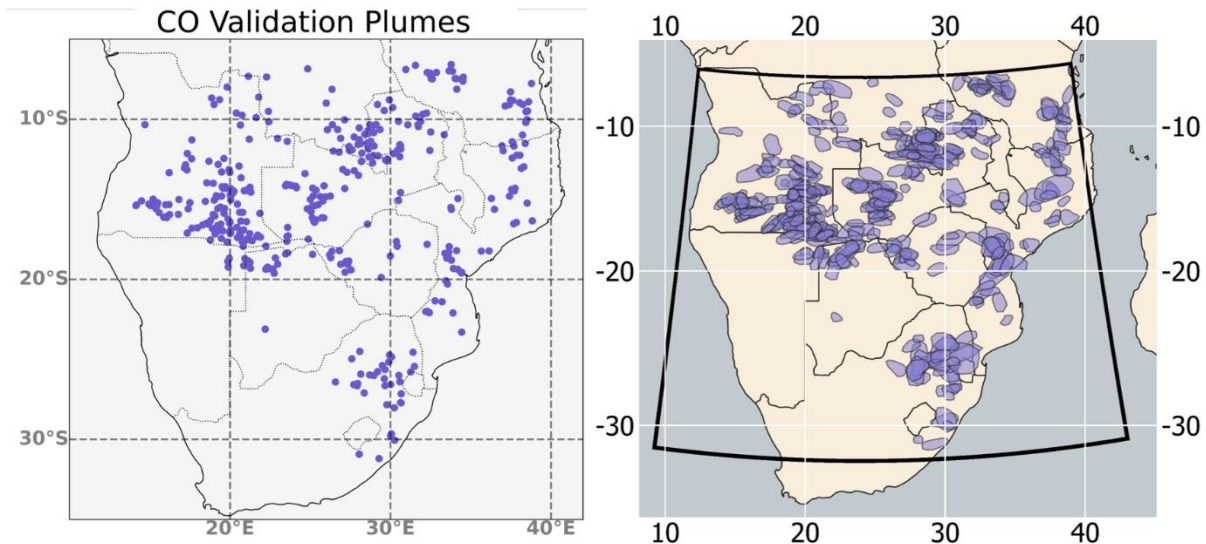


**Figure 5.8** The mean location (*left*) of CO plumes identified in the S5P product between 15<sup>th</sup> June and 29<sup>th</sup> August 2019 and the bounding polygons used to define the area over these plumes (*right*).

Over the full simulation period 384 individual plumes were identified in the S5P column CO product, mainly over areas having significant fire emissions in the FREM inventory (see **Figure 5.3**). In the region of highest fire activity (in the north west of the domain) relatively few plumes were identified because column CO over this area was consistently high in the S5P product and individual plumes could not be easily distinguished for much of the simulation period. **Figure 5.9** presents daily mean in-plume CO as a function of time and shows that - unlike in full domain and ROI CO comparisons (**Table 5.2**) and AOD comparisons (**Table 5.3**) – the difference between modelled and observed total CO does not vary significantly by month. Modelled daily in-plume CO on most days is higher than the equivalent observed S5P CO.

Total column CO values for all identified plumes are shown in **Figure 5.10**. Compared to daily total CO over the full domain (**Figure 5.7** and **Table 5.2**) the overestimation of modelled CO increases from 13% to 19% and  $r$  increases from 0.83 to 0.89. **Figure 5.10** also shows that larger CO plumes tend to have a higher bias towards modelled CO than smaller plumes. This may arise from the FREMv2 inventory's intrinsic 'small fire' boost which is discussed further in **Section 5.4.2.2** and is also mentioned in **Chapter 4**.

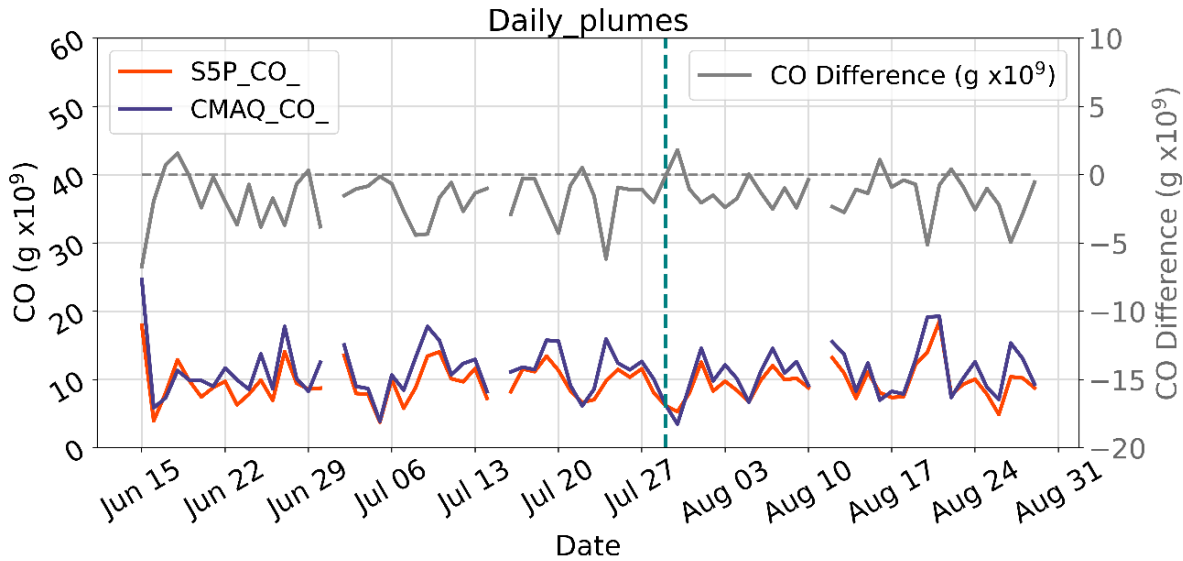


**Figure 5.9** Daily total mean CO observed in each plume as determined by CMAQ and the S5P product. The difference between modelled and observed total in-plume CO is plotted by a solid grey line and a vertical dotted line on 29<sup>th</sup> July indicates the start of the second simulation

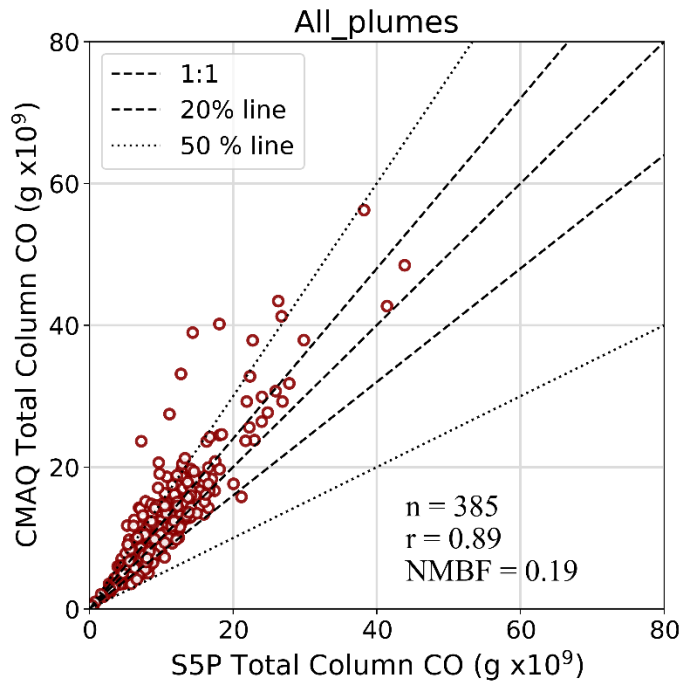


**Figure 5.10** The relationship between fire emitted CMAQ total CO and fire emitted S5P measured total CO for individual smoke plumes identified in the S5P CO product. The Pearson's correlation and NMBF of the dataset is shown along with dotted lines indicating the 1:1, 20% and 50% lines.

### 5.3.3 CMAQ AOD Comparisons to AERONET

CMAQ produces diagnostic files containing modelled AOD at several different wavelengths, including at 381 nm and 550 nm. CMAQ AOD at 381 nm is compared against AERONET AOD measurements at 380 nm at each of the six AERONET sites shown in **Figure 5.1**. Hourly and daily mean AOD averaged across the six sites, as determined from modelled and observed AOD, are shown in **Figure 5.11**. Modelled and observed AOD do not agree as well as comparisons of CO and CMAQ delivers a higher (but within 55%) AOD than AERONET for the majority of the simulation. CMAQ AOD does, however, capture the temporal pattern of AOD well, particularly in the case of hourly AOD. The accurate representation of temporal patterns is likely due to the high temporal resolution of the SEVIRI FRP data used in generating fire emissions in the FREMv2 inventory. Differences between modelled and observed AOD when averaged over all sites tend to be weighted towards an overestimation by the model.

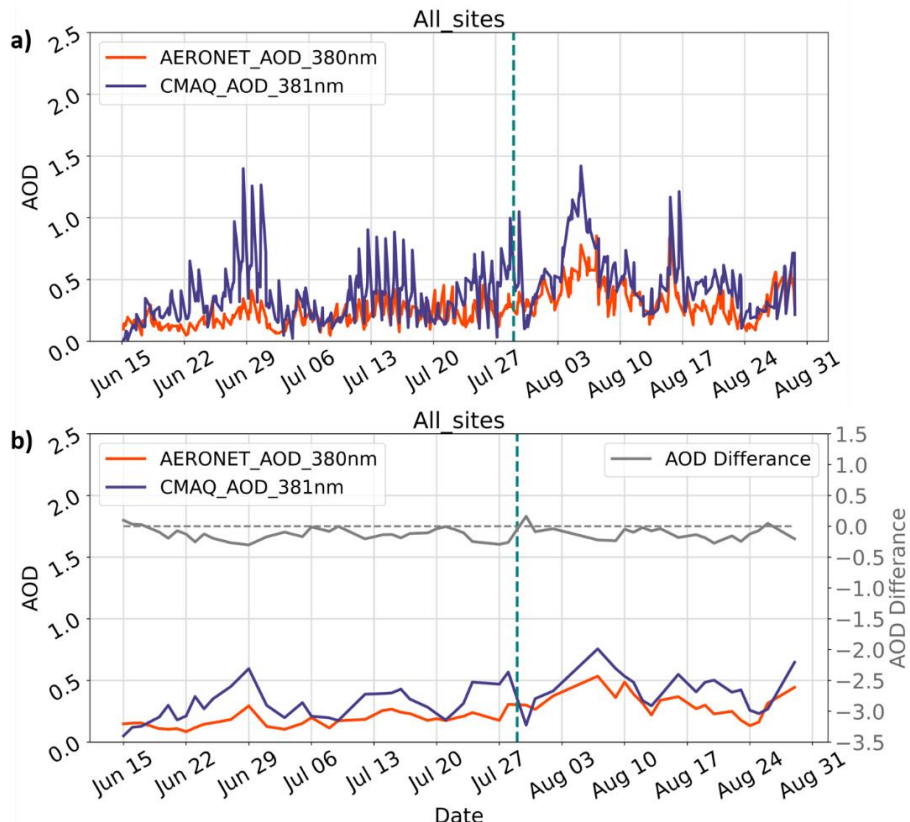


**Figure 5.11** a) Hourly and b) daily AOD averaged over all six AERONET sites, both from the CMAQ simulations and AERONET observations. In daily mean AOD (b) the difference between model and observation is plotted by a solid grey line and a vertical dotted line on 29<sup>th</sup> July indicates the start of the seconds simulation.

A comparison of hourly AERONET and CMAQ AOD values at individual AERONET sites is shown in **Figure 5.12**. At all AERONET sites the temporal pattern of AOD is well captured by CMAQ simulations, with model AOD generally increasing and decreasing at similar times as AERONET. This indicates that fire activity is being correctly detected in regions close to the AERONET sites and that the meteorological fields of the model are transporting aerosols relatively accurately. Comparisons of daily mean AOD at each site (**Figure 5.13**) also show that, in general, representation of temporal patters is well characterised in CMAQ. For both the hourly and daily AOD, some key differences occur between modelled and observed AOD and the magnitude of these differences varies significantly between AERONET sites and in time. The Lubango AERONET site shows the greatest difference between modelled and measured AOD, with modelled AOD on some days up to 0.8 (unitless) higher than measured AOD. The Lubango AERONET site is located in the north west region of the domain at the periphery of an area with some of the highest emissions in the domain (**Figure 5.3**). Other AERONET sites away from this north western region show better agreement between modelled and measured AOD - for example Maun Tower and Welgegund. It is however clear that overall, modelled AOD is higher than observed AOD, and that this overestimation by the model is most exaggerated in regions close to areas where fire emissions are high. The extremely high values for modelled AOD at the Lubango (and Misamfu in June) site may result partly from model error - the aerosol mechanism in CMAQ producing unrealistically high modelled AOD values. This is discussed further in **Section 5.4.1**. The Lubango site is also relatively closer to the edge of the domain than any of the other AERONET sites and distortions at the domain boundary may also have some remaining effect on the meteorological and chemical variables here, though likely these are small.

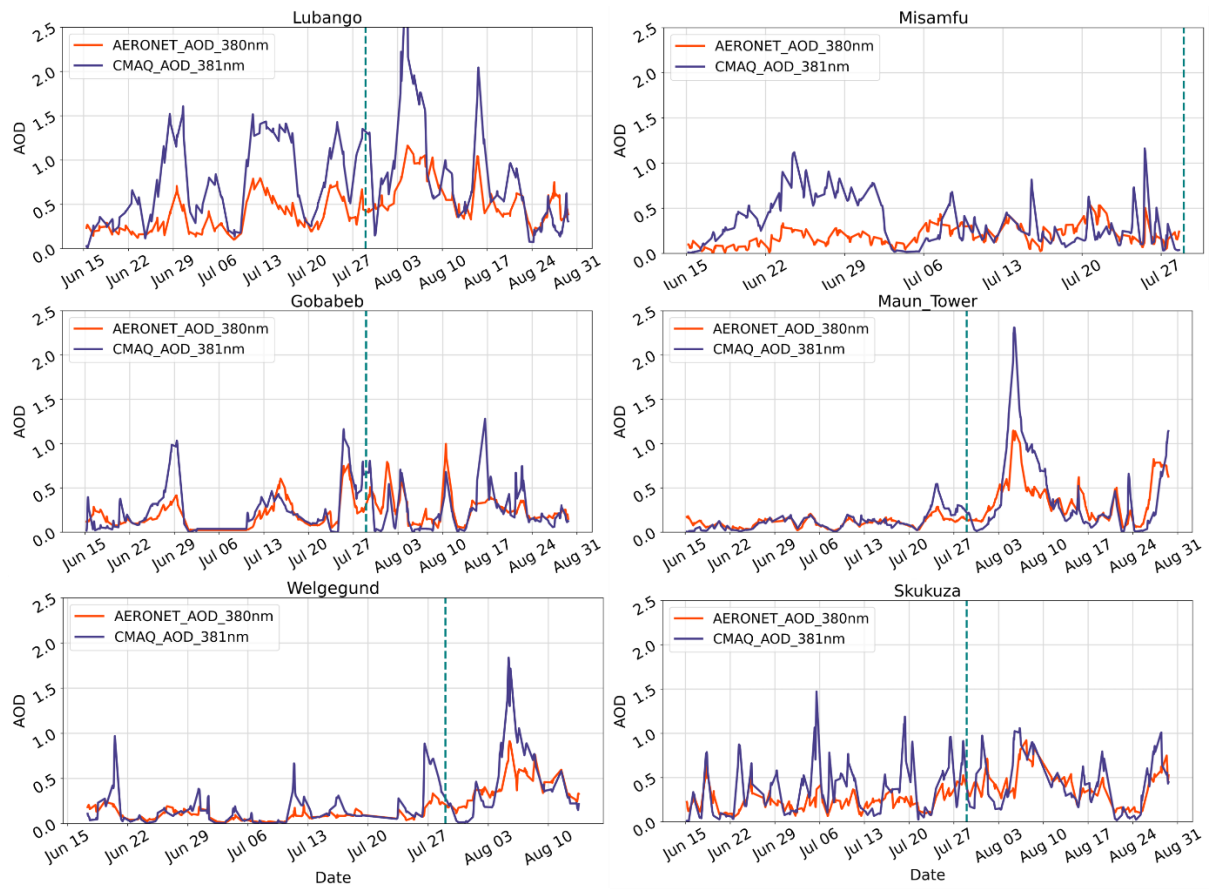


**Figure 5.12** Hourly AOD at each of the six AERONET sites as determined by CMAQ and observed by AERONET. A vertical dotted line on 29<sup>th</sup> July indicates the start of the second simulation. The Misamfu and Welgagund sites did not have Level 2 AERONET data for the full simulation period, and AOD data from these sites were available from 15<sup>th</sup> June until 27<sup>th</sup> July and 13<sup>th</sup> August respectively.

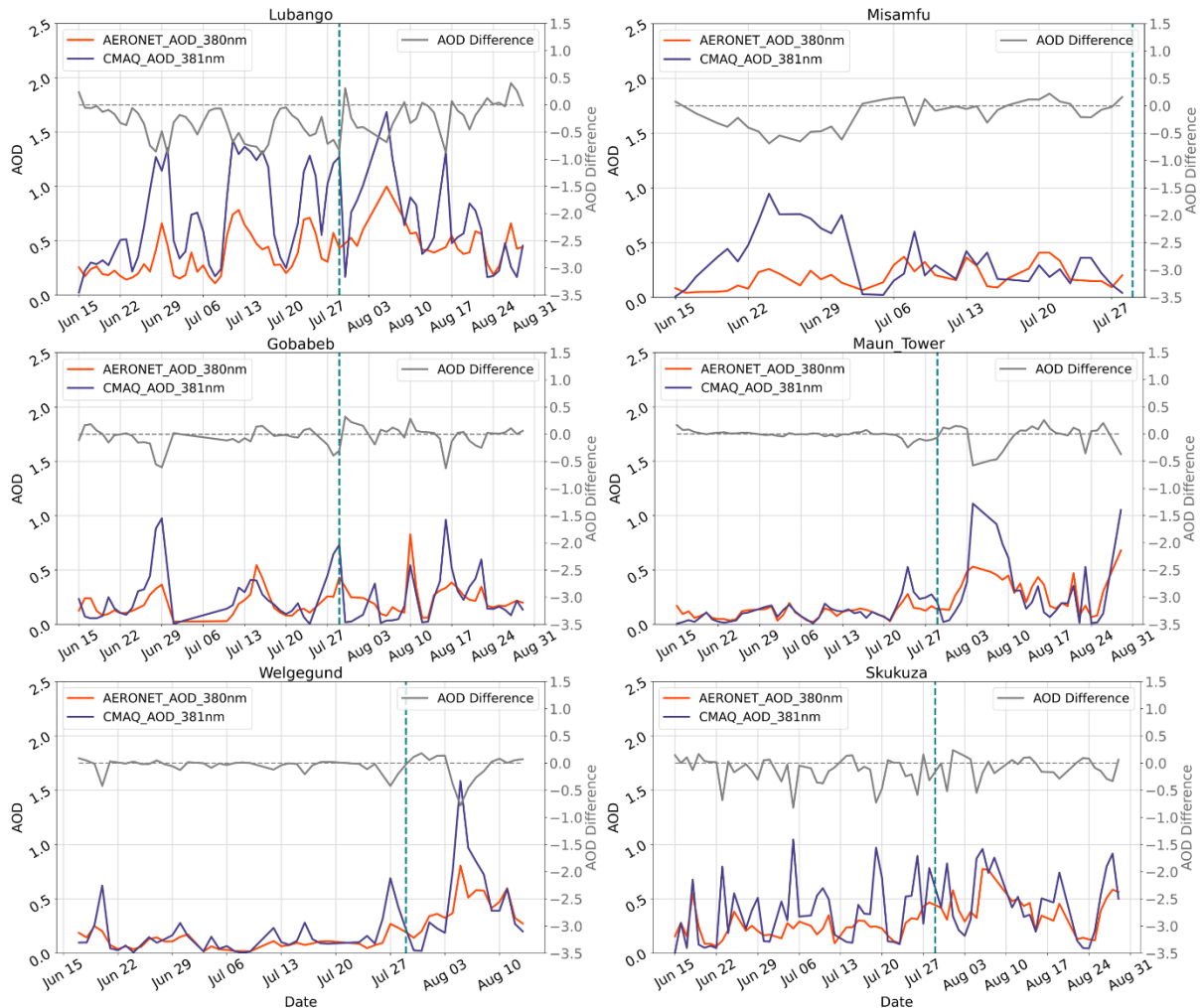


**Figure 5.13** Daily AOD averaged over at each of the six AERONET sites as determined by CMAQ and observed by AERONET. The difference between modelled and observed AOD is plotted by a solid grey line and a vertical dotted line on 29<sup>th</sup> July indicates the start of the seconds simulation. The Misamfu and Welgagund sites did not have Level 2 AERONET data for the full simulation period, and AOD data from these sites were available from 15<sup>th</sup> June until 27<sup>th</sup> July and 13<sup>th</sup> August respectively.

Hourly modelled and observed AOD are plotted against each other in **Figure 5.14** and the r and NMBF value of each AERONET site dataset are presented in **Table 5.3** along with monthly mean AOD for CMAQ and AERONET. NMBF over the simulation period at the six AEONET sites ranges between a 13% and 82% overestimation by the model and r ranges between 0.56 and 0.84, apart from Misamfu where the r is very low at 0.13. The data in **Figure 5.14** can be seen to be generally heteroskedastic and therefore the Pearson's correlation values should be treated with some caution. However, the NMBF metric used herein has been specifically developed to provide a measure of bias for similar such heteroskedastic datasets

(Yu et al., 2006) and therefore the estimates of model under or over estimation are not impacted by this property of the data.

Mean monthly AOD ranges between 0.07 and 0.83 in modelled data and between 0.10 and 0.56 in the observed AERONET data. Lubango accounts for the three highest monthly mean AOD values out of all the AERONET sites in all months (**Table 5.3**). Lubango and Misamfu in June show the greatest overestimation by the model compared to observations, with modelled AOD in June 125% and 283% higher than AERONET AOD respectively. All other sites have much lower monthly NMBF values ranging between a 7% and 63% overestimation by the model and in-fact Gobabeb and Maun Tower underestimate observed AOD by 6% and 45% in August and June respectively. Over the full simulation period these two sites show the overall best agreement with observations, both overestimating AOD by only 13% compared to observations. **Figure 5.3** shows that these sites are relatively far from significant fire activity and this is likely a factor in their good agreement as FREMv2 emissions are almost certainly the main source of perturbation in modelled AOD in these remote locations. When the six AERONET sites are considered together for the full simulation period there is a 55% overestimation of AOD by the model compared to observed AOD, and the best agreement is seen in August where this overestimation falls to 41%. Most sites show a similar trend towards improved correlation between modelled and observed AOD from June to August. With the exception of Misamfu and Skukuza in July ( $r = 0.14$  and  $r = 0.34$  respectively). The monthly Pearson's correlation between modelled and observed AOD ranges between 0.51 and 0.84 and the correlation for all sites over the full simulation period is 0.67. The low  $r$  in Misamfu data appears to be caused by two distinct patterns which, when separated would likely give a stronger correlation individually.

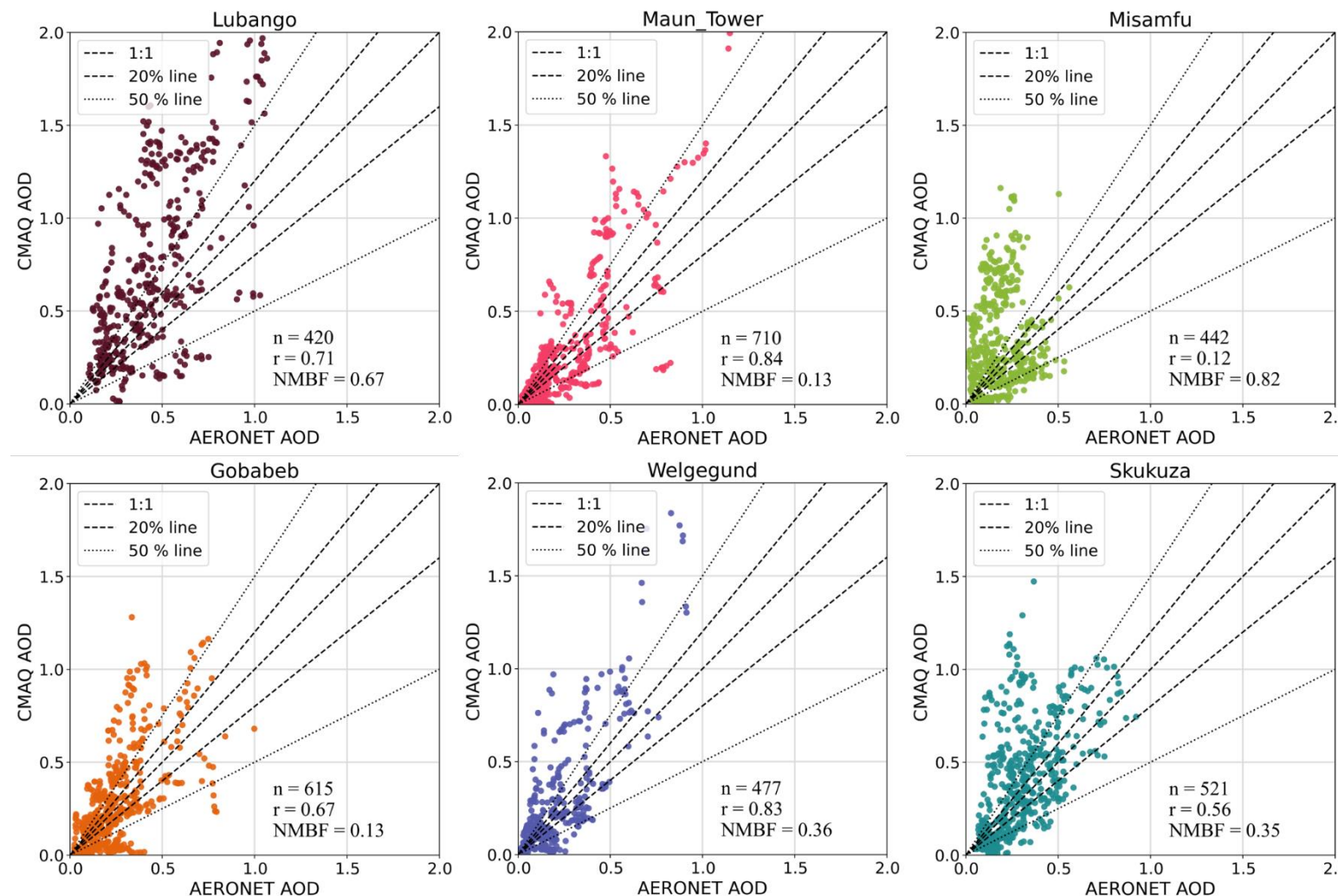


**Figure 5.14** The relationship between hourly CMAQ AOD at 381 nm AERONET measured AOD at 380 nm at each AERONET site. The Pearson's correlation and NMBF of each dataset is shown in figure and dotted lines show the 1:1, 20% and 50% lines.

**Table 5.3** Monthly mean of hourly CMAQ and AERONET AOD, the NMBF of hourly CMAQ AOD with respect to observations and the temporal Pearson's correlation coefficient of hourly AOD over each month and the whole modelled period (15th June to 29th August 2019).

Month	CMAQ Mean	AERONET Mean	NMBF	Pearson's Correlation (r)
<b>Lubango</b>				
June	0.58	0.26	1.25	0.71
July	0.83	0.49	1.02	0.79
August	0.76	0.56	0.34	0.78
All	0.75	0.45	0.67	0.71
<b>Misamfu</b>				
June	0.51	0.13	2.86	0.71
July	0.25	0.22	0.14	0.14
All	0.34	0.19	0.82	0.11
<b>Gobabeb</b>				
June	0.25	0.17	0.50	0.76
July	0.28	0.25	0.10	0.70
August	0.23	0.24	-0.06	0.64
All	0.25	0.22	0.13	0.67
<b>Maun Tower</b>				
June	0.07	0.10	-0.45	0.59
July	0.14	0.12	0.15	0.69
August	0.45	0.39	0.16	0.79
All	0.25	0.22	0.13	0.84
<b>Welgegund</b>				
June	0.14	0.12	0.18	0.57
July	0.16	0.11	0.50	0.62
August	0.54	0.45	0.25	0.84
All	0.24	0.18	0.36	0.82
<b>Skukuza</b>				
June	0.27	0.21	0.26	0.53
July	0.41	0.25	0.62	0.34
August	0.44	0.40	0.10	0.75
All	0.40	0.29	0.35	0.54
<b>All Sites</b>				
June	0.32	0.16	1.04	0.65
July	0.34	0.22	0.56	0.51
August	0.51	0.37	0.41	0.66
All	0.40	0.26	0.55	0.67

CMAQ AODs at each AERONET site were adjusted by a factor of  $1/(1+NMBF)$  using the site-specific NMBF values determined in **Figure 5.14** to produce a ‘bias corrected’ daily mean CMAQ AOD dataset. Essentially, CMAQ AODs at the Lubango, Misamfu, Gobabeb, Maun Tower, Welgagund and Skukuza sites were multiplied by a factor of 0.60, 0.55, 0.88, 0.88, 0.74 and 0.75 respectively. Analogous plots of daily AOD to those in **Figure 5.13** were produced using these bias-adjusted CMAQ AOD values and are shown in **Figure 5.15**. **Figure 5.15** demonstrates again that the temporal trends of AOD at AERONET sites are well captured by the model, and that when modelled AOD is adjusted for the NMBF, results between modelled and observed AOD also agree well in terms of the magnitude of AOD values.

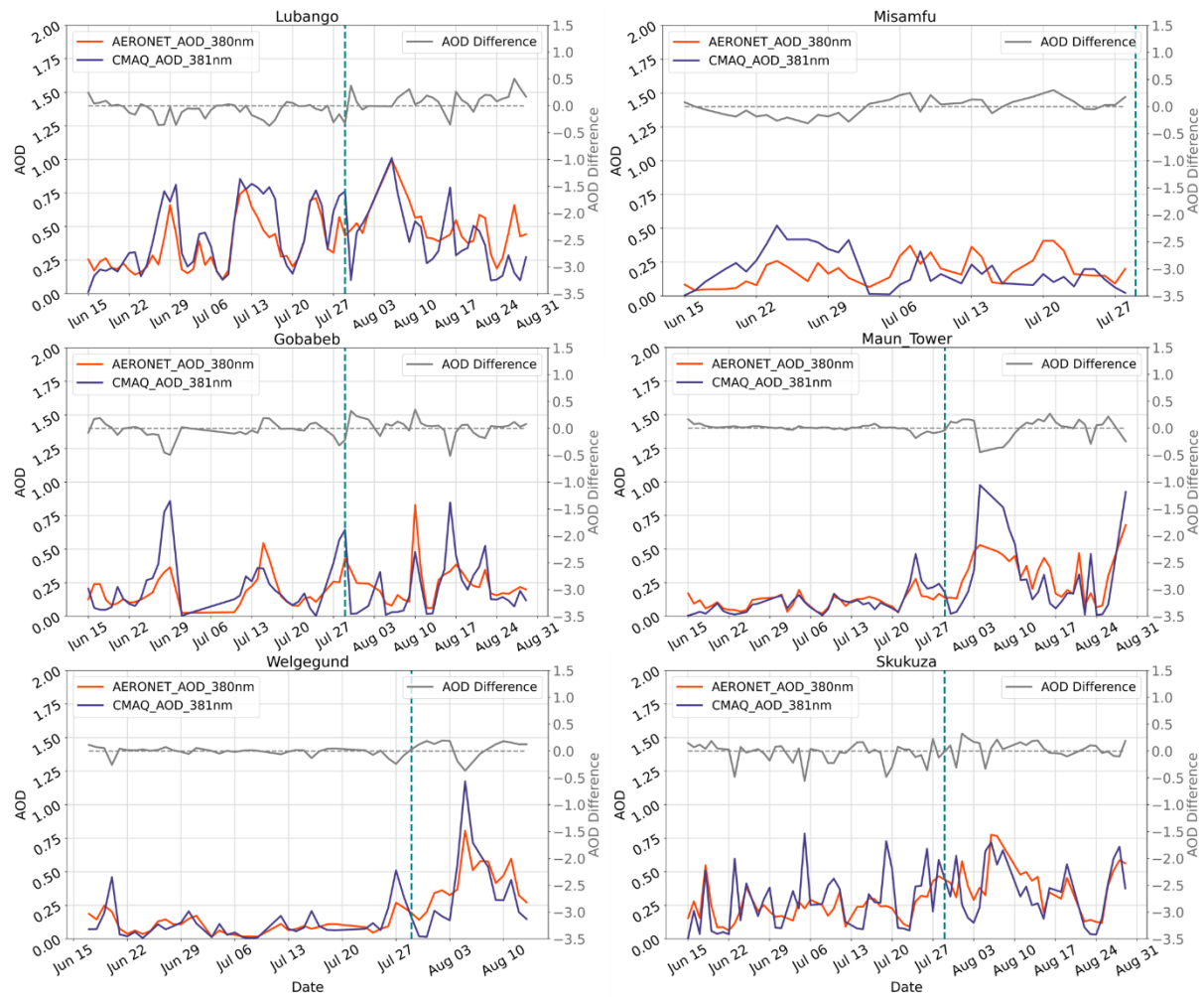


**Figure 5.15** ‘Bias corrected’ daily AOD averaged over at each of the six AERONET sites as determined by CMAQ and observed by AERONET. The difference between modelled and observed AOD is plotted by a solid grey line and a vertical dotted line on 29<sup>th</sup> July indicates the start of the seconds simulation. The Misamfu and Welgagund sites did not have Level 2 AERONET data for the full simulation period, and AOD data from these sites were available from 15<sup>th</sup> June until 27<sup>th</sup> July and 13<sup>th</sup> August respectively.

## 5.3.4 CMAQ AOD Comparisons with MAIAC

### 5.3.4.1 Full Domain and ROIs

CMAQ AOD at 550 nm was compared to the 550 nm MAIAC AOD product which has itself been validated against AERONET data (Lyapustin et al., 2011; Martins et al., 2017; Mhawish et al., 2019) and shows very good agreement (see **Section 4.3**). CMAQ AOD and MAIAC AOD were compared in terms of the full extent of the model domain and the ROIs depicted in **Figure 5.1**. The spatial distribution of monthly mean AOD in the MAIAC product and CMAQ is shown in **Figure 5.16**.

Most notable in **Figure 5.16** are the far higher values of modelled AOD compared with MAIAC AOD observations in most regions, particularly in the north west of the domain which has the highest fire activity (**Figure 5.3**). In this region, modelled AOD is overestimated by between 50% and 100%, with the highest overestimation occurring in June. The model results appear to be dominated by extremes in comparisons to observations as, in other parts of the domain, the model underestimates observed AOD significantly. In these areas, however, AOD values are already low and so this supposed underestimation is not as significant in absolute terms, though it does indicate that - in its base state - the CMAQ model tends to underestimate AOD. Artefacts of the MAIAC product are observed in **Figure 5.16a** which shows where the MAIAC sinusoidal projection tile boundaries have resulted in discontinuous AOD transitions, particularly in June and August along latitudes at 20°S.

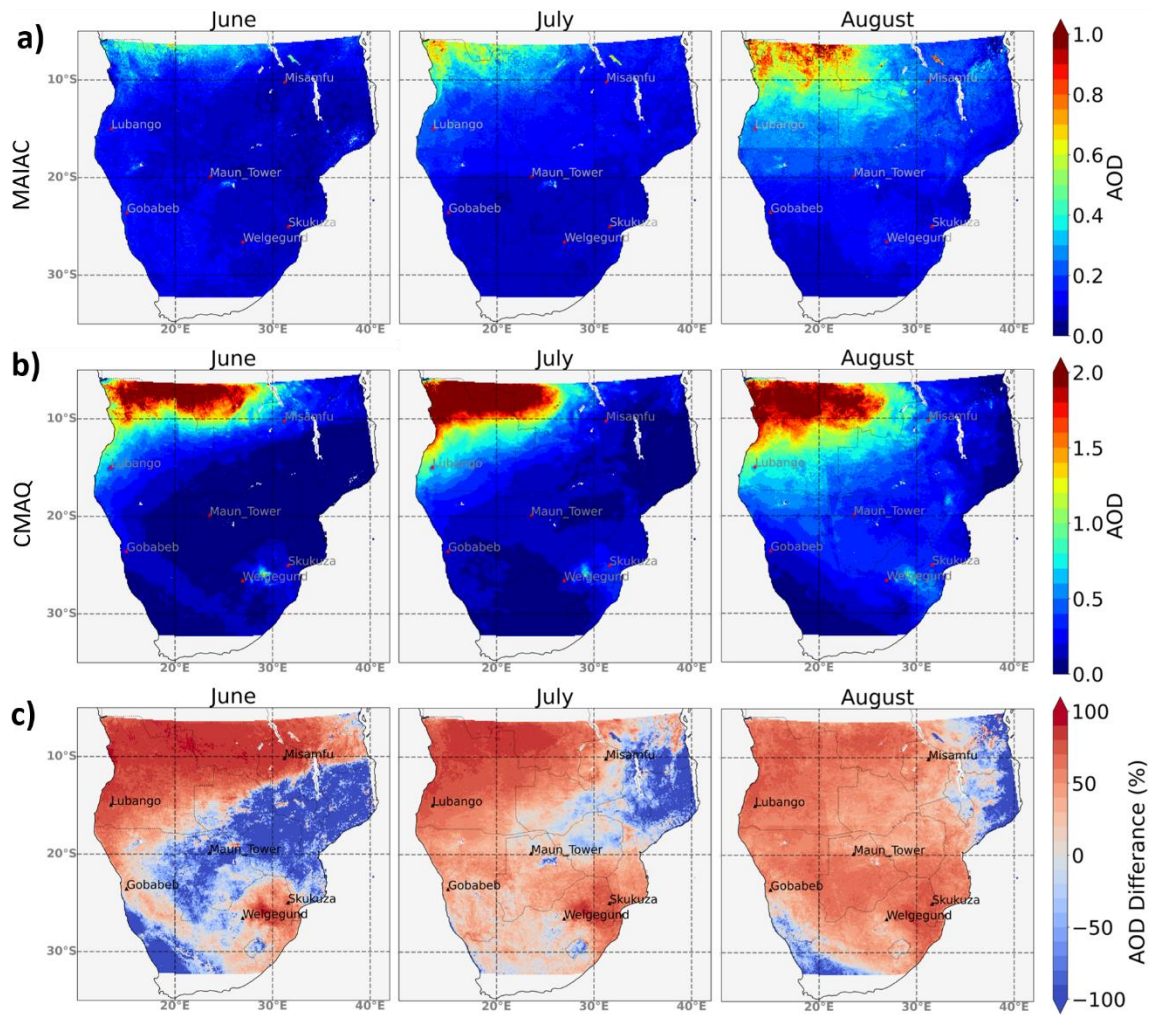


**Figure 5.16** Mapped mean monthly AOD at 550 nm from a) MAIAC and b) CMAQ (note - colour scale differences between a) and b)) during the simulation period from 15<sup>th</sup> June to 29<sup>th</sup> August 2019. c) shows the percentage difference between MAIAC and CMAQ AOD

A comparison of daily modelled and observed mean AOD for each month of the simulation period is shown in **Table 5.4** for the full domain extent and the four ROIs shown in **Figure 5.1**. **Table 5.4** also reports the NMBF and Pearson's correlation ( $r$ ) of each comparison. The results show that CMAQ AODs are significantly overestimated relative to observed AOD, and this overestimation is far greater than in CMAQ CO comparisons to S5P CO. Daily mean CMAQ AOD over the full domain for the full simulation period is higher than MAIAC daily mean AOD by 166%, and when restricted to days in June this increases to 246%. Mean CMAQ AOD in ROI1 – which includes much of the area with the highest fire activity - shows the largest overestimation, ranging between being 231% and 137% higher than MAIAC AOD, depending

on the month of simulation. Conversely ROI2 and ROI3, in which there is less fire activity, show lower NMBF values ranging from an underestimation of 15% to an overestimation of 123% by the model. The correlation between modelled and observed daily means varies by ROI and by month and in most cases  $r > 0.60$  with the exception of ROI2 in June ( $r = 0.45$ ). Correlation between modelled and observed AODs are, in general, lower than the correlation observed between modelled and observed CO.

Daily mean AOD values in the full domain and each ROI are plotted as a function of time in **Figure 5.17**. The time series of mean daily AOD values shows that the best agreement occurs between modelled and observed AOD during periods of low AOD in CMAQ and the largest differences are seen in periods when CMAQ AOD peaks, the most prominent of these occurring between the 3<sup>rd</sup> and 10<sup>th</sup> of August. Temporal patters of periods of high and low daily mean AOD in individual ROIs appear to be in reasonable agreement between CMAQ and MAIAC AOD, despite the relative magnitude of these peaks being overestimated in the CMAQ output.

**Table 5.4** Monthly means of daily CMAQ and MAIAC AOD, in the full extent of the domain and the ROIs shown in **Figure 5.1**, the NMBF of daily CMAQ AOD with respect to observations and the temporal Pearson's correlation coefficient of daily AOD over each month and the whole modelled period (15th June to 29th August 2019).

	CMAQ Mean AOD	MAIAC Mean AOD	NMBF	Pearson's Correlation
<b>Full Domain</b>				
June	0.14	0.04	2.46	0.75
July	0.15	0.05	1.86	0.61
August	0.18	0.79	1.30	0.26
All	0.16	0.06	1.66	0.52
<b>ROI1</b>				
June	0.30	0.09	2.31	0.90
July	0.43	0.15	1.79	0.75
August	0.64	0.27	1.37	0.61
All	0.48	0.18	1.60	0.70
<b>ROI2</b>				
June	0.08	0.09	-0.15	0.45
July	0.100	0.07	0.36	0.69
August	0.24	0.11	1.23	0.60
All	0.15	0.09	0.67	0.64
<b>ROI3</b>				
June	0.09	0.04	1.17	0.89
July	0.12	0.09	0.27	0.73
August	0.27	0.16	0.71	0.76
All	0.16	0.10	0.56	0.80
<b>ROI4</b>				
June	0.07	0.05	0.65	0.70
July	0.12	0.05	1.25	0.65
August	0.18	0.07	1.55	0.79
All	0.13	0.06	1.31	0.81

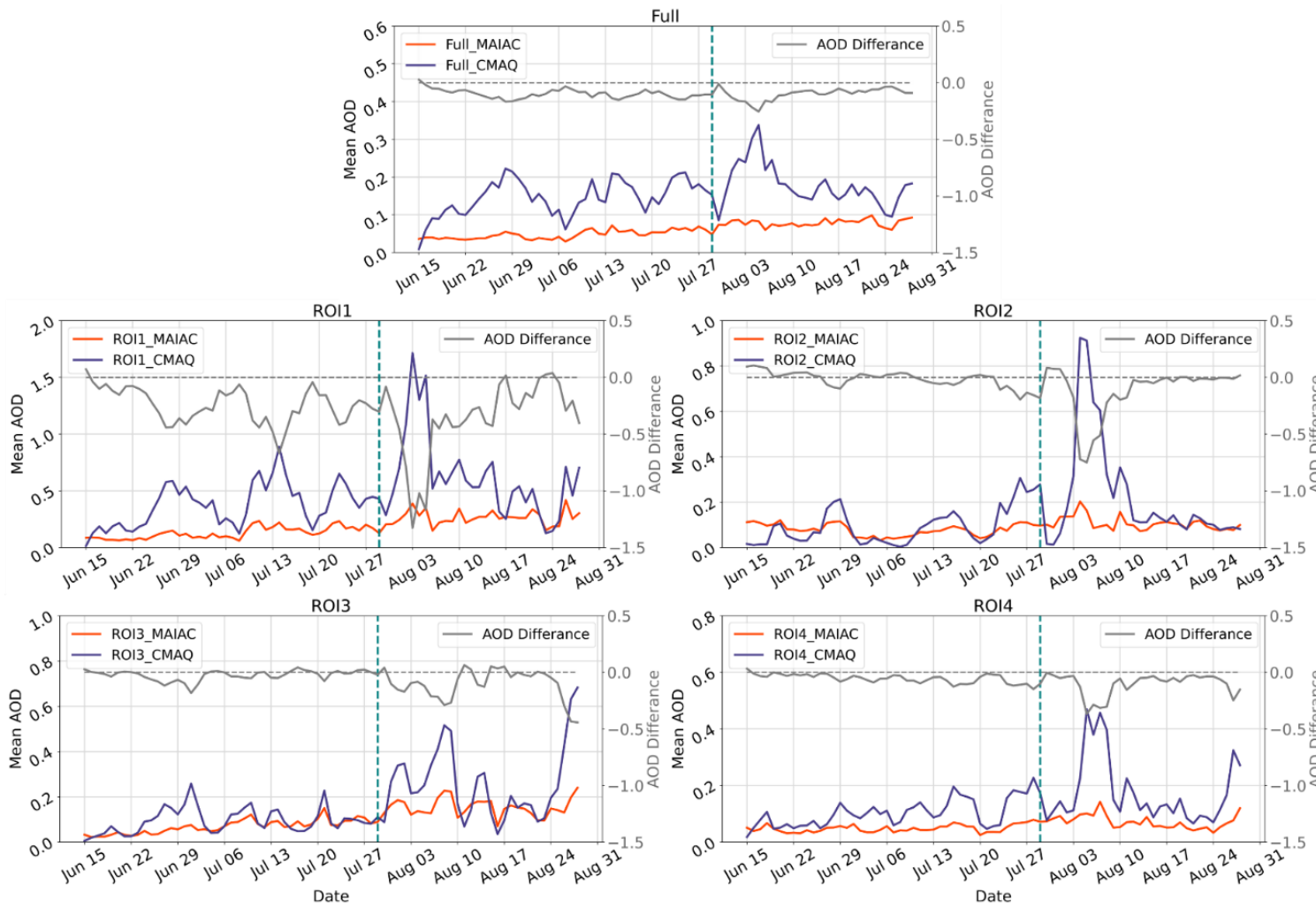


**Figure 5.17** Daily AOD averaged over the full domain extent and the ROIs shown in **Figure 5.1** as determined by CMAQ and observed in MAIAC. The difference between modelled and observed AOD is plotted by a solid grey line and a vertical dotted line on 29<sup>th</sup> July indicates the start of the second simulation.

### 5.3.4.2 Individual Smoke Plumes

The results of **Section 5.3.4.1** initially suggests that - because the highest overestimation of CMAQ AOD compared to MAIAC AOD occurs in regions with the highest fire emissions (**Figure 5.3** and **Figure 5.16**) - the overestimation of AOD likely originates in the FREMv2 emissions inventory used as input in the CMAQ model. To explore this further and attempt to minimise the contribution of model-specific influences on comparisons between CMAQ AOD and MAIAC AOD, modelled and observed AOD are compared for individual smoke plumes observed in the MAIAC AOD product. Individual fire emitted smoke plumes were selected from the MAIAC AOD product in its native 1 km spatial resolution (see **Section 5.2.3.3**). Polygons were used to define plume boundaries and the geographic locations of the 415 plumes identified within the domain over the study period are shown in **Figure 5.18**. Again, individual plumes were matched between modelled and observed AOD data and a 0.1°grid cell buffer was applied to account for variations in the spatial distributions of the plumes. Fire emitted AOD for CMAQ and MAIAC plumes were calculated via **Equation 4.1**

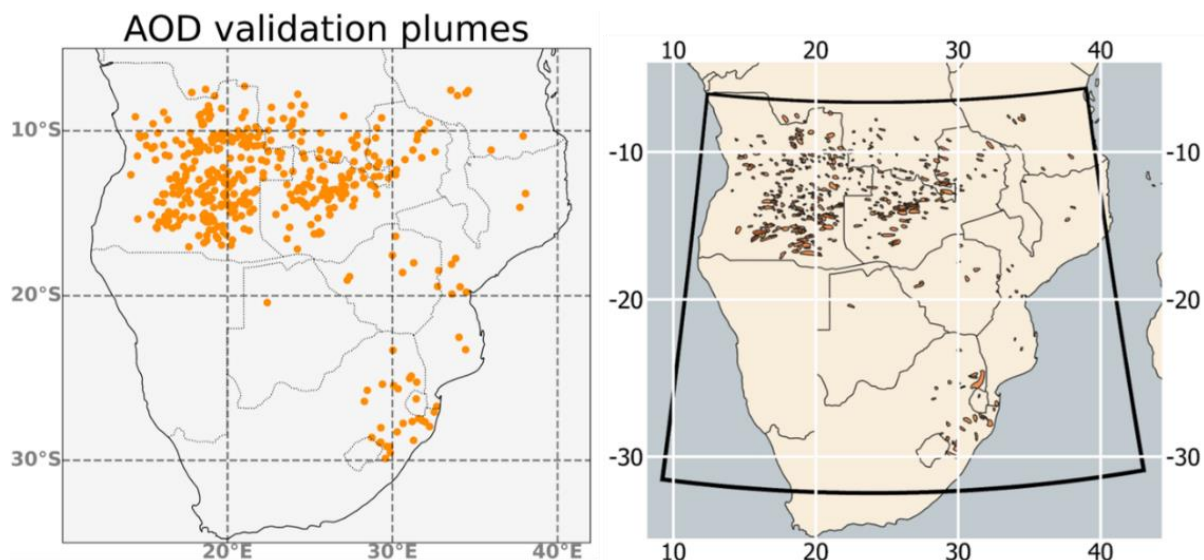


**Figure 5.18** The mean location (*left*) of smoke plumes identified in the MAIAC 1 km AOD product between 15<sup>th</sup> June and 29<sup>th</sup> August 2019 and the bounding polygons used to define the area over these plumes (*right*)

The direct relation between modelled AOD fields and those observed by MAIAC in the same plumes are presented in **Figure 5.19**. There is a large spread in the data, and the Pearson's r is relatively low at 0.47. As with the AERONET AOD comparisons of **Figure 5.14**, the data in **Figure 5.19** (and later **Figure 5.23**) are highly heteroskedastic and therefore the Pearson's correlation coefficient associated with these data should be interpreted with some caution - a Spearman's rank correlation coefficient may be more appropriate for these data in particular. However, the NMBF values are not impacted by heteroskedastic nature of the data and, although CMAQ AOD still shows an overestimation compared to MAIAC, the magnitude of this overestimation is far less than in full domain comparisons - a 25% overestimation by CMAQ compared to MAIAC rather than the 166% found over the full domain (**Table 5.4**). The larger difference between model and observation over the full domain may therefore be related to the CMAQ aerosol mechanism, which advances the physical processes driving the evolution of aerosol species after their emission into the model. This is discussed in more detail in **Section 5.4.1**

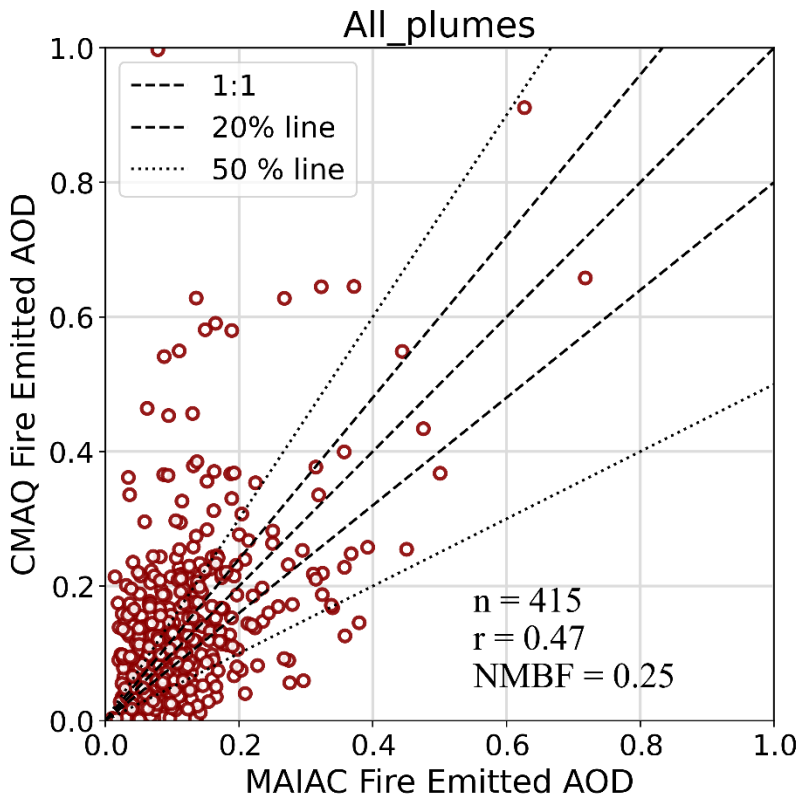


**Figure 5.19** The relationship between fire emitted CMAQ AOD and fire emitted MAIAC measured AOD for individual smoke plumes identified in the MAIAC AOD product. The Pearson's correlation and NMBF of the dataset is shown along with dotted lines indicating the 1:1, 20% and 50% lines.

### 5.3.5 Biome Specific Assessment of Emissions

The fire emissions from the FREMv2 inventory used as input in the WRF-CMAQ model rely on the biome-specific emission coefficient,  $C_{biome}$  (in g MJ<sup>-1</sup>), derived in **Chapter 4** to convert SEVIRI-derived FRP retrievals into estimates of gas and aerosol emission rates from fires. To further investigate the reliability of these biome-specific emission coefficients, the CO plumes of **Section 5.3.2.2** and the AOD plumes of **Section 5.3.4.2** were classified based on the majority vegetation type of the area defined by each plumes' bounding polygon. The biome map developed in **Section 4.4.1** using CCI Landcover and 30 m Landsat tree cover percentage is used to classify CO and AOD plumes and is shown for the CMAQ model domain in **Figure**

**5.20.** The biome classifications are closed canopy forest, high-woodland savanna, low woodland savanna, managed land, shrubland and grassland and details of their classification are detailed in **Section 4.4.1**. Due to the relatively low majority coverage of closed canopy forest and managed land over the domain, only a handful of plumes from fires occurring in these biomes are identified in the MAIAC AOD product, further, AOD plumes in these biomes did not generate statistically significant Pearson's correlation coefficients. However, plumes data in the four other vegetation did produce statistically significant ( $p < 0.05$ ) values for the Pearson's correlation coefficient. CO plumes from all biomes produced statistically significant values for  $r$ . **Figure 5.21** shows the total CO of CMAQ and S5P plumes, separated by biome and as a function of time.

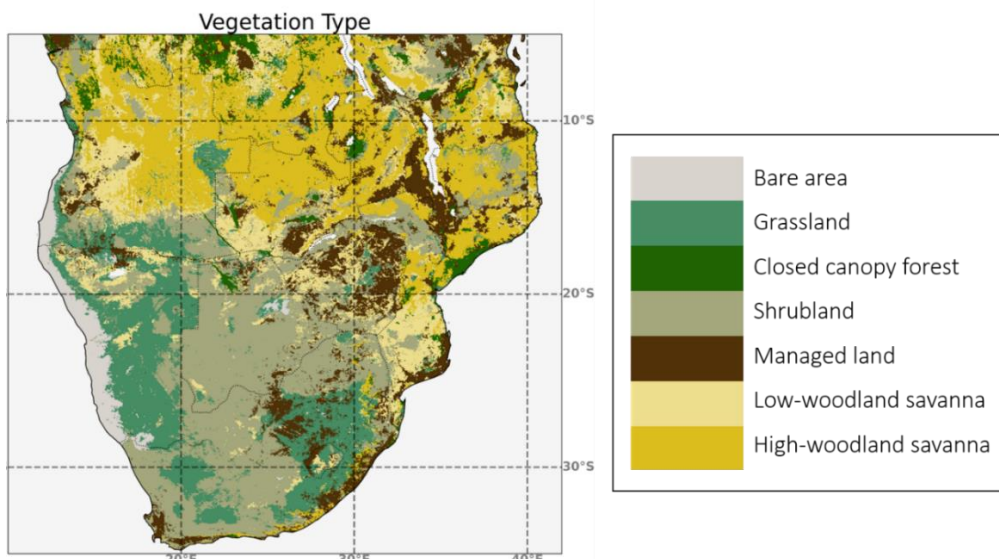


**Figure 5.20** The six biomes defined in **Chapter 4** over the CMAQ model domain, with the addition of bare area.

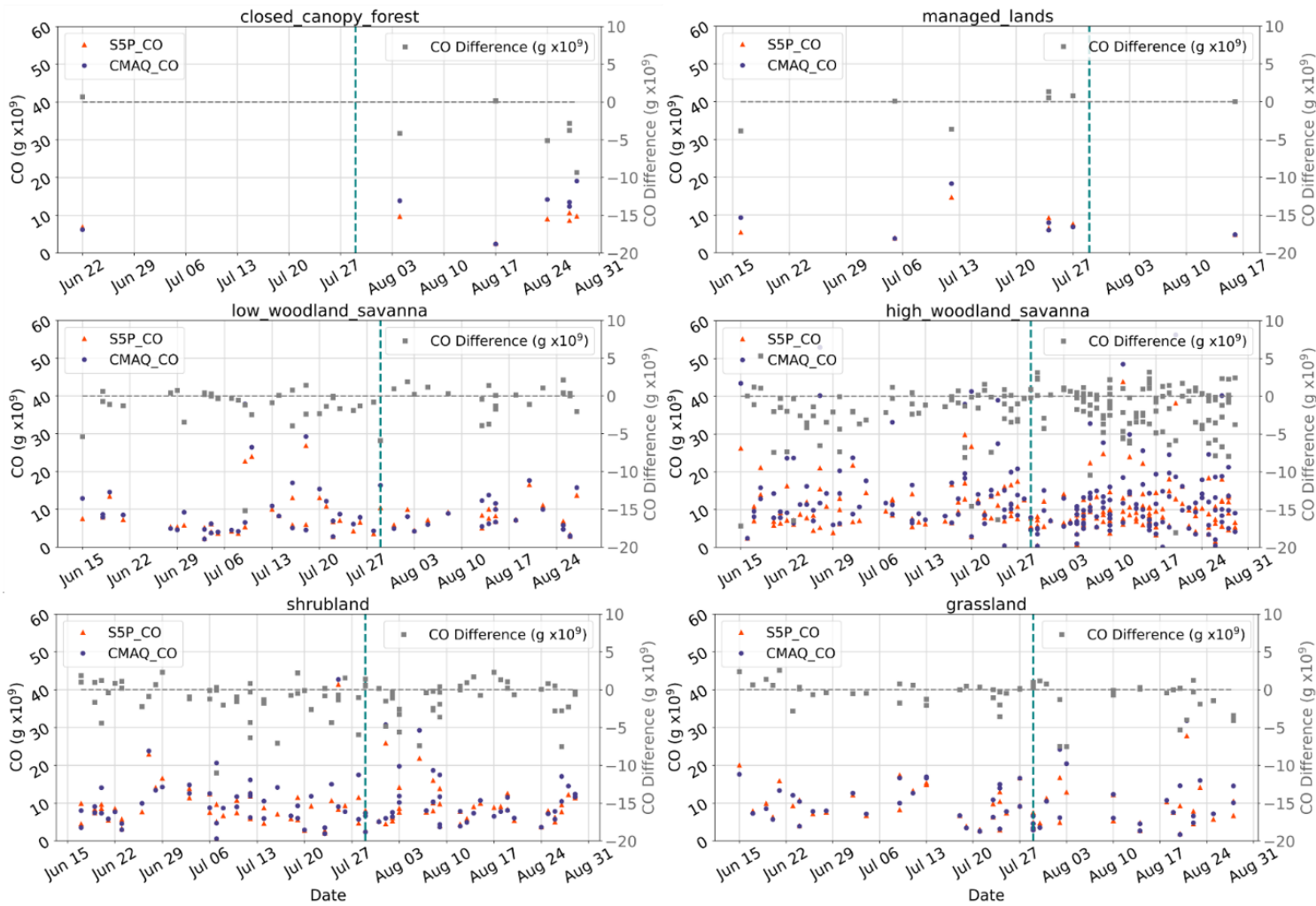


**Figure 5.21** CO observed in each individual plume as determined by CMAQ and the S5P product as a function of time for each of the six biomes. The difference between modelled and observed total in-plume CO is plotted by grey squares and a vertical dotted line on 29<sup>th</sup> July indicates the start of the second simulation.

The timeseries in **Figure 5.21** shows that over the course of the study period observable CO plumes tend to occur in each biome with a relatively consistent frequency, apart from in the case of high-woodland savanna in which an increased number of CO plumes are identified in August. Plumes at certain periods are clustered around similar modelled and measured CO values and these plumes are likely to have been identified over a similar area when prevalent wind conditions and fire activity result in well-defined plume signals in the S5P product.

The direct relation between in-plume total CO from CMAQ and S5P are plotted in **Figure 5.22** for each biome and in-plume mean AODs from CMAQ and the MAIAC AOD product are plotted in **Figure 5.23**. Modelled and observed means of in-plume CO and AOD along with NMBF and Pearson's correlation values for each dataset are detailed in **Table 5.5** and **Table 5.6** for CO and AOD plumes respectively.

The CO plume results in **Table 5.5** and **Figure 5.22** present grassland as having the best agreement between model and observations, with a NMBF of only 0.08 (8% overestimation by CMAQ), while shrubland and low-woodland savanna show a very similar overestimation of model CO by 13% and 12% respectively. High-woodland savanna covers a large portion of the north western region of the domain and overestimates CO by 25% compared to S5P CO. With a significant sample size of 180, this bias is likely quite representative of the performance of modelled CO in this biome. Though there are far fewer CO plumes in closed canopy forest, this biome showed the largest overestimation of CO - by 42%. Overestimation of emissions from these latter two biomes likely combine to contribute most significantly to the overall model overestimation of CO. All biomes show a relatively strong Pearson's correlation between modelled and observed in-plume CO with r values of no lower than 0.87.

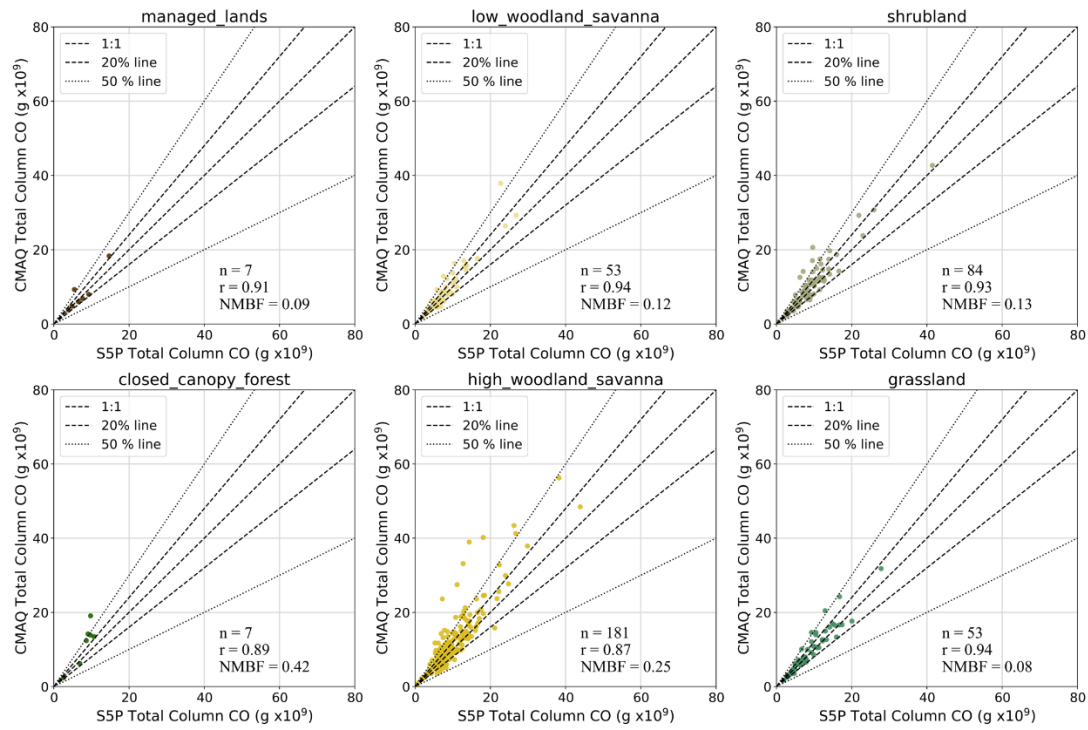


**Figure 5.22** The relationship between fire emitted CMAQ total CO and fire emitted S5P measured total CO for individual smoke plumes identified in the S5P CO product separated by biome. The Pearson's correlation and NMBF of the dataset is shown along with dotted lines indicating the 1:1, 20% and 50% lines.

**Table 5.5** Mean total CO of plumes in each biome as defined by CMAQ and S5P, and the NMBF of CMAQ plume CO with respect to S5P observations and the Pearson's correlation coefficient of between plume CO values of each.

	CMAQ Mean	S5P Mean	NMBF	Pearson's Correlation	N
Low-woodland savanna	9.29	8.27	0.12	0.95	53
High-woodland savanna	12.88	10.23	0.25	0.87	182
Closed canopy forest	11.67	8.20	0.42	0.89	7
Managed land	8.16	7.48	0.09	0.91	7
Grassland	9.81	9.08	0.08	0.94	53
Shrubland	10.17	9.02	0.13	0.93	84

An analogous separation of individual plumes by biome was carried out for modelled and observed AODs (**Table 5.6**). Overall, when all plumes were considered, the comparison between CMAQ and MAIAC plume AOD showed a 25% overestimation by the model (**Figure 5.19**). When separated by biome a 24% overestimation of AOD is seen in the high-woodland savanna biome. It contributes two thirds of the plumes identified in the MAIAC AOD product, so this result is not unexpected. Low woodland savanna plumes have the lowest model overestimation (6%), whereas shrubland and grassland plumes, in contrast to CO plume comparisons (**Table 5.5**), have higher NMBF values (a 37% and 64% overestimation by CMAQ respectively). For the biomes with statistically significant results ( $p < 0.05$ ), r values range between 0.44 and 0.63., showing that there is a much lower correlation between modelled and observed AOD plumes than between modelled and observed CO plumes.

These plume-based comparisons between modelled and observed column CO and AOD may present a more suitable validation of the FREMv2 emission inventory than comparisons over the full domain and ROIs as comparisons are made between areas in which concentration fields are being driven explicitly by fire emissions which have been released very close to the observation time and are likely to be less impacted by uncertainties in model atmospheric and chemical evolution. This point is discussed further in **Section 5.4.1**.

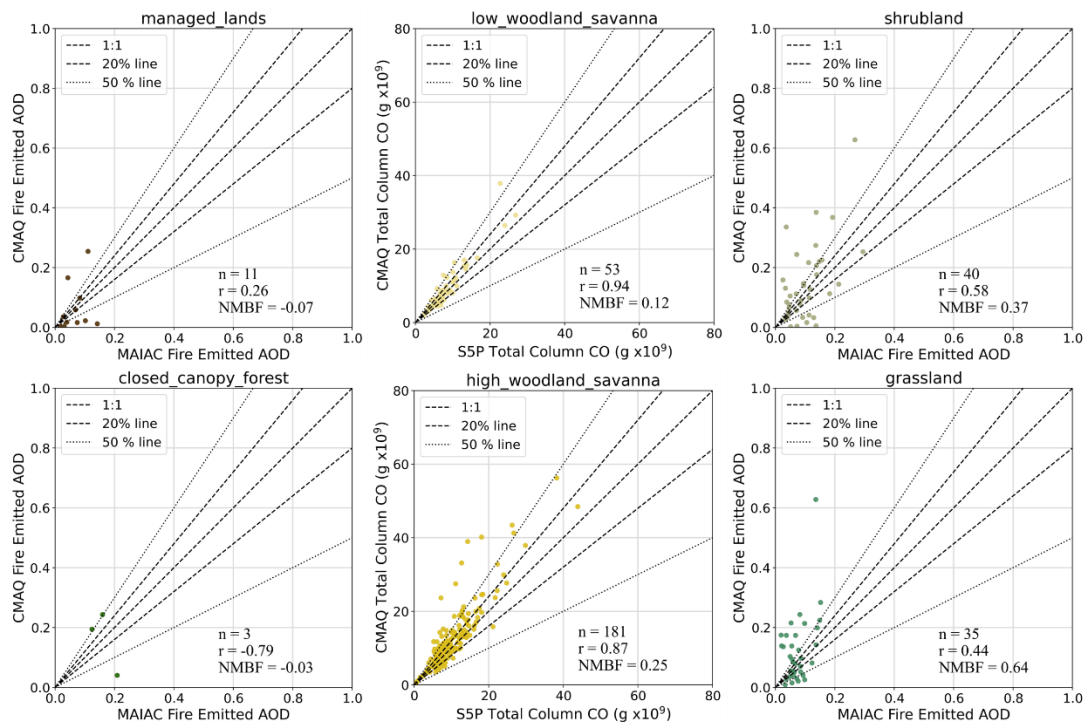


**Figure 5.23** The relationship between fire emitted CMAQ AOD and fire emitted MAIAC measured AOD for individual smoke plumes identified in the MAIAC AOD product separated by biome. The Pearson's correlation and NMBF of the dataset is shown along with dotted lines indicating the 1:1, 20% and 50% lines.

**Table 5.6** Mean AOD of plumes in each biome as defined by CMAQ and MAIAC, and the NMBF of CMAQ plume AOD with respect to MAIAC observations and the Pearson's correlation coefficient of between plume AOD values of each. Red highlighted rows indicate biomes which do not give statistically significant measures ( $p < 0.05$ ).

	CMAQ Mean AOD	MAIAC Mean AOD	NMBF	Pearson's Correlation	N
Low-woodland savanna	0.10	0.10	0.06	0.63	52
High-woodland savanna	0.16	0.14	0.24	0.45	27
Closed canopy forest	0.16	0.16	-0.03	-0.79	3
Managed land	0.06	0.07	-0.07	0.26	11
Grassland	0.12	0.07	0.64	0.44	35
Shrubland	0.14	0.10	0.37	0.58	40

## 5.4 Discussion

The comparisons of CMAQ-generated output with the validation datasets presented in **Section 5.3** show some overestimation of fire-generated CO relative to observations, but far more significant overestimation of AOD. The largest overestimation is seen in comparisons of monthly mean CMAQ AOD and matching MAIAC AOD at 550 nm (**Figure 5.16** and **Table 5.4**), whereas column CO comparisons of **Figure 5.5** and **Table 5.2** show a much lower degree of overestimation.

There may be several causes for this overestimation, including contributions from the process used to re-map FREMv2 emissions from the SEVIRI full disk projection to the WRF-CMAQ domain, uncertainties in the validation datasets themselves or any of the other model related features described in **Section 2.5.1**. However, there are two specific sources that likely dominate the observed overestimation of CO and AOD compared to observations. These are model error originating in the aerosol scheme currently used in these CMAQ simulations, and the FREMv2 emissions themselves being too high. These issues are discussed in the following sections.

### 5.4.1 Model Error in CMAQ

There are several points of evidence indicating that some portion of the overestimation in modelled AOD is caused by features of the CMAQ model and its configuration, rather than the FREMv2 fire emissions inventory used as input. Hereafter in this section ‘model error’ will be used to refer to not only intrinsic errors in the model (i.e. assumptions in dynamic equations and other abstractions in representing atmospheric processes), but also any inappropriate or poorly representative setting selected in the model set up.

The first point indicating the part of model error is the far better agreement seen between S5P CO observations and model CO than between MAIAC AOD observations and model AOD. Full domain comparisons of CMAQ and MAIAC daily mean AOD over the simulation period results in a 166% overestimation of AOD by the CMAQ (**Table 5.4**), whereas the equivalent comparison of CMAQ and S5P CO measures gives only a 13% overestimation of CO by

CMAQ. Yet both particulate matter and CO emissions are delivered via the same FREMv2 methodology (see **Section 5.2.2.2**). This in itself is not indicative of CMAQ model error, however, it does highlight that CO emissions and particulate emissions provided by the same emission inventory (and derived via the same methodology) give drastically different results in terms of their agreement with satellite observations. Given the identical process applied to generate particulate and CO emissions in FREMv2, there are three potential sources for the large difference in agreement observed between model and observations with respect to CO and AOD:

- i) Uncertainty in the emission factors (EFs) used in the conversion of  $C_{biome}^{TPM}$  to emission coefficients for all other species ( $C_{biome}^x$ ; **Equation 4.3**)
- ii) Uncertainty in the S5P CO and MAIAC AOD satellite observations
- iii) Errors in model propagation and the physical and chemical evolution of particulate species and CO, and inappropriate or unrepresentative selections made during CMAQ model set-up and configuration. For example, the physical and chemical schemes selected, and initial default aerosol size distributions assigned to particulate species.

This study applies the EFs of Andreae (2019) which do not diverge significantly from the EFs of Andreae and Merlet (2001). The latter are widely used in other emission inventories such as GFAS (Kaiser et al., 2012). As particulate species and CO emissions in this inventory have not been shown to have drastically different agreement with observations, i) above is unlikely the primary source of the differences in agreement of CO and AOD comparisons in this work. In the case of ii) it is certainly true that satellite products have their own inherent uncertainty, however, the MAIAC AOD product was integral in the generation of FREMv2 emissions themselves - it is hence somewhat unexpected that modelled AOD and observed MAIAC AOD differ by as much as 166%, particularly when compared to CO comparisons where agreement between model and observation is far stronger. This difference in the results from CO and AOD comparisons therefore points towards the potentially more significant influence of iii), model-related error. Similar differences in model-observation bias are seen between MAIAC AOD and S5P CO in comparisons split by month and ROI (**Table 5.2** and **Table 5.5**). Pearson's correlation between model and observation are also far higher for the CO comparisons than for the AOD comparisons (though as previously highlighted, AOD r values

should be treated with some caution). Further to this, in CMAQ CO comparisons with S5P CO the bias in full domain comparisons does not differ drastically from individual plume comparisons - NMBF values are 0.13 and 0.19 respectively (a 13% and 19% overestimation of model CO compared to S5P CO). This is not the case in the AOD equivalent comparisons, where the overestimations of modelled AOD drops from 166% to 25%.

Compared to many other trace gases emitted during biomass burning, CO is moderately stable in the atmosphere with a lifetime varying between around 10 days (in summer) to 2 months (in winter) (Holloway et al., 2000; Edwards et al., 2006). Due to its lifetime and its relatively simple chemistry in the atmosphere CO is often used as a tracer to investigate the role of transport in the redistribution of chemical pollutants. The only sink for atmospheric CO is its reaction with OH radicals which are formed in the photochemical destruction of ozone - hence the variation of CO lifetime during summer and winter (Levy, 1971). OH radicals react with CO to form CO<sub>2</sub> and a H radical and this H radical goes on to either destroy or produce ozone depending on the abundance of NO<sub>x</sub> (Klonecki and Levy, 1997). CMAQ modelled total column CO concentrations will thus be primarily driven by FREMv2 emissions and (anthropogenic emissions), dispersion via the WRF meteorological fields, and the limited reaction of CO with OH radicals (Gipson and Young, 1999).

The representation of aerosol species in air quality modelling, on the other hand, is significantly more complex. Variables such as AOD are influenced by assumptions about particle size distributions, physical processes such as dry and wet deposition, aggregation, and nucleation as well as chemical reactions. The CMAQ aerosol scheme (Binkowski, 1999; and updates Pye, 2016) assigns aerosol particles to three interacting 'modes' or sub-distributions of particle size and the distributions in these three modes are determined by physical and chemical aerosol processes. The aerosol component calculates estimates of visual range, aerosol extinction coefficients and crucially AOD, which are all influenced by the distributions of these interacting particle modes. In this way AOD values in CMAQ are subject to many more model assumptions and processes than are modelled CO values, and this may be a contributing factor in the far larger overestimation seen in AOD comparisons than in CO comparisons.

Since FREMv2 emissions are derived from the relation between SEVIRI FRP and MAIAC AOD observations, it is perhaps surprising that validations against MAIAC AOD do not show better performance than comparisons against S5P column CO, and model error is likely a partial cause of this.

Further evidence to suggest model error is a significant contributing factor is the reduction in bias when MAIAC AOD is compared to CMAQ AOD in terms of individual AOD plumes rather than across the full domain. **Figure 5.19** compares fire emitted AOD from 415 plumes observed in the MAIAC AOD product with the CMAQ AOD observed over the same area close to the MAIAC observation time. In these comparisons a 25% overestimation by the model in terms of AOD is found – far lower than the 166% overestimation found over the full domain extent. These individual plumes represent a comparison between AOD observations and FREMv2 generated emissions close to the source and at times shortly after emission, which minimises the number of model time steps between the emissions being released into the CMAQ and the AOD measures being compared.

The final result pointing to model dynamics being partly responsible for modelled AOD overestimation is demonstrated in the evolution of AOD over the course of the day at specific AERONET sites. The observed and modelled hourly mean AOD at each AERONET site was calculated and is plotted in **Figure 5.24**. Since AOD is measured at wavelengths in the visible range it is only observed (and modelled) in daylight hours and in the CMAQ domain this is roughly between 07:00 and 17:00 hours local time. Of the six AERONET sites, Gobabeb, Maun Tower, Welgegund and Skukuza show a relatively constant mean AOD over the day and these stations are either located at the edge of, or relatively far from, significant fire activity (**Figure 5.3**). The same is true for the Lubango site which is located on the western edge of an area of very high fire activity in the north western portion of the domain. Despite being at a similar proximity to fire activity as the Welgegund and Skukuza sites, however, the temporal profile of mean AOD at the Lubango site is distinctly different from those sites. Having a mean CMAQ AOD below that of AERONET at the start of the day, CMAQ AOD gradually increases to be around double that of AERONET by 13:00 local time at Lubango. Since there is limited fire activity in very close proximity to Lubango (**Figure 5.3**) it can be inferred that westerly winds over the region immediately to the east of Lubango (**Figure 5.4**), are responsible for

blowing smoke from this area of very high fire emissions over the AERONET site in the CMAQ model. Comparable wind directions and speeds are observed in the 10 m wind fields of ERA-Interim (see **Figure 5.4**) suggesting it is likely that fire emissions in reality are also blown westwards over the Lubango site. Indeed, a slight increase in mean hourly AERONET AOD is seen at the site, but CMAQ AOD increases much more significantly. This suggests that the smoke coming from this very high fire emission region in CMAQ is undergoing processes as it ages in the model which generate particle size distributions corresponding to far higher AODs than should be observed. Given the high bias seen at the Lubango site in June and July (125% and 102% overestimation of model AOD respectively, **Table 5.3**) and the results demonstrating that overestimation by the model is much reduced when AOD is compared between individual smoke plumes, this provides evidence supporting the notion that the CMAQ aerosol module and its settings may be causing an additional inflation of modelled AOD values, far beyond any overestimation of emissions by the FREMv2 inventory.

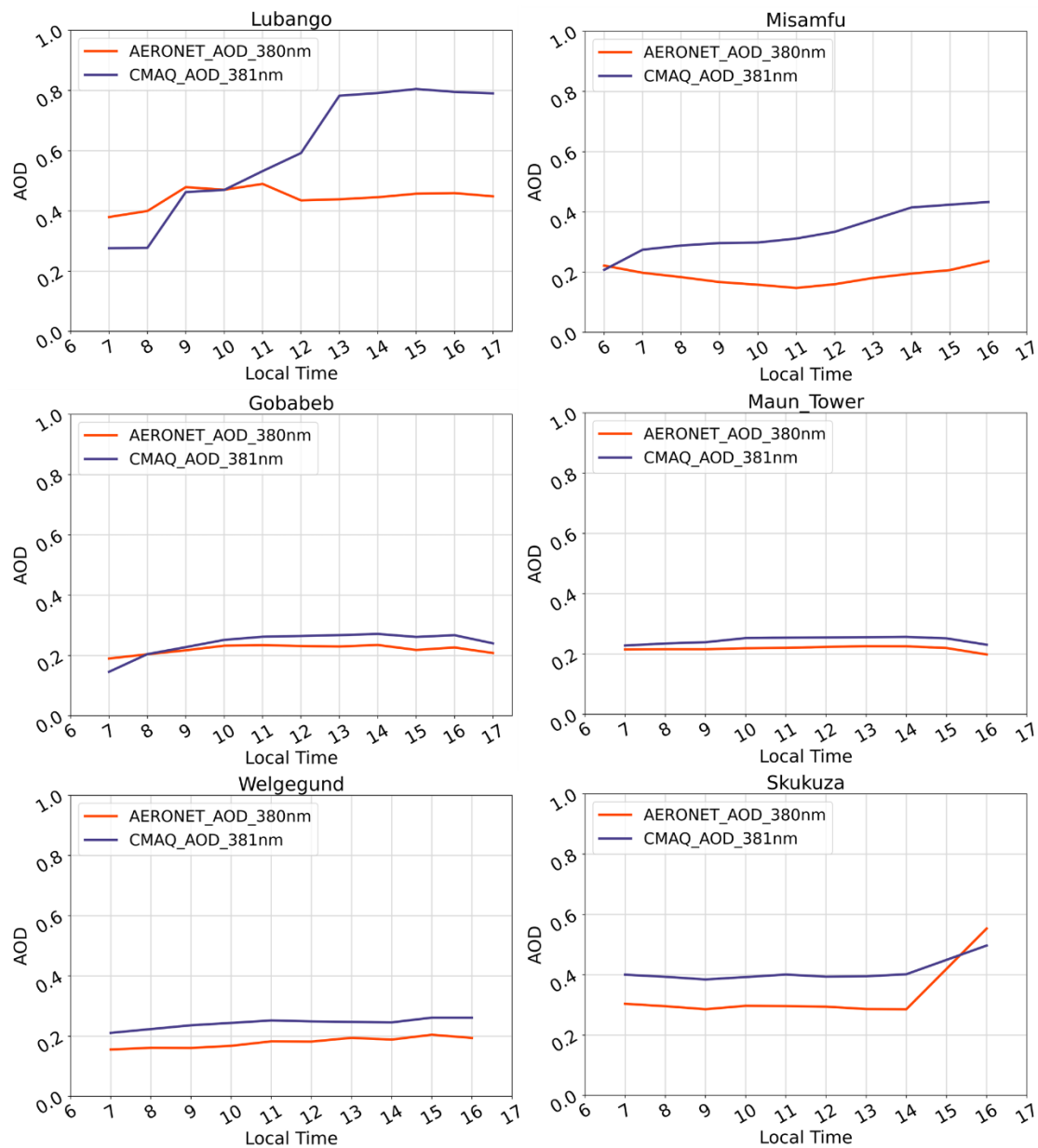


**Figure 5.24** Mean hourly AOD for each of the six AERONET sites as modelled by CMAQ and observed by AERONET.

## 5.4.2 FREMv2 Emissions Overestimation

Notwithstanding the inflation of modelled AOD by the CMAQ aerosol settings, there still remains a positive model bias of about 25% for AOD (using plume comparisons) and between a 13% to 19% for CO (from full domain and individual plume comparisons respectively). This can be attributed to a true overestimation of emissions in the FREMv2 inventory and is most likely primarily caused by two features of the inventory and satellite FRP observations used.

### 5.4.2.1 High-woodland Savanna and Closed Canopy Forest $C_{biome}$ values

The results from **Section 5.3.5** clearly show that, of the six biomes in the model domain, individual plumes in the high-woodland savanna and closed canopy forest biomes show the largest statistically significant overestimation of their in-plume CMAQ modelled CO compared to the equivalent S5P CO measures (25% and 42% respectively).

This indicates that the FREMv2 emission coefficient values,  $C_{biome}$  ( $\text{g MJ}^{-1}$ ), for high-woodland savanna and closed canopy forest are likely too high – causing an overestimation of the FREMv2-determined emissions in regions dominated by these biomes. The majority cover of high-woodland savanna, and partial cover of closed canopy forest in the north western portion of the CMAQ model domain (**Figure 5.20**) and the large overestimation in modelled values of both AOD and CO in this region (**Figure 5.5** and **Figure 5.16**) give further foundation to this suggestion. Particularly as modelled CO values in other regions, dominated by different biomes, are overestimated to lower extent (**Figure 5.22**), despite having significant fire activity (**Figure 5.3**).

In **Chapter 4** the relatively small number of matchup fires used to derive both the closed canopy forest and managed land  $C_{biome}$  values was highlighted as limitation in the FREMv2 approach ( $n=38$  and  $n=29$  respectively for these biomes). It can be seen in **Figure 4.7** that the OLS fit between the TPM and FRE of fire matchups in closed canopy forest is driven by one or two points with high TPM and FRE values, with the resulting  $C_{biome}$  value being determined as  $26.07 \pm 2.50 \text{ g MJ}^{-1}$ . When compared with FEER (Ichoku and Ellison, 2014) the ‘equivalent’  $C_{biome}$  value (see **Section 4.4.3** and **Table 4.2**) for closed canopy forest is significantly lower at  $16.34 \text{ g MJ}^{-1}$  – indicating that the true  $C_{biome}$  for closed canopy forest is

likely lower than it is determined to be in FREMv2. Although closed canopy forest is the majority biome cover in only a portion of the north western region of the CMAQ domain (**Figure 5.20**) there is a significant fractional coverage of the biome in the region (**Appendix C**). Therefore, since a weighted average of  $C_{biome}$  values is used to produce the  $C_e$  product of **Figure 4.8a** (used to generate final FREMv2 emissions inventory input into CMAQ), an overestimation of the closed canopy forest  $C_{biome}$  value would also contribute to the overestimation of fire emissions in regions that are even partially covered by this biome.

In the case of high-woodland savanna, the  $C_{biome}$  value for this biome may be overestimated in FREMv2 due to the simple 20% threshold applied to percentage tree cover (TC) information coming from the Landsat 30 m VCF product (**Figure 4.3a**) which was used to distinguish high and low woodland savanna in the FREMv2 approach (see **Section 4.4.1**).

This threshold value was selected as it produced similarly high  $r^2$  values (0.84) in OLS regressions of both the high and low woodland savanna biomes in fire-matchup datasets (**Figure 4.7**). However, this binary classification may cause SEVIRI FRP pixels that are close to this TC threshold to be associated with quite different  $C_{biome}$  values despite being very similar in terms of available fuel for combustion and measured FRP signal. For example, a high-woodland savanna pixel with 21% TC should have a very similar  $C_e$  value to a low-woodland savanna pixel with 19% TC, but (if a pixel has a majority cover of these respective biomes) the pixels'  $C_e$  values in FREMv2 may be quite different. **Figure 5.25** shows the distribution of percentage TC in all the SEVIRI FRP pixels covering Africa which have a majority cover of either high or low woodland savanna, and also shows the TC threshold used to distinguish these two classes. It can be seen from this plot that high-woodland savanna pixels with TC between 20% and 25% (the second most frequent % TC bin), are assigned a  $C_{biome}$  value of 14.18 g MJ<sup>-1</sup>, but may have a true  $C_{biome}$  value closer to that of a low-woodland savanna pixel (10.65 g MJ<sup>-1</sup>). This binary assignment of  $C_{biome}$  is partially addressed through the use of an average weighting of  $C_{biome}$  values being applied according to a SEVIRI pixel's fractional biome coverage to generate the final  $C_e$  product (see **Section 4.4.3** and Figure 4.8a). However, further work is needed to potentially optimise the use of TC information in the classification of  $C_{biome}$  values – perhaps through use of a non-discrete relationship between  $C_{biome}$  values in woodland savanna biomes and TC.

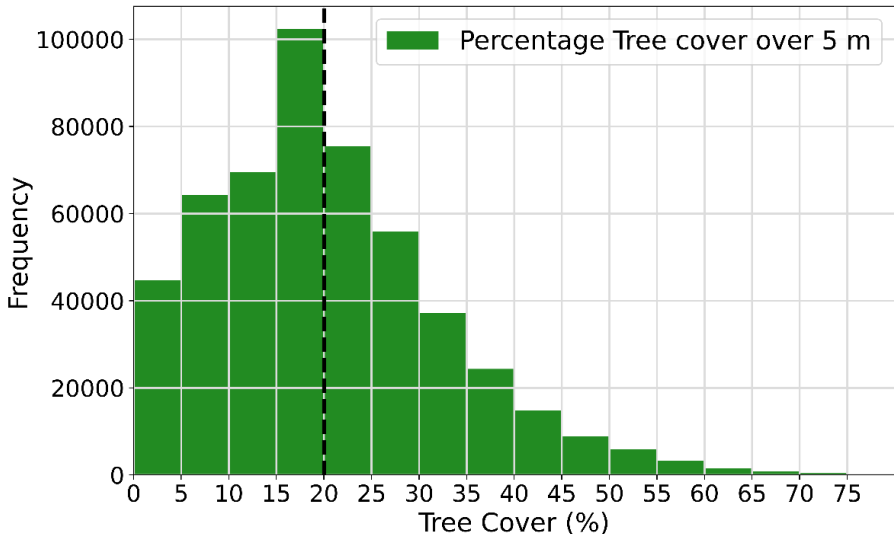


**Figure 5.25** Distribution of % tree cover according to the Landsat 30 m VCF tree cover product in SEVIRI FRP pixels in Africa that are classified as either high or low woodland savanna. The black dotted line denotes the TC threshold used to distinguish these biomes.

A final potential reason for fire emissions in the high-woodland savanna and closed canopy forest biomes being overestimated may be due to landcover changes occurring between 2015 and 2019 in areas dominated by these vegetation types. The CCI Landcover map and Landsat tree cover product used to discriminate vegetation types in FREMv2 used data from 2015 (see **Section 4.4.1**), and the same biome map is used to generate FREMv2 emissions used as input in CMAQ simulations. An overall loss of tree cover between 2015 and 2019 in many parts of northern Angola and the Democratic Republic of Congo is identified in the Global Forest Change dataset of Hansen et al. (2013) who use Landsat 30 m imagery to map global tree cover loss and gain (<http://earthenginepartners.appspot.com/science-2013-global-forest>). These regions of substantial tree cover loss overlap with the northwest region of the CMAQ model domain and will result in areas which are no longer dominated by high-woodland savanna or closed canopy forest being incorrectly assigned as such in the FREMv2 emission inventory. Hence, some SEVIRI FRP pixels in these regions may be applied to FREMv2  $C_e$  values that are no longer appropriate and are too high, thereby causing an overestimation of the fire emissions used as input in CMAQ in these areas.

#### 5.4.2.2 Intrinsic ‘Small fire’ Correction

Underestimation of FRP by the SEVIRI FRP-PIXEL product compared to higher spatial resolution polar-orbiting active fire products (taken at the same observation time) has been demonstrated in multiple studies (Freeborn et al., 2014; Roberts et al., 2015; Hall et al., 2019). This effect, which originates in the larger pixel footprint area of SEVIRI causing the minimum detectable FRP of a fire to be raised above that of the polar orbiting data, was demonstrated and investigated in relation to SEVIRI VZA in **Chapter 3**. To account for this under detection of low FRP fires, both the SEVIRI FRP-GRID product (which provides a summary of the FRP-PIXEL product at 5° resolution) and the first version of FREM (Mota and Wooster, 2018) apply a ‘small fire’ adjustment factor (an upward adjustment of 46%) to FRP and FRE values (Roberts et al., 2015; Wooster et al., 2015; Mota and Wooster, 2018). This factor was derived based on the finding that over sufficiently large time and space integration periods, SEVIRI measures a total FRP of around only 50% of what MODIS measures when it observes at the same time. In the developments to the FREMv2 methodology described in **Chapter 4**, it was argued that this bias from undetected low FRP fires in the SEVIRI product may be inherently accounted for in the derivation of the FREMv2  $C_{biome}$  values. This is because the same degree of FRP underestimation would be present in the fires used to derive the  $C_{biome}$  values as those which they are subsequently applied to. This is far more the case for FREMv2 than the original FREMv1 coefficients, because FREMv2 used the 1 km MAIAC aerosol product to derive the coefficients and thus could encompass a range of small to large fires in its coefficient derivation, compared to the larger fires that had to be the focus when the 10 km MODIS AOD product was used for FREMv1.

Crucially, this means that, compared to the FREMv1 method, FREMv2 includes many more FRE-TPM matchup fires that are likely to have associated missing FRP pixels below the FRP minimum detection threshold of SEVIRI. These matchups from small fires likely contain some underestimation of FRE from fires that a) contribute to the AOD (and TPM) observed in MAIAC but b) whose FRP signal is not detected and included in FRE totals. This inclusion of fire generated TPM but not some component of FRE is argued to result in an inherent ‘small fire’ correction being included in FREMv2  $C_{biome}$  values and in any emissions estimates generated from them.

In the context of the overestimation of FREMv2 emissions seen in **Section 5.3**, this may be a contributing factor - particularly in the north western region of the domain (**Figure 5.16** and **Figure 5.5**) and the relative better agreement in other parts of the domain. The argument being that this inherent small fire correction in FREMv2 is, on average, appropriate for regions where there are relatively more small fires who's FRP is less well characterised in the SEVIRI product, but that in areas where fires are larger this results in an overestimation of emissions. This suggestion is supported by the results seen in **Figure 5.10** which show that when all CO plumes are considered, the largest plumes have an increased bias towards modelled CO whereas smaller plumes show relationships closer to unity. A similar tendency of large AOD plumes to have a higher bias towards CMAQ is seen in **Figure 5.19**, however for the reasons previously discussed modelled AOD is likely to be subject to greater model error than CO and data in AOD plumes is much more scattered than CO plumes.

Overall, however despite this small overestimation, the agreement between modelled and measured CO is considered extremely strong, and clearly far better than that of the AOD for the reasons discussed above.

## 5.5 Conclusions and Further Work

This work presents an evaluation of the FREMv2 fire emissions inventory developed in **Chapter 4**, conducted by comparing WRF-CMAQ simulations - which use FREMv2 emissions as input - with observations of AOD from six ground-based AERONET sites, the 1 km resolution MAIAC AOD product and the Sentinel-5P TROPOMI column CO product. The simulation covers a 3000 km<sup>2</sup> region over southern Africa and runs over a period from the 15<sup>th</sup> June to 29<sup>th</sup> August 2019.

The meteorological fields produced by the WRF model are used to drive the CMAQ chemistry model and when compared to the ERA-Interim global weather model (**Figure 5.4**), overall, WRF replicates 2 metre temperature spatial patterns well. WRF wind speed (m s<sup>-1</sup>) and direction at 10 metres capture similar large scale trends as observed in ERF-Interim but

include mesoscale variations in wind speed which are not observed in the global model, likely caused by topographical features in the WRF model's higher spatial resolution.

CMAQ CO results show good agreement with Sentinel-5P CO observations – CMAQ overestimates CO by 13% and 19% with r values of 0.87 and 0.91 for full domain (**Figure 5.7** and **Table 5.2**) and individual CO plume comparisons (**Figure 5.10**) respectively. In evaluations against ground-based data, model AOD at 381 nm is compared against AERONET observations of AOD at 380 nm and when averaged over all six measurement sites CMAQ daily mean AOD overestimates AOD by 55% and has a r of 0.67. In general, the CMAQ results capture temporal patterns of AOD well (**Figure 5.12** and **Figure 5.13**), however the bias and correlation between model and observation vary significantly between sites and by month of the simulation, with the best agreement being observed in August (**Table 5.3**). When a site-specific bias correction is applied to the CMAQ AOD at each AERONET site, both the temporal patterns and magnitude of AOD measures agree well between these bias-adjusted model AODs and observations. The MODIS MAIAC AOD product is compared with CMAQ AOD at 550 nm and when considered over the full domain extent CMAQ shows a significant bias – the model overestimates AOD by 166%. The largest differences between modelled and observed AOD occur in the northwest region of the domain associated with the highest fire emissions (**Figure 5.3**) and the bias is strongest in June and July (**Figure 5.16**). Despite this bias, temporal patterns of AOD are well represented by CMAQ (**Figure 5.17**) and when considered at the scale of individual plumes, the bias in modelled AOD is much reduced showing only a 25% overestimation. These comparisons of simulation results with observations demonstrate that CO fields are likely more accurate than AOD in the model.

Data from individual plume comparisons between CMAQ output and MAIAC AOD and S5P CO were used in tandem with the biome classification map used of **Chapter 4** for emission coefficient derivation, to extend the evaluation in this study to assess the robustness of FREMv2 emission coefficients with respect to vegetation type. Results from AOD and CO comparisons gave differing indications as to the performance of emission coefficients in each biome (**Table 5.6** and **Table 5.5**). However, CO comparisons showed that high-woodland savanna which dominates the north of the model domain (**Figure 5.20** The six biomes defined in **Chapter 4** over the CMAQ model domain, with the addition of bare area.**Figure 5.20**) and

contains some of the highest fire activity (**Figure 5.3**), shows the greatest overestimation of modelled CO (24%).

The results demonstrate a clear difference in the agreement between modelled AOD and CO with respect to observations, and evidence as to the cause of this points to issues associated with CMAQ model error originating in the treatment of aerosols in terms of their microphysical processes within CMAQ (**Section 5.4.1**). However, the overestimation of CO and some component of AOD overestimation does come from the FREMv2 fire emissions themselves. This is most likely due to the overestimation of FREMv2  $C_{biome}$  values for high-woodland savanna and closed canopy forest (**Section 5.4.2.1**) and potentially an intrinsic ‘small fire’ correction introduced by the FREMv2 methodology (**Section 5.4.2.2**).

There are several other sources of uncertainty in this validation study which may also affect results which are related to both the FREMv2 emissions themselves, and the validation methodology. These uncertainties come from:

- i) the mass extinction efficiency used to convert fire emitted AOD to TPM in the FREMv2 derivation of TPM emission coefficients (see **Chapter 4**)
- ii) the emission factors of Andreae (2019) used to generate gas and particulate species emissions from the FREMv2 TPM emission coefficients.
- iii) the metrological fields generated by WRF, particularly the wind fields
- iv) the initial and boundary conditions for meteorology (NCEP FNL) and chemistry (WACCM) used.
- v) the AERONET AOD, MAIAC AOD and Sentinel-5P CO observations themselves.

The work presented here highlights multiple avenues for improvements which could be pursued in future research. Further evaluations using WRF-CMAQ should aim to resolve issues associated with model AOD overestimation. Alterations to CMAQ model configuration, and updates to how emission are incorporated into the model should be explored. For example, a more accurate representation of plume injection heights such as are employed by Baldassarre et al. (2015) should be applied and investigation into the initial aerosol particle modes assigned in the model to fire emissions should be tested for their

impact. Inclusion of a CMAQ control simulation and model runs using different emission inventories such as GFAS (Kaiser et al., 2012) and GFED (van der Werf et al., 2017) would also be helpful to accurately compare the appropriateness of the FREMv2 emissions inventory relative to other commonly used emission inventories.

In the scope of future work to improve fire emissions inventories in general, the results indicate the potential value of the development of a top-down methodology similar to FREM but based on the relation between S5P CO and SEVIRI FRP. The results from comparisons between CMAQ CO and S5P CO in full area, ROI, and individual plume comparisons (**Table 5.2** and **Figure 5.10**) show that over the full simulation period modelled and observed CO are well correlated (all but two have  $r > 0.75$ ) and have a relatively low bias ( $-0.03 < \text{NMBF} < 0.19$ ). This strong agreement, particularly the strong correlation values indicate that the transport and evolution of CO is well represented in the CMAQ model. FREMv2 emissions of CO, even if slightly overestimated, are robust to model error and quantify fire generated CO well. A top-down methodology that uses CO in emission coefficient derivation would also benefit from the removal of assumptions about aerosol radiative properties that are currently made in the AOD-based top-down methodologies in the form of the mass extinction coefficient (Ichoku and Ellison, 2014; Mota and Wooster, 2018) used to convert AOD to TPM.

# Chapter 6 Summary of Findings, Conclusions and Future Work

This Chapter presents the findings of this thesis in relation to the specific research objectives outlined in **Section 2.6**. Overall conclusions and impactions of the work are discussed and finally, suggestions for topics of future work are detailed.

## 6.1 Summary of Findings in Relation to Specific Research Objectives

**Objective 1: To investigate the impact of sensor view zenith angle (VZA) on the detection of AF and characterization of FRP in geostationary satellite active fire products – specifically the FRP-PIXEL product generate by the two SEVIRI sensors operating onboard Meteosat-11 (MSG) and Meteosat-8 (MSG-IODC) which image Africa from different locations using different view zenith angles.**

The work carried out to address this objective is presented in **Chapter 3**. An evaluation of the SEVIRI FRP-PIXEL product from both Meteosat-11 (M11) and Meteosat-8 (M8) was carried out through inter-comparisons of these two active fire (AF) products, and then also with the widely used MODIS MYD14/MOD14 AF products. The products were compared in terms of their AF detection performance and FRP characterization –mainly through per-area and per-fire evaluations. These comparisons showed that both SEVIRI products had similar AF error of omission rates (70%), which were within the range of previous validation studies carried out on the SEVIRI FRP-PIXEL product (Wooster et al., 2005; Roberts and Wooster, 2008; Freeborn et al., 2014; Roberts et al., 2015). However, M8 showed overall FRP totals over Africa

closer to those of the MODIS AF product. The spatio-temporal extent of the evaluation conducted is the largest and longest (1 year, whole of Africa) yet, extending the analyses of previous studies (Roberts et al., 2005, 2015; Roberts and Wooster, 2008; Freeborn et al., 2014), and capturing a greater amount of the variation in the performance of the SEVIRI product against MODIS than previously determined and using MSG-IODC for the first time.

Direct comparisons between M11 and M8 at their full temporal resolution (15 minute) confirmed the overall higher number of AF detections, and higher per-area and per-fire FRP measures of the M8 product as compared to the M11 product. However, this difference does not only point to improved performance of the M8 product, because it was shown to be related partly to a significant number of false AF detections in the M8 product which occurred at VZA  $> 40^\circ$ . Per-fire comparisons between the two SEVIRI products were used to focus only on fires believed to be true detections in both sensors, and  $FRP_{DIFF}$  and  $VZA_{DIFF}$  values were used to determine that for every degree of increased SEVIRI VZA difference between the two satellite views, on average there was a decrease of  $\sim 1.2$  MW in per-fire FRP induced. Discounting the areas of false active fire detections, the observed higher overall regional scale FRP values provided by M8 were shown to originate in the fact that many areas with the highest fire activity in Africa are located closer to the Meteosat-8 sub-satellite position (SSP; located over East Africa) than the Meteosat-11 SSP (located over offshore West Africa). This results in SEVIRI pixels of M8 having a smaller footprint area (and therefore a lower FRP detection limit) and atmospheric path in these locations as compared to M11, and thus M8 detects more fire pixels and a higher overall FRP total.

Per-area comparisons between M8 and M11 and the MODIS AF product, and direct comparisons between M11 and M8 were stratified by biome. Statistical tests showed that in all three AF products the majority of the six biomes defined had distinctly different per-area FRP signals. The sensitivity of FRP to SEVIRI VZA was shown to vary by biome, with vegetation types having increased tree canopy cover (e.g. high-woodland savanna) being more strongly impacted by VZA variations than those without (e.g. grassland). This is likely caused by tree canopy interception of the FRP signal of fires burning at the surface in the former biomes, something that has been demonstrated using simulations by (Roberts et al., 2018).

**Objective 2: To develop methodological improvements to the FREM top-down approach for landscape fire emissions estimation (Mota and Wooster, 2018) which address its key sources of uncertainty and limitations, and to apply these developments to produce an updated fire emission inventory for Africa**

Chapter 4 presents work addressing this objective, and resulted in the publication of peer reviewed research paper (Nguyen and Wooster, 2020). The work in Chapter 4 includes further updates not included in the published paper and which are therefore included in this thesis independently of the published work.

Improvements to the relatively recent “top-down” Fire Radiative Energy Emissions (FREMv1; Mota and Wooster, 2018) approach to biomass burning emissions calculations were developed and implemented to address the main sources of uncertainty in the FREMv1 methodology. Key was the use of the MODIS MAIAC (MCD19A2) 1 km AOD product in the derivation of smoke plume total particulate matter (TPM) and subsequently smoke emission coefficients,  $C_{biome}$  (in g MJ<sup>-1</sup>). This addressed issues with the previous use of the 10 km MODIS AOD product by Mota and Wooster (2018) in FREMv1, which has been shown to be unsuited to providing AOD measurements in thicker smoke and has a rather coarse spatial resolution meaning it cannot resolve smaller plumes (Lyapustin et al., 2012; Raffuse et al., 2013; He et al., 2017). The 10 km MODIS AOD product also includes rather conservative cloud masking that masks some areas of smoke as cloud (Levy et al., 2013; Livingston et al., 2014), and is impacted by the MODIS bow-tie effect (Sayer et al., 2015; Mhawish et al., 2019). It was demonstrated in this work that the latter of these issues caused use of the MODIS 10 km AOD product to provide inflated smoke plume TPM estimates in plumes which were observed at VZA > 20° (which is commonly exceeded since MODIS extends observations out to VZA ≈ 65°).

Around 1000 fire-smoke plume matchups between the FRP data held within the SEVIRI FRP-PIXEL product of Meteosat-11 and the 1 km MAIAC AOD product were used to generate smoke emission coefficients for six African biomes. These six biomes were differentiated using an updated landcover map and high-resolution 30 m Landsat-derived data of % tree cover (above 5 m), the latter introduced to further stratify the woodland savanna biome - which contributes the most in terms of annual FRE in Africa. Other improvements introduced

included an improved method for quantification of the background AOD value used in TPM estimation, and the use of meteorological reanalysis data to assess and then minimise the impact of relative humidity on the mass extinction efficiency,  $\beta_e$  ( $m^2 g^{-1}$ ) value used in the conversion of fire emitted AOD to TPM. Finally, the work included a spatio-temporal expansion of the data used in the derivation of smoke emission coefficients compared to FREMv1 – a full year of data from both NHAF and SHAFF was used. The  $C_{biome}$  values derived in FREMv2 were between 22% and 60% lower than those of FREMv1.

The new FREMv2 methodology was used to generate a pan-African landscape fire emissions inventory, focusing on TPM but also including the carbonaceous gases CO<sub>2</sub>, CO and CH<sub>4</sub> and covering the period from 2013 to 2018. This FREMv2 emission inventory was compared with those of GFASv1.2 (Kaiser et al., 2012), GFEDv4.1s (van der Werf et al., 2017), and two versions of FEERv1 (Ichoku and Ellison, 2014). FREMv2 annual mean TPM emissions were within 7% of the two versions of the FEERv1 inventory – one which applies the FEER  $C_e$  product to GFASv1.2 FRP measures while the other applies  $C_e$  values to the SEVIRI FRP-PIXEL product. FREMv2 TPM emission estimates were significantly higher than those of GFASv1.2 and GFEDv4.1s (by 80% and 43% respectively). The higher estimates of FREMv2 appear to be substantiated by independent assessments showing that the aerosol emissions of GFASv1.2 for example require upscaling by a factor of between 2.2 and 4.1 to deliver matching magnitudes between modelled and observed AODs (Kaiser et al., 2012) and that GFED(v3) also underestimates total carbon emissions (Randerson et al., 2012).

FREMv2 carbonaceous gas emissions totals were used to estimate total carbon emissions and then dry matter consumed (DMC) across Africa. Estimates of fuel consumption per-unit area,  $F_c$  (in  $kg.m^{-2}$ ), were obtained through division of DMC by the FireCCISFD11 20 m burned area product (derived from Sentinel-2 data). In some areas FREMv2  $F_c$  values were higher than those of GFEDv4.1s by up to 2.0  $kg\ m^{-2}$  but over the majority of Africa, FREMv2  $F_c$  values were between zero and 0.5  $kg\ m^{-2}$  higher than those of GFED. When separated by biome, median  $F_c$  values for shrubland and low-woodland savanna were within 11% of the mean  $F_c$  values from field-measurements of African savanna (Van Leeuwen et al., 2014).

**Objective 3: Conduct an evaluation of the fire emission inventory developed in Chapter 4 via its use within a chemical transport model (CTM) and comparison of the output simulated atmospheric fields with independent ground-based and satellite-based data**

The work conducted in **Chapter 5** addresses this objective. The FREMv2 fire emission inventory developed in **Chapter 4** was used as input in a CTM (CMAQ) which was coupled to a NWP model (WRF), and the concentration fields for various different gas and aerosol species were simulated over southern Africa for the period June to August 2019.

WRF meteorological fields agreed relatively well with ERA-Interim reanalysis data in terms of its temperature (at 2 metres) and wind fields (at 10 metres). Model generated total column CO comparisons to the Sentinel-5P TROPOMI (S5P) total column CO product showed very good agreement ( $r = 0.83$ ) between modelled and observed CO concentrations. Model CO was higher than S5P CO, but over the full domain was within 13% of the observed total S5P CO measures. The bias shown by the CMAQ CO values was highest over areas of high fire activity, and when total column CO was compared between individual modelled and observed smoke plumes, modelled CO values were overall 19% higher than measured S5P CO values for the same plumes. When time series of modelled and observed CO are compared, the temporal patterns of observations are extremely well matched between the two, indicating that WRF meteorological fields perform relatively well across the simulation domain.

Modelled AOD fields were generated by CMAQ at 381 nm and 550 nm and these were compared to AERONET ground-based observations of AOD at 380 nm and the 1 km MODIS MAIAC AOD product at 550 nm. Again, the temporal patters of AOD in AERONET data and MAIAC AOD data were well replicated by the CMAQ AOD fields – these were hourly and daily in the case of AERONET data, and daily in the case of MAIAC data. However, modelled AOD comparisons to AERONET and MAIAC AOD showed greater overestimation than when modelled CO was compared with S5P CO. Modelled AOD over the simulation period was between 13% and 82% higher than at the six AERONET sites (with  $r$  mostly between 0.54 and 0.84) and over the full domain CMAQ AOD was 166% higher than MAIAC AOD ( $r = 0.52$ ). When AOD fields were compared between the model and MAIAC AOD for individual plumes however, overestimation by the model was greatly reduced to only 25% ( $r = 0.47$ ).

Separation of individual validation smoke plumes by biome showed that the greatest overestimation of model CO occurred in the high-woodland savanna biome (25%) and the closed canopy forest biome (42%). Investigations concluded that model error is a significant source of the extreme overestimation of CMAQ AOD when compared with AERONET and MAIAC AOD data. However, a component of the overestimation originates in the FREMv2 emissions themselves – between 13% and 19% based on CO comparisons. This most likely comes from the overestimation of the FREMv2  $C_{biome}$  values for high-woodland savanna and closed canopy forest which are applied to SEVIRI FRP to generate the model-ingested fire emissions. The former due to the binary tree cover threshold used to distinguish between the high and low woodland savanna biomes, and latter due to the relatively few fire matchups from large plumes used to derive its  $C_{biome}$  value. Potential other sources for overestimation could originate in land cover changes between 2015 and 2019 and an intrinsic ‘small fire’ boost that is a consequence of the FREMv2 methodology.

## 6.2 Overall Conclusions and Implications

This PhD project aimed to better understand the application of geostationary satellite active fire datasets in the quantification of landscape fire in Africa, and to develop and evaluate improvements to methods of estimating fire emissions from these data using so-called ‘top-down’ approaches.

Geostationary satellite active fire data have been once again confirmed to provide unique records of fire due to their high temporal resolution coverage. However, for the first time this has been done using co-incident data from two Meteosat satellites operating concurrently from different positions, evidencing that observations are dependent on the and that this dependence is also effected by biome. It may be possible to use this information or extinctions of it to determine basic adjustment factors (or a function) that could be applied to generate an ‘idealised’ close-to-nadir product that is closer to what would be observed if a region’s fire activity had been observed at the a sensors nadir SSP.

In the scope of fire emissions, it is clear that the updated FREMv2 fire emissions estimation approach provides estimates that appear reasonable in terms of their magnitude, particularly

in the case of CO - which is estimated not directly but from the TPM emissions estimates and the TPM and CO EFs of each biome. The TPM emissions may be somewhat too high, particularly in the high-woodland savanna and closed canopy forest biomes, but in comparison to GFED and GFAS, seem possibly to be close to the truth. This is especially the case since the larger differences seen with regards to the comparisons between the simulated and observed AOD data come primarily from model error. It is therefore expected that the FREMv2 methodology will be used in future to provide real-time emissions estimates based on geostationary FRP data streams, potentially adjusted for the effect of satellite VZA variations as described above

## 6.3 Recommendations for Future Work

A number of areas are highlighted by the research conducted in this PhD thesis that could be extended in future work:

### **Future work related to AF detection and FRP measurements of geostationary satellite products**

- Although the occurrence of false AF detections in the Meteosat-8 SEVIRI FRP-PIXEL (M8) product was identified (**Section 3.3.4**) and potential causes discussed, the M8 product remains effectively unusable at VZA beyond  $\sim 40^\circ$  due to this issue. Hence, a more in-depth AF detection analysis at varying VZAs is needed to determine an exact threshold above which these false fire detections dominantly occur. Further evaluation should focus on approaches to effectively ‘mask out’ these false AF detections, for example using time of year (**Figure 3.19**) and/or information from the SEVIRI Quality Product, which can be applied to the dataset until this issue is resolved in the operational M8 product.

### **Further work to improve top-down emissions estimation methodologies**

- As was highlighted in **Section 4.6**, one of the main sources of uncertainty in the top-down methodologies discussed, and developed, in this thesis (FREMv1, FREMv2, FEER and Lu et al. (2019)) is the smoke mass extinction efficiency,  $\beta_e$  ( $m^2 g^{-1}$ ), used to convert fire-emitted AOD to TPM in the derivation of smoke emission coefficients,  $C_{biome}$ . **Chapter 5** demonstrated the good agreement between FREMv2 modelled CO emissions and Sentinel-5P total column CO observations, indicating the potential of satellite observed CO being used in top-down emissions estimation methodologies. Future work should therefore aim to apply an approach similar to the FREMv2 methodology to derive biome-specific CO emission coefficients,  $C_{biome}^{CO}$ , directly from matchups between smoke plumes observed in the Sentinel-5P total column CO product and geostationary-based FRP observations. This approach would remove the requirement for  $\beta_e$ , thereby eliminating this source of uncertainty and would also benefit from the use of data from a far newer sensor and may therefore be better suited for the end of the MODIS era (MODIS is more than 20 years old and may have a limited operational lifetime remaining). The lower spatial resolution of the S5P CO data ( $7 \text{ km}^2$  at nadir) may limit the minimum size of smoke plume (and fire) included in  $C_{biome}^{CO}$  derivation, however, the FREMv2  $C_{biome}^{TPM}$  values of **Chapter 4** could be easily compared to determine the effect of this on final emission coefficients through the application of emission factor ratios
- **Chapter 3** demonstrated the impact of VZA on geostationary AF detection and showed that any ‘small fire’ correction applied to these datasets should ideally vary with VZA. Additionally, **Section 5.4.2.1** highlighted the need for an increased number of fire-smoke matchups to better determine the FREMv2  $C_{biome}$  for closed canopy forest - whose value is currently derived from relatively few fire matchups. Therefore, future updates to the FREMv2  $C_{biome}$  values (or indeed and newly developed  $C_{biome}^{CO}$  values) would benefit from an increased number of fire-smoke matchups to (i) enable stratification of  $C_{biome}$  values by VZA and (ii) to improve the statistical significance of  $C_{biome}$  values currently determined from relatively few fire-smoke matchups (managed land and closed canopy forest). This exercise would require many more fire-smoke matchups than were used in FREMv2 to provide a sufficient number of data

points from each biome and from each range of VZAs. Consequently, improved automation of the fire-smoke matchup identification process would be advantageous, perhaps through machine learning approaches for feature detection and through use of the MAIAC AOD product's in-built 'smoke test' (Lyapustin et al., 2011). The dataset used for matchups should also be extended over several years.

### **Future work related to the improvement of emission inventory evaluation**

The evaluation conducted using WRF-CMAQ in this thesis could be expanded and improved in several aspects including:

- A twin simulation with a model domain in NHAF and a simulation period from November to January to determine whether the performance of FREMv2 shown this evolution is consistent with its performance in NHAF. With NHAF being more dominated by fires occurring in the managed land biome (**Figure 4.11**) than SHAf, it would be valuable to determine how appropriate the FREMv2  $C_{biome}$  value for this biome is, considering it was derived from relatively far fewer fire-plume matchups than the other  $C_{biome}$  values.
- Further investigation into the CMAQ model configuration used in the evaluation study of **Chapter 5** is needed, especially in relation to the treatment of aerosols. Aerosol diagnostic files are generated alongside AOD measures and these should be reviewed along with the model files determining the initial assignment of fire emissions into the three aerosol modes discussed in **Section 5.4.1** – the aim being to diagnose and improve model results for AOD through alterations in the CMAQ model configuration and setup.
- Model error will always be introduced in an evaluation study which utilises a CTM and the magnitude and effect of the model error will vary for different CTM systems (Kukkonen et al., 2012). Therefore, the comparison of results from modelling-based evaluations of other emissions inventories should be treated with some care (e.g. Kaiser et al., 2012; Ichoku et al., 2016; Reddington et al., 2016), especially as the

validation datasets, study regions and simulation periods are also different. To confirm the performance of the FREMv2 emissions inventory relative to other state-of-the-art emission inventories, extensions to the evaluation conducted in **Chapter 5** should introduce a control simulation, where no fire emissions are used as input, and simulations that use fire emission inventories such as FEER, GFED, GFAS and/or FINN as input. This would allow comparisons between the different emissions inventories to be made also accounting for model error.

# References

- Abel, S.J., Haywood, J.M., Highwood, E.J., Li, J., Buseck, P.R., 2003. Evolution of biomass burning aerosol properties from an agricultural fire in southern Africa. *Geophys. Res. Lett.* 30(15), pp.10–13.
- Abel, S.J., Highwood, E.J., Haywood, J.M., Stringer, M.A., 2005. The direct radiative effect of biomass burning aerosols over southern Africa. *Atmos. Chem. Phys. Discuss.* 5(2), pp.1165–1211.
- Akagi, S.K., Yokelson, R.J., Wiedinmyer, C., Alvarado, M.J., Reid, J.S., Karl, T., Crounse, J.D., Wennberg, P.O., 2011. Emission factors for open and domestic biomass burning for use in atmospheric models. *Atmos. Chem. Phys.* 11(9), pp.4039–4072.
- Aldersley, A., Murray, S.J., Cornell, S.E., 2011. Global and regional analysis of climate and human drivers of wildfire. *Sci. Total Environ.* 409(18), pp.3472–3481.
- Aminou, D.M., Jacquet, B., Pasternak, F., 1997. Characteristics of the Meteosat 976 second generation (MSG) radiometer/imager: SEVIRI. *Sensors, Syst. Next977 Gener. Satell.* (3221), pp.19–31.
- Amnuaylojaroen, T., Barth, M.C., Emmons, L.K., Carmichael, G.R., Kreasuwun, J., Prasitwattanaseree, S., Chantara, S., 2014. Effect of different emission inventories on modeled ozone and carbon monoxide in Southeast Asia. *Atmos. Chem. Phys.* 14(23), pp.12983–13012.
- Amraoui, M., DaCamara, C.C., Pereira, J.M.C., 2010. Detection and monitoring of African vegetation fires using MSG-SEVIRI imagery. *Remote Sens. Environ.* 114(5), pp.1038–1052.
- Andela, N., Kaiser, J.W., Heil, A., Leeuwen, T.T. Van, Wooster, M., van der Werf, G.R., Remy, S., Schultz, M.G., 2013. Assimilation System ( GFASv1 ) 2013(June).
- Andela, N., Kaiser, J.W., van der Werf, G.R., Wooster, M., 2015. New fire diurnal cycle characterizations to improve fire radiative energy assessments made from MODIS observations. *Atmos. Chem. Phys.* 15, pp.8831–8846.
- Andreae, M.O., 2019. Emission of trace gases and aerosols from biomass burning - An updated assessment. *Atmos. Chem. Phys.* 19(13), pp.8523–8546.
- Andreae, M.O., Merlet, P., 2001. Emissions of trace gases and aerosols from biomass burning. *Global Biogeochem. Cycles* 15(4), pp.955–966.
- Appel, W., Hogrefe, C., Foley, K., Pouliot, G., Gilliam, R., Murphy, B., Pye, H.O., Bash, J., Pleim, J.E., Sarwar, G., Roselle, S., Mathur, R., 2018. Preliminary Evaluation of the CMAQ v5.3 Beta Release, in: 17th Annual CMAS Conference.
- Archibald, S., Lehmann, C.E.R., Belcher, C.M., Bond, W.J., Bradstock, R.A., Daniau, A.L., Dexter, K.G., Forrestel, E.J., Greve, M., He, T., Higgins, S.I., Hoffmann, W.A., Lamont, B.B., McGlinn, D.J., Moncrieff, G.R., Osborne, C.P., Pausas, J.G., Price, O., Ripley, B.S., Rogers, B.M., Schwilk, D.W., Simon, M.F., Turetsky, M.R., van der Werf, G.R., Zanne,

- A.E., 2018. Biological and geophysical feedbacks with fire in the Earth system. *Environ. Res. Lett.* 13(3).
- Arvani, B., Pierce, R.B., Lyapustin, A., Wang, Y., Ghermandi, G., Teggi, S., 2016. Seasonal monitoring and estimation of regional aerosol distribution over Po valley, northern Italy, using a high-resolution MAIAC product. *Atmos. Environ.* 141, pp.106–121.
- Baldassarre, G., Pozzoli, L., Schmidt, C.C., Unal, A., Kindap, T., Menzel, W.P., Whitburn, S., Coheur, P.F., Kavgaci, A., Kaiser, J.W., 2015. Using SEVIRI fire observations to drive smoke plumes in the CMAQ air quality model: the case of Antalya in 2008. *Atmos. Chem. Phys.* 15, pp.8539–8558.
- Balsamo, G., Albergel, C., Beljaars, A., Boussetta, S., Brun, E., Cloke, H., Dee, D., Dutra, E., 2015. ERA-Interim / Land : a global land surface reanalysis data set pp.389–407.
- Berk, A., Cooley, T.W., Anderson, G.P., Acharya, P.K., Bernstein, L.S., Muratov, L., Lee, J., Fox, M.J., Adler-Golden, S.M., Chetwynd, J.H., Hoke, M.L., Lockwood, R.B., Gardner, J.A., Lewis, P.E., 2004. MODTRAN5: a reformulated atmospheric band model with auxiliary species and practical multiple scattering options. *Remote Sens. Clouds Atmos.* IX 5571(February 2015), pp.78.
- Binkowski, F.S., 1999. Aerosols in MODELS-3 CMAQ. *Sci. Algorithms EPA Model. Community Multiscale Air Qual. Model. Syst.* pp.10–23.
- Borsdorff, T., Aan de Brugh, J., Hu, H., Aben, I., Hasekamp, O., Landgraf, J., 2018a. Measuring Carbon Monoxide With TROPOMI: First Results and a Comparison With ECMWF-IFS Analysis Data. *Geophys. Res. Lett.* 45(6), pp.2826–2832.
- Borsdorff, T., Aan de Brugh, J., Hu, H., Hasekamp, O., Sussmann, R., Rettinger, M., Hase, F., Gross, J., Schneider, M., Garcia, O., Stremme, W., Grutter, M., Feist, Di.G., Arnold, S.G., De Mazière, M., Kumar Sha, M., Pollard, D.F., Kiel, M., Roehl, C., Wennberg, P.O., Toon, G.C., Landgraf, J., 2018b. Mapping carbon monoxide pollution from space down to city scales with daily global coverage. *Atmos. Meas. Tech.* 11(10), pp.5507–5518.
- Boschetti, L., Eva, H.D., Brivio, P.A., Grégoire, J.M., 2004. Lessons to be learned from the comparison of three satellite-derived biomass burning products. *Geophys. Res. Lett.* 31(21), pp.2–5.
- Boschetti, L., Roy, D.P., 2009. Strategies for the fusion of satellite fire radiative power with burned area data for fire radiative energy derivation. *J. Geophys. Res. Atmos.* 114(20), pp.1–10.
- Boschetti, L., Roy, D.P., Giglio, L., Huang, H., Zubkova, M., Humber, M.L., 2019. Global validation of the collection 6 MODIS burned area product. *Remote Sens. Environ.* 235(February), pp.111490.
- Bowman, D.M.J.S., Balch, J.K., Artaxo, P., Bond, W.J., Carlson, J.M., Cochrane, M.A., D'Antonio, C.M., DeFries, R.S., Doyle, J.C., Harrison, S.P., Johnston, F.H., Keeley, J.E., Krawchuk, M.A., Kull, C.A., Marston, J.B., Moritz, M.A., Prentice, I.C., Roos, C.I., Scott, A.C., Swetnam, T.W., van der Werf, G.R., Pyne, S.J., 2009. Fire in the earth system. *Science* (80-. ). 324(5926), pp.481–484.

- Calle, A., Casanova, J.L., 2008. Forest fires and remote sensing. *NATO Secur. through Sci. Ser. C Environ. Secur.* (January 2008), pp.261–304.
- Calle, A., González-Alonso, F., de Miguel, S.M., 2008. Validation of active forest fires detected by MSG-SEVIRI by means of MODIS hot spots and AWIFS images. *Int. J. Remote Sens.* 29(12), pp.3407–3415.
- Cao, C., Xiaoxiong, X., Wolfe, R.E., DeLuccia, F., Liu, Q., Blonski, S., Lin, G. (Gary), Nishihama, M., Pogorzala, D., Oudrari, H., Hillger, D., 2017. NOAA Technical Report NESDIS 142 Visible Infrared Imaging Radiometer Suite (VIIRS) Sensor Data Record (SDR) User's Guide Version 1.3. *Noaa* (March).
- Chang, D., Song, Y., 2009. Comparison of L3JRC and MODIS global burned area products from 2000 to 2007. *J. Geophys. Res. Atmos.* 114(16), pp.1–20.
- Chen, D., Wang, Y., McElroy, M.B., He, K., Yantosca, R.M., Le Sager, P., 2009. Regional CO pollution and export in China simulated by the high-resolution nested-grid GEOS-Chem model. *Atmos. Chem. Phys.* 9(11), pp.3825–3839.
- Cheng, Z., Wang, S., Fu, X., Watson, J.G., Jiang, J., Fu, Q., Chen, C., Xu, B., Yu, J., Chow, J.C., Hao, J., 2014. Impact of biomass burning on haze pollution in the Yangtze River delta, China: A case study in summer 2011. *Atmos. Chem. Phys.* 14(9), pp.4573–4585.
- Chevallier, F., Fortems, A., Bousquet, P., Pison, I., Szopa, S., Devaux, M., Hauglustaine, D.A., 2009. African CO emissions between years 2000 and 2006 as estimated from MOPITT observations. *Biogeosciences* 6(1), pp.103–111.
- Chin, M., Ginoux, P., Kinne, S., Torres, O., Holben, B., Duncan, B.N., Martin, R. V., Logan, J.A., Higurashi, A., Nakajima, T., 2002. Tropospheric Aerosol Optical Thickness from the GOCART Model and Comparisons with Satellite and Sun Photometer Measurements. *J. Atmos. Sci.* 59(3), pp.461–483.
- Choi, M.W., Lee, J.H., Woo, J.W., Kim, C.H., Lee, S.H., 2019. Comparison of PM2.5 chemical components over East Asia simulated by the WRF-Chem and WRF/CMAQ models: On the models' prediction inconsistency. *Atmosphere (Basel)*. 10(10).
- Chu, D.A., Kaufman, Y., Ichoku, C., Remer, L.A., Tanre, D., Holben, B., 2002. Validation of MODIS aerosol optical depth retrieval over land 29(12), pp.4–7.
- Chuvieco, E., Yue, C., Heil, A., Mouillot, F., Alonso-Canas, I., Padilla, M., Pereira, J.M.C., Oom, D., Tansey, K., 2016. A new global burned area product for climate assessment of fire impacts. *Glob. Ecol. Biogeogr.* 25(5), pp.619–629.
- Collins, W.D., Bitz, C.M., Blackmon, M.L., Bonan, G.B., Bretherton, C.S., Carton, J.A., Chang, P., Doney, S.C., Hack, J.J., Henderson, T.B., Kiehl, J.T., Large, W.G., McKenna, D.S., Santer, B.D., Smith, R.D., 2006. The Community Climate System Model Version 3 (CCSM3). *J. Clim.* 19(11), pp.2122–2143.
- Crutzen, P.J., Andreae, M.O., 1990. Biomass Burning in the Tropics: Impact on Atmospheric Chemistry and Biogeochemical Cycles. *Science (80- .)*. 250(4988), pp.1669–1678.
- Csiszar, I., Morisette, J.T., Giglio, L., 2006. Validation of active fire detection from moderate-

- resolution satellite sensors: The MODIS example in Northern Eurasia. *IEEE Trans. Geosci. Remote Sens.* 44(7), pp.1757–1764.
- Cusworth, D.H., Mickley, L.J., Sulprizio, M.P., Liu, T., Marlier, M.E., DeFries, R.S., Guttikunda, S.K., Gupta, P., 2018. Quantifying the influence of agricultural fires in northwest India on urban air pollution in Delhi, India. *Environ. Res. Lett.* 13(4).
- Darmenov, A.S., da Silva, A., 2015. The Quick Fire Emissions Dataset (QFED) - Documentation of versions 2.1, 2.2 and 2.4. *NASA Tech. Rep. Ser. Glob. Model. Data Assim.* 38(September).
- Dee, D., Uppala, S., Simmons, A., Berrisford, P., Poli, P., Kobayashi, S., Andrae, U., Alonso-Balmaseda, M., Balsamo, G., Bauer, P., Bechtold, P., Beljaars, A., van de Berg, L., Bidlot, J.-R., Bormann, N., Delsol, C., Dragani, R., Fuentes, M., Geer, A.J., Haimberger, L., Healy, S., Hersbach, H., Hólm, E. V., Isaksen, L., Krallberg, P.W., Köhler, M., Matricardi, M., McNally, A., Monge-Sanz, B.M., Morcrette, J.J., Peubey, C., de Rosnay, P., Tavolato, C., Thépaut, J.-N., Vitart, F., 2011. The ERA-Interim reanalysis: Configuration and performance of the data assimilation system (9), pp.71.
- Deeter, M.N., Edwards, D.P., Francis, G.L., Gille, J.C., Martínez-Alonso, S., Worden, H.M., Sweeney, C., 2017. A climate-scale satellite record for carbon monoxide: The MOPITT Version 7 product. *Atmos. Meas. Tech.* 10(7), pp.2533–2555.
- Derwent, D., Fraser, A., Abbott, J., Jenkin, M., Willis, P., Murrells, T., 2010. Evaluating the Performance of Air Quality Models, DEFRA Pollution Research.
- Dozier, J., 1981. Satellite Identification of surface Radiant Temperature Fields of Subpixel Resolution, in: NOAA Technical Memorandum NESS 113.
- Edwards, D.P., Halvorson, C.M., Gille, J.C., 1999. Radiative transfer modeling for the EOS Terra satellite Measurement of Pollution in the Troposphere (MOPITT) instrument. *J. Geophys. Res. Atmos.* 104(D14), pp.16755–16775.
- Edwards, D.P., Pétron, G., Novelli, P.C., Emmons, L.K., Gille, J.C., Drummond, J.R., 2006. Southern Hemisphere carbon monoxide interannual variability observed by Terra/Measurement of Pollution in the Troposphere (MOPITT). *J. Geophys. Res. Atmos.* 111(16), pp.1–9.
- Ellicott, E., Vermote, E., Giglio, L., Roberts, G., 2009. Estimating biomass consumed from fire using MODIS FRE. *Geophys. Res. Lett.* 36(13).
- Emery, C., Jung, J., Koo, B., Yarwood, G., 2015. Improvements to CAMx Snow Cover Treatments and Carbon Bond Chemical Mechanism for Winter Ozone.
- Emili, E., Lyapustin, A., Wang, Y., Popp, C., Korkin, S., Zebisch, M., Wunderle, S., Petitta, M., 2011. High spatial resolution aerosol retrieval with MAIAC: Application to mountain regions. *J. Geophys. Res. Atmos.* 116(23), pp.1–12.
- EPA, 2019. CMAQv5.3.
- ESA, 2017. European Space Agency Landcover CCI Product User Guide Version 2.0.
- Fisher, D., Wooster, M., Xu, W., 2020. Top-Down Estimation of Particulate Matter Emissions

- from Extreme Tropical Peatland Fires Using (December).
- Flannigan, M.D., Vonder Haar, T.H., 1986. Forest fire monitoring using NOAA satellite AVHRR. *Can. J. For. Researrch* 16(5), pp.975–982.
- Formenti, P., Elbert, W., Maenhaut, W., Haywood, J.M., Osborne, S., Andreae, M.O., 2003. Inorganic and carbonaceous aerosols during the Southern African Regional Science Initiative (SAFARI 2000) experiment: Chemical characteristics, physical properties, and emission data or smoke from African biomass burning. *J. Geophys. Res. D Atmos.* 108(13), pp.1–16.
- Freeborn, P.H., Wooster, M., Roberts, G., 2011. Addressing the spatiotemporal sampling design of MODIS to provide estimates of the fire radiative energy emitted from Africa. *Remote Sens. Environ.* 115(2), pp.475–489.
- Freeborn, P.H., Wooster, M., Roberts, G., Malamud, B.D., Xu, W., 2009. Development of a virtual active fire product for Africa through a synthesis of geostationary and polar orbiting satellite data. *Remote Sens. Environ.* 113(8), pp.1700–1711.
- Freeborn, P.H., Wooster, M., Roberts, G., Xu, W., 2014. Evaluating the SEVIRI fire thermal anomaly detection algorithm across the Central African Republic using the MODIS active fire product. *Remote Sens.* 6(3), pp.1890–1917.
- Giglio, L., 2007. Characterization of the tropical diurnal fire cycle using VIRS and MODIS observations. *Remote Sens. Environ.* 108(4), pp.407–421.
- Giglio, L., Boschetti, L., Roy, D.P., Humber, M.L., Justice, C.O., 2018. The Collection 6 MODIS burned area mapping algorithm and product. *Remote Sens. Environ.* 217(August), pp.72–85.
- Giglio, L., Kendall, J.D., 2001. Application of the Dozier retrieval to wildfire characterization a sensitivity analysis. *Remote Sens. Environ.* 77(1), pp.34–49.
- Giglio, L., Loboda, T. V., Roy, D.P., Quayle, B., Justice, C.O., 2009. An active-fire based burned area mapping algorithm for the MODIS sensor. *Remote Sens. Environ.* 113(2), pp.408–420.
- Giglio, L., Randerson, J.T., van der Werf, G.R., 2013. Analysis of daily, monthly, and annual burned area using the fourth-generation global fire emissions database (GFED4). *J. Geophys. Res. Biogeosciences* 118(1), pp.317–328.
- Giglio, L., Schroeder, W., Justice, C.O., 2016. The collection 6 MODIS active fire detection algorithm and fire products. *Remote Sens. Environ.* 178, pp.31–41.
- Giglio, L., van der Werf, G.R., Randerson, J.T., Collatz, G.J., Kasibhatla, P.S., 2006. Global estimation of burned area using MODIS active fire observations. *Atmos. Chem. Phys.* 6(4), pp.957–974.
- Giles, D.M., Sinyuk, A., Sorokin, M.G., Schafer, J.S., Smirnov, A., Slutsker, I., Eck, T.F., Holben, B., Lewis, J.R., Campbell, J.R., Welton, E.J., Korkin, S., Lyapustin, A., 2019. Advancements in the Aerosol Robotic Network (AERONET) Version 3 database - Automated near-real-time quality control algorithm with improved cloud screening for Sun photometer aerosol optical depth (AOD) measurements. *Atmos. Meas. Tech.* 12(1), pp.169–209.

- Gipson, G.L., Young, J.O., 1999. Chapter 8: Gas-Phase Chemistry, Science Algorithms of the EPA Models-3 Community Multiscale Air Quality (CMAQ) Modeling System.
- Guerrette, J.J., Henze, D.K., 2016. Four dimensional variational inversion of black carbon emissions during ARACTAS-CARB with WRFDA-Chem. *Atmos. Chem. Phys. Discuss.* 5(October), pp.1–51.
- Hall, J.V., Zhang, R., Schroeder, W., Huang, C., Giglio, L., 2019. Validation of GOES-16 ABI and MSG SEVIRI active fire products. *Int. J. Appl. Earth Obs. Geoinf.* 83(August), pp.101928.
- Hansen, M.C., DeFries, R.S., Townshend, J.R.G., Sohlberg, R., Dimiceli, C., Carroll, M., 2002. Towards an operational MODIS continuous field of percent tree cover algorithm: Examples using AVHRR and MODIS data. *Remote Sens. Environ.* 83(1–2), pp.303–319.
- Hansen, M.C., Potapov, P. V., Moore, R.H., Hancher, M., Turubanova, S.A., Tyukavina, A., Thau, D., Stehman, S. V., Goetz, S.J., Loveland, T.R., Kammareddy, A., Egorov, A., Chini, L., Justice, C.O., Townshend, J.R.G., 2013. High-Resolution Global Maps of 21st-Century Forest Cover Change 850(November), pp.850–854.
- Hawbaker, T.J., Vanderhoof, M.K., Beal, Y.J., Takacs, J.D., Schmidt, G.L., Falgout, J.T., Williams, B., Fairaux, N.M., Caldwell, M.K., Picotte, J.J., Howard, S.M., Stitt, S., Dwyer, J.L., 2017. Mapping burned areas using dense time-series of Landsat data. *Remote Sens. Environ.* 198(September), pp.504–522.
- He, Q., Zhang, M., Huang, B., Tong, X., 2017. MODIS 3 km and 10 km aerosol optical depth for China: Evaluation and comparison. *Atmos. Environ.* 153, pp.150–162.
- Heil, A., Kaiser, J.W., van der Werf, G.R., Wooster, M., Schultz, M.G., van der Gon, H.D., 2010. Assessment of the Real-Time Fire Emissions (GFASv0) by MACC. *ECMWF Tech. Memo.* 628(July), pp.1–47.
- Henze, D.K., Turner, M., Kinney, P.L., Jack, D., Li, Y., Mickley, L.J., Jacob, D.J., Shinozuka, Y., Giss, N., Pinder, R., Gilliland, A.B., Rao, S.T., Solomon, D., Dombrowski, S., n.d. Inverse Modeling and Attainment Analysis for Improved Decision Support of PM 2 . 5 Air Quality Regulations.
- Heymann, J., Reuter, M., Buchwitz, M., Schneising, O., Bovensmann, H., Burrows, J.P., Massart, S., Kaiser, J.W., Crisp, D., 2017. CO<sub>2</sub> emission of Indonesian fires in 2015 estimated from satellite-derived atmospheric CO<sub>2</sub> concentrations. *Geophys. Res. Lett.* 44(3), pp.1537–1544.
- Hoelzemann, J.J., Schultz, M.G., Brasseur, G.P., Granier, C., Simon, M., 2004. Global Wildland Fire Emission Model (GWEM): Evaluating the use of global area burnt satellite data. *J. Geophys. Res. D Atmos.* 109(14).
- Holben, B., Tanre, D., Smirnov, A., Eck, T.F., Slutsker, I., Abuhassan, N., Newcomb, W.W., Schafer, J.S., Chatenet, B., Lavenu, F., Kaufman, Y., Castle, J.V., Setzer, A., Markham, B., Clark, D., Frouin, R., Halthore, R., Karneli, A., O'Neill, N.T., 2001. An Emerging Ground-based Aerosol Climatology: Aerosol Optical Depth from AERONET. *J. Geophys. Res.* 106(Dll), pp.12067–12097.

- Holloway, T., Li, H.L., Kasibhatla, P.S., 2000. Global distribution of Carbon monoxide 105.
- Hsu, N.C., Jeong, M., Bettenhausen, C., Sayer, A.M., Hansell, R., Seftor, C.S., Huang, J., Tsay, S.C., 2013. Enhanced Deep Blue aerosol retrieval algorithm: The second generation. *J. Geophys. Res. Atmos.* 118(16), pp.9296–9315.
- Hsu, N.C., Tsay, S.C., King, M.D., Herman, J.R., 2006. Deep Blue retrievals of Asian aerosol properties during ACE-Asia. *IEEE Trans. Geosci. Remote Sens.* 44(11), pp.3180–3195.
- Hsu, N.C., Tsay, S.C., King, M.D., Kaufman, Y., Herman, J.R., Goddard, N., Flight, S., 2004. Aerosol Properties over “ Bright-Reflecting. *IEEE Trans. Geosci. Remote Sens.* 42(3), pp.23.
- Hu, J., Chen, J., Ying, Q., Zhang, H., 2016. One-year simulation of ozone and particulate matter in China using WRF/CMAQ modeling system. *Atmos. Chem. Phys.* 16(16), pp.10333–10350.
- Hu, X., Waller, L.A., Lyapustin, A., Wang, Y., Al-Hamdan, M.Z., Crosson, W.L., Estes, M.G., Estes, S.M., Quattrochi, D.A., Puttaswamy, S.J., Liu, Y., 2014. Estimating ground-level PM2.5 concentrations in the Southeastern United States using MAIAC AOD retrievals and a two-stage model. *Remote Sens. Environ.* 140, pp.220–232.
- Hu, Y., Odman, M.T., Chang, M.E., Jackson, W., Lee, S., Edgerton, E.S., Baumann, K., Russell, A.G., 2008. Simulation of air quality impacts from prescribed fires on an urban area. *Environ. Sci. Technol.* 42(10), pp.3676–3682.
- Huang, K., Fu, J.S., Hsu, N.C., Gao, Y., Dong, X., Tsay, S.C., Lam, Y.F., 2013. Impact assessment of biomass burning on air quality in Southeast and East Asia during BASE-ASIA. *Atmos. Environ.* 78, pp.291–302.
- Huijnen, V., Flemming, J., Kaiser, J.W., Inness, A., Leitão, J., Heil, A., Eskes, H.J., Schultz, M.G., Benedetti, A., Hadji-Lazaro, J., Dufour, G., Eremenko, M., 2012. Hindcast experiments of tropospheric composition during the summer 2010 fires over western Russia. *Atmos. Chem. Phys.* 12(9), pp.4341–4364.
- Huijnen, V., Wooster, M., Kaiser, J.W., Gaveau, D.L.A., Flemming, J., Parrington, M., Inness, A., Murdiyarsa, D., Main, B., Van Weele, M., 2016. Fire carbon emissions over maritime southeast Asia in 2015 largest since 1997. *Sci. Rep.* 6(May), pp.1–8.
- Hurtmans, D., Coheur, P.F., Wespes, C., Clarisse, L., Scharf, O., Clerbaux, C., Hadji-Lazaro, J., George, M., Turquety, S., 2012. FORLI radiative transfer and retrieval code for IASI. *J. Quant. Spectrosc. Radiat. Transf.* 113(11), pp.1391–1408.
- Ichoku, C., Chu, D.A., Mattoo, S., Kaufman, Y., Remer, L.A., Tanre, D., Slutsker, I., Holben, B., 2002. A spatio-temporal approach for global validation and analysis of MODIS aerosol products 29(12), pp.1–4.
- Ichoku, C., Ellison, L., 2014. Global top-down smoke-aerosol emissions estimation using satellite fire radiative power measurements. *Atmos. Chem. Phys.* 14(13), pp.6643–6667.
- Ichoku, C., Ellison, L., Yue, Y., Wang, J., Kaiser, J.W., 2016. Fire and Smoke Remote Sensing and Modeling Uncertainties: Case Studies in Northern Sub-Saharan Africa. *Nat. Hazard Uncertain. Assess. Model. Decis. Support* pp.215–230.

- Ichoku, C., Kaufman, Y., 2005. A method to derive smoke emission rates from MODIS fire radiative energy measurements. *IEEE Trans. Geosci. Remote Sens.* 43(11), pp.2636–2649.
- Ichoku, C., Remer, L.A., Kaufman, Y., Levy, R., Chu, D.A., Tanre, D., Holben, B., 2003. MODIS observation of aerosols and estimation of aerosol radiative forcing over southern Africa during SAFARI 2000. *J. Geophys. Res. Atmos.* 108(D13), pp.n/a-n/a.
- In, H.J., Kim, Y.P., Lee, K.H., 2009. Enhancement of aerosol concentration in Korea due to: The Northeast Asian Forest Fire in May 2003. *Asian J. Atmos. Environ.* 3(1), pp.1–8.
- Inness, A., Ades, M., Agustí-Panareda, A., Barr, J., Benedictow, A., Blechschmidt, A.M., Jose Dominguez, J., Engelen, R.J., Eskes, H.J., Flemming, J., Huijnen, V., Jones, L., Kipling, Z., Massart, S., Parrington, M., Peuch, V.H., Razinger, M., Remy, S., Schulz, M., Suttie, M., 2019. The CAMS reanalysis of atmospheric composition. *Atmos. Chem. Phys.* 19(6), pp.3515–3556.
- Inness, A., Benedetti, A., Flemming, J., Huijnen, V., Kaiser, J.W., Parrington, M., Remy, S., 2015. The ENSO signal in atmospheric composition fields: Emission-driven versus dynamically induced changes. *Atmos. Chem. Phys.* 15(15), pp.9083–9097.
- IPCC, 2013. Climate Change 2013: The Physical Science Basis, Contribution of Working Group 1 to the Fifth Assessment Report of the Intergovernmental Panel on Climate Change.
- Ito, A., Penner, J.E., 2004. Global estimates of biomass burning emissions based on satellite imagery for the year 2000. *J. Geophys. Res. D Atmos.* 109(14), pp.1–18.
- Jackson, J.M., Liu, H., Laszlo, I., Kondragunta, S., Remer, L.A., Huang, J., Huang, H.C., 2013. Suomi-NPP VIIRS aerosol algorithms and data products. *J. Geophys. Res. Atmos.* 118(22), pp.12673–12689.
- Jethva, H., Torres, O., Yoshida, Y., 2019. Accuracy assessment of MODIS land aerosol optical thickness algorithms using AERONET measurements over North America. *Atmos. Meas. Tech.*
- Joro, S., Samain, O., Yildirim, A., van de Berg, L., Lutz, H.J., 2008. Towards an Improved Active Fire Monitoring Product for MSG Satellites.
- Jost, C., 2003. Trace gas chemistry in a young biomass burning plume over Namibia: Observations and model simulations. *J. Geophys. Res.* 108(D13), pp.8482.
- Kaiser, J.W., Heil, A., Andreae, M.O., Benedetti, A., Chubarova, N., Jones, L., Morcrette, J.J., Razinger, M., Schultz, M.G., Suttie, M., van der Werf, G.R., 2012. Biomass burning emissions estimated with a global fire assimilation system based on observed fire radiative power. *Biogeosciences* 9(1), pp.527–554.
- Kasischke, E.S., Penner, J.E., 2004. Improving global estimates of atmospheric emissions from biomass burning. *J. Geophys. Res. D Atmos.* 109(14), pp.1–9.
- Kaufman, Y., Fung, I.Y., Tucker, C.J., 1989. Remote Sensing of Biomass Burning in the Tropics. *Adv. Sp. Res.* 9(7), pp.265–268.
- Kaufman, Y., Kleidman, R., King, M.D., 1998. SCAR-B fires in the tropics: Properties and

- remote sensing from EOS-MODIS. *J. Geophys. Res.* 103(D24), pp.31955.
- Kaufman, Y., Remer, L.A., Ottmar, R., Ward, D.E., Rong-R, L., Kleidman, R., 1996. Relationship between remotely sensed fire intensity and rate of emission of smoke: SCAR-C experiment, in: Levin, J.S. (Ed.), *Biomass Burning and Global Change*. The MIT Press, Cambridge, pp. 685–696.
- Keywood, M., Kanakidou, M., Stohl, A., Dentener, F., Grassi, G., Meyer, C.P., Torseth, K., Edwards, D.P., Thompson, A.M., Lohmann, U., Burrows, J.P., 2013. Fire in the air: Biomass burning impacts in a changing climate. *Crit. Rev. Environ. Sci. Technol.* 43(1), pp.40–83.
- Kiely, L., Spracklen, D. V., Wiedinmyer, C., Conibear, L., Reddington, C.L., Archer-Nicholls, S., Lowe, D.C., Arnold, S.R., Knote, C., Khan, M.F., Latif, M.T., Kuwata, M., Budisulistiorini, S.H., Syaufina, L., 2019. Revised estimate of particulate emissions from Indonesian peat fires in 2015. *Atmos. Chem. Phys. Discuss.* pp.1–29.
- Klonecki, A., Levy, H., 1997. Tropospheric chemical ozone tendencies in CO-CH<sub>4</sub>-NO<sub>y</sub>-H<sub>2</sub>O system: Their sensitivity to variations in environmental parameters and their application to a global chemistry transport model study. *J. Geophys. Res. Atmos.* 102(17), pp.21221–21237.
- Kobayashi, T., Tsend-Ayush, J., Tateishi, R., 2016. A new global tree-cover percentage map using MODIS data. *Int. J. Remote Sens.* 37(4), pp.969–992.
- Kochanski, A.K., Jenkins, M.A., Yedinak, K., Mandel, J., Beezley, J.D., Lamb, B., 2016. Toward an integrated system for fire, smoke and air quality simulations. *Int. J. Wildl. Fire* 25(5), pp.534–546.
- Konovalov, I.B., Beekmann, M., Berezin, E. V., Formenti, P., Andreae, M.O., 2017. Probing into the aging dynamics of biomass burning aerosol by using satellite measurements of aerosol optical depth and carbon monoxide. *Atmos. Chem. Phys.* 17(7), pp.4513–4537.
- Konovalov, I.B., Golovushkin, N.A., Kuznetsova, I.N., Arkhangelskaya, A.A., 2019. Changes of the absorption properties of aerosol from Siberian wildfires due to atmospheric aging: analysis of satellite observations, in: Romanovskii, O.A., Matvienko, G.G. (Eds.), *25th International Symposium on Atmospheric and Ocean Optics: Atmospheric Physics*. SPIE, pp. 660–669.
- Kopacz, M., Jacob, D.J., Fisher, J.A., Logan, J.A., Zhang, L., Megretskaya, I.A., Yantosca, R.M., Singh, K., Henze, D.K., Burrows, J.P., Buchwitz, M., Khlystova, I., McMillan, W.W., Gille, J.C., Edwards, D.P., Eldering, A., Thouret, V., Nedelec, P., 2010. Global estimates of CO sources with high resolution by adjoint inversion of multiple satellite datasets (MOPITT, AIRS, SCIAMACHY, TES). *Atmos. Chem. Phys.* 10(3), pp.855–876.
- Koplitz, S.N., Mickley, L.J., Marlier, M.E., Buonocore, J.J., Kim, P.S., Liu, T., Sulprizio, M.P., DeFries, R.S., Jacob, D.J., Schwartz, J., Pongsiri, M., Myers, S.S., 2016. Public health impacts of the severe haze in Equatorial Asia in September-October 2015: Demonstration of a new framework for informing fire management strategies to reduce downwind smoke exposure. *Environ. Res. Lett.* 11(9).

- Koplitz, S.N., Nolte, C.G., Pouliot, G., Vukovich, J.M., Beidler, J., 2018. Influence of uncertainties in burned area estimates on modeled wildland fire PM2.5 and ozone pollution in the contiguous U.S. *Atmos. Environ.* 191, pp.328–339.
- Koppmann, R., von Czapiewski, K., Reid, J.S., 2005. A review of biomass burning emissions, part 1: gaseous emissions of carbon monoxide, methane, volatile organic compounds, and nitrogen containing compounds. *Atmos. Chem. Phys. Discuss.* (5), pp.10455–10516.
- Korontzi, S., Roy, D.P., Justice, C.O., Ward, D.E., 2004. Modeling and sensitivity analysis of fire emissions in southern Africa during SAFARI 2000. *Remote Sens. Environ.* 92(2), pp.255–275.
- Kuik, F., Lauer, A., Beukes, J.P., Van Zyl, P.G., Josipovic, M., Vakkari, V., Laakso, L., Feig, G.T., 2015. The anthropogenic contribution to atmospheric black carbon concentrations in southern Africa: A WRF-Chem modeling study. *Atmos. Chem. Phys.* 15(15), pp.8809–8830.
- Kukkonen, J., Olsson, T., Schultz, D.M., Baklanov, A., Klein, T., Miranda, A.I., Monteiro, A., Hirtl, M., Tarvainen, V., Boy, M., Peuch, V.H., Poupkou, A., Kioutsoukis, I., Finardi, S., Sofiev, M., Sokhi, R., Lehtinen, K.E.J., Karatzas, K., San José, R., Astitha, M., Kallos, G., Schaap, M., Reimer, E., Jakobs, H., Eben, K., 2012. A review of operational, regional-scale, chemical weather forecasting models in Europe. *Atmos. Chem. Phys.* 12(1), pp.1–87.
- Kumar, S.S., Roy, D.P., Boschetti, L., Kremens, R., 2011. Exploiting the power law distribution properties of satellite fire radiative power retrievals: A method to estimate fire radiative energy and biomass burned from sparse satellite observations. *J. Geophys. Res. Atmos.* 116(19), pp.1–18.
- Lamarque, J.F., Edwards, D.P., Emmons, L.K., Gille, J.C., Wilhelm, O., Gerbig, C., Prevedel, D., Deeter, M.N., Warner, J., Ziskin, D.C., Khattatov, B., Francis, G.L., Yudin, V., Ho, S., Mao, D., Chen, J., Drummond, J.R., 2003. Identification of CO plumes from MOPITT data: Application to the August 2000 Idaho-Montana forest fires. *Geophys. Res. Lett.* 30(13), pp.2–5.
- Landgraf, J., Aan de Brugh, J., Scheepmaker, R.A., Borsdorff, T., Hu, H., Houweling, S., Butz, A., Aben, I., Hasekamp, O., 2016. Carbon monoxide total column retrievals from TROPOMI shortwave infrared measurements. *Atmos. Meas. Tech.* 9(10), pp.4955–4975.
- Larsen, A.E., Reich, B.J., Ruminski, M., Rappold, A.G., 2018. Impacts of fire smoke plumes on regional air quality, 2006–2013 article. *J. Expo. Sci. Environ. Epidemiol.* 28(4), pp.319–327.
- Lavorel, S., Flannigan, M.D., Lambin, E.F., Scholes, M.C., 2007. Vulnerability of land systems to fire: Interactions among humans, climate, the atmosphere, and ecosystems. *Mitig. Adapt. Strateg. Glob. Chang.* 12(1), pp.33–53.
- Lavrov, A., Utkin, A.B., Vilar, R., Fernandes, A., 2006. Evaluation of smoke dispersion from forest fire plumes using lidar experiments and modelling. *Int. J. Therm. Sci.* 45(9), pp.848–859.
- Levy, H., 1971. Normal Atmosphere: Large Radical and Formaldehyde Concentrations Predicted. *Science* (80-). 173(3992), pp.141–143.

- Levy, R., Mattoo, S., Munchak, L.A., Remer, L.A., Sayer, A.M., Patadia, F., Hsu, N.C., 2013. The Collection 6 MODIS aerosol products over land and ocean. *Atmos. Meas. Tech.* 6(11), pp.2989–3034.
- Levy, R., Munchak, L.A., Mattoo, S., Patadia, F., Remer, L.A., Holz, R.E., 2015. Towards a long-term global aerosol optical depth record: Applying a consistent aerosol retrieval algorithm to MODIS and VIIRS-observed reflectance. *Atmos. Meas. Tech.* 8(10), pp.4083–4110.
- Li, F., Zhang, X., Kondragunta, S., 2020. Biomass burning in Africa: An investigation of fire radiative power missed by MODIS using the 375 m VIIRS active fire product. *Remote Sens.* 12(10).
- Li, Z., Guo, J., Ding, A., Liao, H., Liu, J., Sun, Y., Wang, T., Xue, H., Zhang, H., Zhu, B., 2017. Aerosol and boundary-layer interactions and impact on air quality. *Natl. Sci. Rev.* 4(6), pp.810–833.
- Li, Z., Zhao, X., Kahn, R., Mishchenko, M., Remer, L.A., Lee, K.H., Wang, M., Laszlo, I., Nakajima, T., Maring, H., 2009. Uncertainties in satellite remote sensing of aerosols and impact on monitoring its long-term trend: A review and perspective. *Ann. Geophys.* 27(7), pp.2755–2770.
- Lindeberg, T., 1998. Feature Detection with Automatic Scale Selection. *Int. J. Comput. Vis.* 16(2), pp.79–116.
- Liu, H., Remer, L.A., Huang, J., Huang, H.C., Kondragunta, S., Laszlo, I., Oo, M., Jackson, J.M., 2014. Preliminary evaluation of S-NPP VIIRS aerosol optical thickness. *J. Geophys. Res.* 119(7), pp.3942–3962.
- Liu, J., Drummond, J.R., Li, Q., Gilles, J.C., Ziskin, D.C., 2005. Satellite mapping of CO emission from forest fires in Northwest America using MOPITT measurements. *Remote Sens. Environ.* 95(4), pp.502–516.
- Livingston, J.M., Redemann, J., Shinozuka, Y., Johnson, R., Russell, P.B., Zhang, Q., Mattoo, S., Remer, L.A., Levy, R., Munchak, L.A., Ramachandran, S., 2014. Comparison of MODIS 3 km and 10 km resolution aerosol optical depth retrievals over land with airborne sunphotometer measurements during ARCTAS summer 2008. *Atmos. Chem. Phys.* 14(4), pp.2015–2038.
- Loboda, T. V., Giglio, L., Boschetti, L., Justice, C.O., 2012. Regional fire monitoring and characterization using global NASA MODIS fire products in dry lands of Central Asia. *Front. Earth Sci.* 6(2), pp.196–205.
- LSA SAF, 2015. LSA SAF Validation Report - Fire Radiative Power.
- Lu, X., Zhang, X., Li, F., Cochrane, M.A., 2019. Investigating Smoke Aerosol Emission Coefficients using MODIS Active Fire and Aerosol Products — A Case Study in the CONUS and Indonesia. *J. Geophys. Res. Biogeosciences* pp.1–17.
- Lyapustin, A., Korkin, S., Wang, Y., Quayle, B., Laszlo, I., 2012. Discrimination of biomass burning smoke and clouds in MAIAC algorithm. *Atmos. Chem. Phys.* 12(20), pp.9679–

- Lyapustin, A., Wang, Y., 2018. MODIS Multi-Angle Implementation of Atmospheric Correction (MAIAC) Data User's Guide Collection 6.
- Lyapustin, A., Wang, Y., Korkin, S., Huang, D., 2018. MODIS Collection 6 MAIAC algorithm. *Atmos. Meas. Tech.* 11(10), pp.5741–5765.
- Lyapustin, A., Wang, Y., Laszlo, I., Kahn, R., Korkin, S., Remer, L.A., Levy, R., Reid, J.S., 2011. Multiangle implementation of atmospheric correction (MAIAC): 2. Aerosol algorithm. *J. Geophys. Res. Atmos.* 116(3), pp.1–15.
- Martin, M.V., Kahn, R., Tosca, M.G., 2018. A global analysis of wildfire smoke injection heights derived from space-based multi-angle imaging. *Remote Sens.* 10(10).
- Martins, V.S., Barbosa, C.C.F., De Carvalho, L.A.S., Jorge, D.S.F., Lobo, F. de L., de Moraes Novo, E.M.L., 2017. Assessment of atmospheric correction methods for sentinel-2 MSI images applied to Amazon floodplain lakes. *Remote Sens.* 9(4).
- Masuoka, E., Fleig, A., Wolfe, R.E., Patt, F., 1998. Key characteristics of MODIS data products. *IEEE Trans. Geosci. Remote Sens.* 36(4), pp.1313–1323.
- Mehmood, K., Chang, S., Yu, S., Wang, L., Li, P., Li, Z., Liu, W., Rosenfeld, D., Seinfeld, J.H., 2018. Spatial and temporal distributions of air pollutant emissions from open crop straw and biomass burnings in China from 2002 to 2016. *Environ. Chem. Lett.* 16(1), pp.301–309.
- Mhawish, A., Banerjee, T., Sorek-Hamer, M., Lyapustin, A., Broday, D.M., Chatfield, R., 2019. Comparison and evaluation of MODIS Multi-angle Implementation of Atmospheric Correction (MAIAC) aerosol product over South Asia. *Remote Sens. Environ.* 224(February 2018), pp.12–28.
- Morissette, J.T., Giglio, L., Csiszar, I., Justice, C.O., 2005. Validation of the MODIS active fire product over Southern Africa with ASTER data. *Int. J. Remote Sens.* 26(19), pp.4239–4264.
- Morton, D.C., Collatz, G.J., Wang, D., Randerson, J.T., Giglio, L., Chen, Y., 2013. Satellite-based assessment of climate controls on US burned area. *Biogeosciences* 10(1), pp.247–260.
- Mota, B., Wooster, M., 2018. A new top-down approach for directly estimating biomass burning emissions and fuel consumption rates and totals from geostationary satellite fire radiative power (FRP). *Remote Sens. Environ.* 206(February 2017), pp.45–62.
- NCAR, 2020. fortran program to grid the FINN (v1.5 and v2) text files to netcdf files for use in WRF-Chem or global models [WWW Document].
- Nelson, R.M., 2001. Chapter 4 - Water Relations of Forest Fuels, in: Johnson, E.A., Miyanishi, K. (Eds.), *Forest Fires*. Academic Press, San Diego, pp. 79–149.
- Nguyen, H.M., Wooster, M., 2020. Advances in the estimation of high Spatio-temporal resolution pan-African top-down biomass burning emissions made using geostationary fire radiative power (FRP) and MAIAC aerosol optical depth (AOD) data. *Remote Sens. Environ.* 248(November 2019), pp.111971.
- Noyes, K.J., Kahn, R., Sedlacek, A., Kleinman, L., Limbacher, J.A., Li, Z., 2020. Wildfire smoke

particle properties and evolution, from space-based multi-angle imaging. *Remote Sens.* 12(5).

Paugam, R., Wooster, M., Freitas, S., Val Martin, M., 2016. A review of approaches to estimate wildfire plume injection height within large-scale atmospheric chemical transport models. *Atmos. Chem. Phys.* 16(2), pp.907–925.

Pechony, O., Shindell, D.T., Faluvegi, G., 2013. Direct top-down estimates of biomass burning CO emissions using TES and MOPITT versus bottom-up GFED inventory. *J. Geophys. Res. Atmos.* 118(14), pp.8054–8066.

Penner, J.E., Dickinson, R.E., O'Neill, C.A., 1992. Effects of aerosol from biomass burning on the global radiation budget. *Science* (80-. ). 256(5062), pp.1432–1434.

Pereira, J.M.C., Pereira, B.S., Barbosa, P.M., Stroppiana, D., Vasconcelos, M.J.P., Grégoire, J.M., 1999. Satellite monitoring of fire in the EXPRESSO study area during the 1996 dry season experiment: Active fires, burnt area, and atmospheric emissions. *J. Geophys. Res.* 104(D23), pp.30701–30712.

Pfister, G., Hess, P.G., Emmons, L.K., Lamarque, J.F., Wiedinmyer, C., Edwards, D.P., Pétron, G., Gille, J.C., Sachse, G.W., 2005. Quantifying CO emissions from the 2004 Alaskan wildfires using MOPITT CO data. *Geophys. Res. Lett.* 32(11), pp.1–5.

Phuleria, H.C., 2005. Air quality impacts of the October 2003 Southern California wildfires. *J. Geophys. Res.* 110(D7), pp.D07S20.

Plummer, S., Arino, O., Simon, M., Steffen, W., 2006. Establishing a earth observation product service for the terrestrial carbon community: The globcarbon initiative. *Mitig. Adapt. Strateg. Glob. Chang.* 11(1), pp.97–111.

Potter, C.S., Randerson, J.T., Field, C.B., Matson, P.A., Vitousek, P.M., Mooney, H.A., Klooster, S.A., 1993. Terrestrial ecosystem production: A process model based on global satellite and surface data. *Global Biogeochem. Cycles* 7(4), pp.811–841.

Prata, A.J., Carn, S.A., Stohl, A., Kerkmann, J., 2007. Long range transport and fate of a stratospheric volcanic cloud from Soufrière Hills volcano, Montserrat. *Atmos. Chem. Phys.* 7(19), pp.5093–5103.

Prins, E., Feltz, J.M., Menzel, W.P., Ward, D.E., 1998. An overview of GOES-8 diurnal fire and smoke results for SCAR-B and 1995 fire season in South America. *OURNAL Geophys. Res.* 103(98), pp.821–835.

Pye, H.O., 2016. CMAQv5.1 SOA Update [WWW Document].

Quennehen, B., Schwarzenboeck, A., Matsuki, A., Burkhardt, J.F., Stohl, A., Ancellet, G., Law, K.S., 2012. Anthropogenic and forest fire pollution aerosol transported to the Arctic: Observations from the POLARCAT-France spring campaign. *Atmos. Chem. Phys.* 12(14), pp.6437–6454.

Raffuse, S.M., McCarthy, M.C., Craig, K.J., Dewinter, J.L., Jumbam, L.K., Fruin, S., James Gauderman, W., Lurmann, F.W., 2013. High-resolution MODIS aerosol retrieval during wildfire events in California for use in exposure assessment. *J. Geophys. Res. Atmos.*

118(19), pp.11242–11255.

Randerson, J.T., Chen, Y., van der Werf, G.R., Rogers, B.M., Morton, D.C., 2012. Global burned area and biomass burning emissions from small fires. *J. Geophys. Res. G Biogeosciences* 117(4).

Randerson, J.T., Liu, H., Flanner, M.G., Chambers, S.D., Jin, Y., Hess, P.G., Pfister, G., Mack, M.C., Treseder, K.K., Welp, L.R., Chapin, F.S., Harden, J.W., Goulden, M.L., Lyons, E., Neff, J.C., Schuur, E.A.G., Zender, C.S., 2006. The impact of boreal forest fire on climate warming. *Science* (80-). 314(5802), pp.1130–1132.

Reddington, C.L., Morgan, W.T., Derbyshire, E., Brito, J., Coe, H., Artaxo, P., Scott, C.E., Marsham, J., Spracklen, D. V., 2019. Biomass burning aerosol over the Amazon: analysis of aircraft, surface and satellite observations using a global aerosol model. *Atmos. Chem. Phys.* 19(14), pp.9125–9152.

Reddington, C.L., Spracklen, D. V., Artaxo, P., Ridley, D.A., Rizzo, L. V., Arana, A., 2016. Analysis of particulate emissions from tropical biomass burning using a global aerosol model and long-term surface observations. *Atmos. Chem. Phys.* 16(17), pp.11083–11106.

Reid, J.S., Eck, T.F., Christopher, S.A., Koppmann, R., Dubovik, O., Eleuterio, D.P., Holben, B., Reid, E.A., Zhang, J., 2005a. A review of biomass burning emissions part III: Intensive optical properties of biomass burning particles. *Atmos. Chem. Phys.* 5(3), pp.827–849.

Reid, J.S., Hobbs, P. V., Ferek, R.J., Blake, D.R., Martins, J.V., Dunlap, M.R., Liousse, C., 1998. Physical, chemical, and optical properties of regional hazes dominated by smoke in Brazil. *J. Geophys. Res. Atmos.* 103(D24), pp.32059–32080.

Reid, J.S., Hyer, E.J., Prins, E., Westphal, D.L., Zhang, J., Wang, J., Christopher, S.A., Curtis, C.A., Schmidt, C.C., Eleuterio, D.P., Richardson, K.A., Hoffman, J., 2009a. Global monitoring and forecasting of biomass-burning smoke: Description of and lessons from the Fire Locating and Modeling of Burning Emissions (FLAMBE) program. *IEEE J. Sel. Top. Appl. Earth Obs. Remote Sens.* 2(3), pp.144–162.

Reid, J.S., Koppmann, R., Eck, T.F., Eleuterio, D.P., 2005b. A review of biomass burning emissions part II: intensive physical properties of biomass burning particles. *Atmos. Chem. Phys.* 4(5), pp.799–825.

Reid, J.S., Westphal, D.L., Curtis, C.A., Richardson, K.A., Hyer, E.J., Prins, E., Schmidt, C.C., Hoffman, J., Zhang, J., Wang, J., Christopher, S.A., Eleuterio, D.P., 2009b. Global Monitoring and Forecasting of Biomass-Burning Smoke: Description of and Lessons from the Fire Locating and Modeling of Burning Emissions (FLAMBE) Program. *IEEE J. Sel. Top. Appl. Earth Obs. Remote Sens.* 2(3), pp.144–162.

Remer, L.A., Kaufman, Y., Tanre, D., Mattoo, S., Chu, D.A., Martins, J.V., Li, R.-R., Ichoku, C., Levy, R., Kleidman, R., Eck, T.F., Vermote, E., 2005. The MODIS Aerosol Algorithm, Products, and Validation. *J. Atmos. Sci.* 62(4), pp.947–973.

Remer, L.A., Mattoo, S., Levy, R., Munchak, L.A., 2013. MODIS 3 km aerosol product: Algorithm and global perspective. *Atmos. Meas. Tech.* 6(7), pp.1829–1844.

- Rémy, S., Veira, A., Paugam, R., Sofiev, M., Kaiser, J.W., Marenco, F., Burton, S.P., Benedetti, A., Engelen, R.J., Ferrare, R., Hair, J.W., 2017. Two global data sets of daily fire emission injection heights since 2003. *Atmos. Chem. Phys.* 17(4), pp.2921–2942.
- Roberts, G., Wooster, M., 2008. Fire detection and fire characterization over Africa using meteosat SEVIRI. *IEEE Trans. Geosci. Remote Sens.* 46(4), pp.1200–1218.
- Roberts, G., Wooster, M., Freeborn, P.H., Xu, W., 2011. Integration of geostationary FRP and polar-orbiter burned area datasets for an enhanced biomass burning inventory. *Remote Sens. Environ.* 115(8), pp.2047–2061.
- Roberts, G., Wooster, M., Lagoudakis, E., 2009. Annual and diurnal african biomass burning temporal dynamics. *Biogeosciences* 6(5), pp.849–866.
- Roberts, G., Wooster, M., Lauret, N., Gastellu-Etchegorry, J.P., Lynham, T., McRae, D., 2018. Investigating the impact of overlying vegetation canopy structures on fire radiative power (FRP) retrieval through simulation and measurement. *Remote Sens. Environ.* 217(March), pp.158–171.
- Roberts, G., Wooster, M., Perry, G.L.W., Drake, N., Rebelo, L.M., Dipotso, F., 2005. Retrieval of biomass combustion rates and totals from fire radiative power observations: Application to southern Africa using geostationary SEVIRI imagery. *J. Geophys. Res. Atmos.* 110(21), pp.1–19.
- Roberts, G., Wooster, M., Xu, W., Freeborn, P.H., Morcrette, J.J., Jones, L., Benedetti, A., He, J., Fisher, D., Kaiser, J.W., 2015. LSA SAF Meteosat FRP products-Part 2: Evaluation and demonstration for use in the Copernicus Atmosphere Monitoring Service (CAMS). *Atmos. Chem. Phys.* 15(22), pp.13241–13267.
- Roberts, G., Wooster, M.J., 2021. Global impact of landscape fire emissions on surface level PM2.5 concentrations, air quality exposure and population mortality. *Atmos. Environ.* pp.118210.
- Roteta, E., Bastarrika, A., Padilla, M., Storm, T., Chuvieco, E., 2019. Development of a Sentinel-2 burned area algorithm: Generation of a small fire database for sub-Saharan Africa. *Remote Sens. Environ.* 222(March), pp.1–17.
- Roy, D.P., Boschetti, L., Justice, C.O., Ju, J., 2008. The collection 5 MODIS burned area product - Global evaluation by comparison with the MODIS active fire product. *Remote Sens. Environ.* 112(9), pp.3690–3707.
- Roy, D.P., Giglio, L., Kendall, J.D., Justice, C.O., 1999. Multi-temporal active-fire based burn scar detection algorithm. *Int. J. Remote Sens.* 20(5), pp.1031–1038.
- Roy, D.P., Lewis, P.E., Justice, C.O., 2002. Burned area mapping using multi-temporal moderate spatial resolution data-a bi-directional reflectance model-based expectation approach. *Remote Sens. Environ.* 83(1–2), pp.263–286.
- San-Miguel-Ayanz, J., Ravail, N., Kelha, V., Ollero, A., 2005. Active fire detection for fire emergency management: Potential and limitations for the operational use of remote sensing. *Nat. Hazards* 35(3), pp.361–376.

- Sayer, A.M., Hsu, N.C., Bettenhausen, C., 2015. Implications of MODIS bowtie distortion on aerosol optical depth retrievals , and techniques for mitigation pp.8727–8752.
- Sayer, A.M., Hsu, N.C., Bettenhausen, C., Jeong, M., 2013. Validation and uncertainty estimates for MODIS Collection 6 “deep Blue” aerosol data. *J. Geophys. Res. Atmos.* 118(14), pp.7864–7872.
- Sayer, A.M., Munchak, L.A., Hsu, N.C., Levy, R., Bettenhausen, C., Jeong, M., 2014. MODIS Collection 6 aerosol products : Comparison between Aqua ' s e-Deep Blue , Dark Target , and “ merged ” data sets ,.
- Schroeder, W., Giglio, L., 2017. Visible Infrared Imaging Radiometer Suite (VIIRS) 375 m & 750 m Active Fire Detection Data Sets Based on NASA VIIRS Land Science Investigator Processing System (SIPS) Reprocessed Data - Version 1.
- Schroeder, W., Oliva, P., Giglio, L., Csiszar, I., 2014. The New VIIRS 375m active fire detection data product: Algorithm description and initial assessment. *Remote Sens. Environ.* 143, pp.85–96.
- Schroeder, W., Prins, E., Giglio, L., Csiszar, I., Schmidt, C.C., Morisette, J.T., Morton, D.C., 2008. Validation of GOES and MODIS active fire detection products using ASTER and ETM+ data. *Remote Sens. Environ.* 112(5), pp.2711–2726.
- Scott, A.C., Glasspool, I.J., 2006. The diversification of Paleozoic fire systems and fluctuations in atmospheric oxygen concentration. *Proc. Natl. Acad. Sci. U. S. A.* 103(29), pp.10861–10865.
- Seiler, W., Crutzen, P.J., 1980. Estimates of gross and net fluxes of carbon between the biosphere and the atmosphere from biomass burning. *Clim. Change* 2(3), pp.207–247.
- Sembhi, H., Wooster, M., Zhang, T., Sharma, S., Singh, N., Agarwal, S., Boesch, H., Gupta, S., Misra, A., Tripathi, S.N., Mor, S., 2020. Post-monsoon air quality degradation across Northern India: Assessing the impact of policy-related shifts in timing and amount of crop residue burnt. *Environ. Res. Lett.* in press.
- Sexton, J.O., Song, X.P., Feng, M., Noojipady, P., Anand, A., Huang, C., Kim, D.H., Collins, K.M., Channan, S., DiMiceli, C., Townshend, J.R.G., 2013. Global, 30-m resolution continuous fields of tree cover: Landsat-based rescaling of MODIS vegetation continuous fields with lidar-based estimates of error. *Int. J. Digit. Earth* 6(5), pp.427–448.
- Shi, Y., Zang, S., Matsunaga, T., Yamaguchi, Y., 2020. A multi-year and high-resolution inventory of biomass burning emissions in tropical continents from 2001–2017 based on satellite observations. *J. Clean. Prod.* 270, pp.122511.
- Skamarock, W.C., Klemp, J.B., Dudhia, J., Gill, D.O., Ziquan, L., Berner, J., Wang, W., Powers, J.G., Duda, M.G., Barker, D.M., Huang, X.-Y., 2019. A Description of the Advanced Research WRF Model Version 4, NCAR Technical Note NCAR/TN-475+STR.
- Smith, A.M.S., Tinkham, W.T., Roy, D.P., Boschetti, L., Kremens, R., Kumar, S.S., Sparks, A.M., Falkowski, M.J., 2013. Quantification of fuel moisture effects on biomass consumed derived from fire radiative energy retrievals. *Geophys. Res. Lett.* 40(23), pp.6298–6302.

- Sobhani, N., 2018. Computational costs of WRF and WRF-Chem simulations [WWW Document]. NCAR.
- Sofiev, M., Ermakova, T., Vankevich, R., 2012. Evaluation of the smoke-injection height from wild-land fires using remote-sensing data. *Atmos. Chem. Phys.* 12(4), pp.1995–2006.
- Su, X., Tie, X., Li, G.H., Cao, J., Huang, R., Feng, T., Long, X., Xu, R., 2017. Effect of hydrolysis of N<sub>2</sub>O<sub>5</sub> on nitrate and ammonium formation in Beijing China: WRF-Chem model simulation. *Sci. Total Environ.* 579, pp.221–229.
- Superczynski, S., Kondragunta, S., Lyapustin, A., 2017. Evaluation of the multi-angle implementation of atmospheric correction (MAIAC) aerosol algorithm through intercomparison with VIIRS aerosol products and AERONET. *J. Geophys. Res.* 122(5), pp.3005–3022.
- Syrakov, D., Prodanova, M., Georgieva, E., Etropolska, I., Slavov, K., 2016. Simulation of European air quality by WRF-CMAQ models using AQMEII-2 infrastructure. *J. Comput. Appl. Math.* 293, pp.232–245.
- Tanre, D., Kaufman, Y., Herman, M., Mattoo, S., 1997. Remote sensing of aerosol properties over oceans using the MODIS/EOS spectral radiances. *J. Geophys. Res. Atmos.* 102(D14), pp.16971–16988.
- Tansey, K., Grégoire, J.M., Defourny, P., Leigh, R., Pekel, J.F., van Bogaert, E., Bartholomé, E., 2008. A new, global, multi-annual (2000-2007) burnt area product at 1 km resolution. *Geophys. Res. Lett.* 35(1), pp.1–6.
- Tie, X., Madronich, S., Li, G.H., Ying, Z., Zhang, R., Garcia, A.R., Lee-Taylor, J., Liu, Y., 2007. Characterizations of chemical oxidants in Mexico City: A regional chemical dynamical model (WRF-Chem) study. *Atmos. Environ.* 41(9), pp.1989–2008.
- Tosca, M.G., Randerson, J.T., Zender, C.S., 2013. Global impact of smoke aerosols from landscape fires on climate and the Hadley circulation. *Atmos. Chem. Phys.* 13(10), pp.5227–5241.
- Tsela, P.L., Wessels, K., Botai, J., Archibald, S., Swanepoel, D., Steenkamp, K., Frost, P., 2014. Validation of the two standard MODIS satellite burned-area products and an empirically-derived merged product in South Africa. *Remote Sens.* 6(2), pp.1275–1293.
- van der Velde, I., van der Werf, G.R., Houweling, S., Eskes, H.J., Veefkind, J.P., Borsdorff, T., Aben, I., 2020. Biomass burning combustion efficiency observed from space using measurements of CO and NO<sub>2</sub> by TROPOMI. *Atmos. Chem. Phys.* (2), pp.1–65.
- van der Werf, G.R., Randerson, J.T., Giglio, L., Collatz, G.J., Kasibhatla, P.S., Arellano, A. F., J., 2006. Interannual variability in global biomass burning emissions from 1997 to 2004. *Atmos. Chem. Phys.* 6(11), pp.3423–3441.
- van der Werf, G.R., Randerson, J.T., Giglio, L., Collatz, G.J., Mu, M., Kasibhatla, P.S., Morton, D.C., Defries, R.S., Jin, Y., Van Leeuwen, T.T., 2010. Global fire emissions and the contribution of deforestation, savanna, forest, agricultural, and peat fires (1997-2009). *Atmos. Chem. Phys.* 10(23), pp.11707–11735.

- van der Werf, G.R., Randerson, J.T., Giglio, L., Van Leeuwen, T.T., Chen, Y., Rogers, B.M., Mu, M., Van Marle, M.J.E., Morton, D.C., Collatz, G.J., Yokelson, R.J., Kasibhatla, P.S., 2017. Global fire emissions estimates during 1997–2016. *Earth Syst. Sci. Data* 9(2), pp.697–720.
- Van Leeuwen, T.T., van der Werf, G.R., 2011. Spatial and temporal variability in the ratio of trace gases emitted from biomass burning. *Atmos. Chem. Phys.* 11(8), pp.3611–3629.
- Van Leeuwen, T.T., van der Werf, G.R., Hoffmann, A.A., Detmers, R.G., Rücker, G., French, N.H.F., Archibald, S., Carvalho, J.A., Cook, G.D., de Groot, W.J., Hély, C., Kasischke, E.S., Kloster, S., McCarty, J.L., Pettinari, M.L., Savadogo, P., Alvarado, E.C., Boschetti, L., Manuri, S., Meyer, C.P., Siegert, F., Trollope, L.A., Trollope, W.S.W., 2014. Biomass burning fuel consumption rates: a field measurement database. *Biogeosciences Discuss.* 11(6), pp.8115–8180.
- Van Wilgen, B.W., Higgins, K.B., Bellstedt, D.U., 1990. The role of vegetation structure and fuel chemistry in excluding fire from forest patches in the fire-prone fynbos shrublands of South Africa. *J. Ecol.*
- Veefkind, J.P., Aben, I., McMullan, K., Förster, H., de Vries, J., Otter, G., Claas, J., Eskes, H.J., de Haan, J.F., Kleipool, Q., van Weele, M., Hasekamp, O., Hoogeveen, R., Landgraf, J., Snel, R., Tol, P., Ingmann, P., Voors, R., Kruizinga, B., Vink, R., Visser, H., Levelt, P.F., 2012. TROPOMI on the ESA Sentinel-5 Precursor: A GMES mission for global observations of the atmospheric composition for climate, air quality and ozone layer applications. *Remote Sens. Environ.* 120(2012), pp.70–83.
- Vermote, E., Ellicott, E., Dubovik, O., Lapyonok, T., Chin, M., Giglio, L., Roberts, G., 2009. An approach to estimate global biomass burning emissions of organic and black carbon from MODIS fire radiative power. *J. Geophys. Res. Atmos.* 114(18), pp.1–22.
- Vongruang, P., Wongwises, P., Pimonsree, S., 2017. Assessment of fire emission inventories for simulating particulate matter in Upper Southeast Asia using WRF-CMAQ. *Atmos. Pollut. Res.* 8(5), pp.921–929.
- Wang, Z., Vodacek, A., Coen, J.L., 2009. Generation of synthetic infrared remote-sensing scenes of wildland fire. *Int. J. Wildl. Fire* 18(3), pp.302–309.
- Westerling, A.L., Hidalgo, H.G., Cayan, D.R., Swetnam, T.W., 2006. Warming and earlier spring increase Western U.S. forest wildfire activity. *Science* (80-. ). 313, pp.940–843.
- Wiedinmyer, C., Akagi, S.K., Yokelson, R.J., Emmons, L.K., Al-Saadi, J.A., Orlando, J.J., Soja, A.J., 2011. The Fire INventory from NCAR (FINN): A high resolution global model to estimate the emissions from open burning. *Geosci. Model Dev.* 4(3), pp.625–641.
- Wiedinmyer, C., Quayle, B., Geron, C., Belote, A., McKenzie, D., Zhang, X., O'Neill, S., Wynne, K.K., 2006. Estimating emissions from fires in North America for air quality modeling. *Atmos. Environ.* 40(19), pp.3419–3432.
- Wolfe, R.E., Nishihama, M., Fleig, A.J., Kuyper, J.A., Roy, D.P., Storey, J.C., Patt, F.S., 2002. Achieving sub-pixel geolocation accuracy in support of MODIS land science. *Remote Sens. Environ.* 83(1–2), pp.31–49.

- Wolfe, R.E., Roy, D.P., Vermote, E., 1998. MODIS Land Data Storage , Gridding , and Compositing Methodology : Level 2 Grid 36(4), pp.1324–1338.
- Wooster, M., 2002. Small-scale experimental testing of fire radiative energy for quantifying mass combusted in natural vegetation fires. *Geophys. Res. Lett.* 29(21), pp.21–24.
- Wooster, M., Freeborn, P.H., Archibald, S., Oppenheimer, C., Roberts, G., Smith, T.E.L., Govender, N., Burton, M., Palumbo, I., 2011. Field determination of biomass burning emission ratios and factors via open-path FTIR spectroscopy and fire radiative power assessment: Headfire, backfire and residual smouldering combustion in African savannahs. *Atmos. Chem. Phys.* 11(22), pp.11591–11615.
- Wooster, M., Gaveau, D.L.A., Salim, M.A., Zhang, T., Xu, W., Green, D.C., Huijnen, V., Murdiyarso, D., Gunawan, D., Borchard, N., Schirrmann, M., Main, B., Sepriando, A., 2018. New tropical peatland gas and particulate emissions factors indicate 2015 Indonesian fires released far more particulate matter (but Less Methane) than current inventories imply. *Remote Sens.* 10(4), pp.1–31.
- Wooster, M., Roberts, G., Freeborn, P.H., Xu, W., Govaerts, Y., Beeby, R., He, J., Lattanzio, A., Fisher, D., Mullen, R., 2015. LSA SAF Meteosat FRP products-Part 1: Algorithms, product contents, and analysis. *Atmos. Chem. Phys.* 15(22), pp.13217–13239.
- Wooster, M., Roberts, G., Smith, A.M.S., Johnston, J.M., Freeborn, P.H., Amici, S., Hudak, A.T., 2013. Thermal Infrared Remote Sensing, Thermal Infrared Remote Sensing: Sensors, Methods, Applications.
- Wooster, M., Zhukov, B., Oertel, D., 2003. Fire radiative energy for quantitative study of biomass burning: Derivation from the BIRD experimental satellite and comparison to MODIS fire products. *Remote Sens. Environ.* 86(1), pp.83–107.
- Wooster, M.J., Roberts, G., Perry, G.L.W., Kaufman, Y.J., 2005. Retrieval of biomass combustion rates and totals from fire radiative power observations: FRP derivation and calibration relationships between biomass consumption and fire radiative energy release. *J. Geophys. Res. Atmos.* 110(24), pp.1–24.
- Worden, H.M., Deeter, M.N., Edwards, D.P., Gille, J.C., Drummond, J.R., Nédélec, P., 2010. Observations of near-surface carbon monoxide from space using MOPITT multispectral retrievals. *J. Geophys. Res. Atmos.* 115(18), pp.1–12.
- Wu, K., Otoo, E., Shoshani, A., 2005. Optimizing connected component labeling algorithms. *Med. Imaging 2005 Image Process.* 5747, pp.1965.
- Xiao, Q., Zhang, H., Choi, M., Li, S., Kondragunta, S., Kim, J., Holben, B., Levy, R., Liu, Y., 2016. Evaluation of VIIRS, GOFCI, and MODIS Collection 6 AOD retrievals against ground sunphotometer observations over East Asia. *Atmos. Chem. Phys.* 16(3), pp.1255–1269.
- Xu, W., Wooster, M., Kaneko, T., He, J., Zhang, T., Fisher, D., 2017. Major advances in geostationary fire radiative power (FRP) retrieval over Asia and Australia stemming from use of Himawari-8 AHI. *Remote Sens. Environ.* 193, pp.138–149.

- Xu, W., Wooster, M., Roberts, G., Freeborn, P.H., 2010. New GOES imager algorithms for cloud and active fire detection and fire radiative power assessment across North, South and Central America. *Remote Sens. Environ.* 114(9), pp.1876–1895.
- Yang, E.S., Christopher, S.A., Kondragunta, S., Zhang, X., 2011. Use of hourly Geostationary Operational Environmental Satellite (GOES) fire emissions in a Community Multiscale Air Quality (CMAQ) model for improving surface particulate matter predictions. *J. Geophys. Res. Atmos.* 116(4), pp.1–13.
- Yang, Z., Wang, J., Ichoku, C., Hyer, E.J., Zeng, J., 2013. Mesoscale modeling and satellite observation of transport and mixing of smoke and dust particles over northern sub-Saharan African region. *J. Geophys. Res. Atmos.* 118(21), pp.12139–12157.
- Yevich, R., Logan, J.A., 2003. An assessment of biofuel use and burning of agricultural waste in the developing world. *Global Biogeochem. Cycles* 17(4), pp.n/a-n/a.
- Yu, S., Eder, B., Dennis, R., Chu, S.-H., Schwartz, S.E., 2006. New unbiased symmetric metrics for evaluation of air quality models. *Atmos. Sci. Lett.* 7(1), pp.26–34.
- Yurganov, L.N., McMillan, W.W., Dzhola, A. V., Grechko, E.I., Jones, N.B., van der Werf, G.R., 2008. Global AIRS and MOPITT CO measurements: Validation, comparison, and links to biomass burning variations and carbon cycle. *J. Geophys. Res. Atmos.* 113(9), pp.1–14.
- Zhang, F., Wang, J., Ichoku, C., Hyer, E.J., Yang, Z., Ge, C., Su, S., Zhang, X., Kondragunta, S., Kaiser, J.W., Wiedinmyer, C., Da Silva, A., 2014. Sensitivity of mesoscale modeling of smoke direct radiative effect to the emission inventory: A case study in northern sub-Saharan African region. *Environ. Res. Lett.* 9(7).
- Zhang, L., Jacob, D.J., Downey, N. V., Wood, D.A., Blewitt, D., Carouge, C.C., van Donkelaar, A., Jones, D.B.A., Murray, L.T., Wang, Y., 2011. Improved estimate of the policy-relevant background ozone in the United States using the GEOS-Chem global model with  $1/2^\circ \times 2/3^\circ$  horizontal resolution over North America. *Atmos. Environ.* 45(37), pp.6769–6776.
- Zhang, T., Wooster, M., de Jong, M.C., Xu, W., 2018. How Well Does the ‘Small Fire Boost’ Methodology Used within the GFED4.1s Fire Emissions Database Represent the Timing, Location and Magnitude of Agricultural Burning? *Remote Sens.* 10(6), pp.823.
- Zhang, T., Wooster, M., Xu, W., 2017. Approaches for synergistically exploiting VIIRS I- and M-Band data in regional active fire detection and FRP assessment: A demonstration with respect to agricultural residue burning in Eastern China. *Remote Sens. Environ.* 198, pp.407–424.
- Zhang, X., Kondragunta, S., Ram, J., Schmidt, C., Huang, H.-C., 2012. Near-real-time global biomass burning emissions product from geostationary satellite constellation. *J. Geophys. Res. Atmos.* 117(D14), pp.n/a-n/a.
- Zhang, X., Kondragunta, S., Schmidt, C., Kogan, F., 2008. Near real time monitoring of biomass burning particulate emissions (PM2.5) across contiguous United States using multiple satellite instruments. *Atmos. Environ.* 42(29), pp.6959–6972.
- Zhang, X., Liu, J., Han, H., Zhang, Y., Jiang, Z., Wang, H., Meng, L., Li, Y.C., Liu, Y., 2020.

Satellite-observed variations and trends in carbon monoxide over Asia and their sensitivities to biomass burning. *Remote Sens.* 12(5).

Zhou, L., Wang, Y., Chi, Y., Wang, S., Wang, Q., 2019. Contrasting post-fire dynamics between Africa and South America based on MODIS observations. *Remote Sens.* 11(9).

Zhukov, B., Briess, K., Lorenz, E., Oertel, D., Skrbek, W., 2005. Detection and analysis of high-temperature events in the BIRD mission. *Acta Astronaut.* 56(1–2), pp.65–71.

Zhukov, B., Lorenz, E., Oertel, D., Wooster, M., Roberts, G., 2006. Spaceborne detection and characterization of fires during the bi-spectral infrared detection (BIRD) experimental small satellite mission (2001–2004). *Remote Sens. Environ.* 100(1), pp.29–51.

# Appendix A

Legend for the class codes of the CCI Landcover map used in the derivation of the six biomes of FREMv2 (**Table 4.1**).

Value	Label	Color
0	No Data	
10	Cropland, rainfed	
11	Herbaceous cover	
12	Tree or shrub cover	
20	Cropland, irrigated or post-flooding	
30	Mosaic cropland (>50%) / natural vegetation (tree, shrub, herbaceous cover) (<50%)	
40	Mosaic natural vegetation (tree, shrub, herbaceous cover) (>50%) / cropland (<50%)	
50	Tree cover, broadleaved, evergreen, closed to open (>15%)	
60	Tree cover, broadleaved, deciduous, closed to open (>15%)	
61	Tree cover, broadleaved, deciduous, closed (>40%)	
62	Tree cover, broadleaved, deciduous, open (15-40%)	
70	Tree cover, needleleaved, evergreen, closed to open (>15%)	
71	Tree cover, needleleaved, evergreen, closed (>40%)	
72	Tree cover, needleleaved, evergreen, open (15-40%)	
80	Tree cover, needleleaved, deciduous, closed to open (>15%)	
81	Tree cover, needleleaved, deciduous, closed (>40%)	
82	Tree cover, needleleaved, deciduous, open (15-40%)	
90	Tree cover, mixed leaf type (broadleaved and needleleaved)	
100	Mosaic tree and shrub (>50%) / herbaceous cover (<50%)	
110	Mosaic herbaceous cover (>50%) / tree and shrub (<50%)	
120	Shrubland	
121	Evergreen shrubland	
122	Deciduous shrubland	
130	Grassland	
140	Lichens and mosses	
150	Sparse vegetation (tree, shrub, herbaceous cover) (<15%)	
151	Sparse tree (<15%)	
152	Sparse shrub (<15%)	
153	Sparse herbaceous cover (<15%)	
160	Tree cover, flooded, fresh or brakish water	
170	Tree cover, flooded, saline water	
180	Shrub or herbaceous cover, flooded, fresh/saline/brakish water	
190	Urban areas	
200	Bare areas	
201	Consolidated bare areas	
202	Unconsolidated bare areas	
210	Water bodies	
220	Permanent snow and ice	

## Appendix B

The trace gas and aerosol emission coefficients for CMAQ species used to produce emissions input into the CMAQ model (**Section 5.2.2**), calculated for each biome from the application of **Equation 4.3** to the emission factors of Andreae (2019). Specification of each species is detailed at ([https://github.com/USEPA/CMAQ/tree/master/CCTM/src/MECHS/mechanism\\_information/cb6r3\\_ae7\\_aq](https://github.com/USEPA/CMAQ/tree/master/CCTM/src/MECHS/mechanism_information/cb6r3_ae7_aq))

CMAQ Model Species	Closed canopy forest	High-woodland savanna	Low-woodland savanna	Shrubland	Grassland	Managed lands
AACD	7.83	3.76	2.82	2.63	2.49	5.72
ACET	1.50	0.76	0.57	0.53	0.51	0.67
ALD2_PRIMAR	0.00	0.21	0.16	0.15	0.14	3.00
BENZENE	0.90	0.53	0.40	0.37	0.35	0.25
CH4	15.39	4.42	3.32	3.09	2.93	5.42
CO	248.65	112.49	84.49	78.54	74.49	72.05
CO2	3855.20	2692.21	2022.01	1879.61	1782.78	1352.31
ETH	2.64	1.35	1.02	0.94	0.90	0.94
ETHA	2.10	0.68	0.51	0.47	0.45	0.74
ETOH	0.00	0.06	0.04	0.04	0.04	0.00
FACD	1.16	0.34	0.25	0.24	0.22	0.53
FORM_PRIMA	5.72	2.00	1.50	1.39	1.32	1.71
HCL	0.00	0.22	0.16	0.15	0.14	0.17
HONO	2.03	0.77	0.58	0.54	0.51	0.35
IOLE	23.91	18.91	14.20	13.20	12.52	2.82
ISOP	0.52	0.16	0.12	0.11	0.11	0.05
MEOH	6.67	2.19	1.65	1.53	1.45	3.09
NH3	3.18	1.45	1.09	1.02	0.96	0.93
NO2	6.71	4.04	3.04	2.82	2.68	2.27
OLE	0.00	0.00	0.00	0.00	0.00	7.24
PEC	1.21	0.87	0.65	0.60	0.57	0.43
PK	0.77	0.65	0.48	0.45	0.43	0.45
PM25	19.85	10.90	8.19	7.61	7.22	7.70
PMOTHER	1.67	2.12	1.60	1.48	1.41	1.09
POC	10.61	4.94	3.71	3.45	3.27	2.87
PRPA	1.27	0.22	0.16	0.15	0.14	0.15
SO2	1.83	0.76	0.57	0.53	0.50	0.73
TERP	40.21	0.17	0.13	0.12	0.11	0.01
TOLU	0.00	0.31	0.23	0.22	0.21	0.16

## Appendix C

The fractional coverage of the closed canopy forest biome in Southern Africa according to the FREMv2 biome map developed in **Section 4.4.1** based on the CCI Landcover map derived from 300 m PROBA-V imagery.

